Durham E-Theses

FUNCTIONALISATION OF CARBON NANOMATERIALS WITH BIOMOLECULES

AHMED, BNAR,JAWDAT

How to cite:

Use policy

FUNCTIONALISATION OF CARBON

NANOMATERIALS WITH BIOMOLECULES

A thesis submitted for the partial fulfilment of the requirement for the

Degree of

Doctor of Philosophy

In the faculty of Science of

Durham University

By

Bnar J. Ahmed

Durham University

Department of Chemistry

University Science Laboratories

South Road

Durham

2015

Abstract

Carbon nanomaterials, including carbon nanotubes and graphene, with various unique physical and chemical properties are emerging as extraordinary materials for biomedical applications. The aim of this thesis was to functionalise single walled carbon nanotubes and reduced graphene oxide with range of biomolecules including, peptides, peptoids, and ribonucleosides.

The first study investigated the noncovalent interaction between single walled carbon nanotubes and fluoro tagged nano-1 peptide with ^{19}F NMR.

In the second study single walled carbon nanotubes were noncovalently functionalised with a series of antibacterial, chiral, amphiphilic peptoids. The peptoids varied in the number of aromatic residues on the hydrophobic surface of the helix. It was found that peptoid's ability to individually disperse single walled carbon nanotubes increased with increasing the number of aromatic residues.

The third study presented the first experimental noncovalent interaction of ribonucleosides, nucleobases, and ribose with purified and oxidised single walled carbon nanotubes. It was found that cyclic and aromatic ribonucleosides and nucleobases are too small to disperse the hydrophobic nanotube surface by π-π stacking. Furthermore, results showed that the ribonucleosides dispersion ability towards nanotubes depends on the number of oxygen-containing functional groups on the nanotube surface.

In the final research it was found that the flat rigid surface of reduced graphene oxide has a critical role in its noncovalent interaction with peptides and peptoids. Results

showed that biomolecules with higher backbone flexibility can give a higher dispersion affinity towards reduced graphene oxide. Also, it was found that ribonucleosides and their nucleases, and ribose moieties have very limited dispersion affinity towards reduced graphene oxide. Finally, the covalent functionalisation of reduced graphene oxide with cell penetrating peptoid, thymidine, and adenosine was investigated.

Declaration

This work was conducted in the Department of Chemistry at Durham University between September 2011 and August 2015. The work has not been submitted for a degree in this, or any other university. It is my own work, unless otherwise indicated.

Copyright

Acknowledgements

While my name may be alone on the front cover of this thesis, I am by no means its sole contributor. Rather, there are a number of people behind this piece of work who deserve to be both acknowledged and thanked here. First of all, I am forever indebted to my academic supervisors, Prof. Karl Coleman and Dr. Steven Cobb, for their enthusiasm, guidance, patience, and unrelenting support throughout this process.

I would like to acknowledge the members of the Coleman group who have routinely gone beyond their work to fire fight my worries, concerns, anxieties, and answering every question I have ever asked them, you shall always be remembered with a smiling face; postdocs: Dr. David Johnson and Dr. Stephen Boothroyd, soon to be doctors: Ben Dobson, Robert Mora, Mike Tynan, and Lucinda Clarke. I would like to give my special thanks to Dr. Rebecca Edwards, Dr. Lara Small, and Dr. Gabriella Eggimann. In addition, these acknowledgements would not be complete without thanking my current and previous Cobb group members. I have to thank Mr. Douglas Carswell to conducting all the TGA measurements of my samples and for his support and friendship. Also I would like to thank Dr. Alan Kenwright for providing NMR analysis.

I am grateful to the Kurdistan Regional Government KRG, Ministry of Higher Education, and Scientific Research, HCDP programme, which provided me with the financial support to pursue my PhD degree.

Dedication

I dedicate this thesis to my family for their constant support and unconditional love.

Table of Content

List of Figures

List of Schemes

List of Tables

List of Abbreviations

0D	Zero dimensional
2D	Two dimensional
3D	Three dimensional
CNTs	Carbon nanotubes
SWNTs	Signal walled carbon nanotubes
DWNTs	Double walled carbon nanotubes
MWNTs	Multi walled carbon nanotubes
GO	Graphene oxide
rGO	Reduced graphene oxide
HiPco	High pressure decomposition of CO
EA	Electric arc discharge
CVD	Chemical vapour deposition
LA	Laser ablation
DCM	Dichloromethane
DMF	Dimethylformamide
DTT	Dithiothreitol
TFA	Trifluoroacetic acid
TFE	2,2,2-Trifluoroethanol
EtOAc	Ethyl acetate
Sphos	Bis(dibenzylideneacetone)palladium (Pd(dba)$_2$) and 2-Dicyclohexylphosphino-2′,6′-dimethoxybiphenyl

Pd(dba)$_2$	Bis(dibenzylideneacetone)palladium(0)
AFM	Atomic force microscopy
TEM	Transmission electron microscopy
TGA	Thermogravimetric analysis
TGA-MS	Thermogravimetric analysis–mass spectrometry
UV-Vis-NIR	Ultraviolet–visible-near infrared spectroscopy
CD	Circular dichroism
MS	Mass spectrometry
HR-MS (ESI-TQD)	High resolution electrospray ionisation mass spectrometry:
LR-MS (ESI-TQD)	Low resolution electrospray ionisation mass spectrometry
MALDI-TOF	Matrix assisted laser desorption/ionisation–time of flight
RP-HPLC	Reverse phase high-performance liquid chromatography
SDS	Sodium dodecylsulfate
PBS	Phosphate buffered saline
PyBOP	Benzotriazol-1-yl-oxytripyrrolidino phosphonium hexafluorophosphate
DIEA	Diisopropylethylamine
TBTU	O-(Benzotriazol-1-yl)-N,N,N′,N′-tetramethyluronium tetrafluoroborate
TIPS	Triisopropylsilane
Fmoc-SPPS	Fmoc solid phase peptide synthesis
Fmoc	9H-fluoren-9-ylmethoxycarbonyl xi
Boc	tert-butoxycarbonyl

Ala, A	Alanine
Arg, R	Arginine
Glu, E	Glutamic Acid
Gln, Q	Glutammine
Gly, G	Glycine
His, H	Histidine
Phe, F	Phenylalanine
Ser, S	Serine
Trp, W	Tryptophan

Chapter 1

1. THESIS AIMS AND OUTLINE

Many potential applications have been proposed for carbon nanomaterials, carbon nanotubes (CNTs) and graphene, in the fields of nanotechnology, biology, and medicine. For biomedical and biological purposes, the dispersion of carbon nanomaterials in aqueous solvents is a major criteria for their biocompatibility and their bioapplications; hence the use of their composites in therapeutic delivery should meet this basic prerequisite. However, the difficulty of the solubilisation of pristine carbon nanomaterials in aqueous solvents is a potential obstacle to realising their application, mainly due to their hydrophobic character which, coupled with the strong π–π interactions, causes them to aggregate as bundles. Since the unique structure of biomolecules, such as peptide, protein and DNA, endow them with their distinctive biological functions, there is increasing interest in the combination of biomolecules with CNTs unique properties, such as high aspect ratio, light weight, high mechanical strength and electrical and thermal conductivity. However, so far the nature of this interaction yet in not well understood. Thus the aim of this thesis is to investigate the aqueous covalent and noncovalent functionalisation of single walled carbon nanotubes (SWNTs) and graphene based nanomaterials, with a series of biomolecules, including peptides, peptoids, and ribonucleosides in water, both to improve the carbon nanomaterial dispersibility in water and to gain a better understanding of the nature of the interactions. The outline of this thesis is as follows:

Chapter 1

Chapter 2 introduces the CNT and its production methods, properties, purification methods, and functionalisation techniques. It further reviews the literature on the biomolecules used for the dispersion of SWNTs.

Chapter 3 summarises the analytical techniques that have been used in this thesis to characterise CNTs and biomolecules. A brief background of the techniques is provided; but the focus is on how these techniques can be used to analyse CNTs and biomolecules.

Chapter 4 investigates the effect of the N-terminus acetylation of nano-1 peptide on its ability to disperse SWNTs. Additionally; this chapter studies the use of ^{19}F NMR to monitor the binding between a fluorinated nano-1 peptide and the SWNTs surface. Finally, the stability of the nano-1 peptide/SWNT complex against enzyme digestion is investigated.

Chapter 5 investigates the synthesis and characterisation of a series of chiral linear peptoids and their noncovalent interaction with SWNTs which aid dispersion in aqueous medium.

Chapter 6 investigates the interaction between ribonucleosides and SWNTs in aqueous medium. The combined effect of ribonucleoside substituent groups and the oxygen-containing functional groups of the SWNT surfaces on adsorption are investigated

Chapter 7 studies the covalent and noncovalent functionalisation of rGO with biomolecules, specifically peptide, peptoid, and ribonucleosides. The difference in interaction between peptides and peptoids with rGO is explored. The covalent

functionalisation sections studies the functionalisation of rGO with cell penetrating peptoid and ribonucleosides to improve its solubility in water.

Chapter 8 summaries the thesis results and future work of the whole thesis.

2. INTRODUCTION TO CARBON NANOTUBES

2.1.   Background

After the discovery of fullerenes by Kroto *et al*,[1] in 1985, it became evident that sp[2] hybridised graphene layers exist not only in planar honeycomb sheets like in graphite, but also in spherically curved and closed cages. Later, in 1991, Sumio Iijima synthesised and studied a cylindrical form of the buckyball, known as a carbon nanotube. Initially double walled carbon nanotubes (DWNTs) and multi walled carbon nanotubes (MWNTs) were reported along with their crystal structures.[2] Two years later single walled carbon nanotubes (SWNTs) were independently synthesised by Iijima and Ichihashi,[3] and Bethune *et al*.[4] Since then, carbon nanotubes (CNTs) have attracted considerable research interest across a range of disciplines, including physics, chemistry, materials science, medicine, and engineering, owing to their extremely interesting properties and potential for a range of applications.

2.2.   Structure of Carbon Nanotubes

In general, CNTs can be described as a graphene sheet that is rolled into a seamless cylinder and capped with half a buckyball at both ends. Similar to graphite, the structure of a CNT is the orientation of the six-membered carbon bonds (called hexagonal) in the honeycomb periodic lattice along the axis of the nanotube.

Although CNTs and graphite are built of the same basic units, hexagons of sp^2 hybridised carbon atoms, there is a substantial difference between the physio-chemical properties of these materials. A CNT can be viewed as a hollow cylinder formed by seamlessly rolling a graphene sheet capped at both ends in a hemispherical arrangement of carbon networks (**Figure 2-1**).
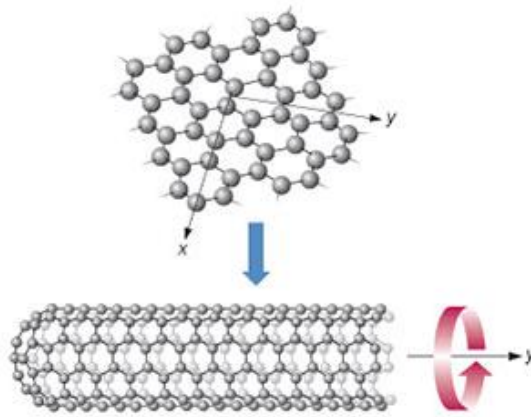
Figure 2-1: Rolling up a graphene sheet to form a nanotube.

The closure of the cylinder results from the inclusion of pentagonal and heptagonal structures during the growth process. Therefore, the character of C–C bonds in CNTs differs from that of graphite as the carbon atoms in a nanotube are pyramidalised due to the curvature of the nanotube sidewall. Additionally, their curvature will cause quantum confinement and σ–π rehybridisation.[5]
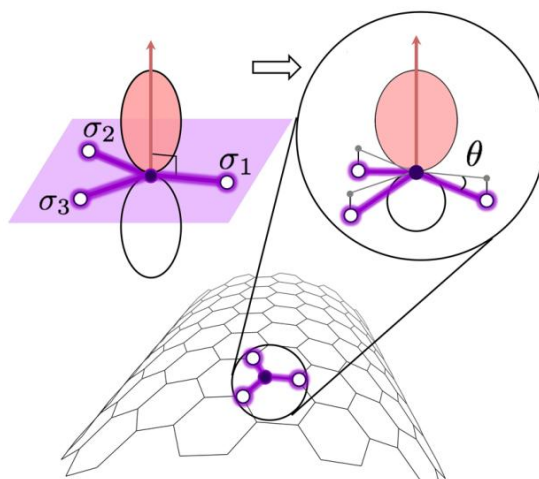
Figure 2-2: Diagram showing the π–orbital in planar graphene and its change when bent to from CNTs. Reprinted figure with permission from (6). Copyright (2011) by the American Physical Society.

As shown in **Figure 2-2**, the three σ bonds which lie in the sp^2 plane are slightly shifted out of plane. As a result, the π–orbital is more delocalised outside the nanotube. That is a big difference with respect to graphite in which the sp^2 hybrid orbitals form three in-plane σ bonds with an out-of-plane π–orbital. The electron cloud distortion induced by the curvature, yields a rich π–electron conjugation outside the tube. This can make CNTs more electrochemically active and electrically and thermally more conductive than graphite. In addition, the CNTs curvature allows topological defects such as pentagons and heptagons to be incorporated into the hexagonal network to form capped, bent, toroidal, and helical nanotubes. The electrons will be localised in pentagons and heptagons because of redistribution of π electrons.

2.2.1.   Types of Carbon Nanotubes

The number of cylinders that constitute a CNT can vary from one to several, giving rise to different kinds of CNTs, namely single walled carbon nanotubes (SWNTs), double walled carbon nanotubes (DWNTs) up to generic multi walled carbon nanotubes (MWNTs).[7] MWNTs were the first to be characterised at atomic resolution (1991)[2,8] followed by their single walled counterparts in 1993[3,4] (**Figure 2-3**). MWNTs generally have a larger outer diameter (2.5-100 nm) than SWNTs (0.6-2.4 nm) and consist of a varying number of concentric SWNT layers, with an interlayer separation of ~ 0.34 nm.[9] SWNTs have a better defined diameter, while MWNTs are more likely to have structural defects, resulting in a less stable nanostructure.[10,11] SWNTs and MWNTs are often seen as straight or elastic bending structures individually or in ropes.
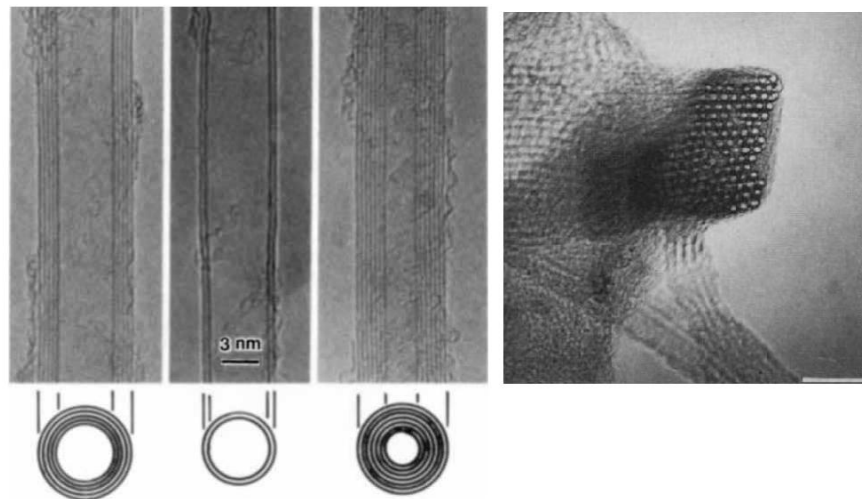
Figure 2-3: High resolution TEM images of CNTs: (**Left**) MWNTs with varying number of graphene layers 5, 2, and 7, Reprinted by permission from Macmillan Publishers Ltd: [Nature] [2], copyright (1991), (**Right**) bundled SWNTs, from [12]. Reprinted with permission from AAAS.

Chapter 2

2.2.2. Chirality of Carbon Nanotubes

The size and orientation of the rolled graphene layer are essential for the structure of the nanotube and therefore its properties.[13] The angle between C–C bonds and the axis of the tube can vary, and the so-called chirality of a SWNT depends on this angle. Therefore, the atomic structure of SWNTs may be described by the tube chirality, or helicity, which is defined by the chiral vector (C_h) and the chiral angle (θ).[14] The chiral vector can be described in terms of the lattice translational indices (n, m) and the unit vectors a_1 and a_2, as shown in equation below:

$$C_h = na_1 + ma_2$$

Where a_1 and a_2 are the unit factors and n and m (integers) are the steps along the directions. The chiral angle θ, determining the degree of "twisting" of the tube, is defined as the angle between the vectors C_h and a_1, which varies in the $0° \leq |\theta| \leq 30°$ range.[15,16] Thus, according to the rolling angle of the graphene sheet, SWNTs can be classified into two groups' structure wise, achiral and chiral. Achiral carbon nanotubes are defined as a SWNT whose mirror image has an identical structure to the original one. The achiral tubes are known as armchair ($\theta = 30°$) and zig–zag ($\theta = 0°$) as shown in **Figure 2-4**.
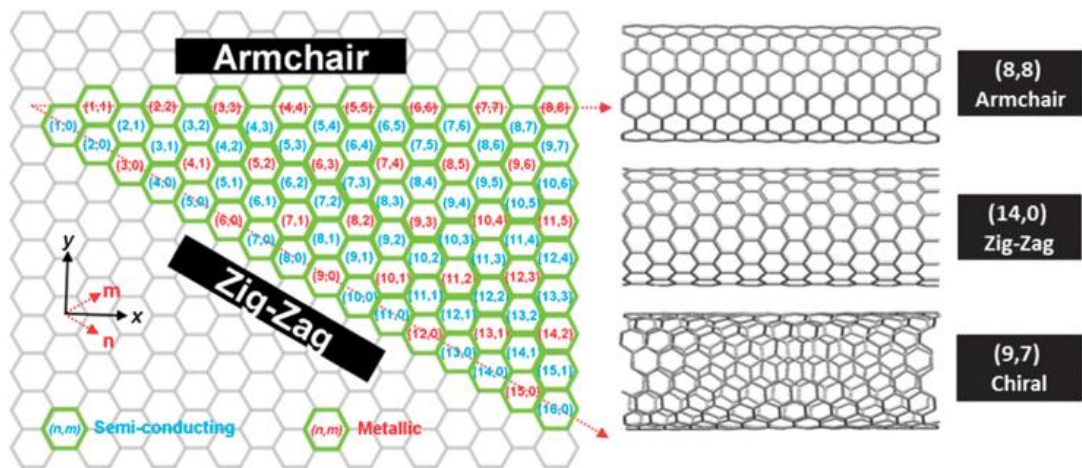
Figure 2-4: SWNT helicity map and examples of (*n*, *m*) chiral vectors that give rise to armchair, zig–zag and chiral nanotube structures with metallic or semi-conducting electronic character. Reproduced from [17] with permission of The Royal Society of Chemistry.

Despite the structural similarity to a single sheet of graphite (graphene), which is a semiconductor with zero bandgap, CNTs may be either metallic or semiconducting.[18] In general, SWNTs are a mixture of metallic and semiconducting material, while MWNTs are regarded as metallic conductors.[19] If the difference n - m is non-zero and divisible by three, the nanotube is considered semi-metallic with a bandgap of the order of meV. If the difference is equal to zero, the nanotube is metallic with a bandgap of zero and is referred to as an armchair-type nanotube. In all other cases where the difference n − m is non-zero and not divisible by three the nanotube is semiconducting with a band gap ranging from approximately 0.5 to 1 eV.[20]

2.3. Synthesis of Carbon Nanotubes

The unique chemical and physical properties of CNTs are determined by the structure of CNTs. Therefore, the synthesis of CNTs with a controlled diameter, chirality, number of graphite layers, length and quality has been a crucial part of CNT research. Several techniques have been successfully applied for the production of CNTs, including electric arc-discharge (EA) method, laser ablation (LA), chemical vapour deposition (CVD), and high pressure decomposition of CO (HiPco). Each technique has both advantages and challenges.

2.3.1. Electric Arc-Discharge (EA)

The electric arc-discharge method (EA), initially used for producing C_{60} fullerenes,[21] was the first reported and is still one of the most widely used techniques for the production of SWNTs.[2] Both fullerenes and nanotubes can be produced once the synthesis conditions are optimised. In this method, an electric arc is struck between two pure graphite electrodes in an inert atmosphere, such as of helium or argon. The arc produces temperatures of around 3000 °C, causing the graphite to evaporate. CNTs are formed by consuming the positive electrode during the process and depositing it on the negative electrode, accompanied by nanoparticles or disordered carbon.[3,22] **Figure 2-5** shows a schematic diagram of an arc-discharge system.
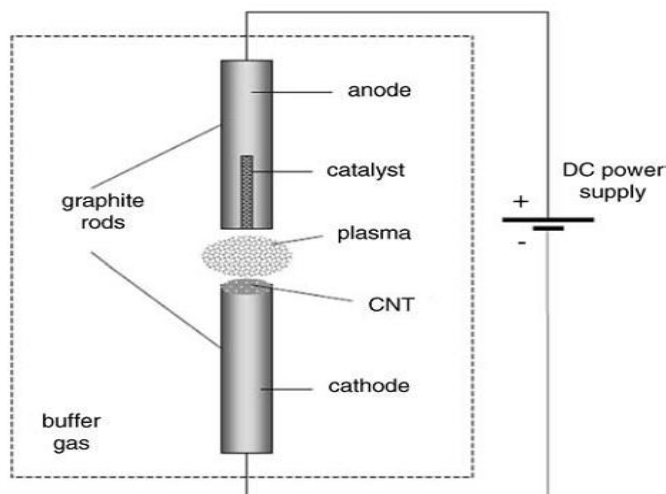
Figure 2-5: Schematic diagram of an arc-discharge system. Reproduced from [23] with permission of John Wiley and Sons.

If both electrodes are graphite and without catalysts, the main product will be MWNTs. Typical sizes for MWNTs are an inner diameter of $1 - 3$ nm and an outer diameter of approximately 10 nm. In order to produce SWNTs, the anode has to be doped with a metal catalyst, such as a transition metal.[3,4,24,25] Usually the diameter of SWNTs is in the range of 1.2 to 1.4 nm. The quantity and quality of the nanotubes obtained depend on various parameters such as the metal concentration, inert gas pressure, kind of gas, the current and system geometry.[26] By adjusting the pressure and catalyst carefully, the diameter of SWNTs and MWNTs can be controlled to a certain degree. Compared to other methods, arc discharge is a more common and easy way to produce a less defective, large scale product. However, more by-products such as amorphous carbon, multi-shell graphite particles and catalytic metal particles are formed during the process and are typically present in amounts up to 30 % by weight of the product.[25]

2.3.2.   Laser Ablation (LA)

The laser ablation technique for synthesising CNTs was first reported by Guo *et al* in 1995.[27,28] In this method, a graphite target containing small amount of catalyst particles is vaporised by an intense laser beam at a temperature of around 1200 °C in an inert atmosphere. The nanotubes formed are then brought away from the high temperature region by an inert gas flow and cooled down on a collector.[27] **Figure 2-6** shows the laser ablation setup.
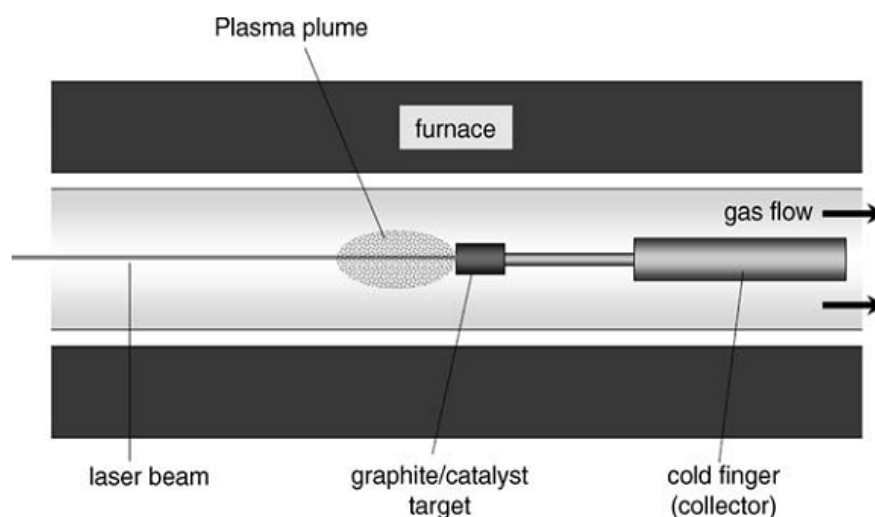
Figure 2-6: Schematics of a laser ablation setup for production of CNTs. Reproduced [23] with permission of John Wiley and Sons.

CNTs produced by laser ablation are purer (up to about 90 % purity) than those produced in the arc discharge process.[12] The average nanotube diameter and diameter distribution is found to vary according to the growth temperature, catalyst composition and other process parameters. Unfortunately, the laser technique is not economically advantageous because the process requires high-purity graphite rods, the laser powers required are high, and the amount of SWNTs that can be produced per day is not as high as the arc-discharge method.[27]

2.3.3. Chemical Vapour Deposition (CVD)

Chemical vapour deposition of hydrocarbons over a metal catalyst is a classical method that since the 1960s has been used to produce various carbon materials like carbon fibers and filaments.[29] Both SWNTs and MWNTs can be grown using a similar approach by decomposing an organic gas over a substrate covered with metal catalyst particles.[30] **Figure 2-7** shows CVD setup for nanotube synthesis.
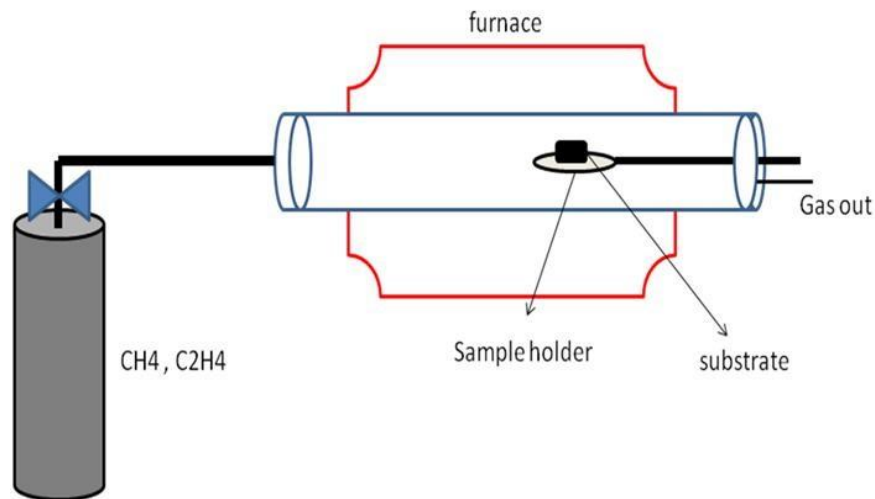
Figure 2-7: Schematics of a CVD deposition oven. Adapted from [31].

Generally, CVD process includes catalyst assisted decomposition of hydrocarbons in a tube reactor at high temperatures. A typical set up for the growth of carbon nanotubes includes blowing acetylene over cobalt and iron catalysts supported on silica or zeolite.[32,33] Although this method is very easy to scale up, it results in a relatively high density of defects along the nanotube walls,[34] which is prohibitive for commercial uses.

2.3.4. High Pressure Decomposition of CO (HiPco)

The high pressure CO disproportionation process (HiPco) is a technique for catalytic production of SWNTs in a continuous-flow gas phase using CO as the carbon feedstock.[35,36] The catalysts used in the HiPco process are formed in the gas phase from a volatile organometallic catalyst precursor introduced into the reactor. The organometallic species decomposes at high temperature, forming metal clusters on which SWNTs nucleate and grow. In this method, SWNTs are produced by flowing CO, mixed with a small amount of the catalyst, such as $Fe(CO)_5$ through a heated reactor. **Figure 2-8** shows the layout of a CO flow-tube reactor.
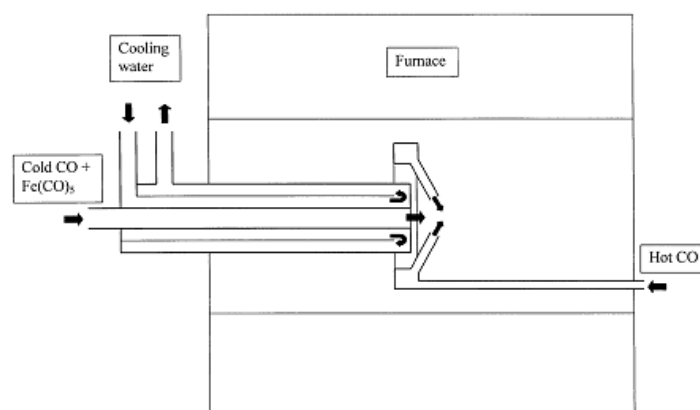
Figure 2-8: Layout of CO flow-tube reactor, showing water-cooled injector and 'showerhead' mixer. Reprinted from [36], Copyright (1999), with permission from Elsevier.

The average diameter of HiPco SWNTs is approximately 1.1 nm, which is typically smaller than SWNTs produced by the laser-oven process, where the average diameter is about 1.3 − 1.4 nm. The dominant impurity in HiPco nanotubes is the metal catalyst, which is encased in thin carbon shells and distributed throughout the sample as 3 − 5 nm size particles.[37] Compared with other techniques, production by

the HiPco method has the advantages of high quality, ease of purification and large scale commercial products.

2.4.   Purification of Carbon Nanotubes

Regardless of the method used for their production, CNTs always contain a number of impurities that are an impediment to more detailed characterisation of their properties and thus their future applications.[13] The most prominent impurities are metallic catalyst particles, amorphous carbon, carbon nanoparticles containing metals, fullerenes, and polyaromatic fragments of graphene sheets. The basic principle of the purification techniques takes the advantage of difference in aspect ratio, oxidation rate between CNTs and carbonaceous impurities, solubility of CNTs, size of CNTs. Thus, purification techniques of CNTs can be categorised into two main group's namely chemical and physical methods. **Figure 2-9** shows the difference between as-synthesised CNTs and chemical and physically purified CNTs.
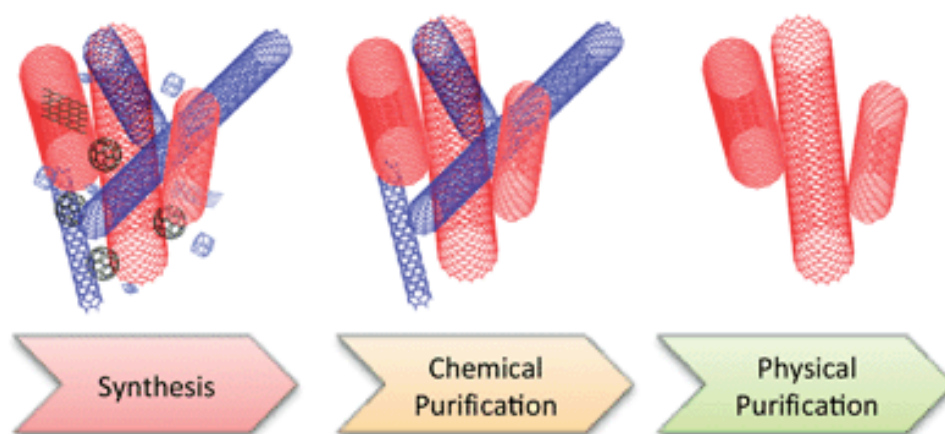
Figure 2-9: Difference between as-synthesised CNTs, chemically and physically purified CNTs. Reproduced from [38] with permission of The Royal Society of Chemistry.

The chemical purification techniques separate CNTs as a function of their reactivity. Compared with CNTs carbonaceous impurities are easily oxidised due to the presence of more dangling bonds and structural defects. The most commonly used chemical purification involves the oxidation of as-synthesised CNTs in both wet and dry conditions, due to the method's practicality, relative simplicity, applicability to both metal catalysts and amorphous carbons, and capability of purifying large quantities of nanotubes. Moreover, oxidation techniques can often introduce oxygenated functional groups, such as carboxylic acids, which serve as a good starting point for subsequent nanotube surface chemistry.[39] The wet condition generally refers to the oxidation using a solution of concentrated acids or strong oxidants; meanwhile the dry condition mainly refers to the oxidation by air, oxygen, or other gases at a controlled temperature. Gas phase oxidation is based on the principle of a selective oxidative etching process, wherein the other carbonaceous species are oxidised at a faster rate than the actual CNTs themselves. After destruction of carbonaceous species, such as amorphous carbon and graphitic carbon layers, the metal catalysts can be removed using acid treatment (e.g. HCl washing). Meanwhile, liquid phase oxidation is most commonly used and typically involves reacting CNTs with oxidising agent (HNO_3, HCl, $KMnO_4/H_2SO_4$, etc.) and/or refluxing in water or H_2O_2. The hydrochloric acid, however, can only attack directly accessible metal particles, whereas concentrated nitric acid leads to quite an efficient removal of metal because the oxidising power of the acid enables it to attack CNTs side wall and even to open the closed tips of nanotubes by generating functional groups containing oxygen, like COOH, C=O, etc. However, upon prolonged acidic action and at high density of defects, the tubes are markedly reduced in length. Thus, the main disadvantage of liquid phase treatments is that they tend to destroy not only

impurities but also the nanotubes. However, with proper control of the reaction conditions, purification of as-synthesised CNTs through the removal of metal catalyst particles may result in higher purity as well as the tips opening.

Besides the removal of foreign material, there is another crucial aspect in the purification of CNTs. Any of the procedures presented in **Sections 2.3** yields tubes with different structure indices (n, m), that vary in diameter and electronic properties. In general, the physical purification techniques are used to remove graphitic sheets, carbon nanospheres (CNSs), aggregates or separate CNTs with different diameter/length ratios. They are based on the differences in diameter, physical size, aspect ratio, gravity and magnetic properties etc. Although they are relatively mild and do not cause severe damages to the tubes, they are normally more complex and less effective compared to the chemical methods, thus leading to a lower purity of CNTs.

2.5.   Properties of Carbon Nanotubes

2.5.1.   Chemical Properties

CNTs and graphite are built of the same basic units, hexagons of sp^2 hybridised carbon atoms. However, the curvature-induced pyramidalisation and misalignment of the π-orbitals of the carbon atoms in CNTs induces a local strain,[40-42] thus CNTs are expected to be more reactive than a flat graphene sheet (**Figure 2-10**).
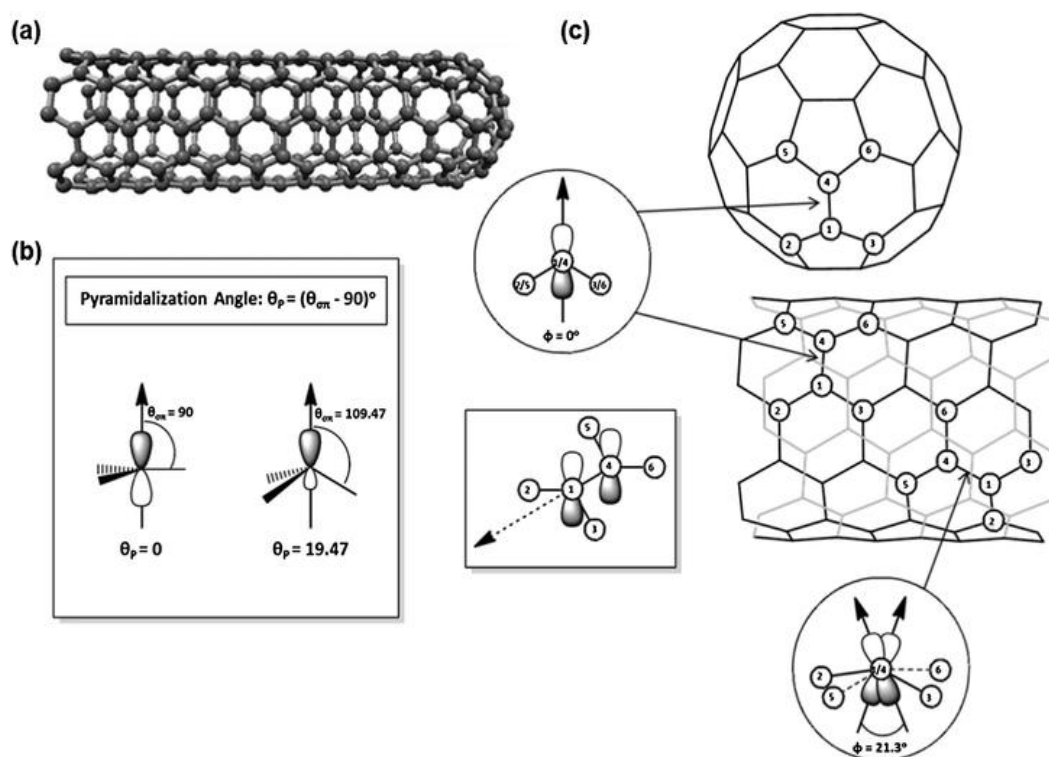
Figure 2-10: Diagrams of (**a**) metallic (5,5) SWNT, (**b**) pyramidalisation angle (θ_P), and (**c**) the π-orbital misalignment angles (φ) along the C_1-C_4 in the (5,5) SWNT and its capping fullerene, C_{60}. Reprinted with permission from [43]. Copyright (2002) American Chemical Society.

The strain in non-planar conjugated organic molecules arises from two principal sources: pyramidalisation of the conjugated carbon atoms, and π-orbital misalignment between adjacent pairs of conjugated carbon atoms.[44,45]

The curvature in CNTs introduces misalignment of π-orbitals within the rolled graphene sheet.[43] Therefore, the π-orbitals of a nanotube are not pointed directly towards the central axis of the nanotube, and some adjacent carbon π-orbitals have a misalignment angle, φ, between them.[46] The reactivity of CNTs arises due to their topology and thus their π-orbital misalignment is likely to be the main source of strain in the CNTs.

It is conceptually useful to divide the CNTs into two regions: end caps and sidewall. The origins of the strain in the end caps and the sidewall of CNTs are somewhat different. In the (5,5) SWNT shown in (**Figure 2-10**, **a**) which is capped by a hemisphere of C_{60}, the pyramidalisation angles are as follows: $\theta_P \approx 11.6°$ (end cap) and $\theta_P \approx 6.0°$ (side wall).[41,43] The end cap of a CNT can be regarded as a hemispherical fullerene, and the C–C bonds in this region of the carbon nanotube therefore experience a similar degree of strain due to pyramidalisation to that of the equivalent fullerene. The reactivity of the fullerenes, which is primarily driven by the enormous strain engendered by their spherical geometry, is reflected in the pyramidalisation angles of the carbon atoms (**Figure 2-10**, **c**). All of the carbon atoms in fullerenes have a pyramidalisation angle θ_P of $11.6°$.[47] For a sp^2 hybridised (trigonal) carbon atom, planarity is strongly preferred, and this implies a zero pyramidalisation angle θ_P, whereas a sp^3 hybridised (tetrahedral) carbon atom requires a pyramidalisation angle θ_P of 19.5 (**Figure 2-10**, **b**). As, all of the carbon atoms in fullerenes and end cap of CNTs have $\theta_P = 11.6°$, therefore, it is immediately clear that their geometry is more appropriate for tetrahedral than trigonal hybridisation. The curvature in the sidewall of a CNT is much less than that in a fullerene of equivalent diameter. The curvature and misalignment of the π-orbitals of the (5,5) SWNT generates a pyramidalisation angle θ_P of $6.0°$ at the side wall, while the hemifullerene end-cap is under significantly more curvature-induced strain, with a pyramidalisation angle θ_P of $11.6°$. Therefore, the C–C bonds in the sidewall of a CNTs are much less reactive than those in the end cap.[17] There are two types of C–C bonds in the sidewall: Those that run parallel to the circumference plane (which is perpendicular to the axis of the CNT), and those at an angle to the circumference plane. As may be seen in **Figure (2-10**, **c)**, the first bond is similar to the situation in

the fullerenes with perfect alignment of the lobes of the π–orbitals, whereas the second bonding geometry requires a twist of the π–bond. In the latter case, the angle between the lobes of the π–orbitals of the adjacent carbon atoms is 0° and 21.3°, respectively; this source of strain in the CNTs that is absent in the fullerenes.[43] This strain due to orbital misalignment leads to a differentiation between the bonds in the CNTs that may be reflected in their relative reactivity. The pyramidalisation angles and the π-orbital misalignment angles of CNTs scale inversely with the diameter of the nanotubes; a differentiation is expected between the reactivity of carbon nanotubes of different diameters. Furthermore, Bonds that are perpendicular to the tube axis, present in armchair CNTs (high chiral angle, 30°) are under greater strain, making these species more reactive than zig–zag CNTs (low chiral angle, 0°) of the same diameter.[48]

2.5.2.   Thermal Properties

With the continually decreasing size of electronic and micromechanical devices, heat removal has become a crucial issue for continuing progress in the electronics industry owing to increased levels of dissipated power.[49] Therefore, there is an increasing interest in materials that conduct heat efficiently for designing the next generations of integrated circuits (ICs) and 3D electronics to prevent structural damage.[50] CNTs occupy a unique place in terms of their thermal conductivity and stability that stem from their unique structure and tiny size.[51] The thermal conductivity of nanotubes along their axis appears superior to that of all materials, including diamond, due to the benefits derived from the strength and toughness of the

sp^2 bond and from the 1D character of nanotubes. The thermal conductivity of bulk mats of SWNTs has been experimentally found to be as high as 200 W/mK at room temperature.[52] Although it has been theoretically predicted that the thermal conductivity of an individual ideal SWNT at room temperature could be as high as 6.600 W/mK, the practical value is usually less owing to the presence of defects in the walls of nanotubes.

CNTs also exhibit excellent thermal stability. However, modified CNTs in general show lower thermal degradation temperatures, as most modification processes involve either damage to CNT structure or introduction of organic materials on CNTs. The damaged CNTs result in the production of amorphous carbon particles that can be burned easily in air flow, and the functional moieties attached on the CNT are also easily burned.

2.5.3. Mechanical Properties

As previously mentioned, CNTs are constructed from sp^2 hybridised carbon atoms of the rolled graphene sheet, which is known to be mechanically stable. Therefore, CNTs mechanical properties are closely related to that of graphene. Among the many types of measurements to determine mechanical strength, the two that arguably stand out the most are Young's Modulus and the tensile strength. The Young's Modulus describes the ratio of stress applied to the amount of resulting strain on the material. The tensile strength describes the maximum amount of stress a material can be subjected to before it breaks. The in plane Young's modulus of graphite is 1.06 TPa.[53] However, in graphite, weak interplanar interactions weaken the system via

shearing of planes from the three dimensional crystal, even at weak applied forces. In contrast to planar graphene, the 1D cylindrical shape provides CNTs with many unique mechanical properties,[54] including a high Young's modulus and a low specific weight. The Young's modulus of SWNTs has been determined to be higher than 1 TPa,[55] which makes them suitable candidates for reinforcing composites and in ultrahigh frequency nano-mechanical resonator applications.

2.6. Functionalisation of Carbon Nanotubes

The lack of solubility and the difficulty of manipulation in many solvents have imposed great limitations to the use of CNTs. As-produced CNTs are insoluble in all organic solvents and aqueous solutions. They also have the tendency to aggregate into bundles/ropes, due to the substantial van der Waals bonding in the tube–tube interactions.[56-58] The substantial intermolecular cohesive forces of 0.5 eV nm^{-1} that exist between the tubes render them insoluble in common organic and aqueous solvents.[59] This lack of solubility is a major disadvantage as it makes them difficult to process and handle. Although, CNTs can be dispersed in some solvents by sonication, precipitation immediately occurs when this process is interrupted. Sonication also damages the sidewalls of the nanotubes.[60,61] Therefore, several approaches for the modification of these quasi one-dimensional structures have been developed. These approaches include side wall functionalisation, endohedral functionalisation, defective sites functionalisation, and noncovalent functionalisation; **Figure 2-11** illustrates the possible CNT functionalisation approaches.[62] CNTs biomedical applications depend on their chemical modifications. Carbon itself has

good biocompatibility, however, when it forms the CNT nanostructure, it can show toxicity.[63,64] The property of water-insolubility is another factor that confines the use of CNTs in the biomedical field. Furthermore, CNTs are considered as ideal carriers for drug delivery, which requires proper chemical functionalisation. Accordingly, chemistry of CNTs in biomedical fields has multiple purposes, such as water-solubilisation, enhancement of functions, and lowering the toxicity of CNTs.
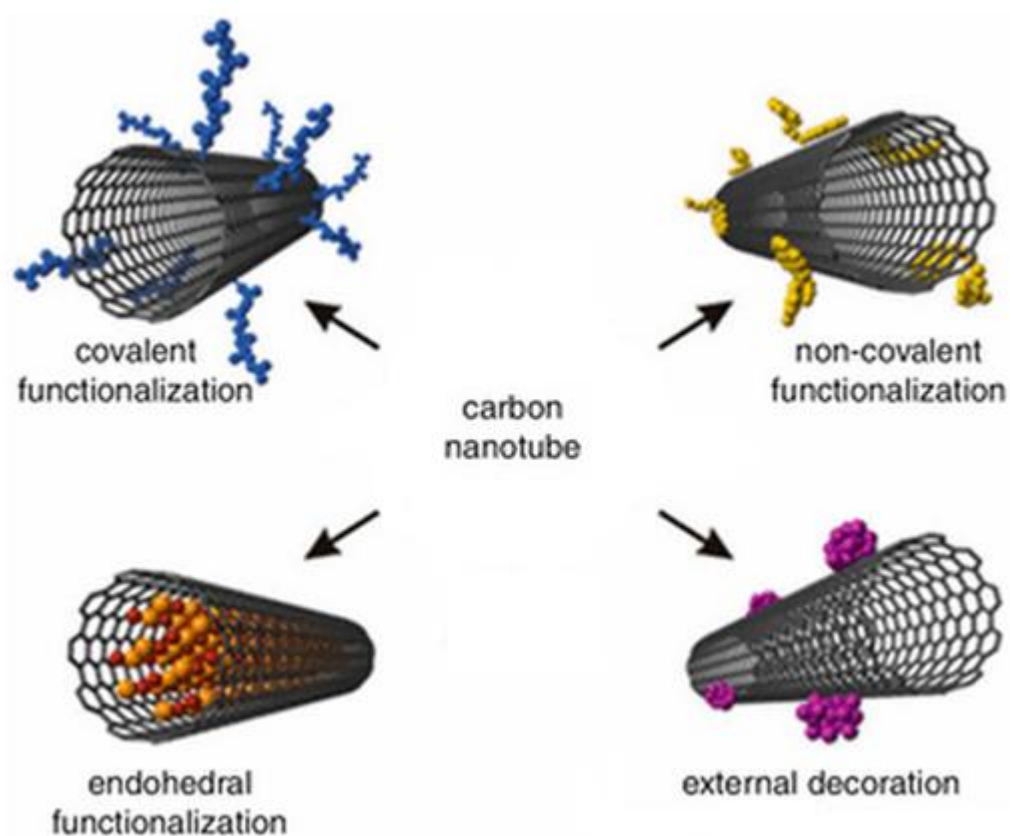
Figure 2-11: Schematic representation of different strategies for the functionalisation of CNTs.

2.6.1.   Covalent Functionalisation of Carbon Nanotubes

Covalent functionalisation is perhaps the most efficient form of obtaining well dispersed CNTs in aqueous solution due to the presence of polar functional groups on the CNT surfaces.[65] Dispersion of covalently functionalised CNTs is achieved through the disruption of the van der Waals forces between nanotube bundles by the introduction of functional groups on the CNT surfaces. The drawbacks of covalent functionalisation are that they invariably introduce defects to the sidewalls, thus resulting in significant changes in the CNTs physical properties.[66] Defects in CNTs are important as they offer an option for further functionalisation. Defects, therefore are a promising starting point for the development of the covalent chemistry of CNTs.[62] The end caps of CNTs tend to be composed of highly curved fullerene-like hemispheres, which are therefore highly reactive compared with the side walls. The sidewalls themselves contain defect sites such as pentagon-heptagon pairs called Stone-Walls defects, sp^3-hybrideised defects, and vacancies in the nanotube lattice (**Figure 2-12**).
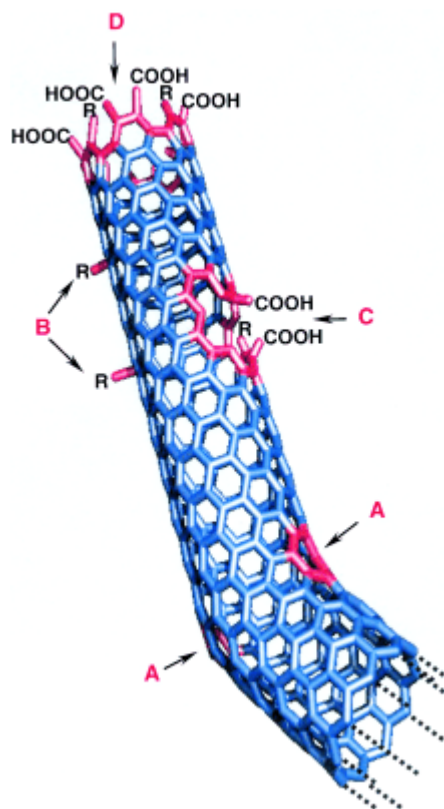
Figure 2-12: Typical SWNT defects: (**A**) bend in structure due to Stone-Wales defects, (**B**) sp^3 hybridised carbons, (**C**) holes in the sidewall and (**D**) SWNT open end terminated with COOH groups. Reproduced from [62] with permission of John Wiley and Sons.

CNTs' direct covalent functionalisation can be performed at either at the end caps of nanotubes or at their sidewalls which have many defects. This process can be made by reaction of a CNT with molecules of a high chemical reactivity,[67] such as fluorine, nitrenes, carbenes, and radicals. However, this approach is usually associated with a change in CNTs' hybridisation from sp^2 to sp^3 and a simultaneous loss of conjugation. **Table 2-1** summaries the most common covalent functionalisation methodologies of CNTs.

Methodology	Functional Group Added	Degree of Functionalisation	Solubility
Diazonium[68-71]	Aryl	1 FG in every 10 carbons in SDS/water and 1 FG in every 25 carbons in organic solvent or neat	0.8 mg mL^{-1} in DMF
Fluorination[72]	Fluorine	1 FG in every 2 carbons	1 mg mL^{-1} In 2- propanol
Radical Chemistry[73]	Alkyl	-	-
Nitrene[74]	Aziridene	1 FG in every 50 carbons	1.2 mg mL^{-1} in DMSO
Bingel reaction[75]	Cyclopropane	1 FG in every 50 carbons	
Dichlorocarbene[76]	Cyclopropane	1 FG in every 25 carbons	-
Free-radical additions[77]	Perfluorooctyl	-	-
Reductive alkylation[78]	Alkyl	1 FG in every 31 carbons	

Table 2-1: Common SWNT Sidewall Functionalisation Methodologies.

The most common direct functionalisation approach is via carboxylation. In addition to improving the purity of CNTs, carboxylation increases CNT dispersion by reducing the van der Waals forces between nanotubes bundles. However, the oxidation by acids introduces defects on the CNT walls, shortens the length of tubes, and invariably changes the intrinsic chemistry of the CNT. Generally, CNT oxidation affords opened tubes with oxygen-containing functional groups at both the sidewall and the tube endings. These groups can then be used as chemical anchors for further derivatisation.

Indirect covalent functionalisation takes advantage of chemical transformations of carboxylic groups at the open ends and holes in the sidewalls.[67] These carboxylic groups might have existed on the as-grown CNTs and also be further generated

during oxidative purification. These functional groups have a rich chemistry and allow the CNTs to be used for further chemical reactions, such as silanation, polymer grafting, esterification, thiolation, alkylation and arylation and even some biomolecules.[79,80] The CNTs functionalised in this way are soluble in many organic solvents because the addition of a polar group makes the normally hydrophobic tubes hydrophilic.[62]

2.6.2. Noncovalent Functionalisation of Carbon Nanotubes

Functionalisation of CNTs using covalent methods has shown promising results for providing useful functional groups on the CNTs surface, thus yielding a very stable and effective derivatisation. However, covalent functionalisation process inevitably creates a large number of defects on the sidewalls and/or the end tips of CNTs. In many extreme cases, CNTs are broken into smaller pieces, resulting in severe degradation of the mechanical and electronic properties of the CNTs and disruption of their π electron system.[46]

On the other hand, noncovalent functionalisation of CNTs enhances the dispersibility and solubility of pristine CNTs while preserving the sp^2 structure of the nanotubes and, thus, their electronic characteristics. Therefore, noncovalent functionalisation is an alternative method to overcome the drawbacks of the covalent functionalisation. The term dispersion refers to homogeneously distributed nanotubes in a colloidal state also including small bundles, while solution implies that the nanotubes appear individualised, e.g. the nanotube bundles are exfoliated. According to the interactions between the CNTs and the guest molecules, the noncovalent functionalisation

methods can be further classified as the, wrapping,[81] adsorption,[82] and endohedral methods.[83]

The large aromatic and hydrophobic character of CNTs make them ideal surfaces for noncovalent interaction with molecules via van der Waals, π–π stacking or hydrophobic forces. Therefore, long chain molecules such as polymers and peptides, and DNA (containing π electrons) which featuring a helical shape are especially apt to wind around nanotubes.[84] The π–π interaction is an electrostatic interaction in which the offset and/or orientation of the π orbitals on opposing molecules maximise the σ-π attractive interactions while minimising the opposing π-π repulsive interactions. Such interactions with CNTs can be surprisingly strong, depending on the molecules, and even capable of withstanding temperatures > 400 °C. The physical adsorption of molecules such as anionic surfactants onto the SWNTs surface is designed to lower the surface tension of SWNTs, effectively preventing the formation of aggregates. The surfactant-treated SWNTs overcome the van der Waals attraction by electrostatic/steric repulsive forces.[85] The efficiency of this method depends strongly on the type of surfactants used and chemistry of the medium. Another approach for the noncovalent modification of SWNTs is the filling of their inner cavity; in this method, guest atoms, molecules, inorganic nanoparticles, such as C60, Ag, Au, and Pt, or biomolecules, such as proteins, are stored in the inner cavity of SWNTs through the capillary effect.[46, 65] Comparison of the catalytic activities of immobilised enzymes with those of the free species in the hydrolysis of penicillin showed that a significant amount of the inserted lactamase remained catalytically active, implying that no drastic conformational change had taken place. DNA can also be entrapped in the inner hollow channel of nanotubes by simple adsorption to

form natural nano test tubes. Molecular dynamic simulations showed that both van der Waals and hydrophobic forces were important for the dynamic interactions of the components.[86,87] The combination of CNTs and guest molecules is particularly useful in catalysis, energy storage, nanotechnology, nanofluidics, and molecular scale devices because the incorporation process allows their individual properties to be integrated in the hybrid materials, thus creating unique properties that cannot be achieved with individual components acting alone.[32]

2.7. Aqueous Dispersion of Carbon Nanotubes

Considerable effort has been made to develop approaches for reproducible dispersion of individual CNTs. Mechanical dispersion methods separate nanotubes from each other, but can also fragment the nanotubes, decreasing their aspect ratio.[88] Chemical methods based on surface functionalisation of CNTs improve their chemical compatibility with the target medium and reduce their tendency to agglomerate. However, aggressive chemical functionalisation usually introduces structural defects resulting in inferior properties for the tubes. Thus, noncovalent treatment is particularly attractive because of the possibility of adsorbing various groups on CNTs surface without disturbing the system of the graphene sheets. The aqueous dispersion of noncovalent approaches are based on interactions of the hydrophobic part of the adsorbed molecules with nanotubes sidewalls while aqueous solubility is provided by the hydrophilic part of the molecules.[89] The charging of the nanotube surface by adsorbed amphiphilic molecules prevents nanotube aggregation by the coulombic repulsion forces between modified CNTs. The noncovalent treatment of

CNTs with biomolecules has been widely used in the preparation of both aqueous to obtain high weight fraction of individually dispersed nanotubes.

2.7.1.   Polymers Composites

CNTs are considered ideal materials as reinforcing fibers due to their exceptional mechanical properties. Therefore, CNT/polymer composites will not only possibly improve the mechanical and electrical properties of polymers, but are also considered to be a useful approach for incorporating CNTs into polymer-based devices. Noncovalent functionalisation with polymers usually involves the physical adsorption and/or wrapping of the polymer to the CNTs surface. A common strategy to impart functionality, water solubility, and biocompatibility to CNTs is the noncovalent functionalisation via PEGylation.[90-92] The formed composites exhibit high stability in aqueous solutions at different pH values, at elevated temperatures, and in serum. Therefore, PEGylated/CNTs are very powerful materials for *in vivo* applications, including drug delivery or imaging.[93-95]

2.7.2.   Surfactants

Surfactant molecules offer one of the highest potentials when considering noncovalent approaches to nanotube dispersions in water.[69,96,97] The dispersion mechanism is believed to be primarily due to hydrophilic and hydrophobic interactions, where the attraction between the CNT surface and the surfactant's hydrophobic segment facilitates adsorption while the hydrophilic group associates

with water.[85] Surfactants can be classified as anionic, cationic, non-ionic or zwitter-ionic according to the charge on their hydrophilic group.[98] The adsorption of surfactants onto the CNT surface usually depends on the chemical characteristics of the surface, surfactant molecules and solvent. Thus, CNT dispersions involving ionic surfactants are believed to be stabilised by electrostatic repulsion between the hydrophilic head groups.[99] The mechanism by which non-ionic surfactants adsorb onto a CNT hydrophobic surface is based on a strong hydrophobic attraction between the solid surface and the surfactant's hydrophobic tail.[98] Thus, the ability of non-ionic surfactants to suspend CNTs is due the size of the hydrophilic group, with the efficiency of the surfactant increasing with molecular weight due to enhanced steric repulsion.[100]

The physical adsorption of surfactant onto the CNT surface is designed to lower the surface tension of CNTs, thus preventing the formation of aggregates. The surfactant-treated CNTs overcome the van der Waals attraction by electrostatic/steric repulsive forces. The efficiency of this method depends strongly on the surfactant type, surfactant concentration, CNTs diameter[101,102] and dispersion conditions.

The presence/absence of different functional groups defines the efficiency of the dispersion of CNTs in solution. Vaisman *et al.*[98] suggested that non-ionic surfactants be reserved for dispersing nanotubes in organic solvents while ionic surfactants are preferable for creating aqueous dispersions. However, the anionic sodium dodecylbenzene sulfonate (NaDDBS) had the highest dispersive in water ability ratio followed by non-ionic Triton X-100 (TX100) and lastly anionic sodium dodecylsulfate (SDS). π–π stacking interactions of the benzene rings on CNT surface are believed to increase the adsorption ratio of surfactants. Thus, NaDDBS and

TX100 were believed to disperse SWNTs better than SDS because they contain a benzene ring, which allows for a greater interaction with the SWNTs. However, the difference between TX100 and NaDDBS was attributed to head group size; the larger head group of TX100 lower its packing density compared to NaDDBS. Although, SDS and NaDDBS have the same length of the alkyl chain but the latter has a phenyl ring attached between the alkyl chain and the hydrophilic group. The presence of the phenyl ring makes NaDDBS surfactant more effective for solubilisation of nanotubes than SDS, due to the aromatic stacking formed between the SWNTs and phenyl rings of NaDDBS within the micelle (**Figure 2-13**).

Figure 2-13: Schematic representation of how surfactants may adsorb onto the nanotube surface. Reprinted with permission from [103]. Copyright (2003) American Chemical Society.

Similarly, Rastogi et al.[104] found that benzene ring in a series of non-ionic surfactants, TX100, Tween 20, Tween 80 and SDS, affects their dispersion ability towards MWNTs. They found that TX100 displayed the highest dispersing power of the four which was again attributed it to its ability to adsorb more strongly than the others to the MWNTs through π–π stacking. Tween 80 was the next best because of its longer tail while Tween 20 was more effective than SDS due to its bulkier head group which provided greater steric stabilisation.

2.7.3. Protein

Proteins, also known as polypeptides, are naturally amphiphilic organic compounds consisting of amino acids arranged in a linear chain and folded into 3D form. Interactions between proteins and CNTs could play a key role in the biological applications of CNTs.[105] Thus, proteins have become widely used as CNT dispersing agents and extensively reviewed.[106,107] Proteins consist of numerous active groups such as hydroxyl, amino, thiol, carboxyl acidic, and others, which provides sites for further surface functionalisation of the CNTs.[108,109] Thus, interaction between a protein and a CNT surface are most likely to be complicated by involving many types of noncovalent forces such as electrostatic, π–π stacking, and hydrophobic interactions. Due to the aromatic nature of CNTs, it is rather common that protein-CNT interactions are rationalised in terms of π–π stacking with aromatic amino acids. In particular, histidine and tryptophan appear to have the highest affinity for CNTs.[110] However, studies found that protein amphiphilicity is another key property that appears to promote interaction of proteins with CNTs in aqueous media.[111] Although, electrostatic interactions are generally considered to play a minor role in protein-CNT binding, they have been reported in various studies, often taking into consideration the relation between protein charge and pH. For example, Nepal *et al.*[112] demonstrated that proteins, including lysozyme, histone, hemoglobin, myoglobin, ovalbumin, bovine serum albumin, trypsin, and glucose oxidase, were good dispersing agents for SWNTs and that their suitability depends on various factors including the primary structure and pH. Kam *et al.*[113] used the oxidised SWNTs to bind three proteins such as streptavidin protein A (SpA), bovine serum albumin (BSA), and cytochrome c (cyt-c). AFM images showed that the density of

proteins on the sidewalls of SWNTs is the highest for cyt-c, followed by SpA and BSA. Thus, it is most likely that an electrostatic force, between the negatively charged SWNTs and the positively charged protein domains, also contributes to the non-specific binding besides hydrophobic interactions.

Although, direct protein adsorption on CNTs is probably the simplest method to achieve noncovalent binding, it is not devoid of drawbacks. For example, noncovalent adsorption of proteins onto CNTs may partially unfold them and thus lose their biological function. Matsuura *et al.*[114] studied the interaction of egg white lysozyme (LYS), bovine serum albumin (BSA), pepsin and porcine pepsin proteins with SWNTs in water. The main driving force for the dispersion is thought to be by π–π stacking interaction between the side walls of SWNTs and the aromatic groups of the residues in the protein. Although aromatic residues exist on the studied protein, unfolded LYS and BSA can individually disperse SWNTs in aqueous solutions, whereas weakly unfolded pepsin and pepsin cannot. This suggests that the deference in the dispersion properties is probably attributable to protein structural changes that occur during the dispersion process.

On the other hand, indirect adsorptions of proteins to CNTs via anchor molecules not only preserve CNTs properties but also protein structure. Chen *et al.*[115] reported the use of a bifunctional molecule, 1-pyrenebutanoic acid succinimide ester, as a linker to immobilise proteins on SWNT surface. The pyrene moiety in the bifunctional molecule would be π–π stacking with the graphitic nanotube sidewall so that the succinimidyl ester group at the other end of the bifunctional molecule would be available for reaction with primary and secondary amines in the proteins (**Figure 2-14**).
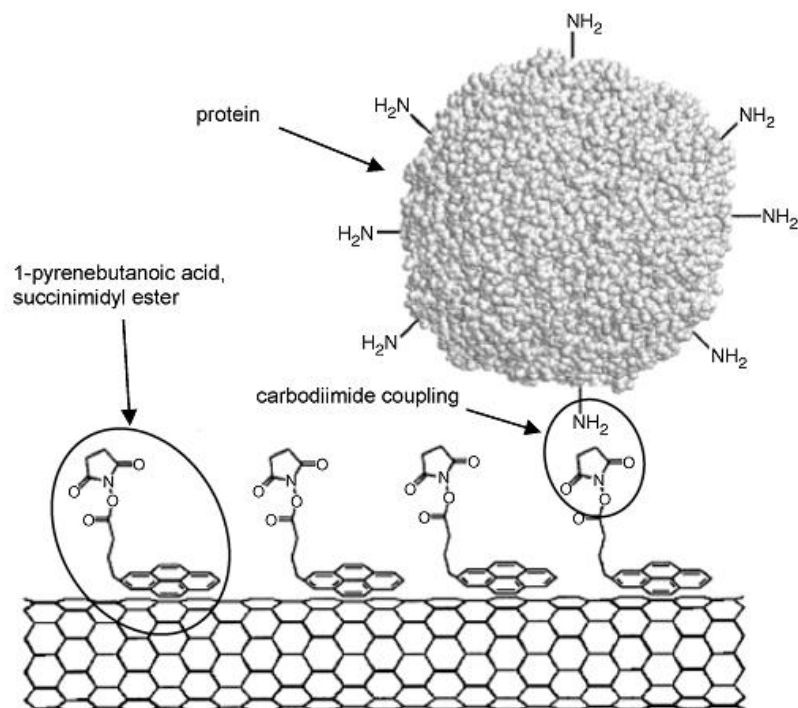
Figure 2-14: Anchored succinimidyl ester to formamide bonds for protein immobilisation on SWNTs. Reprinted with permission from [115]. Copyright (2001) American Chemical Society.

The hollow nature of CNTs allows them to be considered as potential tubular vectors to be filled with biomolecules. The encapsulation of protein into CNTs may control and decrease the overall CNT cytotoxicity. Furthermore, upon the protein encapsulation of a specific protein, the loaded protein could be delivered to the desired site of action, thus protected from protease. Tsang *et al.*[116] confirmed the encapsulation of a series of small proteins, Zn2Cd5-metallothionein, cytochrome C3 and p-lactamase, into end cap opened CNTs by high-resolution transmission electron microscopy (HRTEM). The encapsulated proteins kept a significant amount of their catalytic activity, which indicates that no drastic conformational change had taken place during their immobilisation inside CNTs. Kang *et al.*[117] explored the diameter selectivity of the protein encapsulation in CNTs via molecular dynamics simulations. They suggested that a protein is encapsulated into a CNT with an appropriate

diameter to ensure encapsulation in a spontaneous process; CNTs that are too large offer insufficient initial van der Waals attraction to the protein, for it to move inside the nanotubes.

2.7.4.   Peptides

Peptide conjugation is another alternative and attractive technique for noncovalent dispersion of CNTs in aqueous solution. The peptide dispersal agents function as surfactants in the sense that they lower the surface tension of water around the nanotubes. They have effective hydrophobic and hydrophilic surfaces that are used to interact with both the CNTs and water. Peptides can bind to CNTs via hydrophobic interactions,[118,119] π–π stackings,[110,120,121] and electrostatic interactions.[122] Among them, the π–π stacking interactions between aromatic residues of peptide and CNTs have been listed as a particularly important factor in the binding process. Salzmann *et al*.[123] illustrated the importance of the balance between (charged) hydrophilic and aromatic amino acid residues in polypeptides for the successful dispersion of SWNTs. The π–π stacking interaction between the aromatic amino acids of the polypeptides and the extended π-electron system of CNTs is considered to be the main driving force for polypeptide adsorption onto SWNTs. In this context, they found that tryptophan residues interact more strongly with the SWNTs than tyrosine residues making the peptide of tryptophan and lysine a better dispersing agent for SWNTs compared to the peptide of tyrosine and lysine. Dieckmann *et al*.[124] designed an amphiphilic helical peptide denoted as nano-1. This artificial peptide was constructed on the basis of the preliminary works of Wang *et al*.[125] who used phage

display to identify several peptides with a high affinity for CNTs. An analysis of nano-1 peptide conformations has suggested that the binding sequence is flexible and folds into a structure matching the geometry of the nanotube. **Figure 2-15** schematically illustrates the structure of the peptide and its interaction with a SWNT. The more polar residues are located on one face and have surfactant properties so spontaneously assemble in aqueous solution to minimise the exposure of the hydrophobic surface to the solvent and to present the hydrophilic surface to the aqueous environment
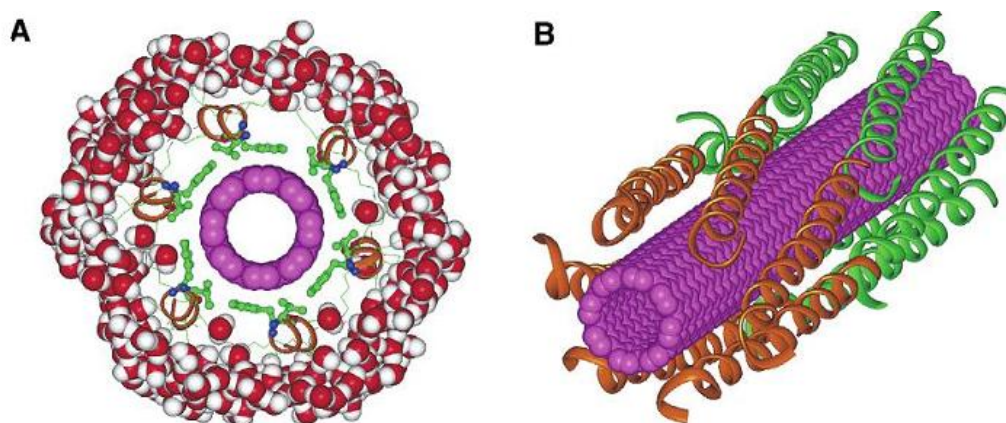
Figure 2-15: Model illustrating potential interactions between nano-1 and SWNT. (**A**) Cross-section view of a SWNT wrapped by six peptide helices. (**B**) View of peptide-wrapped nanotube illustrating the nano-1 peptide helices used in the model. Reprinted with permission from [124]. Copyright (2003) American Chemical Society.

When nano-1 folded into an α-helix, as proposed on the basis of CD spectroscopy, the hydrophobic valine and phenylalanine residues create an apolar surface of the peptide suitable for interacting with the nanotube sidewall. The polar nano-1 residues promote self-assembly through charged peptide-peptide interactions. Zorbas et al.[120] altered the number of heptad-residue repeats and the number of phenylalanine residues (Phe) of nano-1 peptide. It was found that peptides with fewer Phe residues had a decreased ability to disperse SWNTs, suggesting that nano-1 mainly uses Phe

residues to interact with the SWNT side wall through the π-π stacking effect. Li *et al.*[126] studied the effect of pH and degree of oxidation of the electrostatic interaction of two polypeptides, polylysine and polytryptophan, with MWNTs and SWNTs. They found that the adhesion force between polylysine and oxidised MWNTs increased with decreasing pH value and increasing oxidation time. However, the corresponding pH and oxidation-time dependences for SWNTs were found to be much weaker than those of MWNTs. This is thought to be due to the carboxylate groups only attached onto the nanotube tips in the SWNTs, whereas onto both the nanotube tips and sidewall in the MWNTs. Arnold *et al.*[127] found that the MWNTs dispersion using amphiphilic anionic and cationic peptide is controlled by pH of the dispersion. The tested peptides consist of a hydrophobic alkyl chains covalently attached to an amino acid sequence, thus, the net ionic charge of the peptides vary with pH. For instance, at neutral and basic pH, the peptide sequence of PA 1 molecules is negatively charged. In this state, PA 1 molecules homogeneously disperse and functionalise the MWNTs. By reduction of the net charge of the peptide sequence, the ionic repulsion among free peptide amphiphilic molecules and among peptide amphiphilic functionalised MWNTs can be reduced, leading to aggregation.

3. CHARACTERISATION OF CARBON NANOTUBES AND BIOMOLECULES

This section describes the techniques that have been used to characterise CNTs as well as the biomolecules that have been used in this thesis.

3.1. Characterisation of CNTs

Several characterisation and observation methods are available for carbon nanomaterials, each one provides complementary information. The imaging of the carbon nanomaterial morphology is usually performed by electron or probe microscopy. Spectroscopic methods are often applied to characterise the structural and chemical properties of the nanomaterials. This section will focus on both microscopic and spectroscopic techniques used to characterise the synthesised and modified carbon nanomaterials in this thesis.

3.1.1. Vibrational Spectroscopy Techniques

Vibrational spectroscopy is concerned with vibrational transitions due to absorption and emission of electromagnetic radiation. Molecular vibrations can be excited by the absorption of photons of frequencies that exactly match the vibrational frequencies of the molecule, which depend on the forces between its atoms and its geometry.[128] The vibrational energies of the molecule can be studied by vibrational

spectroscopy. Therefore, a Raman spectroscopic method has been used to probe the oscillation of the atoms in carbon nanomaterials to yield complementary types of information about their structure.

3.1.1.1.   Raman Spectroscopy

Raman spectroscopy is a non-destructive powerful technique used to study vibrational, rotational, and other low-frequency modes in a molecule, thus yields spectroscopic fingerprints from the studied sample.[129] It principally differs from IR spectroscopy in that it is concerned with the frequency of the scattered photons by molecules as they undergo rotations and vibrations rather than change in dipole moments due to the absorption of photons. When monochromatic light, usually from a laser in the visible, near-infrared, and near-ultraviolet range, impinges upon a molecule and interacts with the electron cloud of the bonds, a virtual transition to a higher energy level occurs. The molecule then relaxes and returns to the ground state by emission of a photon resulting in two types of light scattering, elastic and inelastic scattering.[128,130] **Figure 3-1** shows the types of photon scattering. In elastic scattering, the light interacts with the molecule but the net exchange of energy (E) is zero, so no change occurs in photon frequency, this process is known as Rayleigh scattering.
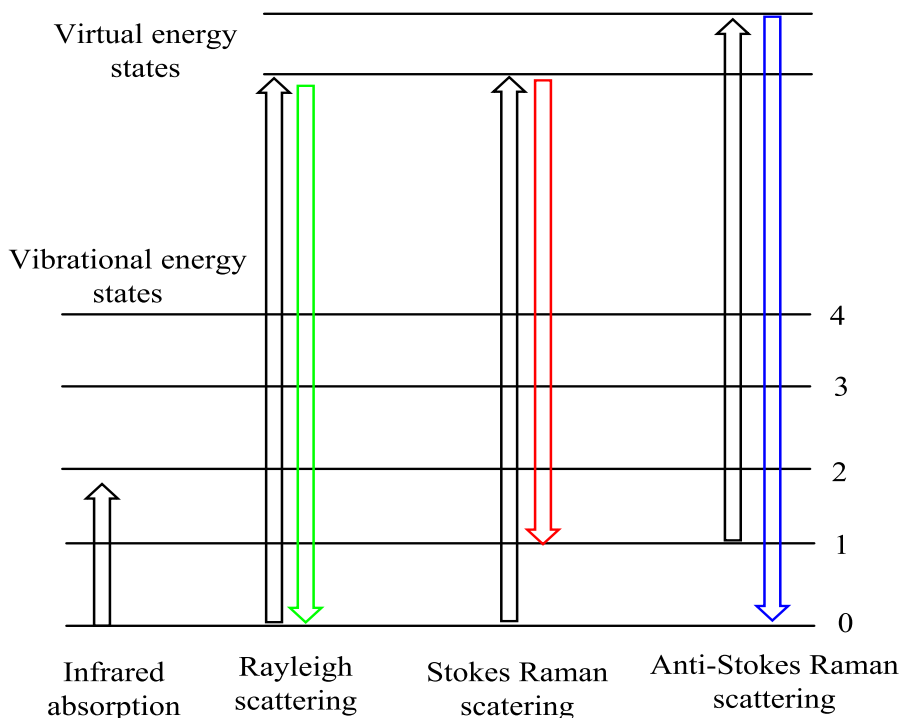
Figure 3-1: Energy-level diagram showing Rayleigh scattering, stokes and anti-stokes Raman scattering.

The Raman effect occurs when the very small part of the incident light is inelastically scattered. The inelastic light scattering is usually accompanied by the shift in photon frequency due to excitation or deactivation of molecular vibrations in which either the photon may lose some amount of energy or gains energy. As a result, the emitted photon frequency will be either shifted to lower or higher energy (blue or red shifted, respectively). The red shifted photons are the most common and usually known as stokes shift, while the blue shifted are designated as anti-stokes Raman scattering respectively.[130] This shift in the frequency is called the Raman shift and is generally represented in wavenumbers (cm^{-1}), inverse of wavelength. In contrast to infrared spectroscopy, Raman spectroscopy is dependent on a change in the polarisability during the vibration, and the Raman intensity is concerned with the polarisability of the vibrating atoms and their bonds present. Raman spectroscopy is

commonly used to characterise all sp^2 graphitic carbon structures from three to zero dimensions, such as 3D graphite,[131] 2D graphene,[132] 1D carbon nanotubes,[15,133] and 0D fullerenes.[15,132,134] Raman spectroscopy of sp^2 carbons provides unique information about crystallite size, clustering of the sp^2 phase, the presence of sp^2-sp^3 hybridisation and the introduction of chemical impurities, doping, defects and other crystal disorder, nanotube diameter, chirality, curvature, and finally the metallic vs. semiconducting behavior.[135] All carbon nanostructures exhibit two characteristic features in their Raman spectra, in the region 800 − 2000 cm^{-1}, the so-called G (graphitic) and D (disordered) peaks, which are sensitive enough to provide unique information about the similarities and differences between them.[136] A typical Raman spectrum of SWNTs can be divided into four important regions; the radial breathing mode (RBM), the disorder mode (D band), the tangential mode (G band), and the G´ (or 2D) band. **Figure 3-2** shows a representative Raman spectrum of SWNTs excited at 633 nm.
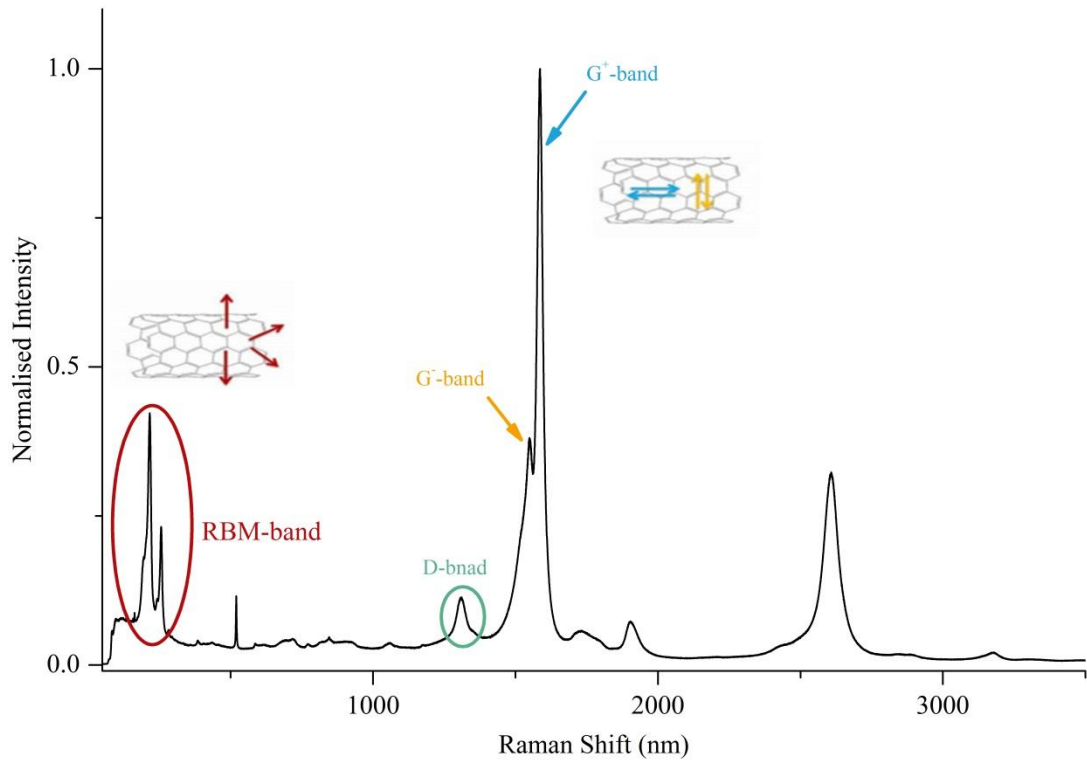
Figure 3-2: Resonance Raman spectrum of purified SWNTs excited at 633 nm and normalised at G-band.

The radial breathing mode (RBM) Raman features corresponds to the atomic vibration of the C atoms in the radial direction in the relation to nanotubes axis. These features are unique to CNTs and occur with frequencies ω_{RBM} between 120 and 350 cm^{-1} for SWNTs for diameters in the range 0.7 nm − 2 nm.[15] These RBM frequencies are therefore very useful for identifying whether a given carbon material contains SWNTs, through the presence of RBM modes, and for characterising the nanotube diameter distribution in the sample. The RBM frequency (ω_{RBM}) is inversely proportional to the diameter of the nanotube (d_t) following the equation below:

$$\omega_{RBM} = A + (B/dt)$$

The A and B parameters are determined experimentally and dependent on environmental effects, such as the degree of individualisation or wrapping of surfactants. Different values of these parameters have been reported which are summarised by Hennrich *et al.*[137] For large diameter tubes (d > 2 nm) the intensity of the RBM feature is weak and is hardly observable.[138] Because of the diameter-selective resonance Raman effect,[139] study of the RBM frequencies for various E_{laser} values can be used for characterising the diameter distribution of SWNTs in a sample. The second important Raman feature is the G-band, which is a Raman-active mode of sp^2 carbons (graphite) and thus all graphitic materials show this spectral feature. The G band in SWNTs which corresponds to tangential planar vibrations of carbon atoms appears in the region between 1500 and 1600 cm^{-1}. Differently from other graphite base nanomaterials, the tangential G mode in SWNTs is a sum of up to six high-energy tangential modes that basically originate from breaking the symmetry of the tangential vibration when the graphene sheet is rolled into a tube.[137,140] However, just the two most intense peaks of the G band are normally considered, these peaks are labelled G^+, which is given by vibrations along tube axis, and the G^-, due to vibrations in the circumferential direction. The G band frequency can be used for nanotubes diameter characterisation; the G^+ band is independent from the diameter, whereas the G^- band is usually diameter dependent. The G^- band frequency (ω_G^-) decreases when decreasing nanotubes diameter (d_t), and this decrease becomes larger as the curvature of the sheet increase. Therefore, the splitting the G band into G^+ band G^- band and can be used for diameter characterisation. Additionally, the G-band is used to distinguish between metallic and semiconducting SWNTs, through strong differences in G band line shapes. The line shape of the G^- mode depends on whether the tube is semiconducting or

metallic. The G$^-$ feature is broadened for metallic SWNTs. Furthermore, the G-band is used to probe the charge transfer arising from doping a SWNT through the G$^+$ frequency (ω_G^+) which is sensitive to charge transfer from dopant additions to SWNTs. The ω_G^+ up-shifts electron acceptors, and downshifts for donors as in graphite intercalation compounds (GICs). Another important Raman is the D band (diamond band, or disorder band), which is observed in the 1300 – 1400 cm^{-1} range and usually shifts to higher wavenumbers as the laser excitation energy is increased. This mode is associated with disorder, specifically, the sp^3 hybridised carbon atoms present in the tube or in the carbonaceous impurities. Therefore, the intensity of this band can be used to determine the defects in the structure, usually expressed as I$_D$/I$_G$ ratio. Moreover, the full-width-at-half-maximum (FWHM) intensity of the D-band of the various carbon impurities is generally much broader than that of CNT D-band, and thus D-band line-width could give an indication of SWNTs purity level. There are other less significant bands that typically present in a SWNTs Raman spectrum, among them is the G′ band. This band is the second strongest after the G mode, but it is actually the overtone of the defect-induced D mode, even though being present even in defect-free nanotubes.

This technique is also used to characterise MWNTs witch show similar Raman features to SWNTs; however, they do not present a defined RBM, because the outer MWNTs tubes restrict their breathing mode. Moreover, the D band is quite intense, often more than the G-band, because of the high extent of defects usually present in MWNTs. Consequently, it is difficult to appreciate an increase in the I$_D$/I$_G$ ratio due to functionalisation. Lastly, the G band splitting is small and smeared out because of

the diameter distribution within MWNTs and the G band usually exhibits a weakly asymmetric line shape.[141]

3.1.2.   Electronic Spectroscopy Techniques

Electronic spectroscopy is concerned with the absorption, emission, and scattering associated with the interaction of ultraviolet-visible (UV-Vis) radiation with the chromophoric system in the molecule.[142] In this type of spectroscopy, the absorption is associated with excitation of electrons from lower to higher energy levels. Since the energy levels of matter are quantised, only light with the precise amount of energy (exact wavelength), can cause transitions from one level to another. This usually involves π−orbitals and lone pairs (non-bonding). **Figure 3-3** illustrates a simple schematic of electronic transitions in the UV-Vis region.
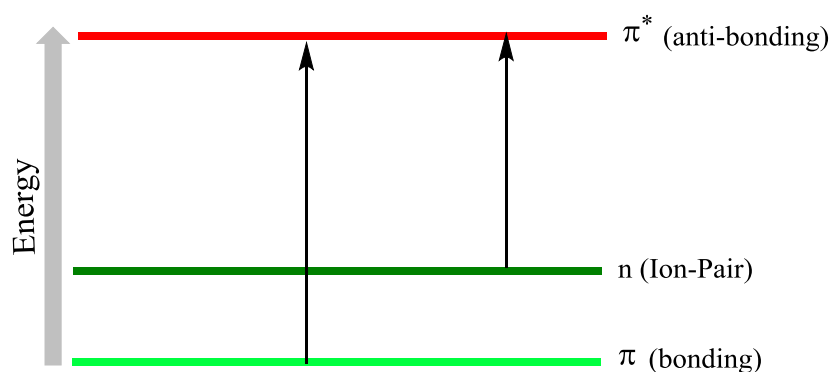
Figure 3-3: Electronic transitions in the UV-Vis region.

In this thesis, ultraviolet-visible-near infrared (UV-Vis-NIR) spectroscopy has been used to characterise the changes of electronic properties of carbon nanomaterials upon their modification.

3.1.2.1.   Ultraviolet-Visible-Near Infrared (UV-Vis-NIR) Spectroscopy

UV-Vis-NIR spectroscopy is an analytical technique which is ideally suited for the characterisation of carbon nanomaterials due to its sensitivity to the changes in their electronic structure and so their optical properties. The electronic structure of CNTs is related to a 2D graphene sheet. However, owing to the 1D nature of the nanotubes, their electronic density of states (DOS) is singular due to folding of the 2D energy bands of graphene layer into the 1D bands of SWNT with an increasing energy separation at decreasing number of energy bands.[143,144] As a consequence, the continuous DOS in graphene divides into a series of spikes in SWNTs known as van Hove singularities (vHSs)[14,145-147] (**Figure 3-4**).
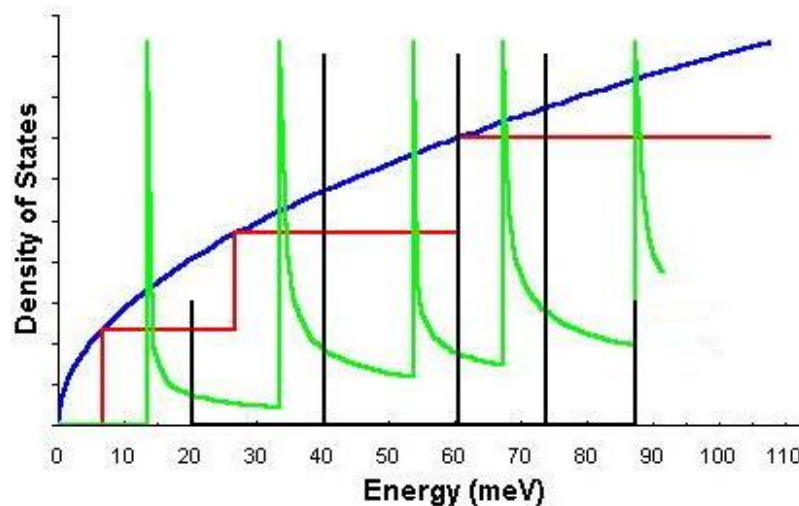
Figure 3-4: Theoretical phonon density of states for 1D quantum (**Black line**) dots, 2D graphene (**Red line**), 3D graphite (**Green line**), and CNTs (**Blue line**). From [146] with permission from AAAS.

The optically allowed electronic transitions between vHSs of SWNTs arise as a series of characteristic sharp peaks in the UV-Vis-NIR range. The sharpness of the peaks usually is not fully appreciable due to the overlap of similar transitions given

by different diameters and chiralities. Each (n, m) SWNTs exhibits a different set of vHSs in its valence and conduction bands; in particular the energy gap varies with the SWNT diameter (d) as $1/d^2$.[148] Therefore, optical absorption can be used to determine nanotube diameter and chirality. The possible electronic transitions in the DOS of semiconducting and metallic SWNTs are explained in **Figure 3-5**.
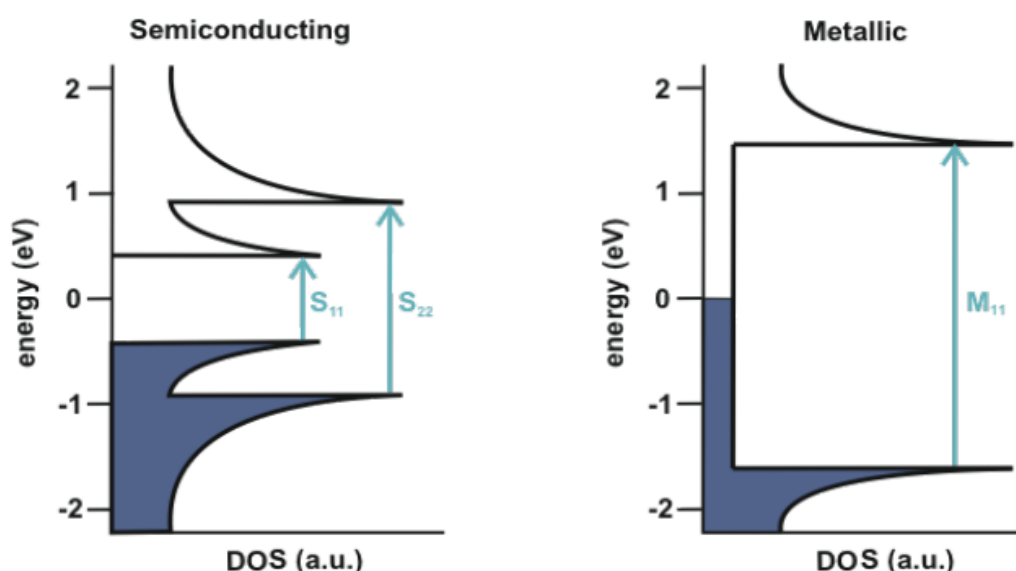
Figure 3-5: Schematic representation of the electronic density of states of a semiconducting and metallic SWNT and the possible transitions between the van Hove singularities. The valence bands are blue colour and the conduction bands are white colour. Reproduced from [149] with permission of The Royal Society of Chemistry.

In SWNTs absorption of UV-Vis-NIR light, the electrons in the vHSs of the valence band are elevated to the corresponding energy levels in the conduction band; denoted as S_{11} and S_{22} in semiconducting SWNTs and M_{11} in metallic SWNTs.[150] The M_{11} transitions for metallic SWNTs are seen as absorption bands in the visible range between $\sim 440 - 645$ nm. The E_{11} and E_{22} transitions for semiconducting SWNTs are seen between $830 - 1600$ nm and $600 - 800$ nm.[151,152] A typical absorption spectrum

of HiPco SWNTs dispersed in an aqueous solution of SDS (1 wt %) after sonication

and ultracentrifugation is displayed in **Figure 3-6**.
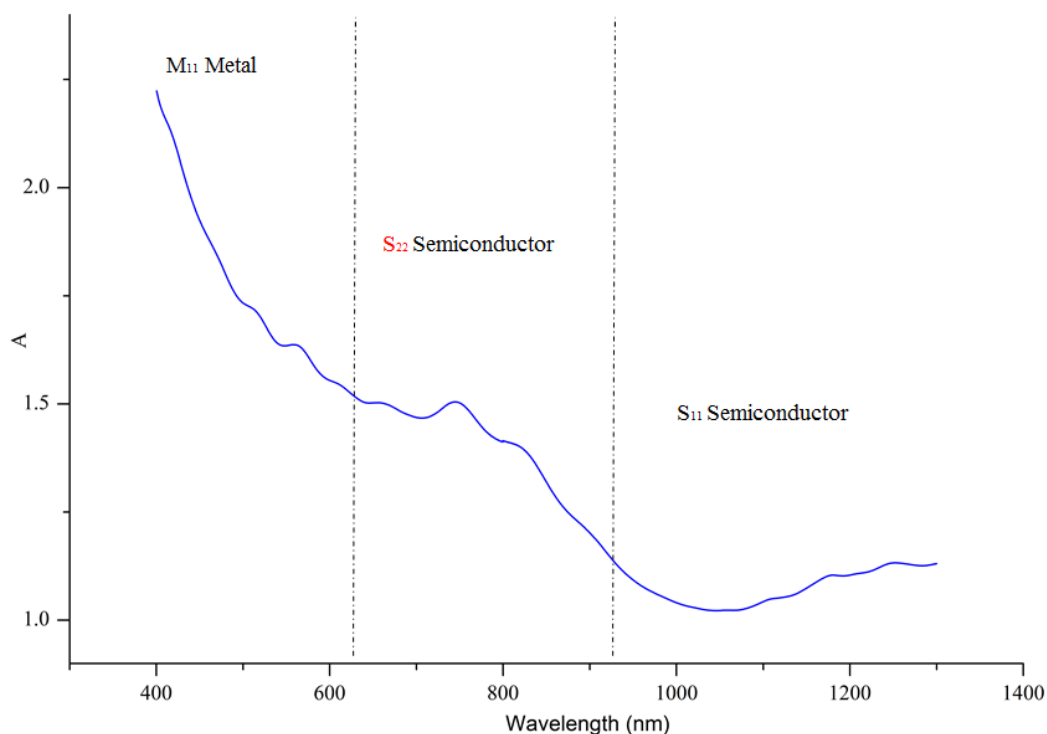
Figure 3-6: UV-Vis-NIR absorption spectrum of HiPco SWNTs aqueous dispersion in 1 wt % SDS showing the M_{11}, S_{11} and S_{22} regions.

The disadvantage of this characterisation is that its usefulness is usually limited to

SWNTs. In fact, the UV-Vis-NIR absorption of MWNTs derive from the overlap of

many different contributions of each tube, consequentially does not result in the

typical well-defined van Hove features of a SWNT spectrum.

The UV-Vis-NIR absorption spectroscopy of SWNTs is widely used to determine

their individualisation degree, purity,[153-155] efficiency of separation procedures,[156]

and dispersion efficiency.[157] The nanotube concentration in the supernatant can be

calculated through application of the Beer-Lambert Law,[158,159] which states that the

absorbance, A, of a sample is dependent on the light path length (l) the concentration (C) of the species and the extinction coefficient (ϵ). It is therefore possible to determine the solubility of a CNT sample in a particular solvent from its UV-Vis-NIR spectrum if the extinction coefficient is known.

3.1.3. Microscopic Techniques

3.1.3.1. Atomic Force Microscopy (AFM)

Atomic force microscope (AFM) is a high resolution scanning probe microscopy technique, which is widely applied to study materials surface properties from the atomic to the micron levels. AFM was used to quantitatively characterise the morphology and roughness of carbon nanotubes surface.[160-162] **Figure 3-7** shows the basic principles of AFM.
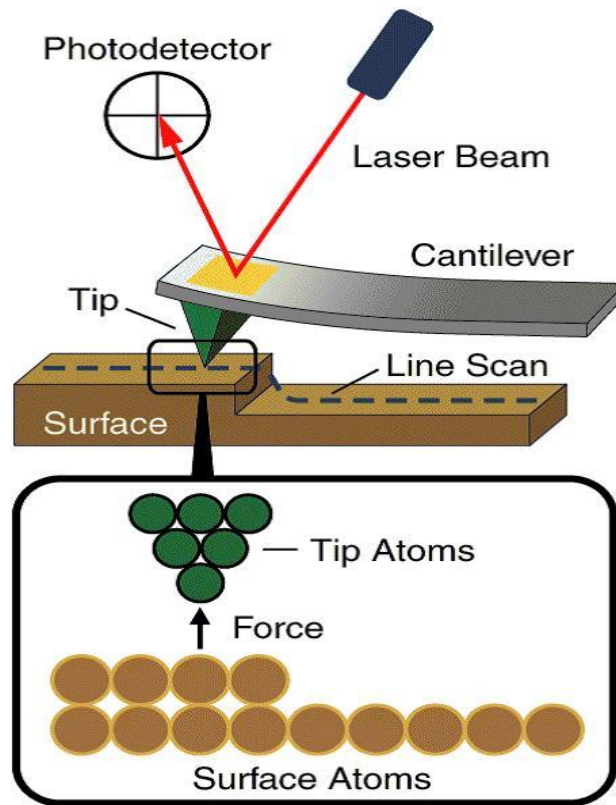
Figure 3-7: Block diagram of principle operation of a (multimode) AFM.[163]

The technique uses a tip that is precisely situated on a flexible silicon cantilever and mounted to a piezoelectric driver for scanning. When the voltage is applied, the tip is brought to a chosen point over the sample surface where the force can repel or attract atoms from the tip leading to a deflection of the cantilever according to Hooke's low.[164] Therefore, the AFM detection system does not directly measure the force between the tip and the sample surface; instead, it senses the deflection of the cantilever. The degree of cantilever deflection, which is caused by the surface topography, is usually measured using a laser light reflected from the surface of the cantilever into a position sensitive detector. AFM can be operated in two modes: namely the contact mode, noncontact mode or "tapping mode". In contact mode the tip actually touches the surface, thus possibility moving objects or damaging soft

samples. In non-contact mode, the tip scans instead the surface at a certain distance and the cantilever is oscillated at a frequency slightly above its resonant frequency where the amplitude of oscillation is typically few nanometres.[165] Thus, this mode does not suffer from tip or sample degradation effects, making it preferable to contact AFM for measuring carbon nanomaterials samples in this thesis. The AFM technique can be used as fast method for the examination of the generation of three-dimensional reconstruction of the sample topography with atomic resolution, and also allows collecting information on the morphology of CNTs, the functional groups present on nanotube surface and diameter/length, dispersion and exfoliation of bundles.[166,167]

3.1.3.2.   Transmission Electron Microscopy (TEM)

Transmission electron microscope (TEM) is a powerful imaging technique that based on the detection of a high energy electron beam transmitted through a thin sample to provide high-resolution morphologic, compositional and crystallographic information. Therefore, it is an important tool for the characterisation of carbon nanomaterials. The basic components of TEM equipment are illustrated in **Figure 3-8**.
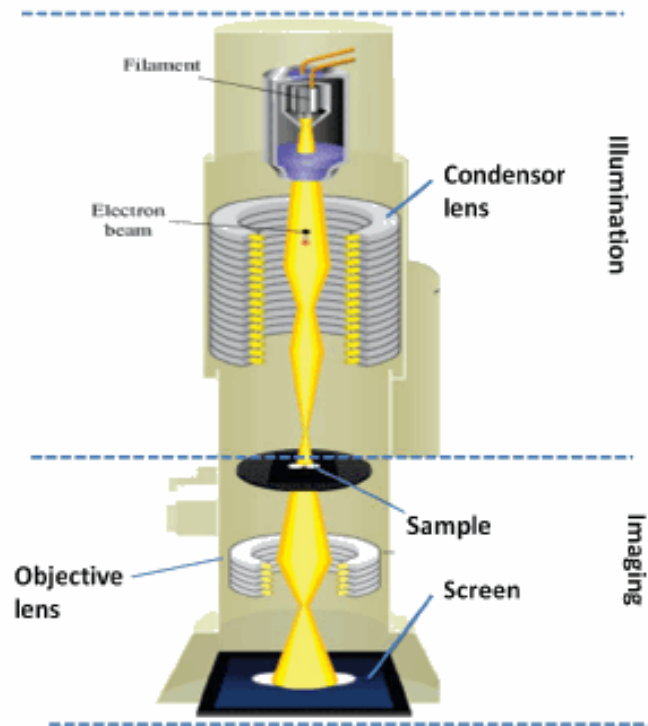
Figure 3-8: Schematic diagram of transmission electron microscope.

TEM operates on the same basic principles as the light microscope but uses electrons instead of light. TEMs use electrons as "light source" and owing to their much lower wavelength it is possible to get a resolution a thousand times higher than with a light microscope.[168] A "light source" at the top of the microscope emits the electrons that travel through vacuum in the column of the microscope. Instead of glass lenses focusing the light in the light microscope, the TEM uses electromagnetic lenses to focus the electrons into a very thin beam. The electron beam then travels through the specimen under study. Depending on the density of the material present, some of the electrons are scattered and disappear from the beam. At the bottom of the microscope the unscattered electrons hit a fluorescent screen, which gives rise to a "shadow image" of the specimen with its different parts displayed in varied darkness according to their density. The image can be studied directly by the operator or

photographed with a camera.[169] The image quality of a certain sample can be manipulated by adjusting the speed of electrons through the electron gun by voltage modification. During the transmission, the speed of electrons directly correlates to electron wavelength: the faster the electrons move, the shorter wavelength and the greater the quality and resolution of the image.[170]

TEM is a key technique in the structural characterisation of CNTs: it provides information on dispersibility, diameter, purity grade, presence of defects, length, and also functionalisation of the nanotubes. However, TEM requires very thin samples, which are electron transparent. Therefore, for TEM analysis, nanotubes are typically deposited on commercial TEM grids. This procedure has two problems: in the deposition process the nanotubes can be damaged, and it does not work reliably if the nanotube density is too low.

3.1.4. Thermogravimetric Analysis (TGA)

Thermogravimetric analysis (TGA) is a destructive analytical technique that determines the thermal stability of materials by monitoring the weight as a function of temperature under a controlled atmosphere, optimised according to the experiment needs; either in inert (N_2 or He), or oxidative (air or pure O_2) atmosphere.[59] Although TGA provides quantitative weight change information about decomposition and volatilisation, it does not generally provide information about the identity of specific gaseous material evolving during the experiment. Therefore, it is often coupled with gas phase mass spectrometry (TGA-MS), and the temperature at which the groups

come off can be indicative of covalent functionalisation since the attached groups will come off at considerably high temperatures compared to adsorbed groups.[171]

TGA analysis has been used to study the thermal stability of carbon nanomaterials. Different forms of nanomaterials have different thermal stability under identical conditions, which is consistent with the differences in their structures. For example, disordered or amorphous carbons tend to be less thermally stable than the well graphitised structures, because of their lower activation energies for oxidation or due to the presence of a large number of active sites.[172-174]

TGA characterisation of SWNTs is used to quantify the quality of as-produced SWNT samples, as well as to track the effects of the purification and modification process. Their combustion temperature usually depends on a number of parameters, such as diameter, amount of metal catalyst particles, defects and derivatisation moiety on the nanotube walls.[172,174]

TGA in an oxidising atmosphere has become a relevant tool for purity analysis by accurately estimating the amount of metal catalyst particles remaining in the sample.[173] Metal impurities in the sample have a considerable influence on the thermal stability, therefore impure tubes burn at lower temperatures due to the presence of metal particles.[39] Meanwhile, TGA analysis of modified SWNTs under inert atmospheres can be used to determine the weight loss upon heating and their degree of functionalisation. This is based on the fact that SWNTs have high thermal stability up to 800 °C, where most functional moieties are not stable. Therefore, it is possible to ascribe the weight loss at lower temperatures to the organic material present in the sample to estimate the degree of functionalisation[59] (**Figure 3-9**).
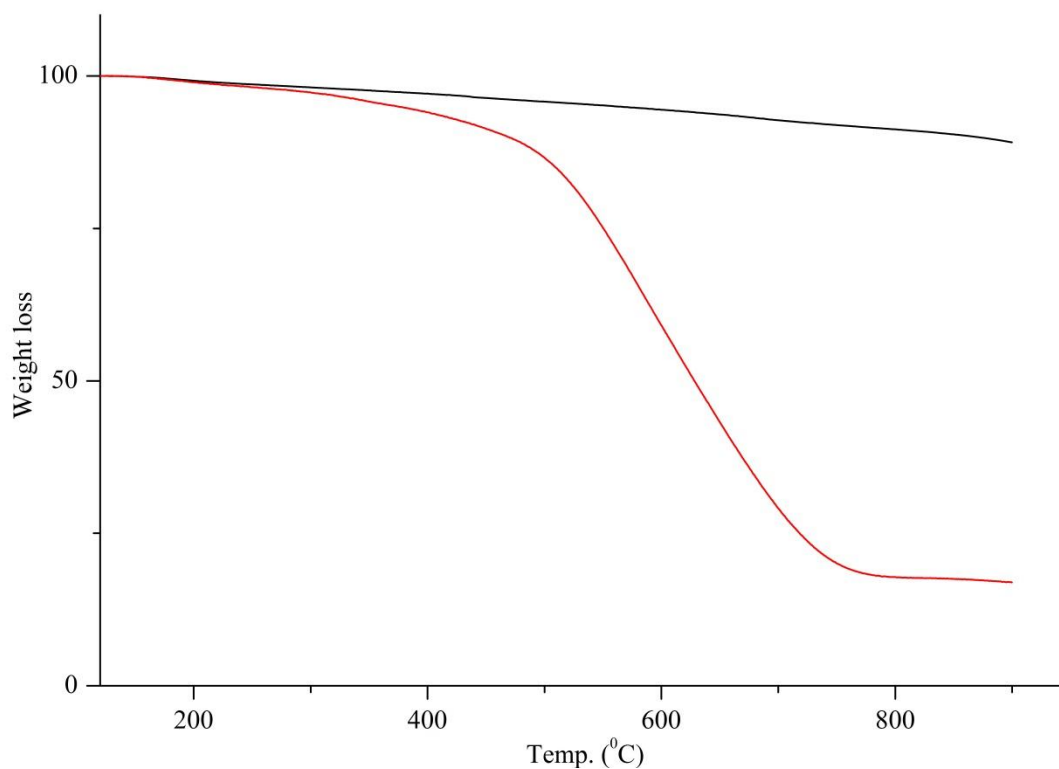
Figure 3-9: TGA analysis of pristine purified HiPco SWNTs: (**Black line**) under N_2, (**Red line**) under air.

3.2.   Characterisation of Biomolecules

The modification of CNTs with biomolecules requires knowledge of the concentration, structure, electronic environment, and binding stoichiometry. For this purpose, this section gives a brief overview of the characterisation techniques used.

3.2.1.   Mass Spectrometry (MS)

Mass spectrometry (MS) is an analytical technique for determining masses of free ions in high vacuum for determining the elemental composition and chemical structures of molecules.[175] Among the analytical techniques, the use of mass

spectrometry (MS) to identify and characterise biological molecules holds a special place because it measures an intrinsic property of a molecule with very high sensitivity.[176,177]

A mass spectrometer works by introducing the sample into the ionisation source of the instrument. In the source, the sample molecules are ionised then extracted into the analyser region of the mass spectrometer where they are separated according to their mass (m) to charge (z) ratios (m/z). There is a variety of analysers, namely the magnetic sector, the quadrupole, and the time of flight. The separated ions are detected and the signal fed to a data system where the results can be studied and processed.[178] **Figure 3-10** shows a simplified schematic diagram of a mass spectrometer
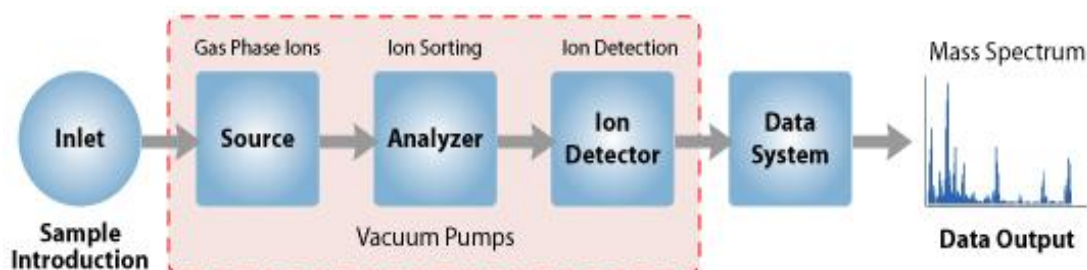
Figure 3-10: Simplified schematic diagram of a mass spectrometer.

Many ionisation methods are available and the choice of ionisation method depends on the nature of the sample and the type of information required from the analysis. This data shown in this thesis depends on the data generated from liquid chromatography-mass spectrometry (LC-MS). The identification of molecules by LC-MS follows a different principle; typically liquid chromatography is coupled to tandem mass spectrometry. This methodology combines efficient separations of

biological materials and sensitive identification of the individual components by mass spectrometry. In a typical LC-MS experiment, the analyte is eluted from a reversed-phase column to separate the peptides by hydrophobicity, and is ionised and transferred with high efficiency into the mass spectrometer for analysis. After the components in the sample are separated, they pass through a mass detector. The mass detector response and the time it takes for a compound to pass from the injector to the detector (retention time) of the compound of interest may then be compared to a reference material.

3.2.2. Matrix-Assisted Laser Desorption/Ionisation (MALDI)

Matrix-assisted laser desorption/ionisation (MALDI) is utilised to identify the synthesised biomolecules. MALDI is well proven as a soft and efficient ionisation technique used in mass spectrometry for the analysis of biomolecules and large organic molecules, in which a laser is used to achieve desorption and ionisation of the sample of interest. **Figure 3-11** illustrates the principle of MALDI-TOF-MS.
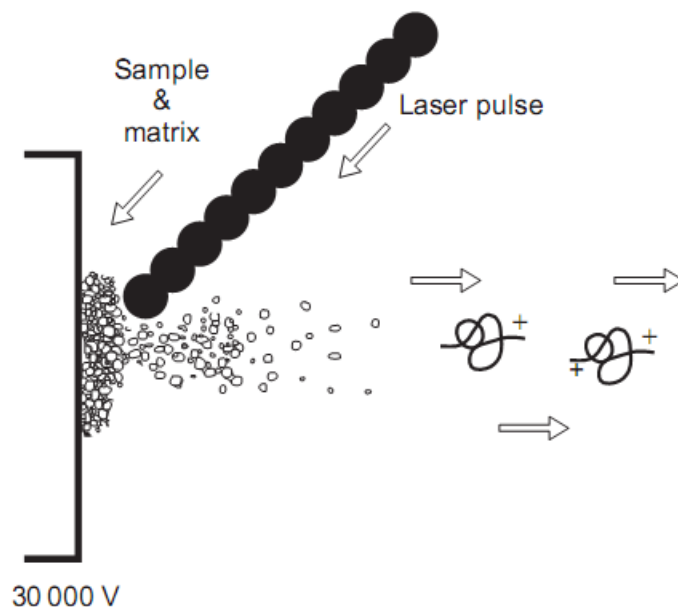
Figure 3-11: MALDI-TOF-MS

The mechanism of ion formation in the MALDI process is not yet fully understood. The MALDI process is a complicated process, and there is no single mechanism that can explain the origin of all ions observed in a MALDI spectrum. Generally, the MALDI analysis involves three stages, first, mixing the analyte with the matrix, co-crystallised on an electrically conducting target, e.g. a stainless steel plate, the matrix chosen should strongly absorb the laser energy and pass some of that energy to the analyte. Secondly, energy in the form of a short laser pulse of a specific wavelength is utilised to ablate and ionise the analyte/matrix mixture. The matrix will absorb the photon energy and rapid heating will occur which creates a microexplosion so the analyte is brought into the gas phase and ionised. Finally, the charged analyte ions are moved to the mass analyser, where the ions are accelerated in a high voltage region and further ion separation occurs based on the mass-to-charge ratio. This analyser is called time of flight (TOF). Since all ions receive the same energy, the lighter ions arrive earlier at the detector than the heavier ones.

3.2.3. High Performance Liquid Chromatography (HPLC)

Purification of biomolecules, such as proteins, peptides, and amino acids, can be a challenging task because of their low solubility in both hydrophilic and hydrophobic media. High performance liquid chromatography (HPLC) is an analytical technique for identification and quantitation of a wide variety of non-volatile or semi-volatile organic compounds in a mixture. It utilises a compound's intrinsic affinity for both a mobile phase and a stationary phase to achieve the separation.

There are three major modes of HPLC traditionally employed in peptide purification utilising differences in peptide size (size-exclusion HPLC [SEC]), net charge (ion-exchange HPLC [IEX]), and hydrophobicity (reversed-phased HPLC [RP-HPLC]). Within these modes, mobile phase conditions may be manipulated to maximise the separation potential of a particular HPLC column. In this thesis the RP-HPLC has been used for the purification of the synthesised peptides and peptoids that have been used for the modification of carbon nanomaterials. RP-HPLC is generally superior to other HPLC modes in both speed and efficiency. In addition, the availability of volatile mobile phases makes it ideal for both analytical and preparative separations.

3.2.4. Circular Dichroism (CD) Spectroscopy

Circular dichroism (CD) spectroscopy is the most widespread technique used for estimating the secondary structure, folding, binding properties of proteins and polypeptides in solution.[179] Briefly, this spectroscopic technique depends upon the unequal absorption of left-handed and right-handed circularly polarised light.

It detects wavelength-dependent differences in the absorption of right and left circularly polarised light by optically active molecules. This is achieved by determining the ellipticity of plane polarised light at different wavelengths. This effect occur when a chromophore is chiral (optically active) either intrinsically by reason of its structure, or by being covalently linked to a chiral canter, or also by being placed in an asymmetric environment.[180] The major optically active groups in peptides and proteins are the amide bonds of the peptide backbone and the aromatic side chains. They have regions where the peptide chromophores are in highly ordered arrays, such as α-helices and β-pleated sheets.[181] When circularly polarised light impinges on a peptide, the peptide's electronic structure gives rise to characteristic bands in specific regions in the far-UV of the CD spectrum, reflecting the electronic excitation energies.[182] The weakest energy transition in the peptide chromophore is an $n \rightarrow \pi^*$ transition observed at 210 – 220 nm, which involves non-bonding electrons of the oxygen of the carbonyl group. However, the strongest energy one is an absorption band centered at 190 nm because of $\pi \rightarrow \pi^*$ transition involved the π-electrons of the carbonyl. Hence, depending on the orientation of the peptide bonds in the arrays, the wavelengths of the transitions can be increased or decreased, and the intensity of the transitions can be enhanced or decreased. As a consequence, many common secondary structure motifs, such as the α-helix, β-pleated sheets, β-turns, and poly-L-proline II (P2), have distinctive shapes and magnitudes in the far-ultraviolet (**Figure 3-12**).
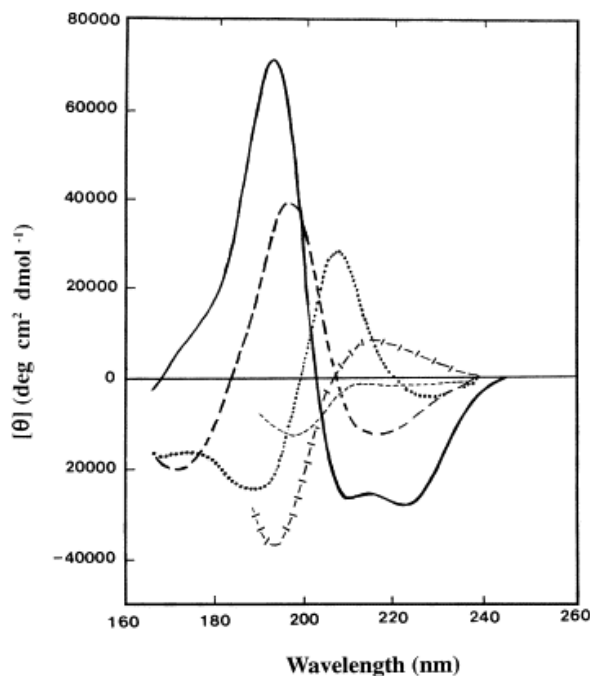
Figure 3-12: Far UV CD spectra associated with various types of secondary structure. (**Solid line**) α-helix, (**Long dashed line**) anti-parallel β-sheet, (**Dotted line**) type I β-turn, (**Cross dashed line**) polyproline (PPII), (**Short dashed line**) irregular structure. Reprinted from [183], Copyright (2005), with permission from Elsevier.

In an α-helix conformation, the peptide backbone follows a helical path and is stabilised by hydrogen bonds between backbone amide and carbonyl groups. The CD spectrum of an α-helix usually shows an intense positive band at 190 nm and a negative band at 208 nm. These bands arise from the exciton splitting of electronic transitions from the amide non-bonding π orbital to the anti-bonding π orbital, π*. While its negative band located at about 220 nm arises from the electronic transition from an oxygen lone pair orbital, n, to the π* orbital.[182,184]

β-sheets form by interstrand hydrogen bonds between either parallel or antiparallel β strands, and are much more flexible than α-helix.[185,186] The characteristic CD features of the β-sheet are considerably less intense signals than helices and show far more variation in spectral characteristics. It usually shows a small negative band at ~ 218

nm which is attributed to ($\pi \to \pi^*$) transitions, and positive band at ~ 196 nm assigned to the ($n \to \pi^*$) transition.[185] The polyproline (PPII) helix spectrum is characterised by a strong negative peak at ~ 200 nm. The CD spectra above 200 nm, however, show considerable variation ranging from a positive band near 218 nm to a negative shoulder near 220 nm.[184,185] Unordered peptide's structures (often also referred to as random coil or disordered) have variable spectra that are generally similar to the PPII spectra,[187,188] but tend to be slightly blue shifted, have slightly smaller amplitudes, and can lack the higher wavelength positive peak. They often also have small negative amplitudes at wavelengths at 195 nm which is attributed to ($\pi \to \pi^*$) transitions and a positive at ~ 212 nm due to ($n \to \pi^*$) transitions.[189,190].

4. SYNTHESIS OF A FLUORINATED PEPTIDE FOR NONCOVALENT FUNCTIONALISATION OF SWNTs

4.1. Introduction

Peptides are particularly attractive for SWNT noncovalent functionalisation because of their biocompatibility and high specificity for other biomolecules and materials. Furthermore, they are well-known for their ability to self-assemble into a wide range of secondary structures.[191] The ability of a peptide to disperse SWNTs appears to depend upon the peptide's binding affinity to the sp^2 hybridised surface of the carbon nanotube and its amphiphilic properties. Amphiphilic peptides act as surfactants in the sense that they lower the interfacial energy of the nanotube water interface, thus allowing them to be dispersed in the aqueous phase.[192,193] Additionally, coating SWNTs with peptides offers a suitable noncovalent approach for debundling as they permit the organisation of individually dispersed SWNTs into useful assemblies.[194]

Peptides can adopt a range of secondary structures, the most common being random coils, α-helices, β-strands,[195] extended (micellar), and cyclic[196] (**Figure 4-1**). Peptides with all of these different secondary structures have been used to disperse CNTs, with varying degrees of success.[197]
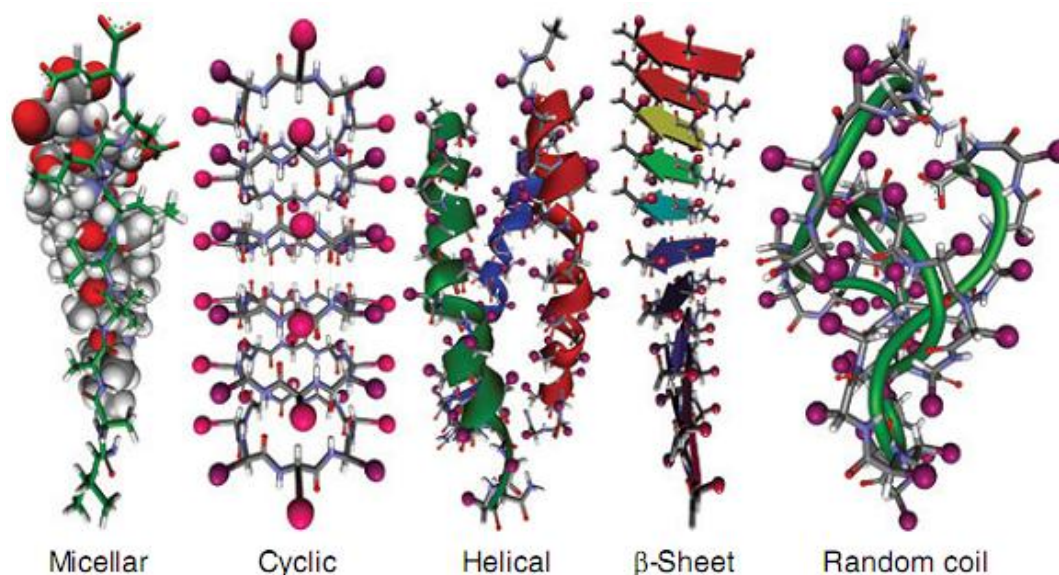
Figure 4-1: Molecular models of peptide secondary structures. Reproduced from [198] with permission of John Wiley and Sons.

The simplest peptides known to bind to SWNTs are random coil peptides, whose sequences are not designed to form specific secondary structures, or specific peptide aggregates. Such peptides rely on aromatic residues to drive SWNT interactions, while the remaining sequence serves to stabilise the peptide-SWNTs complex and prevent reaggregation.[125,198] These peptides have a high degree of freedom to rearrange on the SWNTs surface and obtain the most stable conformation. Therefore, SWNTs defects, in the form of carboxyl and hydroxyl groups, have a limited effect on the peptide's affinity to disperse the SWNTs.[199,200] Despite this ability to disperse SWNTs, with potential for biocompatibility, random coil peptides have limited utility as dispersal agents due to the lack of control over their arrangement on SWNTs.

It has been shown that amphiphilic β-strand peptides can disperse SWNTs, and the composites formed lead to enhanced optical and physicochemical properties for

selected tube types.[118,201,202] The dispersion ability of these peptides is proportional to the length of the β-strand region, as well as the length of the hydrophilic termini.[203,204] These results agree with molecular mechanics and dynamics simulations that show that β-sheets can assemble into β-barrels wrapping around the SWNTs.[202,205] However, with an increasing hydrophilic termini length the peptides lose the ability to form β-strand and hence successfully disperse the carbon nanotubes.

The α-helix secondary structure is the most common helical form of peptides. It consists of a seven-residue repeating sequence (*a b c d e f g*) which completes approximately two turns of the helix.[191,206] An amphiphilic helix presents two different faces, a more hydrophobic face (*a* and *d* positions) and a more hydrophilic face (*b*, *c*, *e*, *f, g* positions). The interactions between α-helical peptides and a SWNT surface can stabilise the peptide/SWNT complex, and also can control the carbon nanotube assembly thus creating ordered functional structures through peptide-peptide interactions.[127] Helical peptide interactions with a SWNT surface include three types of potential interactions; intra-peptide interactions, peptide–peptide interactions, and peptide–nanotube hydrophobic interactions. Intra-peptide interactions, which can be optimised by controlling a peptide's design, are important in determining the helical propensity of the peptide. Helical propensity plays an important role in determining the peptide's ability to disperse SWNTs.[203,207,208] For example, highly helical peptides are not always great dispersal agents, due to their tendency to aggregate. While peptides with lower helical propensity are able to disperse nanotubes, yet may be less likely to attain an organised folded structure when bound to the nanotube surface.[203,207] Therefore, it is important to fine-tune

intra-peptide interactions to suit the desired degree of interaction. Dieckmann *et al.*[124] designed synthesised the amphiphilic α-helix peptide, named nano-1, and demonstrated that it could bind to SWNTs using phenylalanine (Phe) and tyrosine (Tyr) (as well as artificial analogue nitro-phenylalanine) side groups distributed along one face of the peptide helix (**Figure 4-2**). Zorbas *et al.*[209] isolated long, individual SWNTs wrapped with nano-1 peptide in aqueous solution.
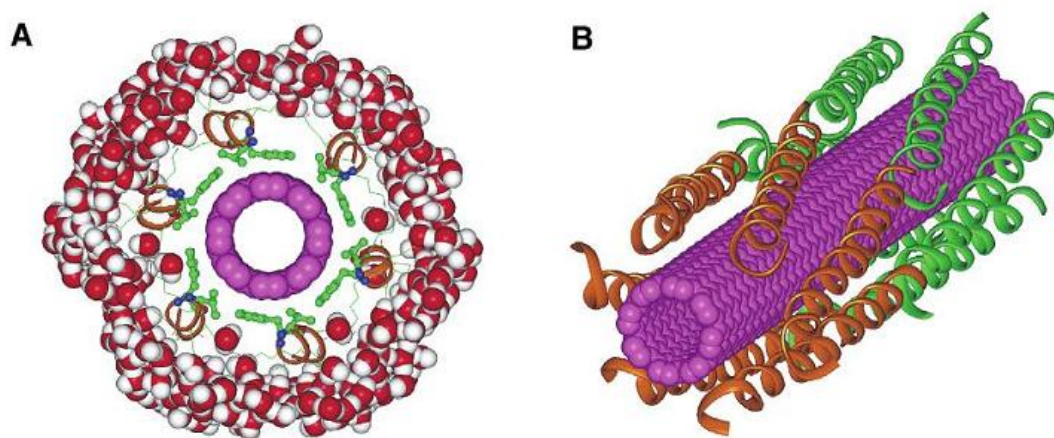
Figure 4-2: Model illustrating the interactions between nano-1 and SWNT. (**A**) Cross-section view of a SWNT (pink cylinder) wrapped by six peptide helices. (**B**) View of nano-1 peptide-wrapped SWNTs. Reprinted with permission from [124]. Copyright (2003) American Chemical Society.

Peptide-peptide interactions, which can be driven by hydrophobic, H-bonding, and charge-charge interactions, in the presence of SWNTs, play an important role in SWNTs dispersal, as they control the assembly of the helical peptides and their arrangement on the SWNTs surface. Dieckmann showed that the self-assembling properties of helical nano-1 peptide were important in controlling the size and morphology of peptide/SWNT fibers. The nano-1 peptide was designed so that favourable charge-charge peptide-peptide interactions would occur among the peptides coating the exterior surfaces of separate nanotubes, leading to

oligomerisation of the peptide-coated nanotubes into higher-order structures. Additionally, they used atomistic molecular dynamics simulations (MD) of nano-1 wrapped SWNTs to study the molecular details of the peptide-SWNT and peptide-peptide interactions (**Figure 4-3**). This showed that the peptides could form inter-peptide hydrogen bonds through their hydrophilic residues to completely shield the SWNTs from contact with water to stabilise the multi-peptide/SWNT complex.[210]
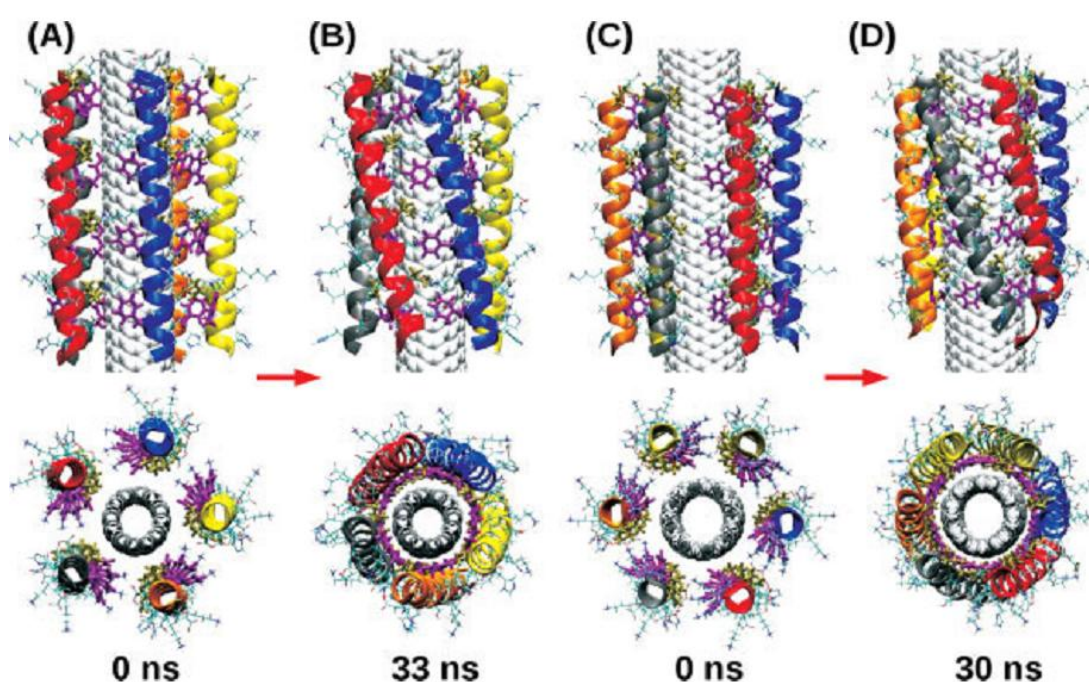
Figure 4-3: Snapshots from MD simulations for nano-1 peptide interaction with (6,6) SWNT (**A** and **B**) and (8,8) SWNT (**C** and **D**) systems. (**A**) and (**C**) illustrate the initial conformations, whereas (**B**) and (**D**) illustrate the final conformations after 33 ns of simulation for (6,6) SWNT and 30 ns of simulation for the (8,8) SWNT system, respectively. Reproduced from [210] with permission of John Wiley and Sons.

Of the three types of potential interaction, the interactions between the peptide and the nanotube are the most important, without this the peptide would not disperse the SWNTs.[126] This interaction usually depends on the aromatic interactions between the hydrophobic face of a helical peptide with the carbon nanotube's surface form one

side. On the other side, the aliphatic interactions of the peptide's hydrophilic face with the solvent form a stable dispersion. The importance of the peptide's aromatic content on the peptide-SWNTs binding affinity has been highlighted by several researchers.[87,200,207,211,212] Aromatic residues, such as phenylalanine (Phe), tyrosine (Tyr), and tryptophan (Trp), in the helical core increase the peptide–nanotube affinity and the efficiency of the peptide as a dispersal agent. Tomasio *et al.*[87] used MD simulations to investigate the binding affinity of a range of peptide sequences adsorbed on graphite and a carbon nanotube. Their results showed that a tryptophan rich peptide had a stronger-binding affinity toward SWNTs than tyrosine or phenylalanine rich-peptides. These results agree with recent experimental observations, such as the direct AFM measurements reported by Li *et al.,*[126] which revealed that poly-tryptophan exhibited greater adhesion on nanotubes than poly-lysine. Dieckmann *et al.*[213] reported that among the three aromatic amino acids (phenylalanine (Phe), tyrosine (Tyr), and tryptophan (Trp)) tested, sequences containing tryptophan showed the greatest affinity for SWNTs, while tyrosine (Tyr) was found to be more selective for individual SWNTs. Phenylalanine (Phe) was the aromatic residue with the lowest affinity for SWNTs. Atomic force microscopy measurements and optical absorption spectroscopy revealed that the ability to disperse individual SWNTs increased with an increasing number of aromatic residues in the peptide, indicating that π–π stacking interactions play an important role in peptide dispersion of SWNTs.[120] All of the previous experimental measurements of SWNTs noncovalent interaction with peptides proved that various forms of aromatic molecules binding to SWNTs can effectively disperse the nanotubes, indicating that this interaction is quite strong due to the aromatic nature of

the π–π stacking. Therefore, it is not surprising that aromatic residues also have an affinity for graphitic surfaces.

Although, aromatic residues in the helical peptide increase the peptide-nanotube affinity and the efficiency of the peptide as a dispersal agent, it is necessary to balance the overall affinity of the aromatic residues with the peptide's helical propensity. Overloading the hydrophobic core with high affinity aromatic residues has the potential to perturb helix formation and cause peptide aggregation, in which case the peptide might bind to the nanotube surface in a more random fashion.[198]

Salzmann *et al.*[123,214] demonstrated the importance of the balance between hydrophilic and aromatic residues in the dispersion of SWNTs. They found that the optimisation of the pyrene content in the synthesised 4-(pyren-1-yl)butanoylated polylysine (PBPL) dispersing agent leads to a maximal dispersing effect of the SWNTs. **Figure 4-4** shows PBPL structure and a representation of a PBPL/SWNTs conjugate.
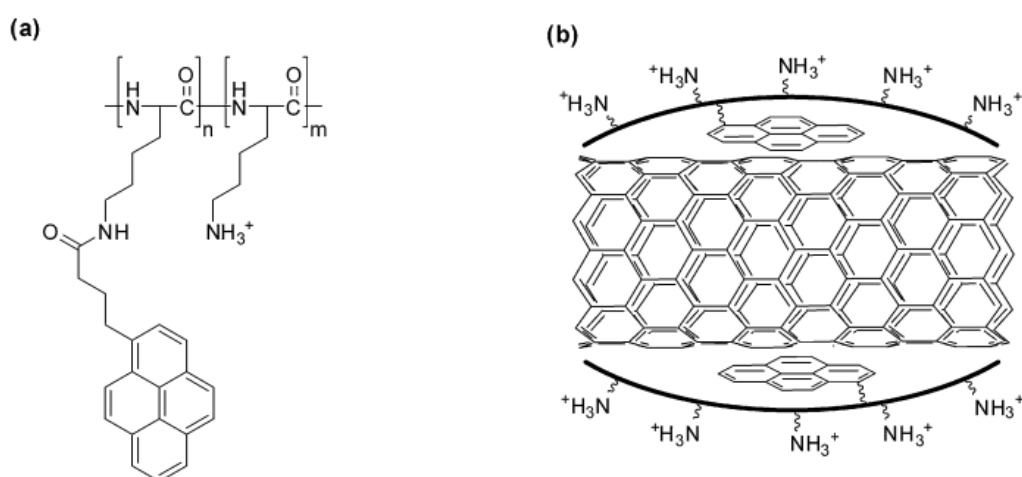
Figure 4-4: (**A**) Chemical structure of 4-(pyren-1-yl)butanoylated polylysine(PBPL) (**B**) Schematic representation of a PBPL/SWCNT conjugate. Reproduced from [214] with permission of The Royal Society of Chemistry.

Despite the number of experimental methods which have been used to study the interaction of SWNTs with peptides, the nature of this interaction is not yet fully understood. However, understanding the mechanism(s) of peptide interaction with SWNTs aids the understanding of the molecular basis of increasing the solubility of nanotubes. Thus, their interaction mechanism(s) is a critical focus of investigation. A number of modelling studies have attempted to understand the nature of the peptide-nanotubes interactions. Several studies have used a variety of computational methods, such as MD simulations and DFT calculations in an attempt to gain insight into the atomic scale mechanisms underlying the strong affinity of peptide sequences to nanotubes. Wallace *et al.*[215] performed multi-scale MD to study the adsorption profile of the nano-1 peptide on a SWNTs surface. They found that the peptide interacts with SWNT in a preferred orientation, such that its hydrophobic surface is in contact with the tube. Chiu *et al.*,[216] in a similar study performed full MD of a single nano-1 peptide at various water/hydrophobic interfaces, including water/graphite and water/SWNTs. They found that the peptide α-helix cannot match its hydrophobic face to the rigid planar graphite surface without partially unfolding. In contrast, it curves on the SWNT surface in α-helical conformation to simultaneously maximise its hydrophobic contacts with the SWNT and its hydrogen bonds with water (**Figure 4-5**).
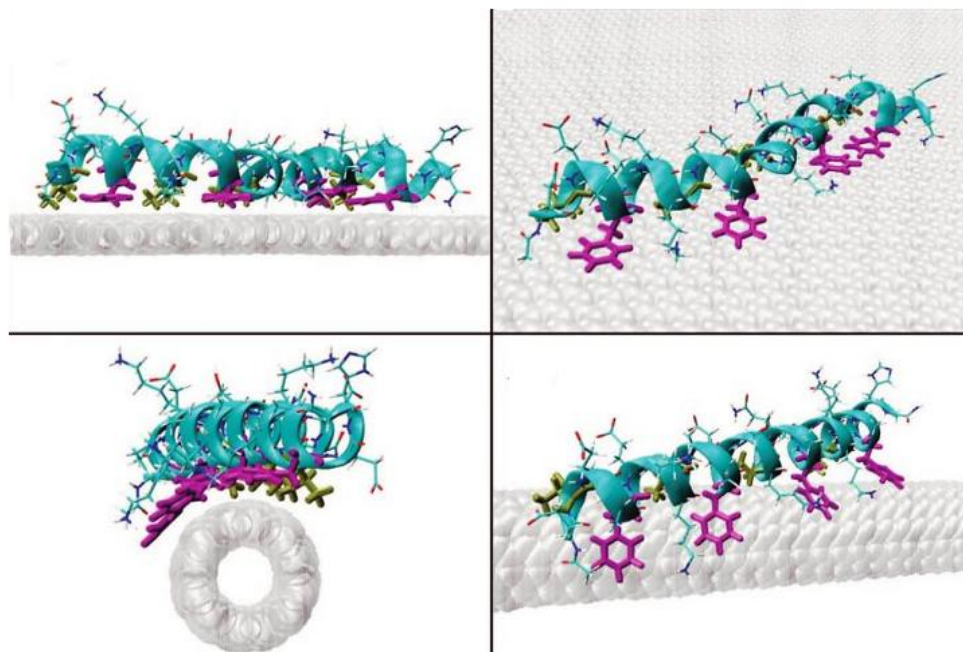
Figure 4-5: Representative nano-1 configurations from the MD simulations with water/graphite (**Right**) and with water/CNT (**Left**). Reprinted with permission from [216]. Copyright (2008) American Chemical Society.

Among CNTs characterisation techniques nuclear magnetic resonance (NMR) been used to reveal more information about SWNTs functionalisation. It has been utilised to study the effects of oxidisation, bending, and twisting of SWNTs on their electronic properties and to locate the defects in the SWNTs structure.[217-221] Nelson et al.[222] used ^{1}H NMR chemical shifts to study the impact of o-, p-, and m- directing effects of electrophilic aromatic substituents on phenyl groups covalently bonded to SWNTs. Marega et al.[223] used diffusion based NMR experiment (1D DOSY) for the characterisation of covalently modified CNT derivatives.

Due to the considerable progress in fluorescence labelling and observation techniques for biological molecules, SWNTs have been visualised using a conventional optical microscope with the aid of fluorescent tags.[224] Yet these

characterisation techniques give limited information about the type, structure, and degree of functionalisation to utilise the SWNTs in applications. Therefore, more research groups are employing NMR as a characterisation technique to reveal information about SWNTs functionalisation. ^{19}F NMR has been employed as an alternative reporter nucleus in NMR studies of labelled biopolymers covalently functionalising nanotubes.[225] Coleman *et al.*[75] used a Bingel reaction to create carbene and diethyl bromomalonate, which attacks the sidewall of SWNTs. The resulting material was tagged with fluorine and gold, and then observed with ^{19}F NMR and AFM. Holzinger *et al.*[226] used ^{19}F NMR to monitor the photo induced radical addition of pentafluorinated alkyl to SWNTs (**Figure 4-6**). The pentafluorinated alkyl sidewall functionalised SWNTs was confirmed with boarding pentafluorinated alkyl signal. Kumari *et al.*[227] used the DFT methods to compute the full ^{19}F NMR shifts to differentiate between the zig-zag and chiral forms of fluorinated SWNTs.
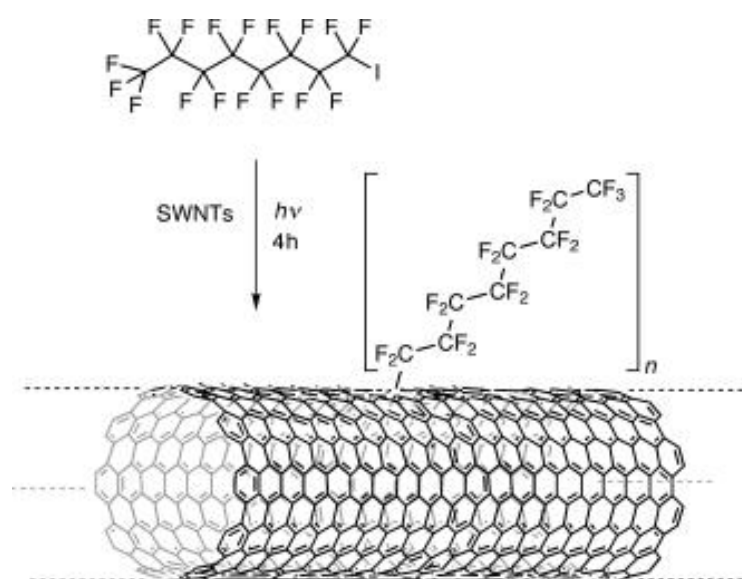
Figure 4-6: Sidewall functionalisation by the addition of a radical. Reproduced from [226] with permission of John Wiley and Sons.

The introduction of fluorine into organic molecules has become a very attractive area of synthetic and medicinal chemistry.[228] The presence of fluorine in biological molecules often results in significant changes in their chemical, physical, and biological properties.[229] Among the large family of bioactive fluorinated compounds, fluorinated amino acids[230] and peptides[231] are of value in medicinal chemistry as enzyme inhibitors, anti-tumour agents and antibiotics.[228] Fluorinated amino acids have found a variety of applications in peptide and protein science. Incorporation of the unique electronic properties of fluorine into amino acids creates a new and exciting class of building blocks for peptide and protein modification and provides an opportunity to study their conformational properties and metabolic processes by ^{19}F NMR.[232]

This chapter investigates the effect of nano-1 peptide's α-helical stability, through N-terminus acetylation, on its ability to disperse SWNTs. Also, a synthesise of a fluorine tagged nano-1 peptide was carried out in order to ascertain whether ^{19}F NMR can be used to monitor the binding of α-helical peptides to SWNTs surface. Finally, the nano-1 peptide/SWNTs complex's stability against enzyme digestion was investigated.

Chapter 4

4.2. Results and Discussion

4.2.1. Synthesis and Characterisation of Modified Nano-1 peptides

The amphiphilic α-helical nano-1 peptide, which is based on a previously characterised peptide Coil-V_aL_d,[233] is reported to act as a surfactant in order to disperse SWNTs in aqueous solution.[124,234] The original nano-1 sequence is Ac-EVEAFEKKVAAFESKVQAFEKKVEAFEHG-CONH$_2$, which is a repeating heptad designated $(a\ b\ c\ d\ e\ f\ g)_n$, where a through g refer to the positions in the linear sequence. When folded into an α-helix, hydrophobic residues in positions a and d will generate an apolar face of the helix, whereas more hydrophilic residues in the other positions will form a more polar surface (**Figure 4-7**).
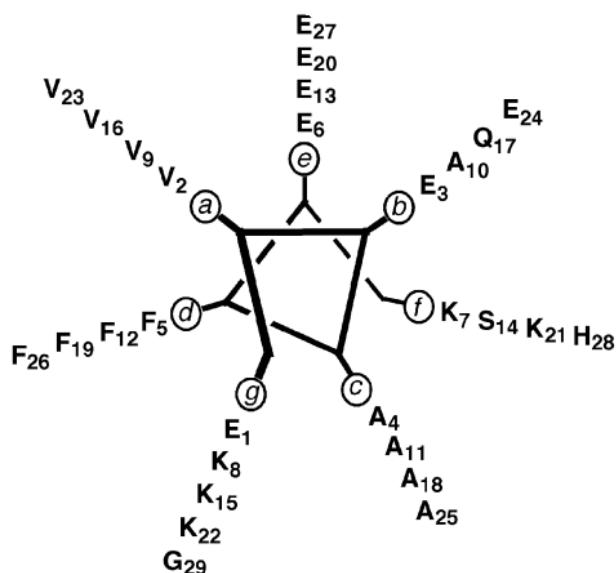
Figure 4-7: Helical wheel diagram showing positions of nano-1's residues in the α-helix.

The original design of nano-1 has an acetylated N-terminus, to remove charge from the terminus and thus making it less polar to increase its affinity for SWNTs. Several investigators have shown that charged residues near the peptide's N-terminus

destabilise the α-helix through a repulsive electrostatic interaction with the helix dipole of the peptide.[235-237] It has been suggested that capping of the N-terminus may stabilise an α-helix by forming an additional hydrogen bond to a main chain NH group. Furthermore, it has been found that N-terminus capping effects are more prominent in a short peptide than long sequence peptides.[238] Therefore, the first main focus of this section is to study the effect of peptide's N-terminus acetylation on the peptide ability to disperse SWNTs by modifying the original N-terminus design of nano-1 peptide. In order to study the effect of N-terminus capping on short peptides vs. long peptides, four modified versions of nano-1 were synthesised. The second focus was to synthesis a fluorinated nano-1 peptide which was used to study the interaction between the peptides with the surface of SWNTs via ^{19}F NMR.

4.2.1.1. Synthesis of Nano-1 Peptides

The original design of nano-1 peptide, $(V_aF_d)_{4/4}$, has an acetylated and amidated N- and C-termini, respectively.[124] However, in order to assess the effect of N-terminus acetylation on the peptide's polarity and thus affinity towards the hydrophobic surface of SWNTs two versions nano-1 peptide have been synthesised. The first has an acetyled N-terminus and named acetylated nano-1, Ac-$(V_aF_d)_{4/4}$. While the second has a free N-terminus and named free N-terminus nano-1, H_2N-$(V_aF_d)_{4/4}$. Fmoc-SPPS was used for the synthesis of two versions of nano-1 peptide. The synthesis of acetylated nano-1 and free N-terminus nano-1 were carried out using an automated CEM Liberty microwave peptide synthesiser. Peptide synthesis was carried out on Rink amide (AM) resin to ensure that an amidated C-terminus was provided upon

cleavage from the resin, and O-(Benzotriazol-1-yl)-*N,N,N',*N'-tetramethyluronium tetrafluoroborate (TBTU) was used as a coupling reagent. Considering that the synthesis of the 29 amino acid, nano-1 peptide synthesis was performed in two steps as shown **Scheme 4-1**.
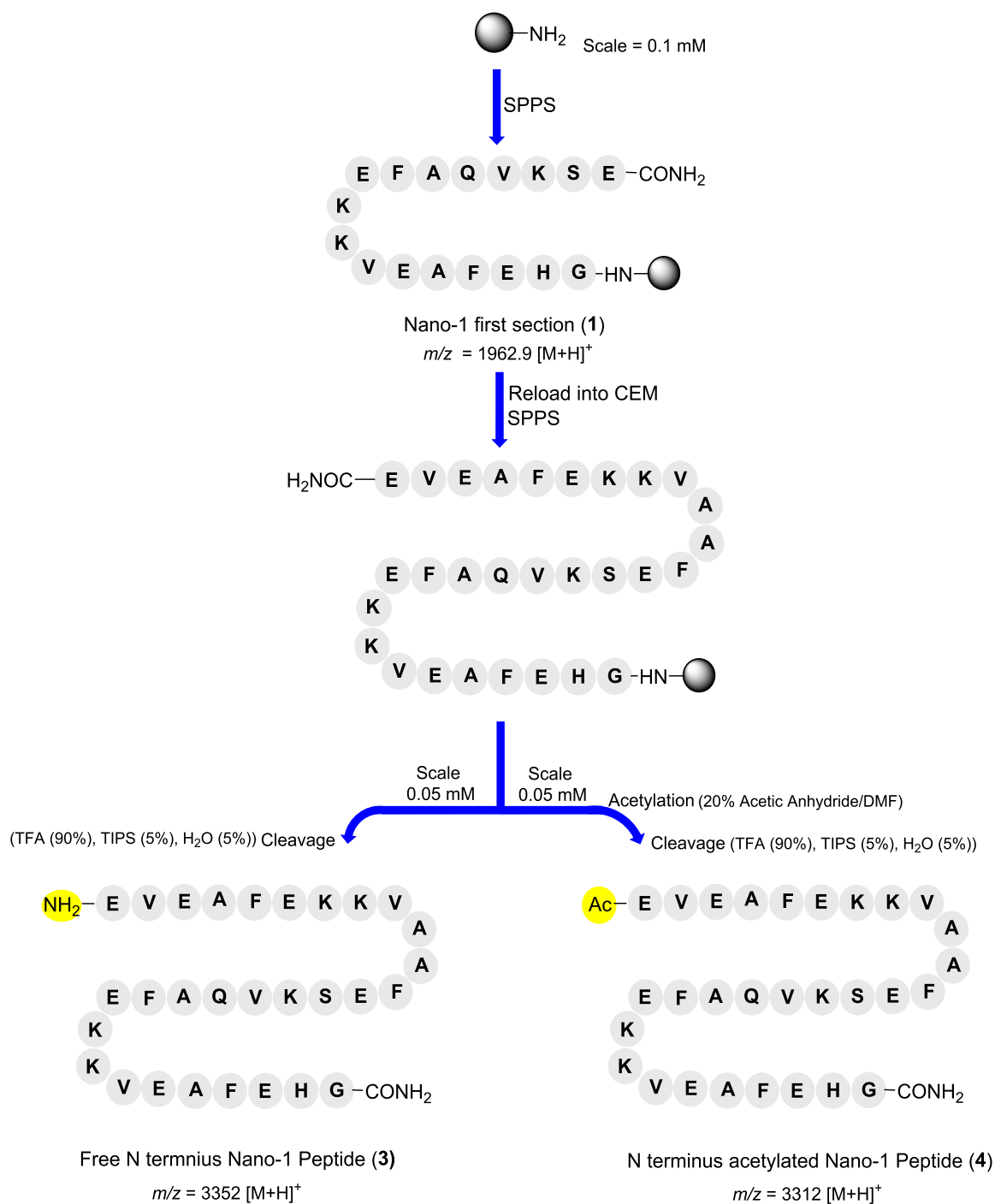
Scheme 4-1: Synthesis of nano-1 peptides.

The first step was synthesis of the first 17 amino acids in the peptide sequence, resin-H$_2$N-ESKVQAFEKKVEAFEHG-CONH$_2$, named first section nano-1 (**1**). This peptide left on the resin, so it could be reloaded into the peptide synthesiser to complete the peptide sequence in the second step of the synthesis. A small scale cleavage was carried out and MALDI-TOF analysis confirmed the successful coupling of the first 17 amino acids of nano-1 peptide to the Rink amide resin (**Figure 4-8**).

m/z [M + H]$^+$ = 1962.9
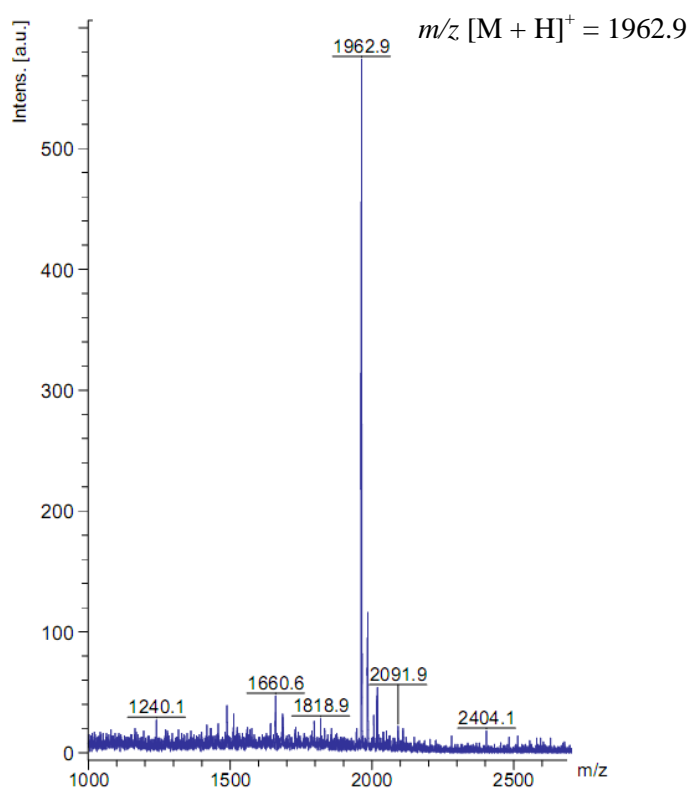
Figure 4-8: MALDI-TOF for first 17 amino acids of nano-1 peptide (**1**).

The second step involved reloading of nano-1 first section (**1**) into the peptide synthesiser to complete the 29 amino acid nano-1 peptide sequence (**2**). In order to produce the two versions of the nano-1 peptide; the peptide linked resin (**2**) was then divided into two halves. The first half was cleaved from the resin to yield free N

terminus nano-1 peptide (**3**). MALDI-TOF analysis of the crude was used to confirm

the presence of the correct peptide (**Figure 4-9**).
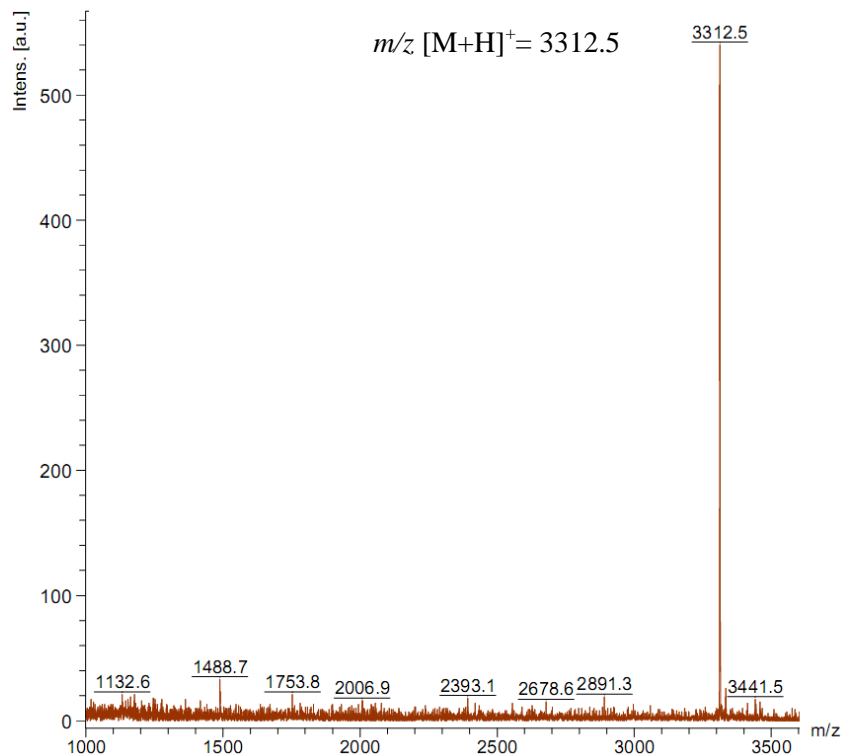
Figure 4-9: MALDI-TOF for free N-terminus nano-1 peptide, **3**

The other half of the peptide linked to resin peptide was acetylated using 20 % acetic

anhydride/DMF, and then the acetylated peptide (**4**) cleaved from the resin and

MALDI-TOF analysis of the crude peptide was used to confirm the presence of the

acetylated N-terminus nano-1 peptide (**Figure 4-10**).
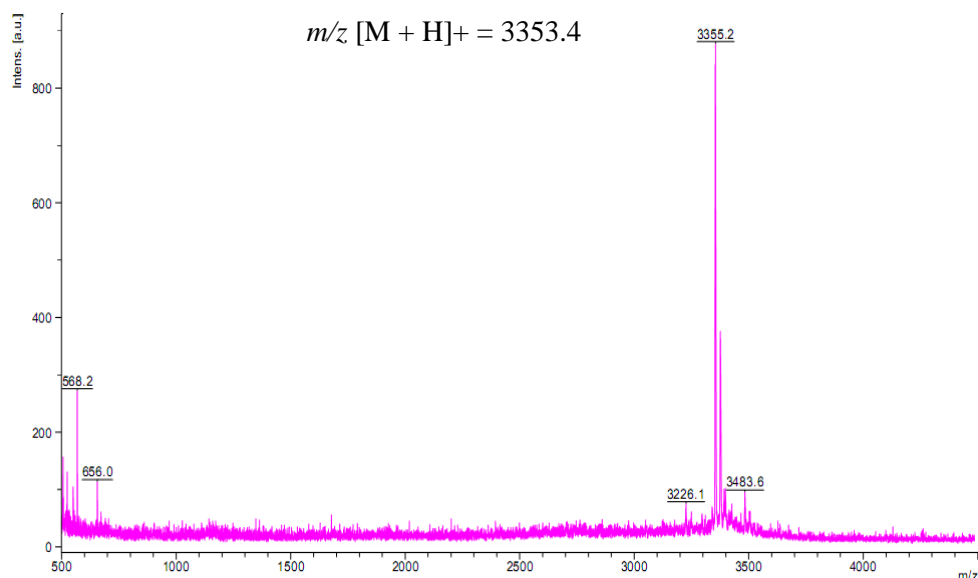
Figure 4-10: MALDI-TOF for acetylated nano-1 peptide, **4**.

4.2.1.2. Synthesis of Short Nano-1 Peptides

The one heptad of nano-1 peptide, $(V_aF_d)_{1/4}$, was first synthesised by Zorbas.*et al.*[120] to understand the importance of aromatic content in nano-1 peptide on its ability to disperse SWNTs. The one heptad nano-1 peptide reported had an acetylated and amidated N- and C-termini, respectively, Ac-EVEAFEKKY-CONH$_2$. It had been suggested that N-terminus acetylation improves the stability of α-helical in short peptide more than in long sequence peptide.[237,238] Therefore, the main aim of this section is to synthesise two versions of the one heptad nano-1 peptide, $(V_aF_d)_{1/4}$, with and without acetylated N-termini. They are named as acetylated short nano-1, Ac-$(V_aF_d)_{1/4}$, and free N-terminus short nano-1, H$_2$N-$(V_aF_d)_{1/4}$, respectively. These peptides will be used to disperse SWNTs to understand how acetylation of the N terminus in a short peptide affects the dispersion of SWNTs (**Section 4.2.2**).

Both peptides, acetylated short nano-1 (Ac-$(V_aF_d)_{1/4}$), and free N-terminus short nano-1 (H$_2$N-$(V_aF_d)_{1/4}$), were synthesised using the general microwave assisted SPPS procedure. The synthesis of each peptide was carried out on Rink amide (AM) resin using the same method used in the synthesis of nano-1 peptides (**Section 4.2.1.1**). Then synthesised peptides were cleaved from the resin, and purified using reverse phase HPLC (RP-HPLC). Fractions that were shown by mass spectrometry analysis to contain the desired were pooled and lyophilisation afforded the peptide as a white powder. MALDI-TOF analysis of the purified free N-terminus short nano-1(**5**) and acetylated short nano-1(**6**) confirms the presence of the correct peptide, (**Figure 4-11**) and (**Figure 4-12**) respectively.
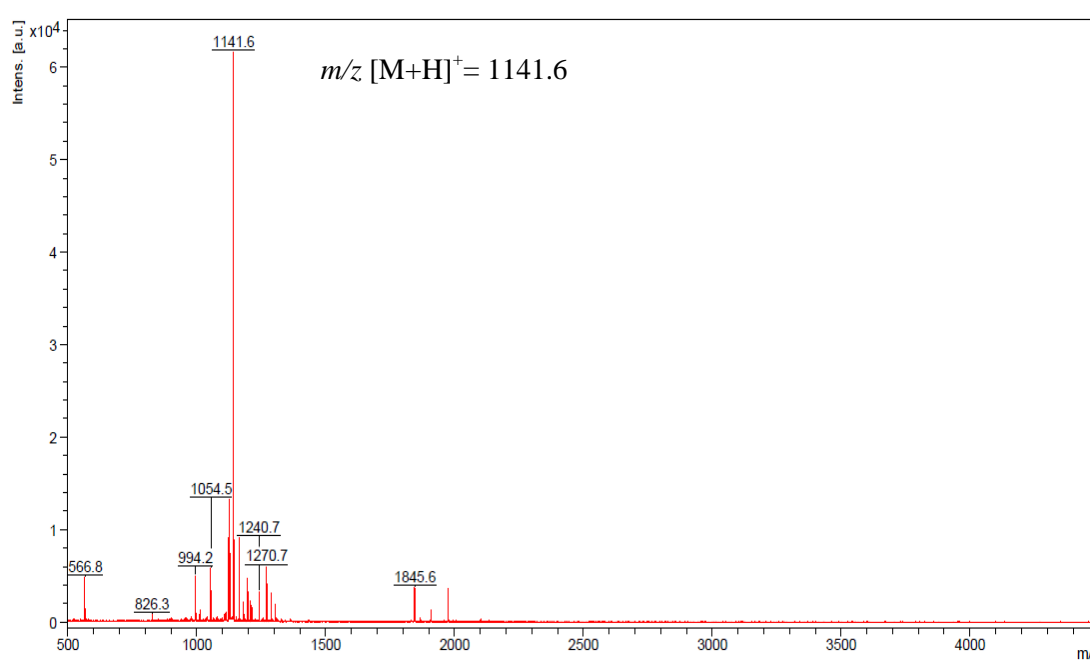
Figure 4-11: MALDI-TOF of free N-terminus short nano-1, **5**.
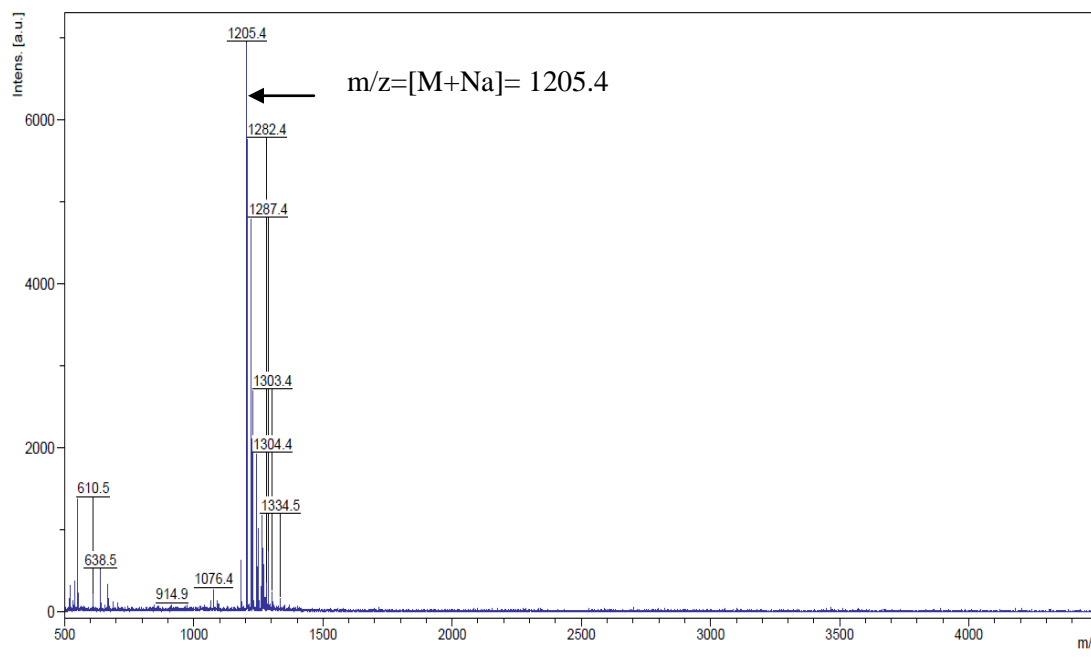
Figure 4-12: MALDI-TOF of N-terminus acetylated short nano-1, **6**.

4.2.1.3. Synthesis of a Fluorinated Nano-1 Peptide

Peptide structure, and ultimately its function, is largely induced by side chain interactions and determined through the specific amino acid sequence. Thus synthesis of non-proteinogenic amino acids has attracted wide attention in an attempt to create new peptide properties through modified α-amino acids.[239,240] Fluorine tagged amino acids have been designed to provide ^{19}F NMR signature spectroscopic signals for use as sensors for the study of binding between nano-1 peptide and the surface of SWNT. First a ^{19}F labelled phenylalanine was synthesised and then coupled with the first stage of nano-1 while still attached to resin (**1**). The proposed synthetic route to the target ^{19}F labelled phenylalanine (**7**) is shown in **Scheme 4-2**; the key step involves a Negishi coupling that will be used to form a bond between a substituted benzene ring and an orthogonally protected L-serine (**10**).
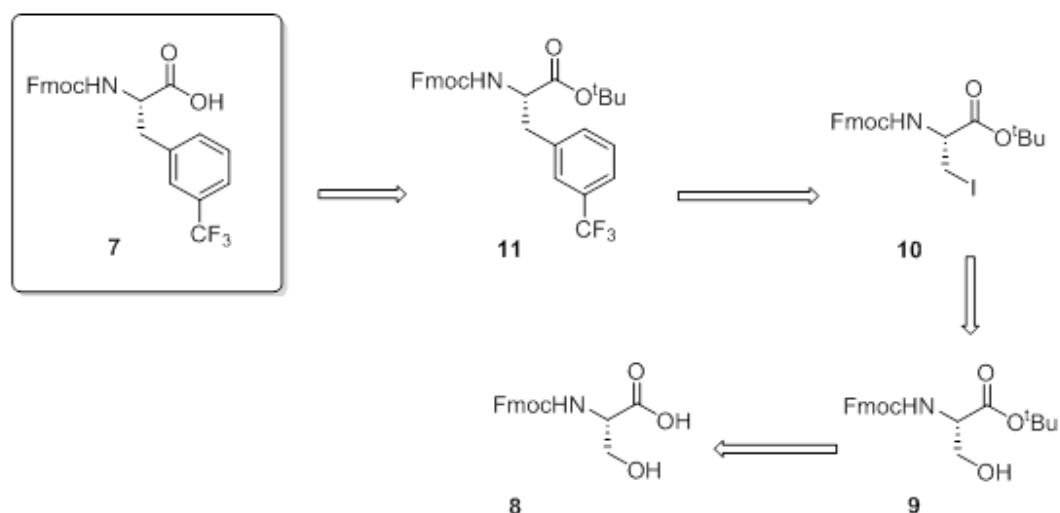
Scheme 4-2: Proposed synthetic route to amino acid target (**7**).

The key intermediate in the synthesis was the orthogonally protected iodo-alanine (**10**), which was prepared in two steps from commercially available Fmoc-Ser-OH (**8**) (**Scheme 4-3** and **Scheme 4-4**). The first step involved protection of the free carboxyl ester: this was achieved by treatment of **8** with 1.5 equivalents of ^{t}Bu-2,2,2-trichloroacetimidate in EtOAc at room temperature (**Scheme 4-3**). The orthogonally protected serine (**9**) was obtained as a white powder after column chromatography. **9** was fully characterised by ^{1}H-NMR and ESI-MS and the data obtained matched that previously reported.[241,242] The yield of 63 % is due to the formation of an unwanted impurity that was assumed to be the di-*t*-Butyl protected serine.
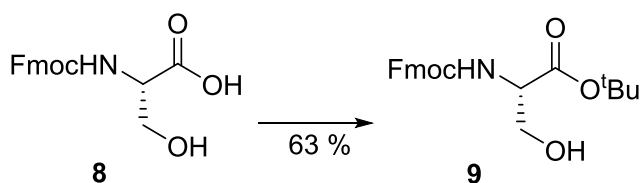
Scheme 4-3: Preparation of orthogonally protected serine (**9**). Reagents and conditions: ^{t}Bu-2,2,2-trichloroacetimidate, EtOAc, rt,16 h.

Conversion of **9** to the protected iodo-alanine (**10**) was achieved via reaction with iodine, imidazole and triphenylphosphine (PPh$_3$). The reaction proceeded in good yield (68 %) to give **10** as a white powder after column chromatography. **10** was fully characterised and the beta CH$_2$ protons in the ^{1}H NMR displayed the expected up field/down field shift (from 3.92 ppm to 3.59 ppm) and the characteristic 516.3 [M+Na]$^+$ isotope was observed in the mass spectra obtained.
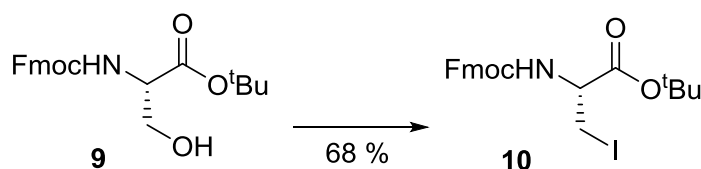
Scheme 4-4: Iodination of (**9**). Reagents and conditions: I$_2$, PPh$_3$, imidazole, DCM, rt, 16 h.

The final stage in the synthesis of fluorinated amino acid (**11**) involved a Negishi reaction step, which is a palladium-catalysed cross-coupling reaction between α-amino acids and organozinc iodides to synthesis of complex molecules by providing an efficient means of (C–C) bond formation.[243-248] For the preparation of **11**, iodo-alanine (**10**) was reacted with 3-iodobenzotrifluoride in a solution of iodine (I$_2$) in dry DMF with suspended zinc and catalysed by Bis(dibenzylideneacetone)palladium (Pd(dba)$_2$) and 2-Dicyclohexylphosphino-2′,6′-dimethoxybiphenyl (Sphos) (**Scheme 4-5**) to give a good yields (65 %) after column purification. Since the major drawback of the Negishi coupling is the relative sensitivity of organozinc reagents towards oxygen and moisture,[249] the reaction is carried out in dry DMF and under argon atmosphere.
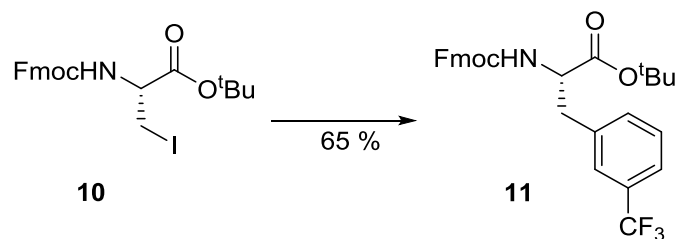
Scheme 4-5: Synthesis of fluoro tagged phenylalanine (**11**). Reagents and conditions: Pd(dba)$_2$, zinc, Sphos, 3-Iodobenzotrifluoride, dry DMF, inert atmosphere, 16 h.

The trifluoro-phenylalanine (**11**) was fully characterised. ^{19}F-NMR analysis (**Figure 4-13**) showed two different fluorine environments, one at - 62.84 ppm and a second one at - 62.97 ppm. This implies that rotation about the C−C bond from the benzene ring to the CF$_3$ group is restricted. The splitting in the CF$_3$ peak is similar to published spectra of CF$_3$-labeled amino acids.[250,251]
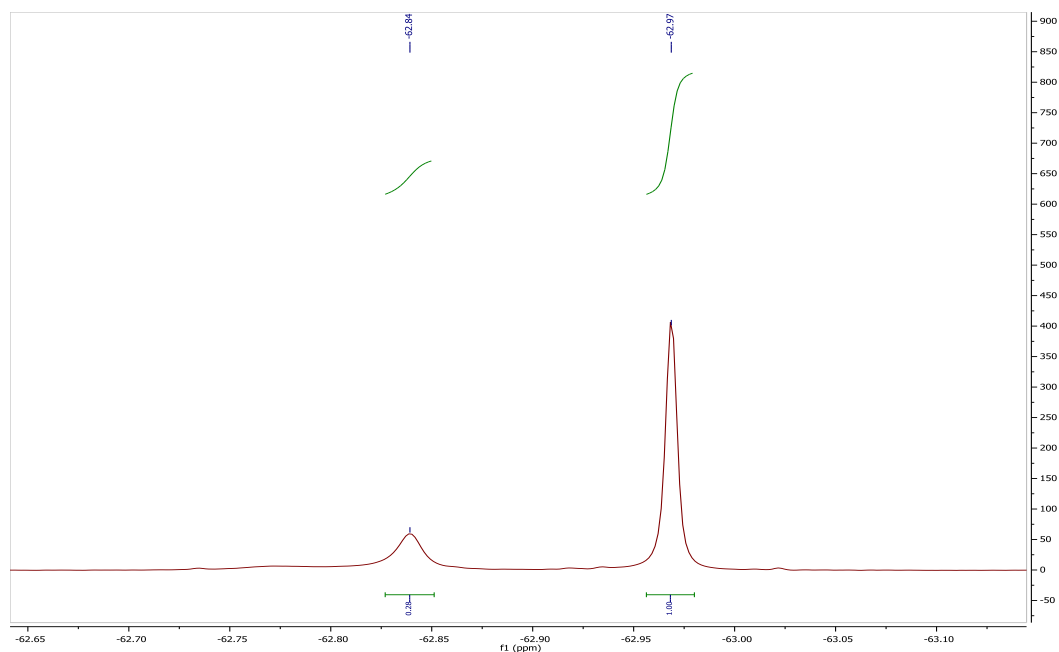
Figure 4-13: The doubling of the fluorine peaks in the ^{19}F NMR spectra of **11** in D$_2$O.

For the synthesis of the fluorinated nano-1 peptide (**13**), a free carboxylic acid on the fluoro amino acid is needed. Therefore, deprotection of the t-butyl ester from **11** was achieved by stirring the protected amino acids in a mixture of DCM and TFA for 5 hours (**Scheme 4-6**), which afforded the product in 76 % yield.
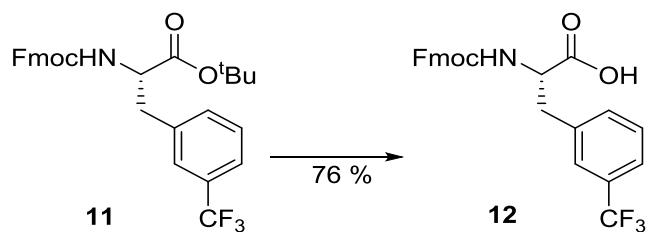
Scheme 4-6: C-terminus deprotection of **11**. Reagents and conditions: TFA, DCM, rt., 5 h.

The free C-terminus fluoro tagged amino acid (**12**) was coupled with the first section of the nano-1 peptide (**1**) though a manual SPPS coupling at room temperature. The fluoro peptide-resin was then reloaded into the peptide synthesiser; the rest of nano-1 peptide sequence was coupled using the microwave coupling. When all of the amino acids were coupled, a final Fmoc deprotection step was carried out using 20 % piperidine/DMF, and the peptide was then cleaved from the resin, **Scheme 4-7** illustrates the synthesis route of **13**.
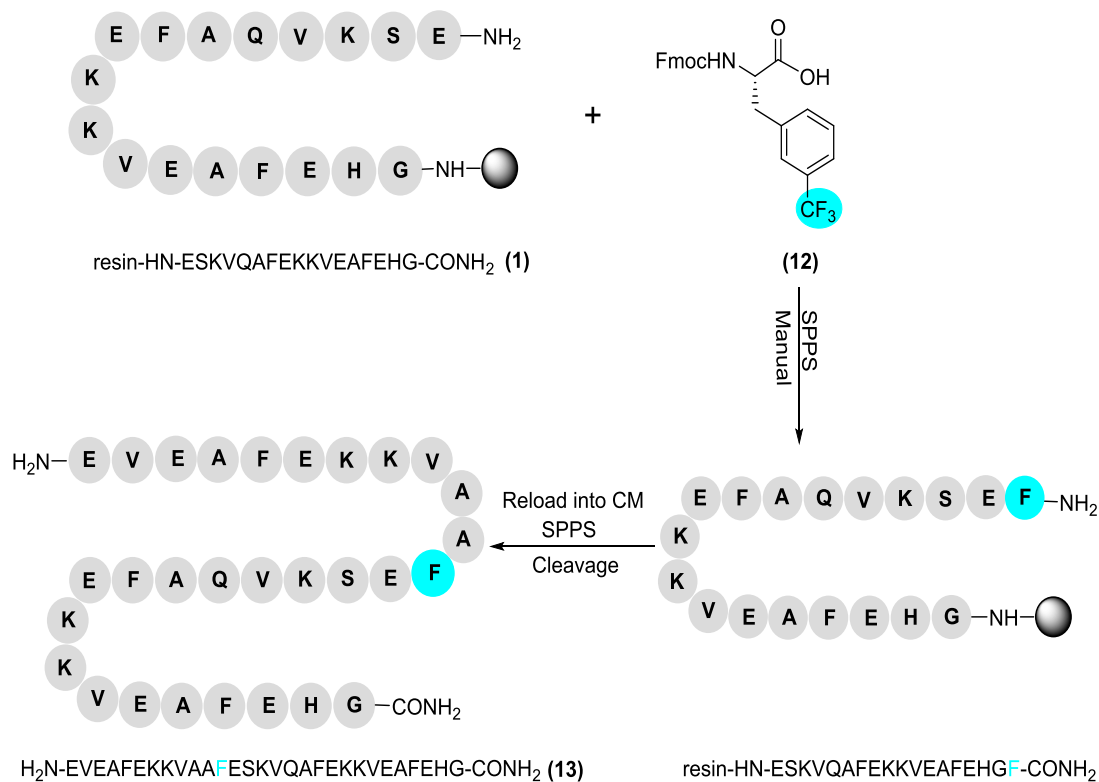
Scheme 4-7: The synthetic route to fluorinated nano-1 peptide, **13**.

MALDI-TOF mass analysis of the crude peptide was used to confirm the presence of the correct peptide. Then fluorinated nano-1 peptide (**13**) was purified using reverse phase HPLC (RP-HPLC). Fractions that were shown by mass spectrometry analysis to contain **13** were pooled and lyophilisation afforded the peptide as a white powder.

4.2.1.4.   Circular Dichroism of Synthesised Peptides

The circular dichroism (CD) spectroscopy is used to characterise the secondary structures of synthesised peptides. The CD spectra were collected at 100 μM concentration in phosphate buffered saline solution (PBS). This low concentration was chosen to prevent intermolecular interactions which may affect the CD values

obtained. The data is presented in mean residue ellipticity units which take into account the chain length and concentration of samples. The CD spectra of synthesised peptides are shown in **Figure 4-14**. The original design of nano-1 peptide has a 3.6 residues per turn.[124] Thus the one heptad nano-1 peptide, (Ac-$(V_aF_d)_{1/4}$) which is 9 amino acid residues, is found to be too short to form a helix.[120] Similarly, both of the synthesised short nano-1 peptides, acetylated short nano-1 (**6**) and free N terminus short nano-1 (**5**), are not expected to be able to adopt a significant degree of α-helical structure. Therefore, this section focuses on the CD characterisation of the synthesised nano-1 peptides, free N-terminus nano-1 (**3**), acetylated nano-1 (**4**), and fluorinated nano-1 peptide (**13**).
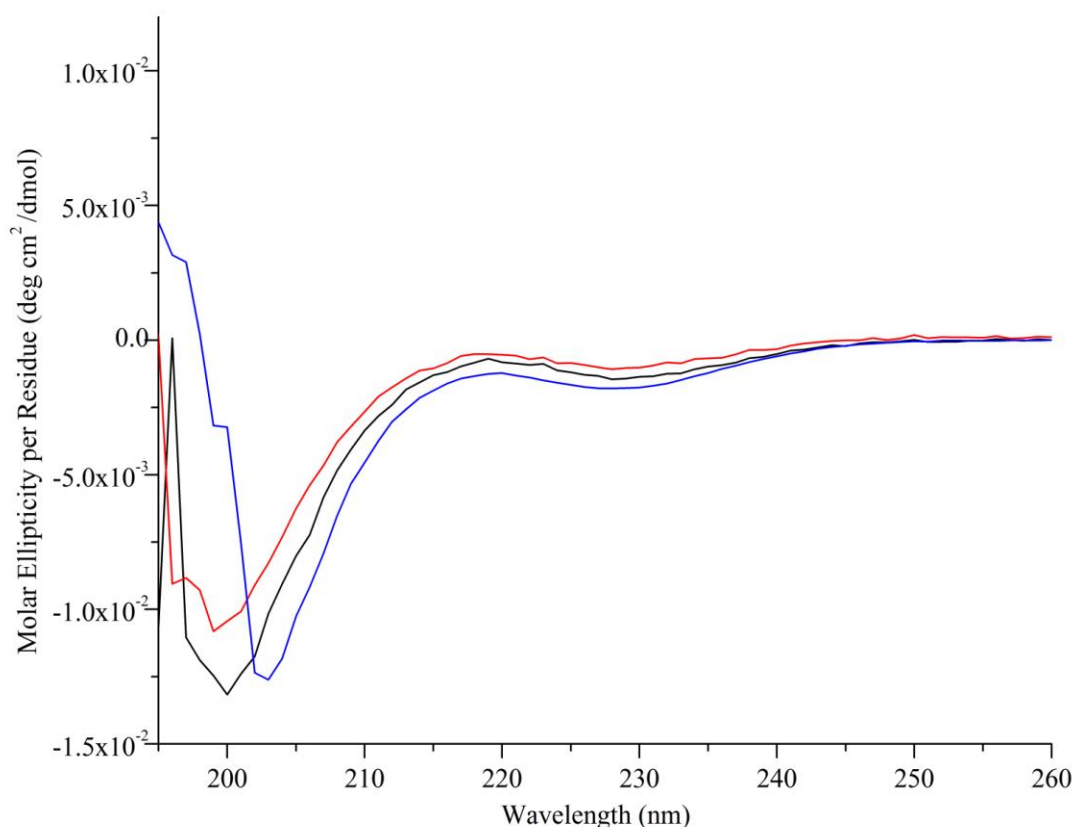
Figure 4-14: CD spectra of synthesised nano-1 peptides. (**Black line**) free N terminus nano-1 (**3**), (**Red line**) Ac nano-1 (**4**), and (**Blue line**) fluorinated nano-1 peptide (**13**).

The CD spectra of acetylated nano-1 (**4**) shows strong negative band at ~ 200 nm and a weaker band at ~ 226 nm, suggesting a mixture of helical and unordered conformations, which is in agreement with previously published studies.[120,124,252,253] The CD spectrum of free N-terminus nano-1 peptide (**3**) shows similar bands to acetylated nano-1 (**4**) spectra (a strong negative band at ~ 200 nm and a weaker band at ~ 226 nm). This indicates that N-terminus capping did not have any major effect on the nano-1 peptide's helicity. Furthermore, the CD spectrum of fluorinated nano-1 peptide (13) was found to exhibit similar peaks to the CD spectra of synthesised nano-1 peptides (**3** and **4**). This implied that the modification on the phenylalanine (Phe) residue with the CF_3 group does not affect the peptide's helicity.

4.2.2.   Dispersion of SWNTs with Nano-1 Peptides

Previous studies have demonstrated that nano-1 peptide, $(V_aF_d)_{4/4}$, coats and debundles SWNTs and promotes the assembly of the coated nanotubes into novel hierarchical structures.[120,124] Phe residues in nano-1 (**Section 4.2.1**) can interact with the SWNT's hydrophobic surface via π–π stacking interaction. Among different types of SWNTs, HiPco produced SWNTs have been used here in the dispersion experiments. The HiPco process usually produces large amounts of high-quality SWNTs. However, they typically contain ~ 35 wt% impurities (i.e. iron nanoparticles). Therefore, before the noncovalent interaction of HiPco SWNTs with the synthesised nano-1 peptides (**Section 4.2.1**), HiPco SWNTs were purified in a two-step method. First, as-produced HiPco SWNTs were heated at 400 ℃ for 30 min to break the carbon shell around the metal catalyst. Then, catalyst nanoparticles were

dissolved by stirring the SWNTs in (6 M) HCl solution overnight. The purified SWNTs were characterised by Raman, UV-Vis-NIR, and TGA (see **Appendix A**). Furthermore, the extinction coefficient of purified SWNTs was experimentally determined by making a series of dilutions of purified SWNTs dispersion in 1 % SDS solution at 700 nm (see **Appendix B**). However, the calculated extinction coefficient (ε_{700} = 37.3 mL mg^{-1} cm^{-1}) is found to be lower than the previously reported value of 39.0 mL mg^{-1} cm^{-1} for purified SWNTs at the same wavelegnth.[159]

The dispersant concentration plays an important role in the ability to disperse CNTs, however due to the limited amount available of the synthesised peptides it was not possible to determine if the concentration of 1.0 mM used was high enough to saturate the system (meaning that a further increase dispersant would not affect the amount of CNT suspended) or not (meaning that an increase in dispersant would further increase the amount of CNT suspended). Nano-1 peptide/purified SWNT complex was prepared by mixing 1.0 mg of purified SWNTs with 1.0 mM of the synthesised peptide solution via probe ultrasonication for 15 min in an ice bath. **Table 4-1** shows the synthesised peptides used in SWNTs dispersions.

Type of modification	Dispersant Peptide	No. residues
	Free N terminus nano-1 (**3**)	29
	Acetylated nano-1 (**4**)	29
N terminus capping	Free N terminus short nano-1(**5**)	12
	Acetylated short nano-1 (**6**)	12
Fluoro Tagged Phe	Fluorinated nano-1 (**13**)	29

Table 4-1: List of modified nano-1 peptides used to disperse purified SWNTs.

The sonication was followed by centrifugation to remove bundled and aggregated nanotubes to afford a homogeneous supernatant dispersion. Differences among the modified nano-1 peptides/purified SWNT dispersions were observed visually. The darker solutions indicating a higher concentration of SWNTs. **Figure 4-15** shows an image of modified nano-1 peptides/SWNT complexes and purified SWNTs dispersion in water as a control after sonication and centrifugation.
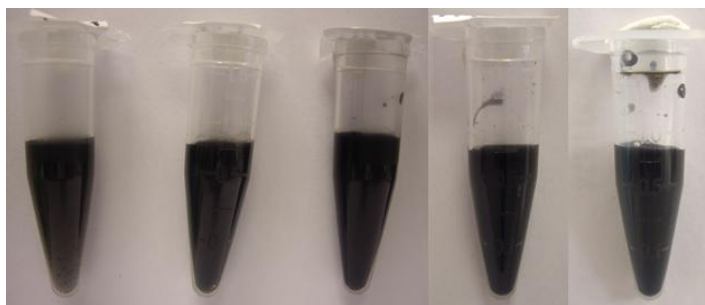
Figure 4-15: Peptide/purified SWNTs complex aqueous dispersion after sonication and centrifugation. Dispersion from right to left: fluorinated nano-1(**13**)/purified SWNTs, Ac nano-1(**4**)/purified SWNTs, free N-terminus nano-1(**3**)/SWNTs, Ac short nano-1(**6**)/purified SWNTs, free N-terminus short nano-1(**5**)/purified SWNTs.

Based on the SWNTs supernatant colour intensity, short nano-1 peptides, free N terminus (**5**) and acetylated (**6**), appears to disperse less efficiently than nano-1 peptides, free N terminus (**3**) and acetylated (**4**), and fluorinated nano-1 peptide (**13**). More detailed characterisation of the quality and quantity of the dispersed SWNTs can be obtained from the UV-Vis-NIR absorption spectra of the dispersion. **Figure 4-16** shows the UV-Vis-NIR spectra of dispersed purified SWNTs with a series of modified nano-1 peptides in water.
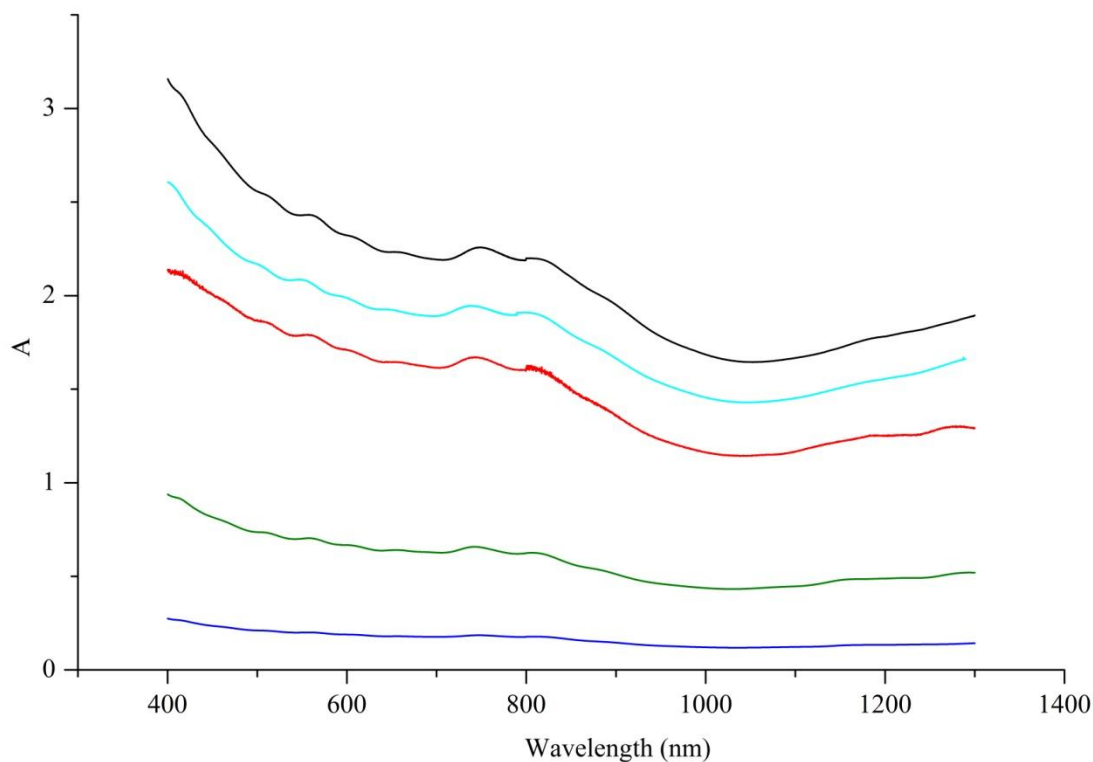
Figure 4-16: UV-Vis-NIR absorption spectra of modified nano-1 peptides/purified SWNTs complexes dispersion. (**Black line**) Ac nano-1(**4**)/purified SWNTs, (**Cyan line**) fluorinated nano-1(1**3**)/purified SWNTs, (**Red line**) free N terminus nano-1(**3**)/purified SWNTs, (**Green line**) Ac short nano-1(**6**)/purified SWNTs, (**Blue line**) free N terminus short nano-1(**5**)/purified SWNTs.

Individual nanotubes are active in the UV–Vis region and exhibit characteristic bands corresponding to additional absorption due to 1D van Hove singularities. Bundled CNTs, however, are hardly active in the wavelength region between 200 and 1300 nm. Modified nano-1 peptides/purified SWNTs complexes absorption spectrum shows well-resolved features absorption peaks that extend throughout the metallic (~ 440 – 645 nm) and semiconducting nanotubes (830 – 1600 nm, and 600 – 800 nm) absorption regions. This indicates that the nanotubes dispersed as individuals and/or as very small bundles in aqueous solution by the dispersant peptides. UV-Vis absorption intensity is proportional to the amount of SWNTs dissolved in the solution. Thus, UV-Vis-NIR absorption is used to determine the

concentration of the dispersed SWNTs in the supernatant through application of the Beer-Lambert Law and calculated extinction coefficient of purified SWNTs at 700 nm (ε_{700} = 37.3 mL mg^{-1} cm^{-1}). **Table 4-2** shows the concentration of dispersed nanotubes.

Dispersion	Conc. of Purified SWNTs µg mL^{-1}
SDS/purified SWNTs (control)	196.4
Free N terminus nano-1(**3**)/purified SWNTs	434.7
Acetylated nano-1(**4**)/purified SWNTs	586.9
Free N terminus short nano-1(**5**)/purified SWNTs	47.4
Acetylated short nano-1(**6**)/purified SWNTs	167.9
Fluorinated nano-1(**13**)/purified SWNTs	506.0

Table 4-2: Concentration dispersed purified SWNTs by modified nano-1 peptides. Nano-1 peptides concentration: 1 mM mL^{-1}, SDS concentration: 1 % by weight.

Table 4-2 shows that the concentration of dispersed nanotubes by the SDS solution is less than that of the four heptad nano-1, acetylated nano-1 (**4**), free N-terminus nano-1 (**3**), and fluorinated nano-1 (**13**). However, it is higher than the concentration of dispersed nanotubes with the one heptad nono-1 peptides, acetylated (**6**) and free N-terminus (**5**). The concentration of dispersed purified SWNTs by the four heptad nano-1 is higher than that of short nano-1. These results agree with the previous studies.[120,213] Furthermore, the concentration of the aqueous dispersion of acetylated short nano-1 (**6**)/purified SWNTs complex was found to be higher than free N-terminus short nano-1 (**5**)/purified SWNTs complex. Acetylated short nano-1 (**6**) dispersed purified SWNTs at a concentration of 167.9 µg mL^{-1}, whereas free N-terminus short nano-1 (**5**) gave 47.4 µg mL^{-1}. On the contrary, four heptad nano-1 peptides, acetylated (**4**) and free N terminus (**3**), dispersed almost similar amount of

purified SWNT; acetylated nano-1 (**4**) dispensed 586.9 µg mL^{-1} of purified SWNTs, while free N-terminus nano-1 (**3**) dispensed 434.7 µg mL^{-1}. These results show that peptide's N-terminus capping has a greater effect on short nano-1 peptides ability to disperse nanotubes comparing to nano-1 peptides; short nano-1 peptide is 9 amino acid residues, while nano-1 peptide is 29 amino acid residues. These results can be rationalised by the fact that N-terminus capping stabilise an α-helix by forming an additional hydrogen bond to a main-chain NH group.[237,238,254] The concentration of purified SWNTs dispersed by fluorinated nano-1 peptide (**13**) was found to be similar to nanotubes dispersed by four heptad nano-1 peptides (**3** and **4**). This suggests that the fluorinated phenylalanine residue did not have a major effect on either peptide's helicity, or its ability to fold around the nanotubes surface.

4.2.3. ^{19}F NMR of Fluorinated Nano-1 Peptide/Purified SWNTs Complex

Fluorinated nano-1 peptide (**13**)/SWNTs composite was prepared so that the interaction between the nanotube and the peptide could be monitored with ^{19}F NMR.[255,256] The idea was that the signal in the ^{19}F NMR spectrum for the fluorinated nano-1 peptide (**13**) would change as it went from being free in the solution to being immobilised on the SWNT. This binding should broaden the ^{19}F NMR signal, perhaps to the extent that it becomes unseen.[256] ^{19}F NMR will be sensitive to changes in the van der Waals or electrostatic environments expected with the binding.

Trifluoroacetic acid (TFA) used in the cleavage cocktail of fluorinated nano-1 peptide (**13**) is known to have a strong ^{19}F NMR peak at -78.5 ppm. Thus, Trifluoroethanol (TFE) was added to fluorinated nano-1 peptide (**13**)/purified

SWNTs complex dispersion to act as an external reference peak of a known shift and relative intensity, -77 ppm. Thus, the relative integrals of ^{19}F NMR peaks mentioned will be as a ratio of the integral for the peak to the integral for the TFE peak. The ^{19}F NMR spectrum of fluorinated nano-1 peptide (**13**) has been recorded as a control sample. As seen in **Figure 4-17**, the peptide solution in deuterium oxide (D$_2$O) displays the relative peak intensities of 0.7 at - 62.24 ppm. Upon the interaction of the peptide with purified SWNTs, the peptide's peaks have disappeared, **Figure 4-18**. This suggests that the peptide is bound to nanotube's surface, thus its CF$_3$ δ_F ^{19}F NMR peak has broaden to the extent that it is unseen in the spectra.
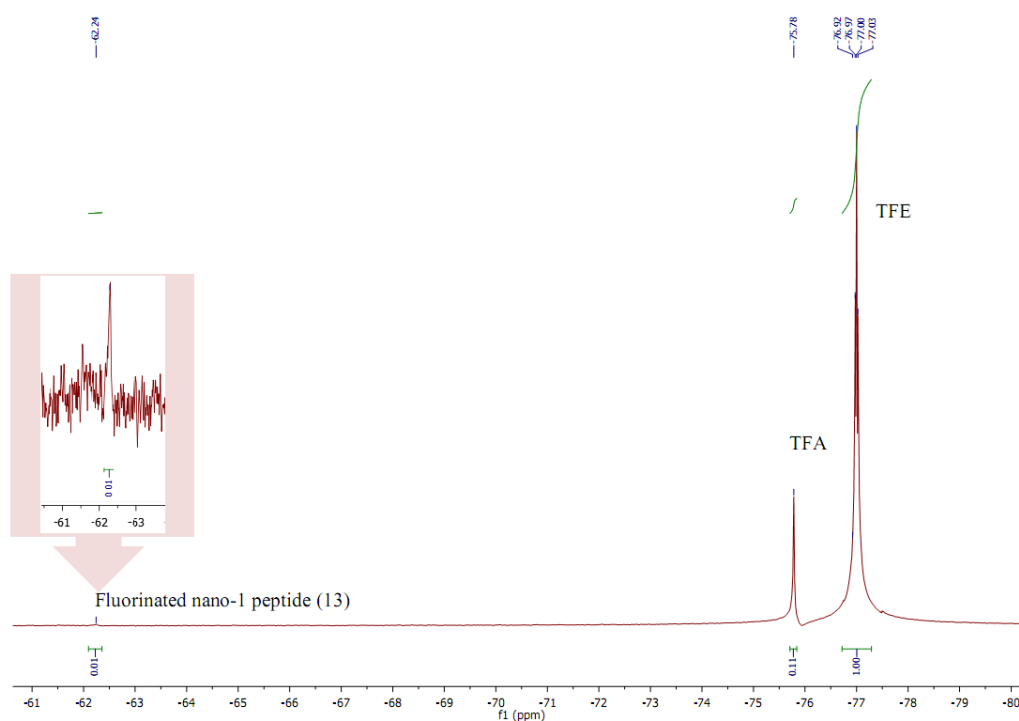
Figure 4-17: ^{19}F NMR spectra of fluorinated nano-1 peptide (**13**) (control) in D$_2$O.
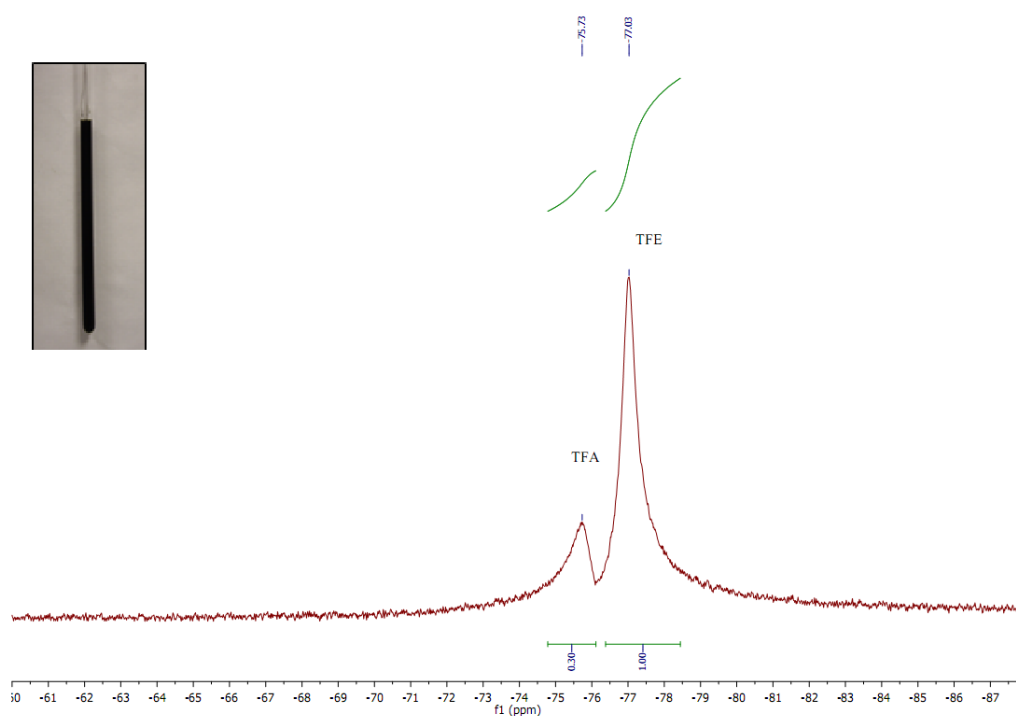
Figure 4-18: ^{19}F NMR spectra of fluorinated nano-1 peptide (**13**)/purified SWNTs composite dispersion in D$_2$O. Inset picture shows the dispersion before running the ^{19}F NMR analysis.

It was thought that after the dispersed purified SWNTs sediment from the solution the ^{19}F NMR signal of the peptide would reappear. However, ^{19}F NMR spectra of the dispersion did not show any peaks as shown in **Figure 4-19**. This is thought to be due to the fact that the peptide has sedimented from the dispersion while still noncovently attached to the SWNTs. Therefore, more research needs to be done on this project.
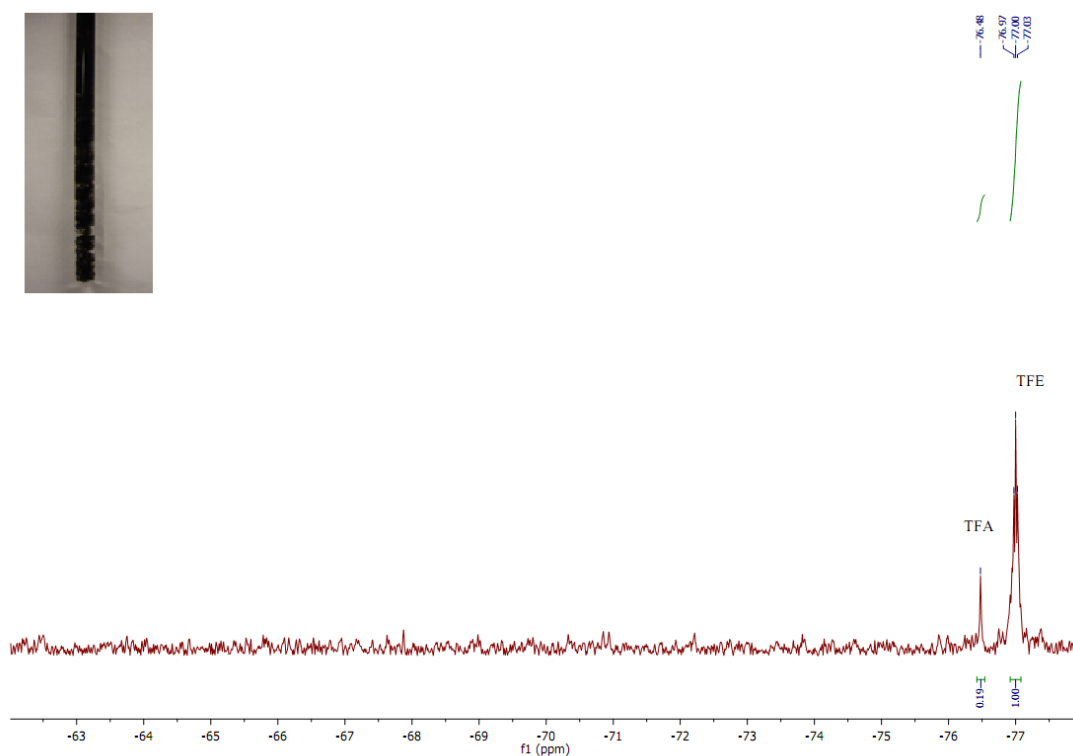
Figure 4-19: ^{19}F NMR of fluorinated nano-1 peptide (**13**)/purified SWNTs composite in D_2O after sedimented from the dispersion. Inset picture shows the crashed out purified SWNTs before running the ^{19}F NMR analysis.

4.2.4. Enzyme Digestion of Nano-1 Peptide/SWNTs Complex

Functionalised SWNTs are able to cross cell membranes and accumulate in the cytoplasm, and even reach the nucleus, without being cytotoxic (concentrations up to 10 mM).[257-259] Therefore, they could act as carriers that transport and deliver bioactive components into cells. In fact, SWNTs enhance the uptake of molecules that have previously demonstrated a low cellular penetration.[260] For example, the cellular uptake of free peptides is often extremely poor, thus their conjugations to nanotubes' surfaces allow improvements in the delivery of such biological molecules.[260] This is due to the fact that nanotubes have a high loading capacity, due

to their high aspect ratio, have the potential to be the ideal shuttle for peptide molecules.[261] For example Pantarotto *et al.*[262,263] were the first to develop a vaccine delivery system by covalently linking bioactive peptides to amino-derivatised SWNTs. Since then many aspects concerning the dispersion, stability and the behaviour of SWNTs in biological settings have already been investigated in separate studies. Peptide stability toward proteolytic degradation is important for its therapeutic applications as a means of increasing the plasma half-life.[264,265] However, relatively little is known about SWNTs/peptide hybrids regarding enzymatic degradation. This section studies the stability of peptide/SWNTs hybrids as a function of enzyme digestion. The results discussed in (**Section 4.2.2**) showed that Ac nano-1 peptide (**4**) exhibited high dispersion ability towards purified SWNTs due to π−π stacking of the peptide aromatic residues on the surface of SWNT. Trypsin cleaves peptides at the C-terminal side of positively charged residues (arginine (Arg), and lysine (Lys)).[266] Trypsin digestion of Ac nano-1(**4**) (as a control sample) and Ac nano-1(**4**)/purified SWNTs dispersion incubated with 5 μL trypsin in the presence of 2 μL dithiothreitol (DTT) at 37 °C for 24 h were performed. The distribution of Lys and Arg residues in Ac nano-1 (**4**) is such that trypsin digestion yields peptide fragments, shown in **Table 4-3** and **Figure 4-20.**

Peptide	Calculated Mass (Exact Mass)	Digested Peptide Fragment Sequence	Observed Mass ([M+H]$^+$, *[M+2H]$^{2+}$, **[M+4H]$^{4+}$)
Ac nano-1 peptide (**4**) (Ac-EVEAFEKKVAAFESKVQAFEKKVEAFEHG-CONH$_2$)	3352	KKVEAFEHG-Amide	916.4
		KVAAFESKV	751.12
		KKVEAFEHG	*458.44
		KVEAFEHG	*394.57
		KVAAFESKV	*376.23
		KVQAFEKK	*361.23
		KKVVEAFEHG	**229.17

Table 4-3: LR-MS (ESI-TQD) data for Trypsin/DTT digested Ac nano-1(**4**) (control).

95
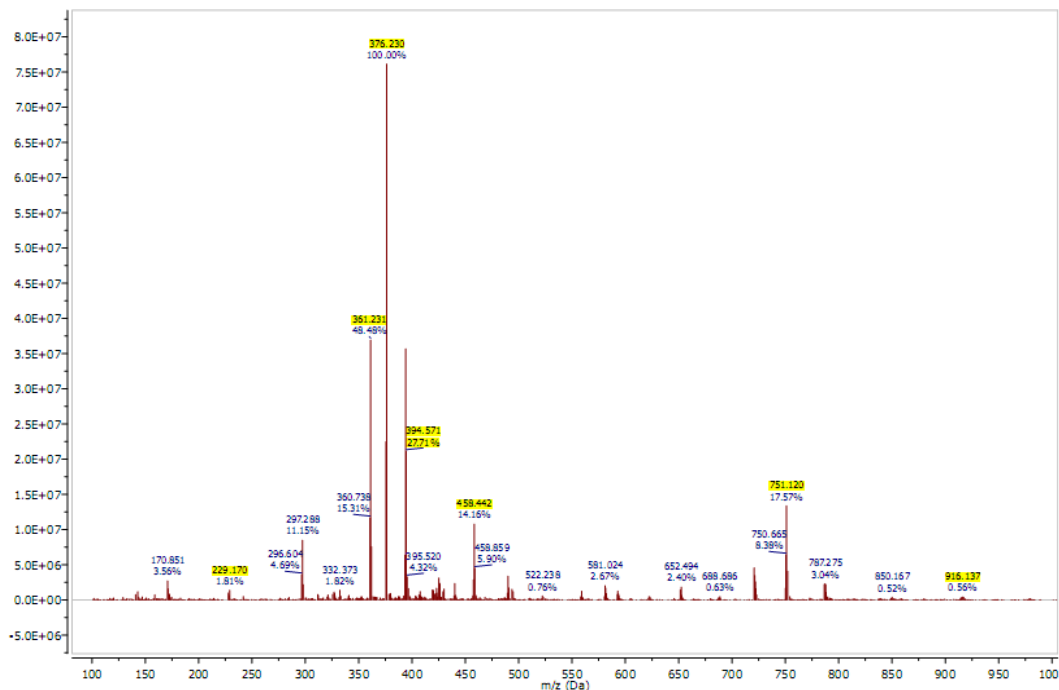
Figure 4-20: Mass spectrum of trypsin/DTT digested Ac nano-1(**4**) (control).

After the trypsin/DTT incubated with the Ac nano-1(**4**)/purified SWNTs dispersion, the dark black colour of the dispersion indicates that the nanotubes are still dispersed by Ac nano-1(**4**) is seen (**Figure 4-21**).
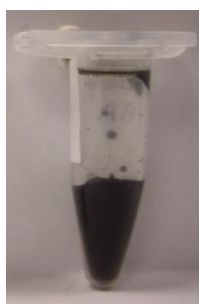
Figure 4-21: Ac nano-1(**4**)/purified SWNTs dispersion after incubation with trypsin/DTT.

Mass spectra of the digested Ac nano-1(**4**)/purified SWNTs show the digested peptide fragments peaks, similar to the control sample. However, its mass spectrum also shows the undigested peptide peak which is highlighted in **Figure 4-22**. It is

Chapter 4

thought that folding of the peptide around nanotube surface protects it from trypsin
degradation. Thus, mass spectra of Ac nano-1(**4**)/purified SWNTs dispersion
incubation with trypsin/DTT shows undigested peptide peaks, which are free in the
solution.
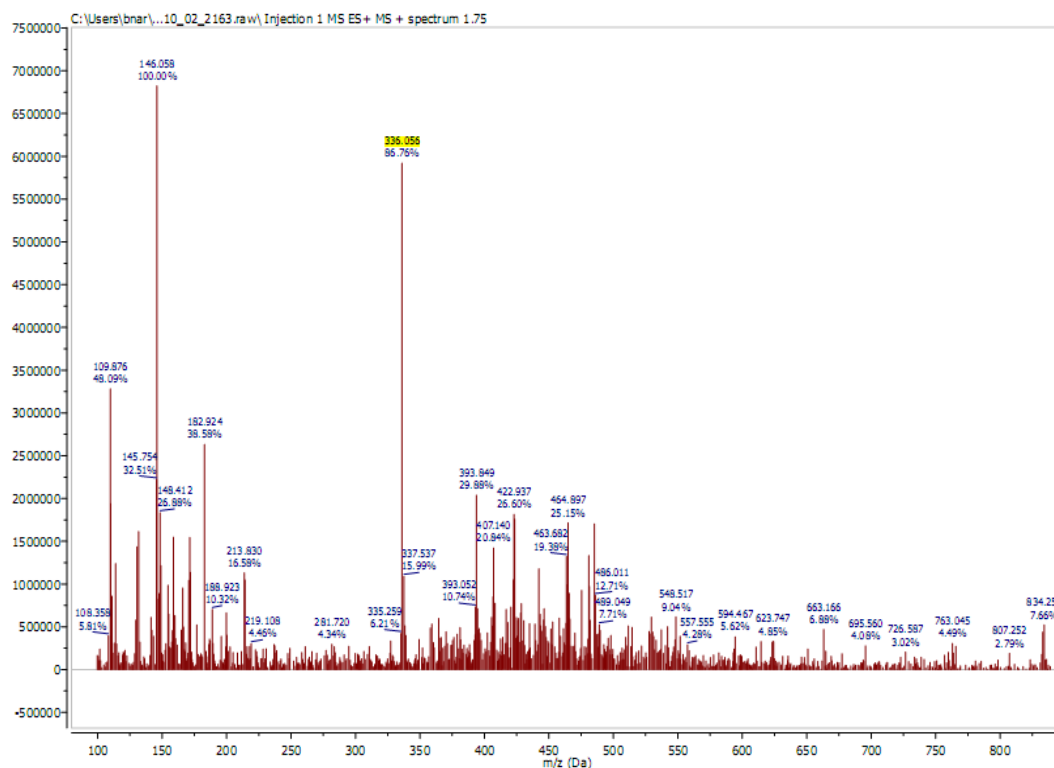
Figure 4-22: Mass spectrum of Ac nano-1(**4**)/purified SWNTs dispersion after incubation
with trypsin/DTT.

Similarly, the trypsin degradation of Ac short nano-1(**6**)/purified SWNTs complex
was investigated. **Table 4-4** summarises the mass of trypsin digested fragments of
Ac short nano-1 (**6**) (control). The calculated fragments were observed in the mass
spectra of digested peptide (control), which indicates a complete degradation of the
peptide. (**Figure 4-23**) highlights the digested Ac short nano-1 (**6**) (control).

Peptide	Calculated Mass (Exact Mass)	Digested Peptide Fragment Sequence	Observed Mass ([M+H]$^+$, *[M+2H]$^{2+}$)
Ac short nano-1 (**6**) Ac-EVEAFEKKY-CONH$_2$	1182.5	Ac-EVEAFEKKY-Amide	*592.6
		Ac-EVEAFEKK	511.5

Table 4-4: LR-MS (ESI-TQD) data for trypsin/DTT digested Ac short nano-1(**6**) (control).
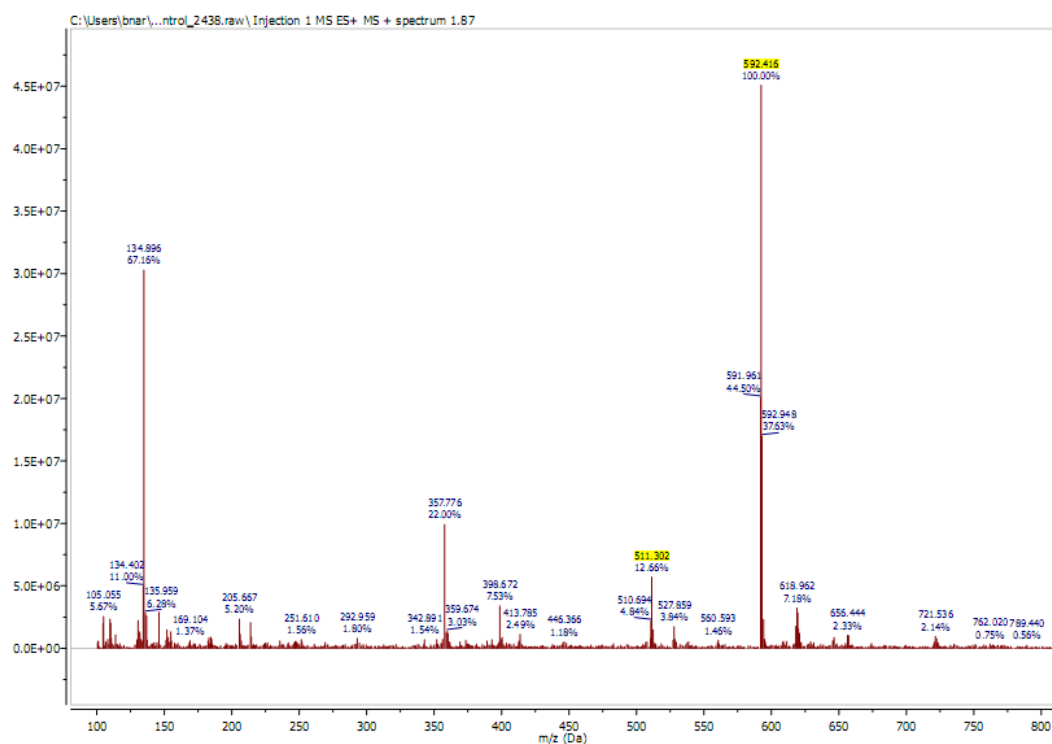
Figure 4-23: Mass spectrum of trypsin/DTT digested Ac short nano-1(**6**) (control).

Figure 4-24 shows that purified SWNTs crashed out from the dispersion after Ac short nano-1(**6**)/purified SWNTs incubation with trypsin/DTT.

Chapter 4

Figure 4-24: Ac nano-1(**4**)/purified SWNTs complex after incubation with trypsin/DTT.

The trypsin digested Ac nano-1(**6**)/purified SWNTs dispersion was analysed by mass spectroscopy, **Figure 4-25**. The mass spectra shows that Ac short nano-1(**6**) wrapped around the nanotube surface were completely digested resulting in a series of fragments similar to control sample. Both the full length and short nano-1 peptides interact with the SWNT in a dynamic manner. Ac short nano-1 (**6**) is likley to undergo a more rapid exhange between bound and unbound states (i.e. it does not bind to the SWNTs as strongly as the full length nano-1 (**4**)) and thus it is to be expceted that peptide **6** should show a great amount of degradation compared to Ac nano-1 peptide (**4**). This is exaclty what the data from the afforementioned degradation studies supports.
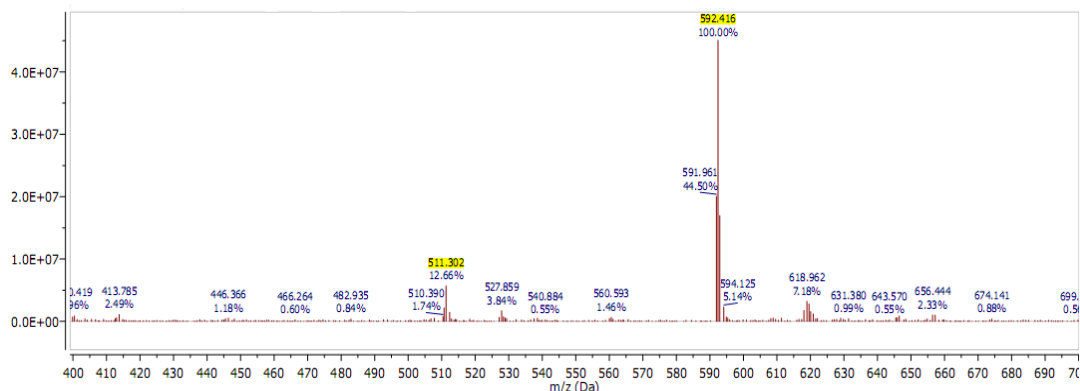
Figure 4-25: Mass spectrum of trypsin/DTT digested Ac short nano-1(**6**)/purified SWNTs.

4.3.   Conclusion

In conclusion, the effect of N-terminus acetylation on a peptides efficiency to disperse SWNTs has been studied. Knowing that peptide's N-terminus acetylation has a greater effect on short peptides helical stability compared to long sequence peptides, thus four modified versions of a previously reported nano-1 was synthesised. The short versions of nano-1 peptide, acetyled and free N-terminus short nano-1, had a lower ability to dispense SWNTs than nano-1 peptides, acetyled and free N-terminus short nano-1. However, it was found that acetyled short nano-1had a better tendency to disperse the nanotubes than its free N-terminus. Whereas, N-terminus of the synthesised nano-1 peptide, acetyled and free N-terminus nano-1, did not significantly affect their ability to disperse SWNTs. Additionally, a fluorinated nano-1 peptide has been synthesised to study the interaction between the peptide with the surface of SWNTs with ^{19}F NMR. The ^{19}F NMR of fluorinated nano-1 peaks has disappeared from the spectra after its interaction with SWNTs. This is thought to be due to peptide's noncovalent bonding to the nanotube's surface, thus broaden its $CF_3\, \delta_F\,^{19}$F NMR peak to the extent that it is unseen in the spectra. Finally, this chapter presents the first investigation of enzymatic degradation of peptide/SWNTs composite. It was found that when Ac nano-1 (**6**) was non-covalently mixed with SWNTs that it was enzymatically digested more slowly than short Ac nano-1 peptide (**4**) by trypsin. This thought to be due to the more rapid exchange that short Ac nano-1 peptide (**6**) will have between its SWNT bound and unbound forms compared to to full length Ac nano-1 (**4**) (*NB- this hypothesis makes the reasonable assumption that a peptide will only be digested when unbound and free in solution*).

5. PEPTOID NONCOVALENT FUNCTIONALISATION OF SINGLE WALLED CARBON NANOTUBES

5.1.   Introduction

Noncovalent functionalisation of SWNTs with surfactants facilitates the modification of their hydrophobic surfaces and imparts dispersibility without changing their electronic properties.[98] The surfactants act to lower the energetic cost of hydrophilic/hydrophobic interfaces, allowing for water-insoluble materials to be dispersed in the aqueous phase.[216] However, the commonly used surfactants for SWNTs dispersion do not facilitate higher order-structures or impart biocompatibility for biomedical applications.[267] Thus, alternative biomolecules, such as α-peptides,[209] proteins,[115,268] amino acids,[269,270] enzymes,[271] and DNA,[272-274] have been explored to import biocompatibility to SWNTs dispersions. All of the aforementioned biomolecules are unique in their ability to fold and self-assemble into specific secondary structures through hydrogen bonds, van der Waals forces, hydrophobic interactions, and electrostatic interactions.[275] Thus, it is widely accepted that various noncovalent intermolecular interactions, such as π–π, CH–π, and van der Waals interactions, play a significant role in promoting the biomolecules wrapping around SWNTs.[276] Consequently, α-peptides can naturally assemble into a wide range of configurations and so they can spontaneously assemble onto nanotubes. It has been shown that by coating SWNTs with amphiphilic helical α-peptides offers a suitable noncovalent approach for debundling SWNTs. Additionally, peptide functionalised SWNTs permits the organisation of individually dispersed nanotubes

into useful assemblies for developing SWNT-based nanomaterials or nanodevices.[209] Therefore, for biomedical applications efforts have been devoted to exploring the potential biological applications of SWNTs/peptide conjugates.[257] However, polypeptides are susceptible to degradation by proteases, have limited thermal stability, and are effected by environmental influences such as pH, solvent polarity, and ionic strength. Additionally, studies suggested that helical wrapping of relatively rigid peptides on the highly curved surface of the SWNTs hinders their ability to interact with the cylindrical SWNT surface.[277] Therefore, there is a need to investigate peptidomimetics which while retaining the required peptide properties to interact with SWNTs have stability towards biodegradability and display backbone rigidity. In recent years, by taking inspiration from peptides, non-natural oligomers that mimic the fundamental molecular features of α-peptides have been synthesised. These include, γ-peptides,[278] β-peptides,[279] and most recently peptoids. Peptoids (oligomers of *N*-substituted glycines) were developed in the late-1980s by Farmer and Ariëen as novel peptidomimetic that would mimic the biological function of bioactive α-peptides.[280]

Peptoids are non-natural oligomers in which the side chain of an α-amino acid is shifted to the backbone amide nitrogen. Consequently, as the backbone nitrogen atom in peptoids carries an alkyl side chain peptoids lack both hydrogen bonding capacity and stereogenicity along the backbone. Thus, they are generally more flexible than peptides, as their tertiary backbone amides can easily adopt both *cis* and *trans* conformations.[281,282]A schematic comparison of peptide and peptoid structure is given in **Figure 5-1**.
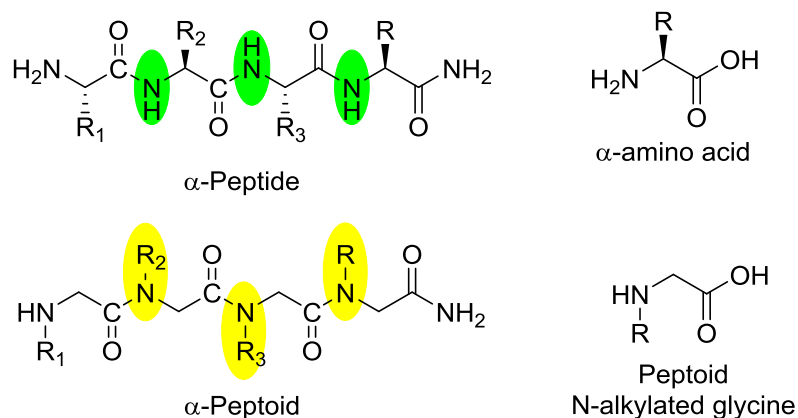
Figure 5-1: A comparison of the structures of generic α-peptoid and peptide oligomers.

A lack of hydrogen bonding ability has several important implications for the secondary structure of peptoids. Peptoids also have enhanced proteolytic stability, bioavailability and cellular uptake relative to α-peptides.[283].

The peptoids are constructed from C- to N-terminus by either the monomer[284] or submonomer[284] methods, which are analogous to standard solid-phase methods for peptide synthesis (**Scheme 5-1**).
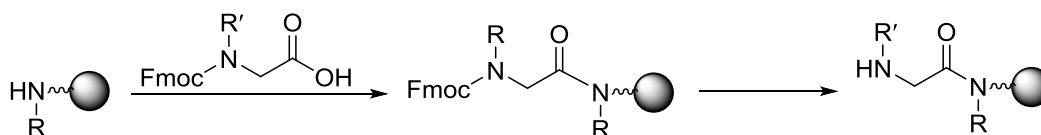
Scheme 5-1: Peptoid synthesis methods (**A**) monomer method (**B**) Submonomer method.

The invention of the submonomer solid-phase synthesis method by Zuckermann was a major breakthrough for peptoid synthesis[284] (**Scheme 5-1**, **B**). This method is based on alternating the acylation reaction with a haloacetic acid of a resin-bound secondary amine, uses a carbodiimide or other suitable carboxylate activation method. Then introduce the side chain by S_N2-nucleophilic displacement of the halogen with an excess of primary amine. This can be accomplished either manually or automatically using a synthesiser.[285,286]

Due to peptoid oligomers' lack of conformational rigidity in comparison to α-peptides, displaying the proper amide side chain functionality is critical for their folding. However, even without the hydrogen bonding capacity and the chiral backbone, researchers have developed methods to stabilise helical, loop and turn motifs in peptoids to fold into well-defined secondary structures depending on electrostatic and steric interactions,[283,287-289] giving rise to random coils or well-defined secondary structures (e.g., helices) in some cases. It has been shown that several types of noncovalent interactions, including, hydrophobic,[290,291] ionic,[292,293] hydrogen bonding,[294] and aromatic interactions,[295,296] can all stabilise peptoid secondary structures. For example, introducing of bulky chiral substituents in peptoid amide side chains engenders a steric repulsion between side chains, and has promising implications for the design of stably folded peptoid.[287] Similarly, negatively charged side chains cause charge-charge repulsion with backbone carbonyls and exhibit polyproline type I helix structure.[297,298] In addition, hydrophobic interactions[299] and n–π* interactions have also been predicted to play a role in peptoid folding.[300]

An extensive body of work, including computational,[297] solution phase 2D-NMR, circular dichroism (CD), electron spin resonance spectroscopy (EPR) and X-ray signal crystal diffraction (SC-XRD) experiments, has demonstrated that the peptoid's helix is induced to bulky aromatic groups adjacent to the nitrogen on the main chain. These significantly reduce the conformational freedom in the chain backbone. Several common monomers used for this purpose are shown in **Figure 5-2**.

(*S*)-*N*-(1-phenylethyl) glycine   (*S*)-*N*-(sec-butyl) glycine   (*S*)-*N*-(1-cyclohexylethyl)glycine

*N*spe   *N*ssb   *N*sch
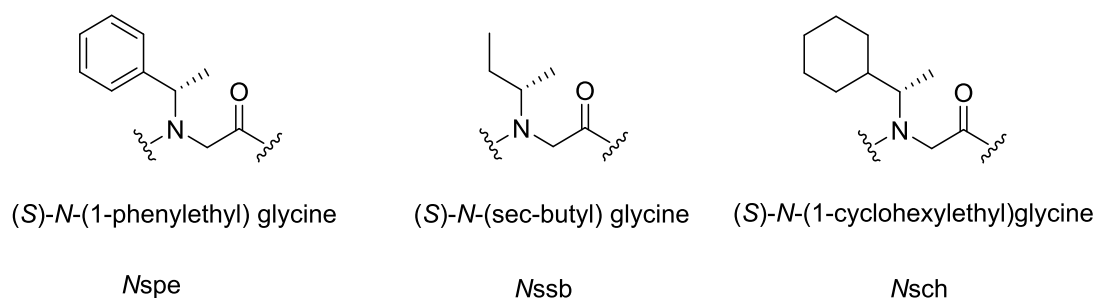
Figure 5-2: Common sub-monomers, used to induce a helical secondary structure in peptoid oligomers.

As a consequence, the backbone freedom is limited to a certain range of angles to prevent electronic repulsions with the aromatic rings of the side chain and neighbouring carbonyl groups of the peptoid backbone. Therefore, the helix formation is largely controlled by the steric and electronic properties of the sub-monomers used.[297,301-306] Therefore, the bulky side chains induce repeated *cis* amide bond conformation and the chirality at the α-position induces handedness of helical structure along the peptoid backbone. The peptoid helix and threaded loop represent the best characterised peptoid secondary structural motifs, which are adopted by peptoids comprised mainly of α-chiral monomers. A peptoid's helix is usually a three-residue-per-turn helix with all-*cis* amide bonds, similar structures to the type-I polyproline peptide α-helices that are commonly seen in proteins **Figure 5-3**.[307,308]
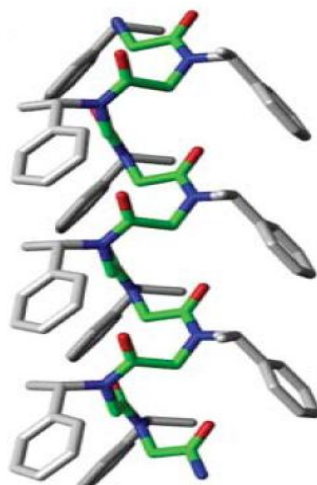
Figure 5-3: A representative model of the peptoid helix (Nspe)$_{10}$. The structure has been generated using molecular mechanics. The backbone is highlighted in green. Reproduced from [307] with permission of The Royal Society of Chemistry.

In the early 2000's, Barron developed a set of predictive rules for helix formation in peptoids best helicity is observed if the bulky side chain contains an aromatic group at the i and $i + 3$ positions.[236] However, in case of hetero oligomeric peptoids can fold into stable helices if at least 50 % of the monomers contain a chiral centre. Furthermore, the helices are stabilised if the C-terminal residue is α-chiral and also as the peptoid chain increases in length, i.e. decamers and longer.[301,302,304,305,307] The helix can be recognised by a CD spectrum with well-defined peaks at 192, 202 and 218 nm, similar to the CD spectra of α-peptide helices, and this pattern serves as a useful diagnostic for helical structure in peptoids.

In the previous study, **Chapter 4**, it was found that the noncovalent interaction between nano-1 peptides and purified SWNTs increases with increasing the number of aromatic amino acid residues in the peptide. However, the absence of backbone

hydrogen bonds and thus flexible conformation in peptoid makes it a strong candidate for the dispersion of carbon nanotubes.

This chapter investigates the synthesis and characterisation of a series of chiral linear peptoids, followed by a discussion of their noncovalent interaction with SWNTs produced by the HiPco method to aid their dispersion in aqueous medium. The functionalised SWNT material was characterised by UV-Vis-NIR, and Raman spectroscopy, and the location and distribution of the functional groups determined using atomic force microscopy (AFM), and transmission electron microscopy (TEM). This is first research in which peptoids have been used for the dispersion of CNTs.

5.2. Results and Discussion

5.2.1. Synthesis of Chiral Peptoid Library (Carried out by Hannah L. Bolt, Cobb group)

Given the helical structural dependence of amphiphilic peptide binding to SWNTs, it is reasonable to expect that the binding interaction should be optimal for a flexibly helical structure. Given peptoids lack of conformational rigidity, they could be considered as good candidates for interacting with the curved side wall of SWNT. Taking the inspiration from the importance of aromaticity content in peptide's amphiphilic helical on SWNTs' dispersion, **Chapter 4**, the first part of this project has focused upon the synthesis of series of α-chiral linear peptoids for interacting with and dispersing SWNTs.

Previous research has revealed that a decrease in the α-helical content of the peptide facilitates their adsorption onto curved walls of CNTs.[309] Varying the percentage of α–chiral aromatic side chains along with the chain length affects the helicity in a peptoid. Thus, in order to evaluate the role of aromatic residues, and degree of helicity of peptoids toward their interaction with SWNTs, a series of peptoids were synthesised of the same sequence, based on the previous work of Barron[310] but varying in the number of residues. As a peptoid helix has 3 residues per turn and is stabilised by the incorporation of one or more aromatic faces running parallel to the helix axis (i.e., aromatic side chains at the i, i + 3 positions). The synthesised peptoid sequences were is chosen to contain a repeating motif of three residues with the repeating subunit structure: (*N*lys*N*spe*N*spe)$_n$, (**Figure 5-4**).

N-(4-aminobutyl) glycine
*N*lys

N-(1-phenylehyl) glycine
*N*spe

(*N*lys*N*spe*N*spe)$_n$
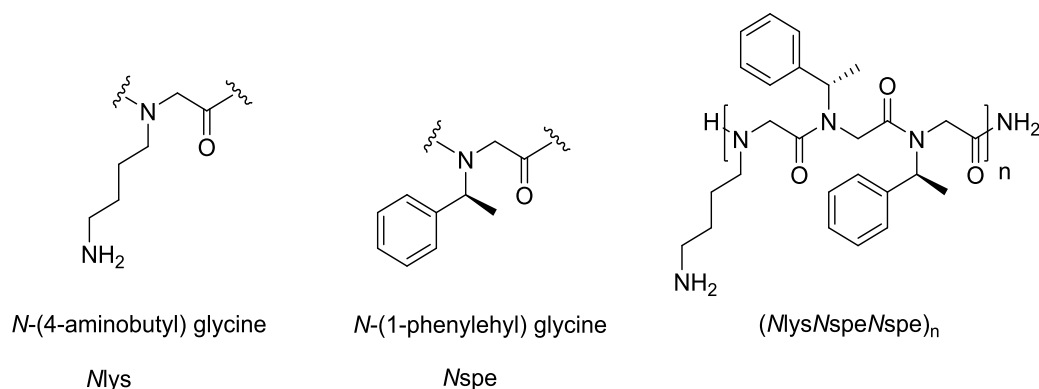
Figure 5-4: Monomers used in peptoid synthesis and peptoid's motif.

The chiral aromatic residue (*N*spe) is used to induce a repeated *cis* amide bond conformation. It is also introduces handedness of helical structure along the peptoid backbone, because it can exhibit not only steric repulsions between bulky side chains, but also electronic repulsions between aromatic π and carbonyl lone-pair electrons.[287] The bulky nature of the aromatic residue leads to a water-insoluble

peptoid, and since water solubility is a critical property of most biologically active molecules and for the CNTs dispersion in aqueous medium, lysine-type side chain (*N*lys) was included in the oligomer. The hydrophilic monomer aids the water solubility of the peptoid and encourages the formation of an amphiphilic helix in solution. The peptoids have two faces, the hydrophobic groups on one face and the hydrophilic groups on the other face. Additionally, because the helical structure is further stabilised at longer peptoid oligomer lengths, a series of varying length peptoids were synthesised as shown in **Table 5-1**.

Peptoid Motif	No. Residues	No. Aromatic Residues (*N*spe)
(*N*lys*N*spe*N*spe)$_2$ (**14**)	6	4
(*N*lys*N*spe*N*spe)$_3$ (**15**)	9	6
(*N*lys*N*spe*N*spe)$_4$ (**16**)	12	8
(*N*lys*N*spe*N*spe)$_6$ (**17**)	18	12

Table 5-1: Summary of the synthesised peptoids structure.

5.2.1.1. Circular Dichroism of Synthesised Peptoids

Peptoids share the same backbone structure as peptides and that backbone amide groups are also the predominant chromophores in peptoids. Since, the amide bond is acutely sensitive chromophore to the structural; solvation, and electronic environment, circular dichroism (CD) spectroscopy can allow rapid assessment and classification of a peptoid's secondary structure. **Figure 5-5** shows the CD spectra observed for all of the synthesised peptoids. All spectra were collected at 50 µM concentration in phosphate buffered saline solution (PBS), to prevent intermolecular interactions which may affect the CD values obtained.
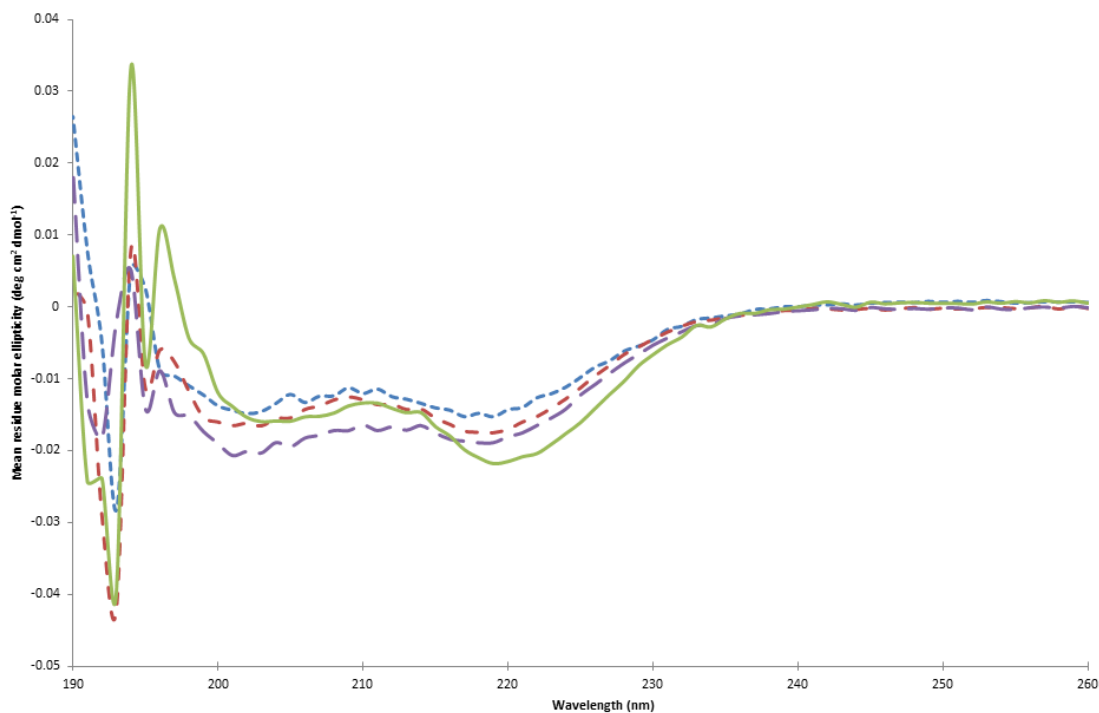
Figure 5-5: CD spectra of synthesised peptoids. (**Green line**) (*N*lys*N*spe*N*spe)$_6$ (**17**), (**Purple line**) (*N*lys*N*spe*N*spe)$_4$ (**16**), (**Red line**) (*N*lys*N*spe*N*spe)$_3$ (**15**), (**Blue line**) (*N*lys*N*spe*N*spe)$_2$ (**14**).

The electronic interactions occur between backbone carbonyls and the π–electron clouds of the aromatic rings in *N*spe lead to the formation of a distinct helical structure that in turn gives rise to an exaction split π–π* transition in the CD spectrum, as observed for peptide-helices.[297] Therefore, the synthesised peptoids gave characteristic CD spectral features at ~ 202 nm and 218 nm, which suggests that these peptoids are forming helices in solution and confirms results from Barron.[310] The peak intensities increased with chain length due to helix stabilisation provided by cooperative interactions that propagate down the ordered chain. Since peptoid helices often have 3 residues per turn, it is unsurprising that a 6 residue peptoid (**14**) shows weaker helicity as it is too short to form a fully a helix. However, a CD spectrum of a 18 residues peptoid (**17**) does not show the characteristic CD spectrum

of helical structure, an alternative explanation would be that exciton and coupled oscillator interactions between aromatic side chains (*N*spe) can make substantial contributions to the CD profile.[297]

5.2.2. Noncovalent Functionalisation of SWNTs with Peptoids

5.2.2.1. Noncovalent Functionalisation of Purified SWNTs with Peptoids

Purified SWNTs (see **Appendix A**) were noncovalently functionalised by dispersion in aqueous solutions of 1.0 mM of a series of synthesised peptoids (**Section 5.2.1**) via probe ultrasonication for 15 min in an ice bath. The sonication was followed by centrifugation to give a homogeneous, black dispersion. Visual inspection of SWNT dispersion can provide an initial qualitative evaluation of the effectiveness of a peptoid in dispersing the SWNTs. **Figure 5-6**. The dispersions were characterised using UV-Vis-NIR spectroscopy to determine the relative amount of individual SWNTs versus ropes or bundles in the suspensions and also the net concentration of the dispersed nanotubes.
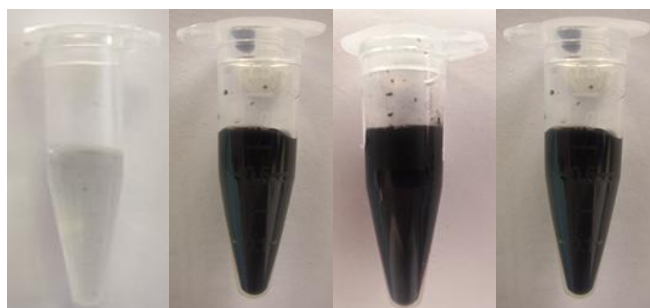
Figure 5-6: Peptoid/purified SWNTs composite aqueous dispersion after sonication and centrifugation. Dispersion from left to right: (*N*lys*N*spe*N*spe)$_2$ (**14**)/purified SWNTs, (*N*lys*N*spe*N*spe)$_3$ (**15**)/purified SWNTs, (*N*lys*N*spe*N*spe)$_4$ (**16**)/purified SWNTs, (*N*lys*N*spe*N*spe)$_6$ (**17**)/purified.
SWNTs

The SWNTs concentration in each dispersion after sonication, centrifugation, and separating the supernatant was determined from optical absorption spectroscopy using the Beer-Lambert law and purified SWNTs extinction coefficient of 37.3 mL mg^{-1} cm^{-1} and absorption values at λ = 700 nm (see **Appendix B**). The noncovalent interaction of peptoids with the side walls of SWNTs is thought to be accomplished in a similar way to the amphiphilic nano-1 peptides previously discussed in **Chapter 4**. Therefore, the efficiency was compared for each system using the UV-Vis-NIR absorption behaviour of the SWNT solutions, **Table 5–2** compares between the dispersion of purified with peptoids and nano-1 peptides.

Dispersant	Total No. Residues	Ratio Hydrophilic/ Hydrophobic	Total No. Hydrophobic Residues	Conc. Dispersed Purified SWNTs µg mL^{-1}
SDS (control)	/	/	/	196.4
(Nlys$N$spe$N$spe)$_2$ (**14**)	6	1:2	4	5.7
(Nlys$N$spe$N$spe)$_3$ (**15**)	9	1:2	6	218.8
(Nlys$N$spe$N$spe)$_4$ (**16**)	12	1:2	8	701.5
(Nlys$N$spe$N$spe)$_6$ (**17**)	18	1:2	12	672.0
Ac(V$_a$F$_d$)$_{4/4}$ (**4**)	29	1:0.16	8	586.9
(V$_a$F$_d$)$_{4/4}$ (**3**)	29	1:0.16	8	434.7
Ac(V$_a$F$_d$)$_{1/4}$ (**6**)	9	1:0.3	2	167.9
(V$_a$F$_d$)$_{1/4}$ (**5**)	9	1:0.3	2	47.4

Table 5-2: Concentration of dispersed purified SWNTs by peptides and peptoids determined for their UV-Vis-NIR absorption after sonication and centrifugation.

Results in **Table (5-2)** show that increasing the number of hydrophobic residues by increasing the peptoid chain length while retaining the same hydrophilic/hydrophobic ratio results in an increase in dispersed nanotube concentration. This is similar to what was found for nano-1 peptides in **Chapter 4**. It was found that the longer nano-

1 peptides (**3** and **4**) dispersed more purified SWNTs than short nano-1 peptides (**5** and **6**). This indicates that number of hydrophobic residues play a key role in nanotubes noncovalent dispersion, thus, it is thought that the synthesised peptoids noncovalently disperse SWNTs through π–π stacking interactions between the peptoid's hydrophobic residues and SWNT surface in similar way to nano-1 peptides. It is worth mentioning that the saturation concentration of the synthesised peptoids was not determined due their limited available amounts, thus increasing the concentration of the peptoid might have resulted in an increase in the concentration of the dispersed SWNTs.

It was found that the concentration of dispersed SWNT by short nano-1 peptides (**3** and **4**) is less than (*N*lys*N*spe*N*spe)$_4$ (**16**) despite the fact that both have the same number of hydrophobic residues (8 hydrophobic residues). Peptide **3** dispersed 434.7 μg mL^{-1} and peptide **4** dispersed 586.9 μg mL^{-1} while peptoid **16** dispersed 701.5 μg mL^{-1} of purified carbon nanotubes. The rationale for the differences in dispersed SWNTs is thought to be due to the decrease in the hydrophilic/hydrophobic ratio between nano-1 peptides (**3** and **4**) and peptoid (**16**) (i.e. **3** and **4** have a 1:0.16 ratio while **16** has a 1:2 ratio). This suggests that although aromatic residues in both the peptide and peptoid sequences play a vital role in their ability to disperse CNTs, the ratio of hydrophilic and hydrophobic residues is very important for the successful dispersion of SWNTs.

The π–π stacking interaction between the hydrophobic residues of the peptoids studied and the extended π–electron system of CNTs is considered to be the main driving force for peptoid adsorption onto SWNTs. It is thought that the flexible peptoids spontaneously fold into spring-like conformations that match the geometry

of carbon nanotube to minimise the interfacial energy of nanotube/water interface. Thus, peptoid hydrophilic residues, *N*lys, occupy one face of peptoid's helix and interact via hydrogen bonding with water to stabilise the peptoid/SWNTs complex, while π–bonds in hydrophobic residues, *N*spe, located on the other face of the helix interact with the delocalised π–bonds in the side wall of SWNT in a similar way to that previously discussed by Dieckmann.[124] **Scheme 5-2** illustrates the proposed noncovalent interaction between peptoid's helix and purified SWNTs.
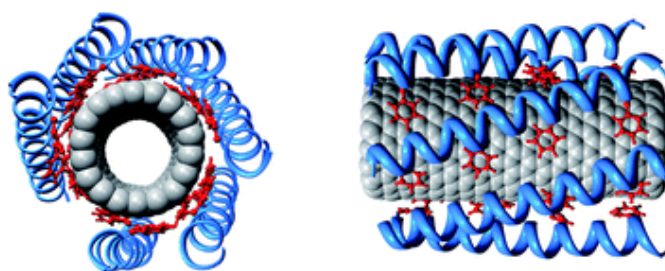
Scheme 5-2: Proposed interaction between purified SWNTs and peptoid **14**. The helical backbone is shown in blue, and the hydrophobic residue (*N*spe) are shown in red.

The well-resolved features in the absorption spectra of the peptoid/SWNT dispersion shown in **Figure 5-7** further demonstrate the debundling of SWNTs in aqueous solution by peptoids. The discrete peaks that extend throughout the metallic (440 – 645 nm) and semiconducting (830 – 1600 nm and 600 – 800 nm) regions due to interband transitions between van Hove singularities in the density of states (DOS) of individual SWNTs, indicating the presence of SWNTs as individuals and/or as very small bundles with these dispersants. Furthermore, they indicate that under applied dispersion conditions a peptoid performs well as a general dispersal agent and does not select for tubes of specific type (metallic or semiconducting).
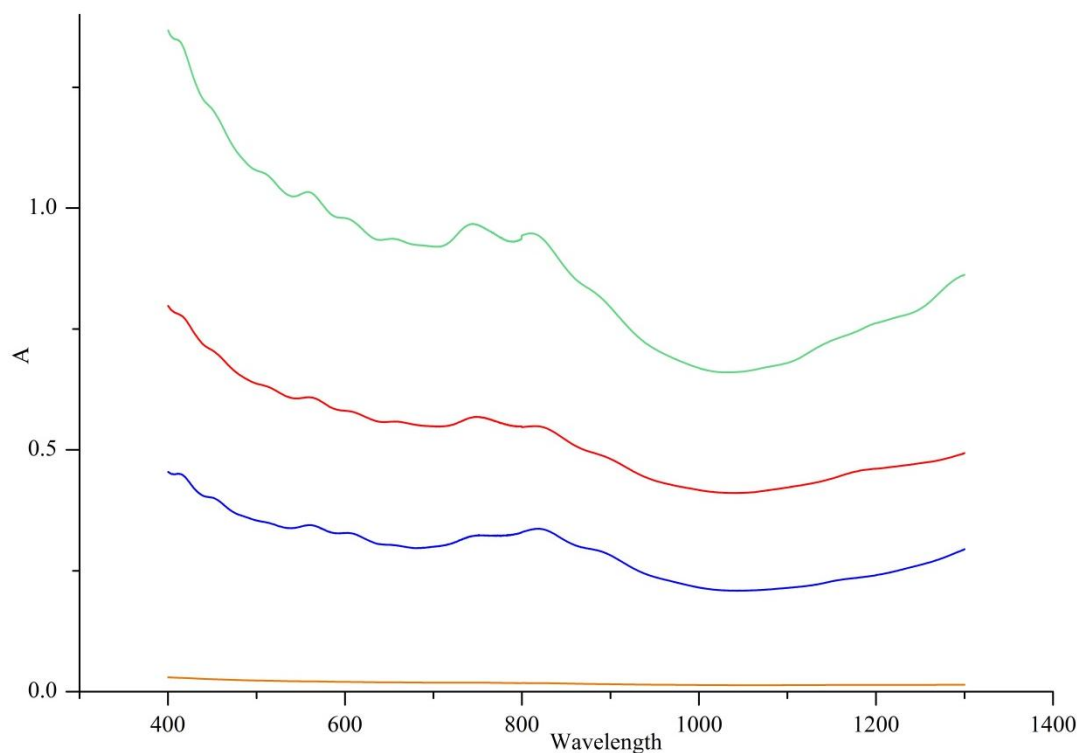
Figure 5-7: UV-Vis-NIR spectra of the dispersed purified SWNTs with peptoids. (**Green line**) (*N*lys*N*spe*N*spe)$_6$ (**17**)**/**purified SWNTs, (**Red line**) (*N*lys*N*spe*N*spe)$_4$ (**16**)**/**purified SWNTs, (**Blue line**) (*N*lys*N*spe*N*spe)$_3$ (**15**)**/**purified SWNTs, (**Orange line**) (*N*lys*N*spe*N*spe)$_2$ (**14**)**/**purified SWNTs

In order to study the stability of peptoid/purified SWNTs aqueous dispersion with respect to time, the concentration of dispersed SWNTs was measured 4 weeks after the initial preparation of peptoid/purified SWNTs dispersion as shown in (**Table 5-3**).

Dispersant	Conc. Dispersed Purified SWNTs µg mL^{-1}	Conc. Dispersed Purified SWNTs After 4 weeks µg mL^{-1}
(*N*lys*N*spe*N*spe)$_2$ (**14**)	5.7	0
(*N*lys*N*spe*N*spe)$_3$ (**15**)	218.8	80.8
(*N*lys*N*spe*N*spe)$_4$ (**16**)	701.5	658.5
(*N*lys*N*spe*N*spe)$_6$ (**17**)	672.0	513.0

Table 5-3: Comparison between the concentration of peptoid/purified SWNTs after 4 weeks.

The above results showed that concentration of dispersed purified SWNTs in all peptoid/purified SWNTs complexes have decreased after 4 weeks comparing to their concentration measured upon the immediate preparation of the complexes. However, (*N*lys*N*spe*N*spe)$_6$ **(17)/**purified SWNTs and (*N*lys*N*spe*N*spe)$_4$ **(16)/**purified SWNTs showed higher dispersion stability comparing to (*N*lys*N*spe*N*spe)$_2$ **(14)/**purified SWNTs and (*N*lys*N*spe*N*spe)$_3$ **(15)/**purified SWNTs. Since all peptoids used in these dispersions have the same hydrophilic/hydrophobic ratio, thus the difference in dispersion stability is thought to be due to difference between peptoids in number of hydrophobic residues. Increasing the peptoid's chain length and thus the total number of hydrophobic *N*spe residues appears to generate more stable SWNT dispersions. This result supports the proposed hypothesis that the key interaction driving the SWNT dispersion is between the peptoid's hydrophobic aromatic residues, (i.e. *N*spe) and CNTs hydrophobic sidewall.

5.2.2.2.   Noncovalent Functionalisation of Oxidised SWNTs with Peptoids

Oxidised SWNTs were noncovalently functionalised with 18 and 6 residue peptoids, **17** and **14** respectively. The peptoid/oxidised SWNTs aqueous dispersions were prepared following the same method for the dispersion of purified with peptoids (**Section 5.2.2.1**). **Figure 5-8** shows the oxidised SWNT aqueous dispersions after sonication with peptoids **17** and **14**.
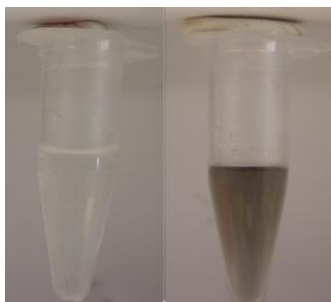
Figure 5-8: Peptoid/oxidised SWNTs composite aqueous dispersion after sonication and centrifugation. Dispersion from left to right: (NlysNspeNspe)$_2$ (**14**)/oxidised SWNTs, (NlysNspeNspe)$_6$ (**17**)/oxidised SWNTs.

The peptoid (**17**)/oxidised SWNTs supernatant colour was darker compared to peptoid (**14**)/oxidised SWNTs. This indicates that the 18 residue peptoid (**17**) has a minimum number of aromatic residues necessary to disperse the oxidised nanotubes; 6 residue peptoid (**14**) does not disperse the oxidised SWNTs. The dispersions were further characterised with the UV-Vis-NIR spectroscopy to determine net concentration of the dispersed nanotubes in each sample. The dispersed nanotube concentration in each supernatant was determined from optical absorption spectroscopy using the Beer-Lambert law and the calculated extinction coefficient of 14.44 mL mg^{-1} cm^{-1} and absorption values at $\lambda = 700$ nm (see **Appendix B**). **Table 5-3** shows the concentration of oxidised SWNTs in each supernatant.

Peptoid	No. Residues	Conc. of Dispersed Purified SWNTs μg mL^{-1}
(NlysNspeNspe)$_2$ (**14**)	6	0.3
(NlysNspeNspe)$_6$ (**17**)	18	44.1

Table 5-4: Concentration of dispersion oxidised SWNTs with peptoids determined for UV-Vis-NIR absorption after sonication and centrifugation.

The absorption spectra of the peptoid dispersed oxidised SWNT is shown in **Figure 5-9**. The 18 residue peptoid (**17**) showed a higher absorption intensity compared to the 6 residue peptoid (**14**). This indicates that the number of aromatic residues present in the peptoid play an important role in dispersing the nanotubes.
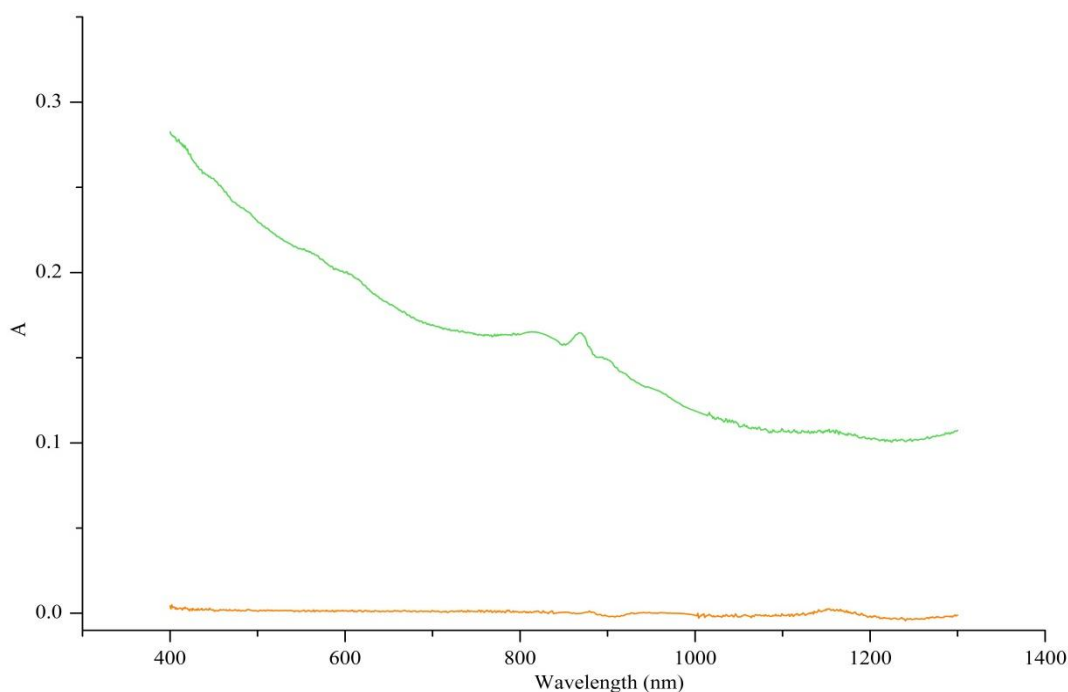
Figure 5-9: UV-Vis-NIR spectra of oxidised SWNTs dispersed by peptoids. (**Green line**) (*N*lys*N*spe*N*spe)$_6$ (**17**)/oxidised SWNTs, (**Orange line**) (*N*lys*N*spe*N*spe)$_2$ (**14**)/oxidised SWNTs.

Compared to purified SWNT dispersions, the same peptoids (**17** and **14**) had a limited adsorption affinity towards oxidised SWNTs. The low adsorption affinity of the peptoids towards oxidised SWNTs is thought to be due to oxygen-containing functional groups attached to the surface of the nanotubes sidewall. These functional groups disrupt the π–π stacking interaction between the peptoid's aromatic residues and the graphitic surface of nanotube, which played an important role in peptoid dispersion of purified SWNTs. This suggests that the observed interaction between

peptoids and purified SWNTs is a result of π–π interactions. Thus, the degree of interaction increases linearly with number of aromatic residues in the peptoid, due to increasing the stacking effect and therefore increases the effectiveness of debundling of the SWNTs nanotubes.

5.2.2.3. Characterisation of Noncovalent Functionalisation of Purified SWNTs with Peptoids

Raman spectroscopy is the most important and versatile technique for the characterisation of covalently functionalised SWNTs.[311] However, it is of less significance for the investigation of noncovalently functionalised SWNTs, due to its non-destructive nature to the sp^2 bonding of the nanotube graphitic honeycomb lattice.[127,312-315] Thus the I_D/I_G ratio cannot indicate the degree functionalisation in noncovalent modification. One of prominent feature in the Raman spectrum of CNTs is their G-band mode. This mode is directly related to the G band in graphite and is due to the in-plane tangential stretching vibration between two carbon atoms in the unit cell. The G band has two components a G^+ mode and a less intense G^- mode. Previous research has confirmed that interaction of electron withdrawing molecules stiffens the Raman of SWNTs G^+ band while donating molecules soften the G^+ band.[316-318] It has been suggested that electron donor molecules interact selectively with semiconducting SWNTs whereas electron acceptors molecules interact with metallic SWNTs giving rise to possible metal↔semiconductor transitions.[319] As previously discussed in **Section 5.2.2.1**, the proposed interaction between the synthesised peptoids and purified SWNTs is through π–π stacking between peptoid's

benzene ring with the graphitic surface of the nanotube. Therefore, to determine if the peptoids coat and debundled the nanotubes, Raman spectra of purified SWNTs (control sample) and peptoid/SWNTs composite dispersion have been measured and the shifts in the G band recorded. The Raman analyses of peptoid/SWNTs composite were measured by drop casting each sample on a silicon substrate and left to dry in air. The Raman analyses were repeated ten times at different areas of the sample to determine that the observed shifts, while small, are real. **Figure 5-10** shows representative Raman spectra of purified SWNTs (control sample) and peptoid/SWNTs composite dispersion, all spectra normalised to the G band.
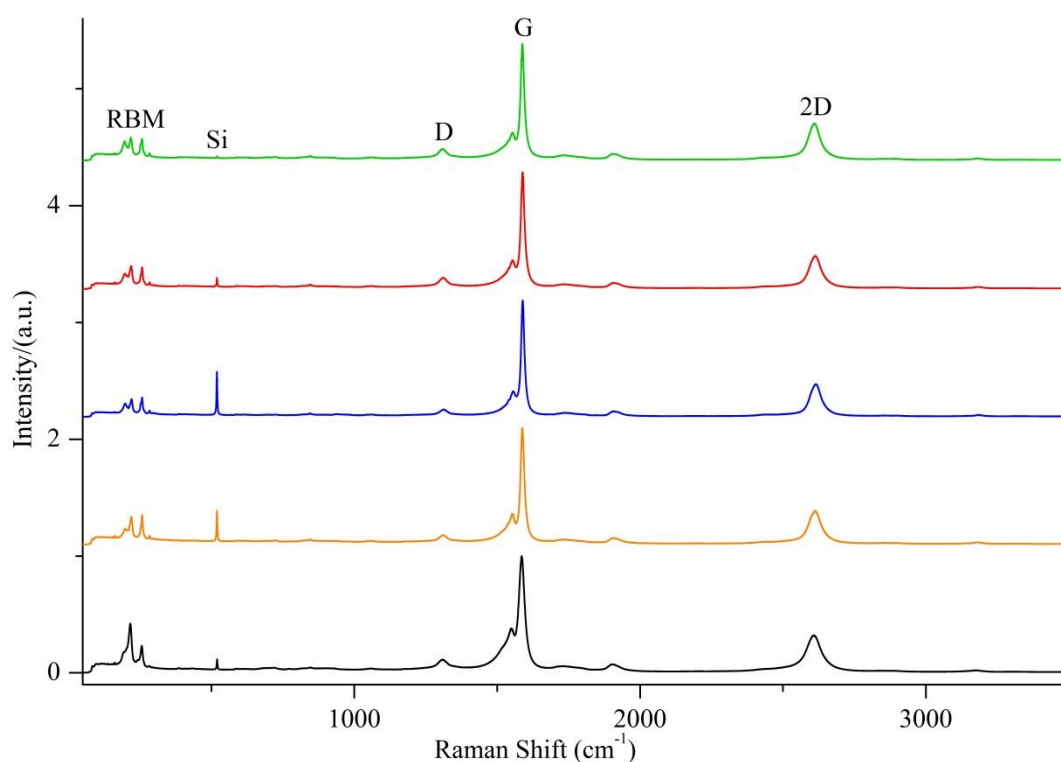
Figure 5-10: A representative Raman spectra (633 nm) of peptoid/purified SWNT composite: (**Green line**) (Nlys$N$spe$N$spe)$_6$ (**17**)/purified SWNTs, (**Red line**) (Nlys$N$spe$N$spe)$_4$ (**16**)/purified SWNTs, (**Blue line**) (Nlys$N$spe$N$spe)$_3$ (**15**)/purified SWNTs, (**Orange line**) (Nlys$N$spe$N$spe)$_2$ (**14**)/purified SWNTs, (**Black line**) purified SWNT (control).

The spectrum shows a number of well-characterised nanotube resonances; in particular, the radial breathing modes (RBMs) in the $100 - 300$ cm^{-1} region, the D-band at ~ 1306 cm^{-1}, the G-band in the $1550 - 1605$ cm^{-1} region, and the 2D-band at ~ 2602 cm^{-1}. The proposed interaction of peptoids with purified nanotubes depends on π-π interaction between peptoid's aromatic residues with the surface nanotube. Therefore, it is not surprising that the noncovalent interaction between purified SWNTs and peptoid results in a G band upshift compared to purified nanotubes (control) (**Figure 5-11**).
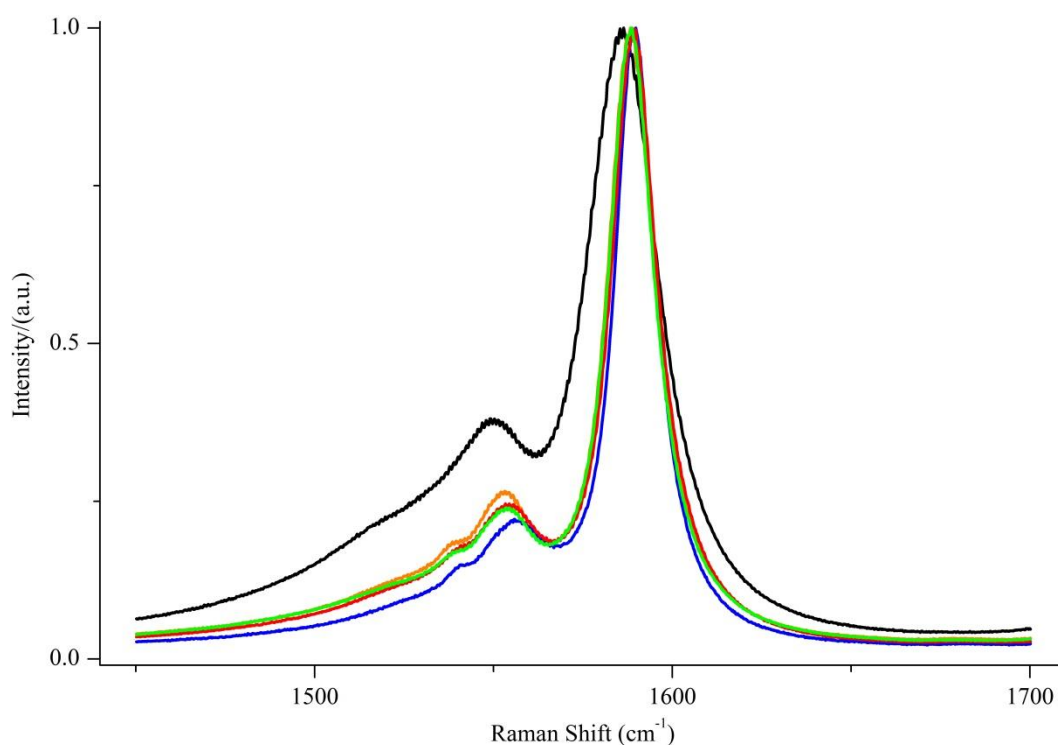
Figure 5-11: A representative Raman G band spectra of peptoid/purified SWNT composites. (**Green line**) (*N*lys*N*spe*N*spe)$_6$ (**17**)/purified SWNTs, (**Red line**) (*N*lys*N*spe*N*spe)$_4$ (**16**)/purified SWNTs, (**Blue line**) (*N*lys*N*spe*N*spe)$_3$ (**15**)/purified SWNTs, (**Orange line**) (*N*lys*N*spe*N*spe)$_2$ (**14**)/purified SWNTs, (**Black line**) purified SWNT (control).

This shift provides further support of peptoids debundling ability as well as for charge transfer between the peptoid and SWNT. **Table 5-4** summaries the measured G band of purified SWNTs (control sample) and peptoids/purified SWNTs.

Dispersion	G band (cm^{-1})	G band upshift (cm^{-1})
Purified SWNTs	1584.7 ± 0.8	-
(Nlys$N$spe$N$spe)$_2$ (**14**)/purified SWNTs	1588.7 ± 0.2	4 ± 0.8
(Nlys$N$spe$N$spe)$_3$ (**15**)/purified SWNTs	1589.1 ± 0.2	4.4 ± 0.8
(Nlys$N$spe$N$spe)$_4$ (**16**)/purified SWNTs	1589.3 ± 0.1	4.6 ± 0.8
(Nlys$N$spe$N$spe)$_6$ (**17**)/purified SWNTs	1588.2 ± 0.4	3.5 ± 0.9

Table 5-5: A summary of G band of purified SWNTs (control) and peptoid dispersed purified SWNTs.

AFM experiments were used to identify individual or bundled SWNTs in the dispersions. The aqueous dispersion of purified SWNTs (control) and peptoid/purified SWNTs composites were diluted by factor 10 and drop cast on a freshly cleaved mica surface. AFM height measurements were performed on sample areas that were free from excess adsorbed peptide and contained SWNTs that appeared not to be coated with peptoid. However, since the AFM measurements were made on dried samples, these values do not represent the true arrangement of the peptoid molecules on the SWNTs in solution. Also, the dilution of the neat dispersions may have resulted in the removal of some of the peptoid molecules adsorbed on the SWNT surface. AFM height analysis of (Nlys$N$spe$N$spe)$_6$ (**17**)/purified SWNTs composite dispersion ranged from 0.7 to 7.4 nm. Since the height of individual SWNTs are known to range from $\sim 0.8 - 1.2$ nm. The AFM results of (Nlys$N$spe$N$spe)$_6$ (**17**)/purified SWNTs composite suggest that most of the

purified present in the composite are individually dispersed. **Figure 5-12** shows a representative AFM image of (Nlys$N$spe$N$spe)$_6$ (**17**)/purified SWNTs dispersion.
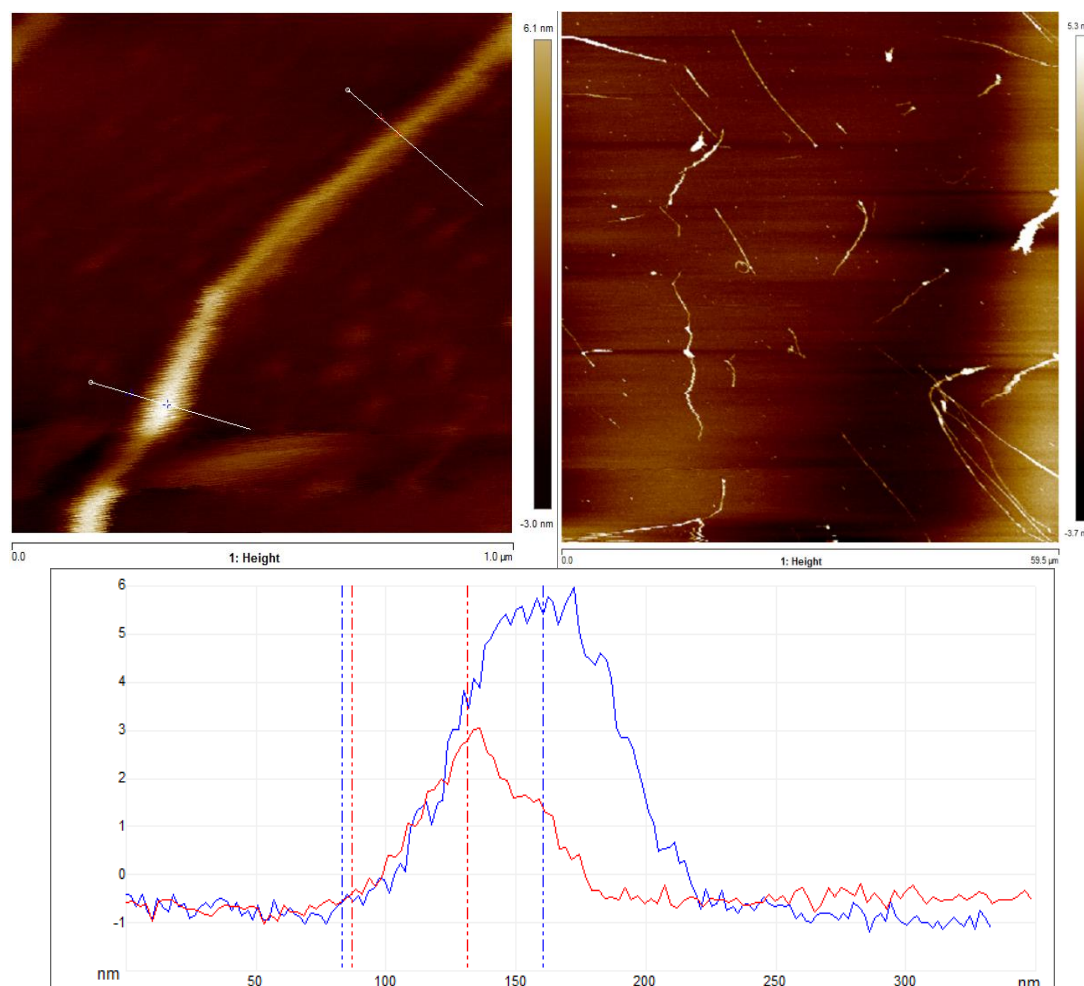
Figure 5-12: AFM images of (Nlys$N$spe$N$spe)$_6$ (**17**)/purified SWNTs dispersion (**top row**) and height analysis (**bottom row**).

Electron microscopy has been used to characterise the (Nlys$N$spe$N$spe)$_6$ (**17**)/purified SWNTs composite. Low-resolution transmission electron microscopy (LRTEM) of the dispersion dried on a TEM grid revealed an extensive network of fibre like materils coated with a web-like film. High-resolution transmission electron microscopy (HRTEM) was used to study the nanoscopic interaction between individual nanotubes and the folded peptoid. **Figure 5-13** shows a representative

high resolution HRTEM and LRTEM image of an individual SWNT efficiently coated by an amphiphilic peptoid.
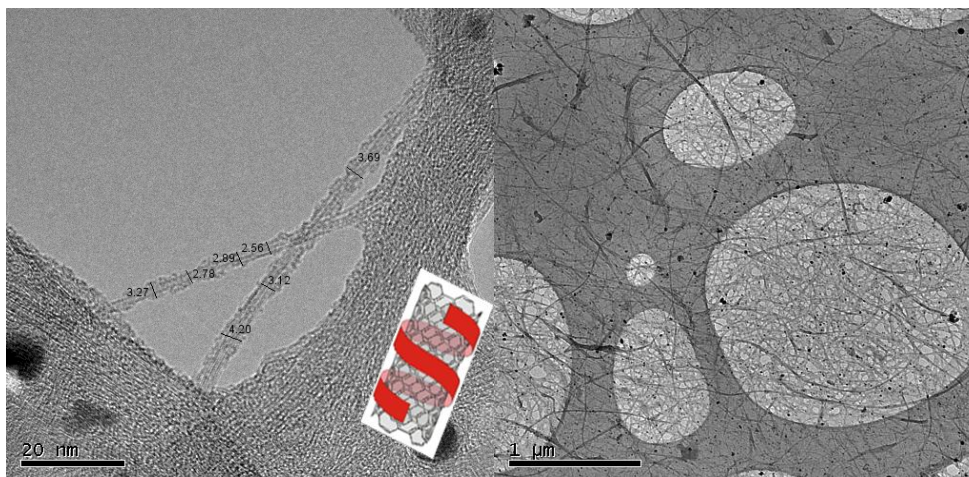
Figure 5-13: TEM images of (*N*lys*N*spe*N*spe)$_6$ (**17**)/purified SWNTs composite: (**Left**) HRTEM of (*N*lys*N*spe*N*spe)$_6$ (**17**)/purified SWNTs composite, (**Right**) LRTEM of (*N*lys*N*spe*N*spe)$_6$ (**17**)/purified SWNTs composite.

The measured average diameter of the (*N*lys*N*spe*N*spe)$_6$ (**17**)/purified SWNTs composite is 3.1 nm, whereas individual SWNT has been previously reported to have an approximate diameter of ~ 2 nm. This indicates that the amphiphilic peptoid disperses purified SWNT into individual tubes or small bundles. These results also closely match those from the interaction amphiphilic peptides with SWNTs.[124,320] As can be seen in the **Figure 5-13** inset, the features of the dispersed SWNTs match the dimensions expected for a flexible chain peptoid associated with the SWNTs surface.

5.3.   Conclusion and Future Work

In summary, a series of chiral amphiphilic peptoids were synthesised based on the work by Barron.[245,321] in which several helical, cationic, facially amphiphilic peptoid with antibacterial activity have been designed. The synthesised peptoids vary in the number of aromatic residues on the hydrophobic surface of the helix yet have the same hydrophilic/hydrophobic ratio. The CD spectra suggested that the peptoids were forming a helical conformation in the solution. UV-Vis-NIR absorption spectra revealed that the peptoids ability to disperse individual SWNTs increases with increasing the number of aromatic residues in the peptoid. Also the stability of these dispersions with respect to time has been studied; (Nlys$N$spe$N$spe)$_6$ (**17**)/purified SWNTs and (Nlys$N$spe$N$spe)$_4$ (**16**)/purified SWNTs showed higher dispersion stability comparing to (Nlys$N$spe$N$spe)$_2$ (**14**)/purified SWNTs and (Nlys$N$spe$N$spe)$_3$ (**15**)/purified SWNTs. Raman spectroscopy was used to probe the peptoid's impact on the electronic structure of the SWNTs. The shift of the Raman G band peak to higher frequencies for the peptoid/purified SWNTs composites are suggestive of a weak charge-transfer interaction in which the peptoid acts as an electron acceptor and the SWNT acts as an electron donor. Altogether, these results suggest that the noncovalent peptoid/SWNT interaction does not perturb the electronic structure of SWNTs. In this context, designed peptoid may provide an accessible means to incorporate the desired electrical properties of SWNTs into biocompatible nanoscale electronic devices. TEM and AFM measurements reveal that the chosen peptoids are capable of fully coating the SWNT surface and dispersing individual SWNTs and will facilitate many applications of SWNTs to medical problems; such as artificial muscles or biomedical sensors that can be placed inside the human body.

Chapter 5

Hybrids of biomolecules and nanomaterials are promising candidates in the development of novel therapeutics and electronic devices. Since peptoids are known for their potential application as a drug due to their resistance to proteases and long life in the human body. The next step for this work would be to study the toxicity, cell penetration, and cellar uptake of the biological active peptoid/SWNT composite. These biological tests will test the possibility of improving the biological activity of peptoids upon their interaction with CNTs. This will open the possibility of using peptoid/CNTs composites in biological and medical applications

6. NONCOVALENT FUNCTIONALISATION OF SWNTs WITH RIBONUCLEOSIDES

6.1. Introduction

The study of the interaction of biomolecules, such as, peptides,[124,127,210] proteins,[107,114,115,268] and DNA[89] with SWNTs has emerged as a separate field in nanotechnology. In particular, the adsorption of DNA on SWNTs surfaces has attracted considerable attention.[322,323] DNA/SWNTs complexes have potential biomedical applications, such as transport of biomolecular agents into cells, optical sensing for biological systems,[324] rapid DNA sequencing,[325] and diagnosis and therapeutic treatment of diseases. This motivated many computational and experimental studies to investigate the interaction of DNA, nucleosides,[325,326] nucleobases,[327-330] and nucleotides[331,332] with SWNTs.

The solubilisation of SWNTs associated both covalently[274,333] and noncovalently with DNA has been intensively investigated to obtain both theoretical and experimental understanding of the DNA/SWNTs interaction.[334-338] The noncovalent interaction of SWNTs with DNA helps the dispersion and separation of SWNTs in aqueous and non-aqueous solution, while leaving their unique physical and electronic properties unchanged. One of the most effective dispersants is single-stranded DNA (ssDNA), which was discovered by Zheng[339] to disperse bundled SWNTs (**Figure 6-1**). The accepted interaction mechanism is helical wrapping, whereby the hydrophobic DNA bases preferentially π–π stacking (noncovalent bonding) on the

nanotube surface, leaving the hydrophilic sugar-phosphate backbone free to interact with the water to promote solubility.[340] Ikeda *et al.*[341] showed that aqueous solubility of SWNTs significantly depends on the number of phosphate groups and the type of base in the oligonucleotides.
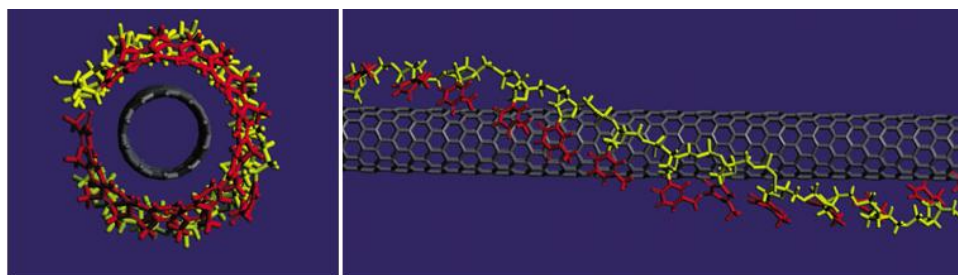
Figure 6-1: The DNA wraps around the hydrophobic surface of SWNTs. Reprinted by permission from Macmillan Publishers Ltd: [Nature Materials] [339], copyright (2003).

Several experimental and theoretical studies found that the dispersity is dependent on the oligonucleotides sequence, thus certain sequences of ssDNA were more effective at dispersing nanotubes than others. In particular, it has been found that pyrimidine based oligonucleotides are superior dispersants to purine based oligonucleotides, due to stronger self-stacking of the pyrimidine based oligonucleotides in aqueous solution.[52] More recently, it has been shown that the interaction of ssDNA wrapping around SWNTs is diameter- and sequence-dependent, making it possible to disperse the naturally hydrophobic SWNTs in water and to sort them by their chirality.[53] These recognition sequence hybrids, which show high selectivity toward their respective chirality SWNTs, suggest a highly ordered ssDNA secondary structure proposed to be stabilised by base-SWNTs adsorption as well as by interbase hydrogen bonding.[338,342,343]

The nucleobase/SWNT composites are interesting in view of the remarkable properties of SWNTs and the recognition properties of nucleobases. The strength of nucleobase stacking on the stability of DNA/SWNT complexes has motivated several computational studies on the nature of such interactions. For example, Johnson *et al.*[344] calculated the nucleobase/SWNTs binding free energy differences for the four bases and found that they follow the trend guanine < adenine < thymine < cytosine in aqueous environment. **Figure 6-2** shows the $\pi-\pi$ stacking between adenine with SWNTs surface. The adenine also has a hydrogen bonding (yellow colour) with water molecules.
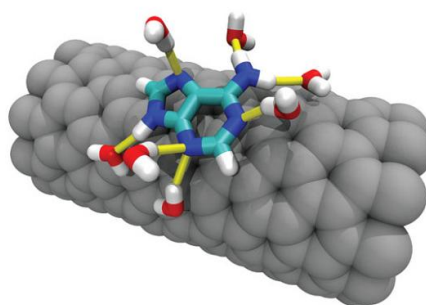
Figure 6-2: Noncovalent interaction between adenine with the hydrophobic surface of SWNTs. Reproduced from [344] with permission of John Wiley and Sons.

Although covalent functionalisation of nanotubes destroys their sp^2 structure, it has been used to attach biomolecules to a nanotube surface. Chris *et al.*[345] used covalent chemistry to functionalise nanotubes with DNA, which provided stability, accessibility, and selectivity during competitive hybridisation when compared to the noncovalent approach. **Figure 6-3** shows the synthesis of a DNA/SWNT complex where the oxidised nanotube is attached to free amino group in the DNA via carbodiimide cross-linker (EDC) coupling chemistry.
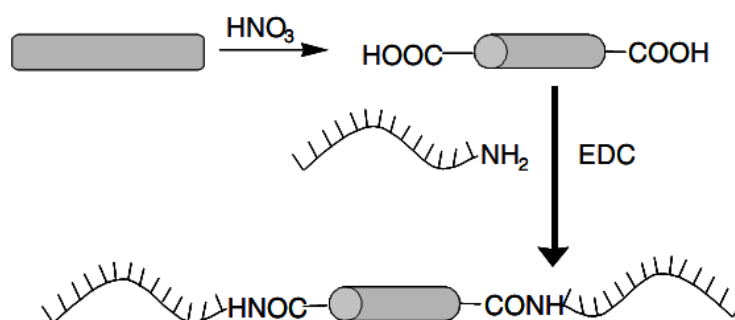
Figure 6-3: Covalent functionalisation of SWNTs with DNA. Capped SWNTs are oxidatively opened and then reacted with amine-terminated single-stranded DNA. Reprinted from [345].

Nucleobases and ribonucleosides were covalently attached to a nanotubes surface by Micoli *et al.*[346,347] The presence of ribonucleosides and nucleobase on the nanotube surface improves the dispersibility of the nanohybrid in polar solvents. It also directs recognition, through hydrogen bonding, of complementary base pairs in nonpolar aprotic solvents (**Figure 6-4**).
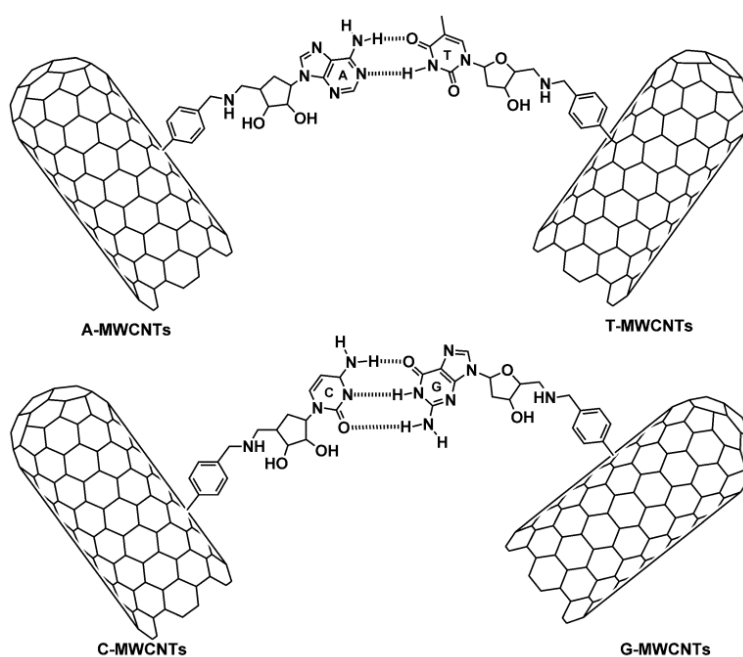
Figure 6-4: Hydrogen bonding between ribonucleoside/SWNTs complexes. Reproduced from [347] with permission of John Wiley and Sons.

Boncel *et al.*[348] synthesised (*R*)-PLA grafted oxidised MWNTs employing the β-D-uridine linker (**Figure 6-5**). They suggested that their method can be used in the fabrication of biodegradable composites for medicinal applications.
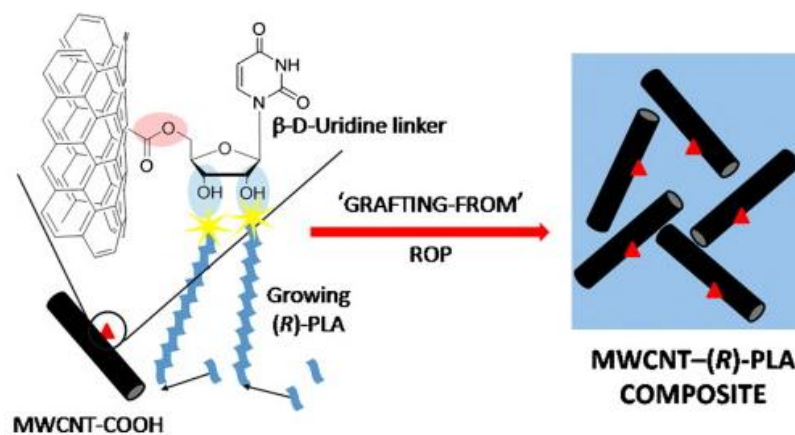
Figure 6-5: Synthesis of the MWNT-CO–(Oβ-Ur)–(R)-PLA composite. Reprinted from Publication [348], Copyright (2013), with permission from Elsevier.

The adsorption of ribonucleosides and nucleobases on the surface of SWNTs are still not reported. This chapter investigates the noncovalent interaction between ribonucleosides and their compounding nucleobases with SWNTs to provide important information about the interaction mechanism.

The objective of the present study was to investigate the interaction between ribonucleosides and SWNTs. In particular, to investigate how the combined effect of ribonucleoside substituent groups and the oxygen-containing functional groups of SWNT surfaces might affect adsorption.

6.2. Results and Discussion

The high surface area of SWNTs is an important factor in the adsorption of biomolecules on their surface. However, the surface area alone is not enough to interpret the adsorption characteristics of biomolecules on SWNTs. Adsorption is affected by other factors, such as biomolecule molecular structure, and the surface chemistry of SWNTs.[349,350] The inner pores of SWNTs are not available for adsorption.[351,352] The adsorption energy and charge transfer of molecules in groove and interstitial sites of the bundles are much higher than those on the surface. Therefore, the outer surface of SWNTs is of major importance for the adsorption of biomolecules.[352,353] The noncovalent interaction of both purified and oxidised SWNTs with ribonucleosides and nucleobases, ribose molecule were investigated in this section.

6.2.1. Oxidation of SWNTs

Two batches of oxidised SWNTs with different degrees of oxidation were prepared. The purified SWNT (**Chapter 4**) was divided into two batches. The first batch was refluxed in 2 M nitric acid, while the second batch was refluxed in 8 M nitric acid. Both batches were refluxed at 120 °C for 4 hours.

The degree of oxidation of oxidised nanotubes (2 M, and 8 M) was estimated using thermogravimetric analysis (TGA) in an inert atmosphere, since any covalent modifications are labile or decompose upon heating. By assuming that all the weight loss is due to the oxidation, an estimation of the degree of oxidation can be made by

comparison with the TGA of oxidised nanotubes with purified SWNTs (control). When the TGA is attached to a mass spectrometer (TGA-MS) analysis of the fragments removed from the nanotube surface upon heating can also be achieved. The TGA-MS of oxidised SWNTs (2 M) and (8 M) show a further weight loss at 600 °C when compared to the purified SWNTs (**Figure 6-6**). 2 M and 8 M oxidised SWNTs lost 6 % and 15 %, respectively, while purified SWNTs lost only 3 % by weight. This corresponds to the presence of approximately 1.0 functional group per 58 and 20 carbon atoms in 2 M and 8 M oxidised SWNTs, respectively.
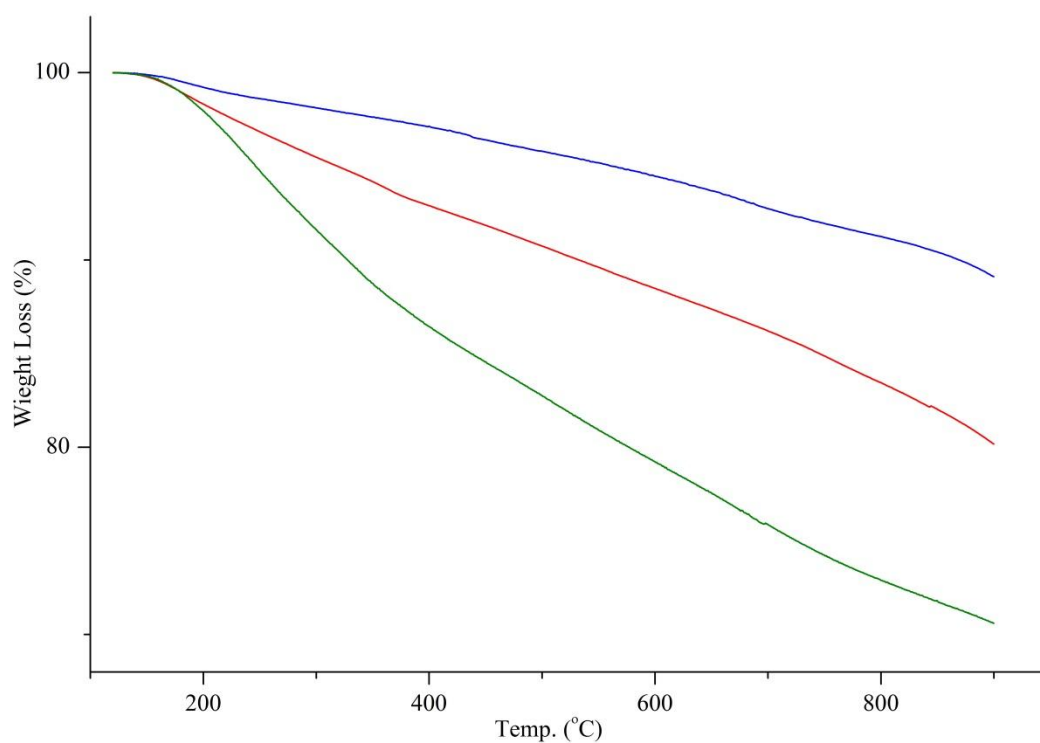
Figure 6-6: TGA of oxidised and purified SWNTs: (**Blue line**) purified SWNTs, (**Red line**) oxidised SWNTs (2 M). (**Green line**) oxidised SWNTs (8 M).

Unmodified SWNTs are known to show a minimal or complete lack of solubility in common organic solvents.[158] Thus, they are typically dispersed in water with the aid of 1.0 % sodium dodecyl sulfate (SDS) solution. The optical absorption spectrum of SDS/purified SWNTs show characteristic absorption peaks in the UV-Vis-NIR range that are due to transitions between van Hove singularities in the density of state (DOS) of SWNTs.[147,354] After undergoing an oxidation to introduce oxygen-containing functional groups to the nanotube surface, the UV-Vis-NIR spectrum of oxidised SWNTs displays a suppression of these van Hove singularities, signifying a disruption of their electronic structure due to covalent modification of the nanotube surface (**Figure 6-7**).[355]
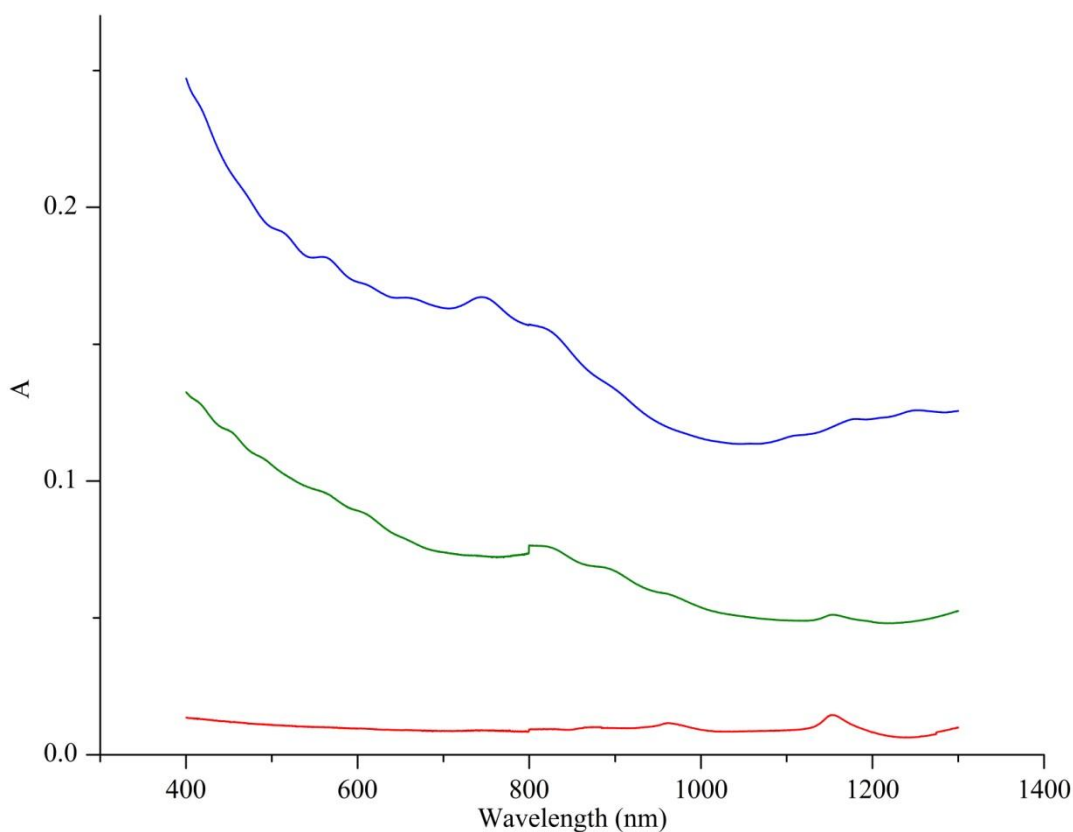
Figure 6-7: UV-Vis-NIR absorption spectra of purified and oxidised SWNTs: (**Blue line**) SDS/purified SWNTs, (**Green line**) oxidised SWNTs (8 M), (**Red line**) oxidised SWNTs (2 M).

The oxidised SWNTs demonstrate an improvement in solubility compared to the purified SWNTs which can be explained as a consequence of the introduction of oxygen functional groups on the nanotube surface. These functional groups form hydrogen bonds with water molecules, thus solubilising the nanotubes in water. The concentration of dispersed oxidised nanotubes was found from their absorbance value at 700 nm and calculated molar extinction coefficient of oxidised SWNTs (see **Appendix B**). The concentration of dispersed 8 M oxidised SWNTs was 249.3 µg mL^{-1}, which is higher than that of 2 M oxidised SWNTs (30 µg mL^{-1}). This indicates that the 8 M nitric acid oxidation result in more oxygen-containing functional groups attached to nanotube surface than 2 M oxidised SWNTs which agrees with the TGA results.

Raman spectroscopy is an analytical technique that allows an assessment of the sidewall composition of the SWNT sample to be made.[356] The degree of functionalisation can be estimated form the Raman I_D/I_G ratios before and after oxidation treatment. However, it should be noted that Raman is not a quantitative tool to accurately determine the amount of functionalisation of the oxidised nanotubes. It is merely used for qualitative comparisons between samples, and at least ten scans on different areas of the samples were completed for this assessment. Oxidised and purified aqueous dispersion were drop-casted to silicon wafer substrate for the Raman measurements. **Figure 6-8** shows a representative Raman spectra of 2 M and 8 M oxidised and purified SWNTs (control).
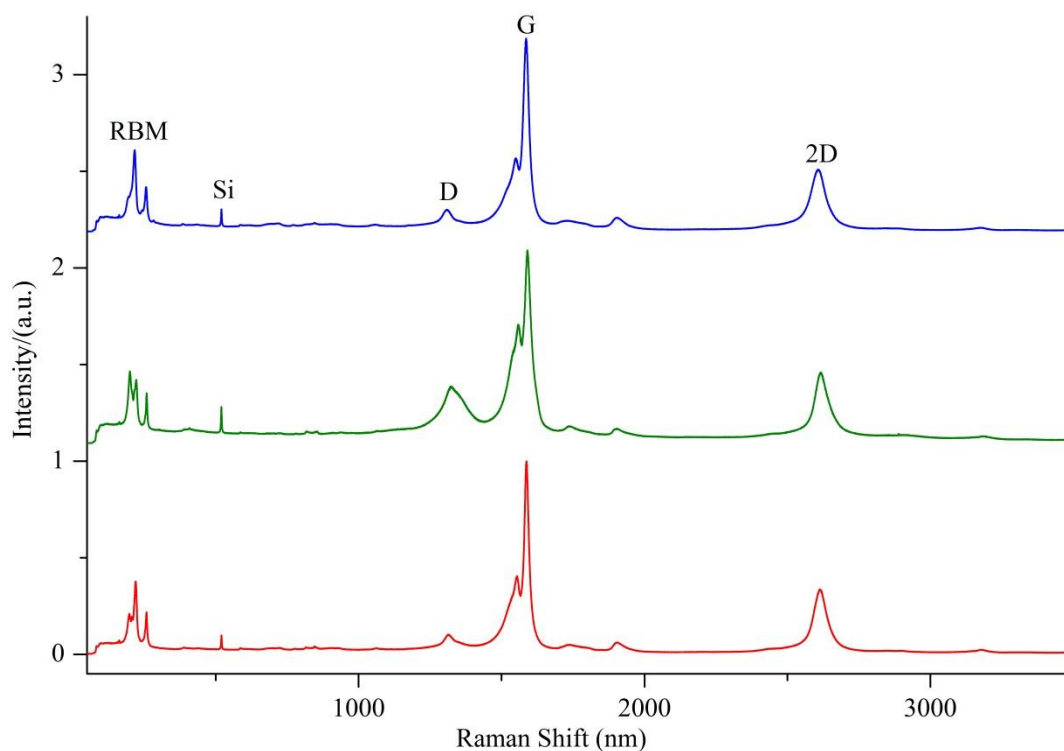
Figure 6-8: A representative Raman spectra (633 nm) of purified and oxidised SWNTs normalised at the G band: (**Blue line**) SDS/purified SWNTs, (**Green line**) oxidised SWNTs (8 M), (**Red line**) oxidised SWNTs (2 M).

As can be observed in Raman spectrum, the characteristic peaks in purified SWNTs, D band at 1309 ± 0.8 cm^{-1}, and G band at 1584.7 ± 0.8 cm^{-1}, are identified. Comparing the ratio I_D/I_G values of functionalised and purified nanotubes, it is observed that after oxidation, the ratio values increase as expected. The I_D/I_G of 8 M and 2 M oxidised SWNTs is 0.29 ± 0.02 and 0.17 ± 0.02, respectively, while it is 0.13 ± 0.07 for purified SWNTs. These results indicate that 8 M oxidised SWNTs have higher amount of functional groups on the side walls than 2 M oxidised and purified SWNTs.

6.2.2.   Dispersion of Purified and Oxidised SWNTs with Ribonucleosides

6.2.2.1.   Dispersion of Purified SWNTs

Previous theoretical studies have suggested that interaction of ribonucleosides with unmodified SWNTs depends mainly on π–π stacking. Thus, this section aims to investigate the noncovalent functionalisation of purified SWNTs with ribonucleosides. 1.0 mM aqueous solutions of ribonucleoside were used to noncovalent to disperse purified SWNTs in water. The aqueous ribonucleoside solutions were prepared by diluting a stock solution (2 mg 10 mL^{-1})[1], and the final concentration was determined by UV-visible absorption. **Figure 6-9** shows the ribonucleosides used in the dispersions.
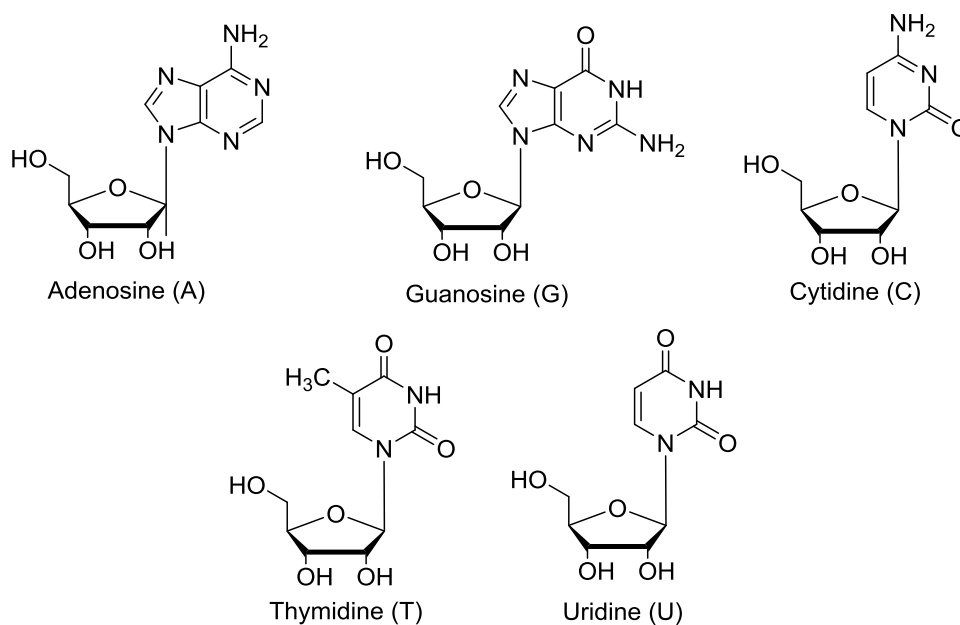
Figure 6-9: Ribonucleosides used in the dispersion of SWNTs.

---

[1] Due to the low solubility of ribonucleosides in water, the 2.0 mg 10 mL^{-1} solution ribonucleosides is a saturated solution.

1.0 mg of purified SWNTs in 1.0 ml of the ribonucleoside solutions were probe sonicated for 15 min in an ice bath. Then the dispersions were centrifuged to accelerate the separation of the supernatant phase, which contains the dispersed and mostly exfoliated purified SWNTs. The ultrasonication step provides the energy to overcome the high van der Waals attraction between the SWNTs, while the ribonucleoside stabilises the exfoliated/individualised nanotubes. Given that SWNTs supernatant colour intensity provide an initial qualitative evaluation of the amount of dispersed SWNTs in the solution. Thus, the quality of ribonucleoside/purified SWNTs aqueous dispersions was studied first by simple visual inspection (**Figure 6-10**).

Figure 6-10: Ribonucleoside/purified SWNTs supernatant in water after sonication and centrifugation: Dispersion from left to right: adenosine/purified SWNTs, guanosine/purified SWNTs, thymidine/purified SWNTs, cytidine/purified SWNTs, and uridine/purified SWNTs.

The clear supernatant of ribonucleoside/purified SWNTs aqueous dispersion suggests that purified SWNTs did not disperse by their noncovalent interaction with ribonucleosides. The dispersions were then characterised with UV-Vis-NIR spectroscopy. UV-Vis-NIR absorption intensity of nanotube dispersion is proportional to their amount of dispersed in the solution. Thus, the low UV-Vis-NIR absorption intensity peaks of the ribonucleoside/purified SWNTs dispersion confirms

that a very small amount of purified SWNTs are present in the supernatant (**Figure 6–11**).
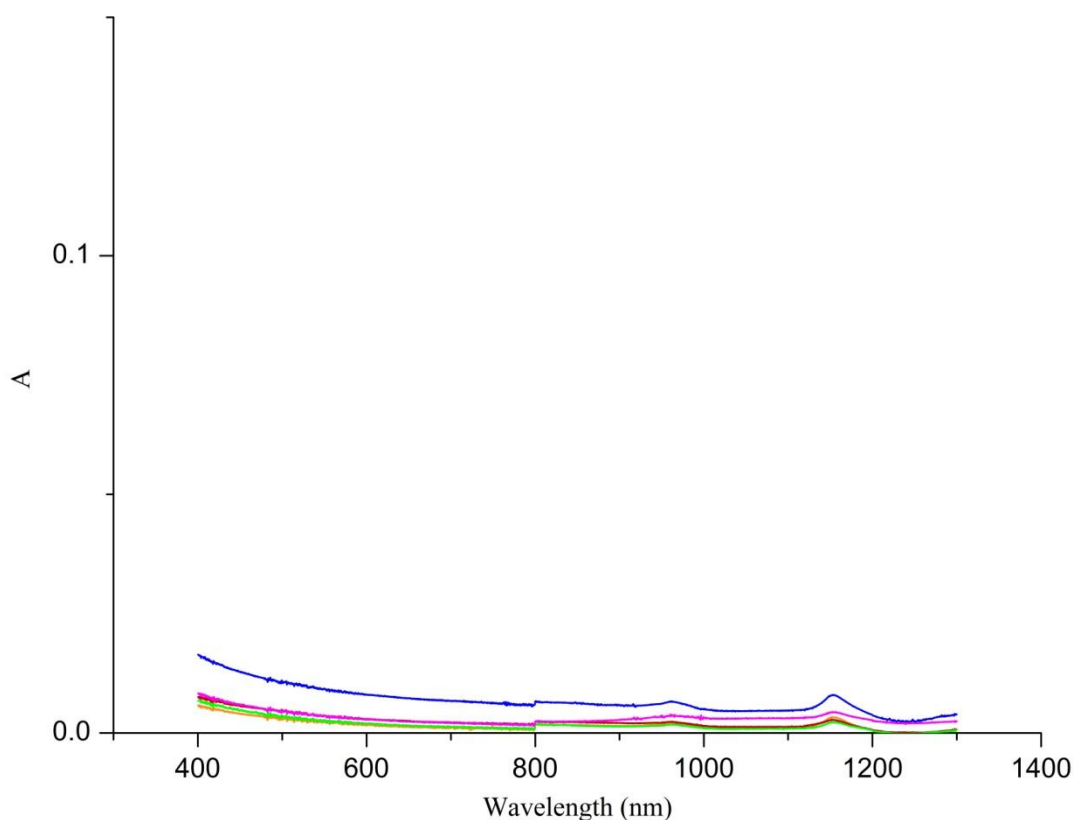
Figure 6-11: UV-Vis-NIR absorption spectra of dispersed purified SWNTs with ribonucleosides. (**Orange line**) adenosine/purified SWNTs, (**Blue line**) guanosine/purified SWNTs, (**Green line**) thymidine/purified SWNTs, (**Red line**) cytidine/purified SWNTs, (**Pink line**) uridine/purified SWNTs.

UV-Vis-NIR absorption of ribonucleoside/purified SWNTs dispersion is used to determine the concentration of dispersed nanotubes in the supernatant through application of Beer-Lambert Law and calculated extinction coefficient of purified SWNTs at 700 nm, $\varepsilon_{700} = 37.3$ mL mg^{-1} cm^{-1} (see **Appendix B**). **Table 6-1** shows the concentration of dispersed nanotubes by ribonucleosides after sonication and centrifugation.

Ribonucleoside	Conc. of Dispersed Purified SWNTs $\mu g \ mL^{-1}$
SDS (control)	196.4
Adenosine	0.1
Guanosine	0.8
Thymidine	0.1
Cytidine	0.2
Uridine	0.2

Table 6-1: Concentration of purified SWNTs dispersed by ribonucleosides determined from UV-Vis-NIR absorption after sonication and centrifugation

The very low concentration of dispersed purified SWNTs is thought to be due to weak hydrophobic interaction/π–π stacking between ribonucleoside and the hydrophobic surface of purified SWNTs. The noncovalent interaction between purified SWNTs with ribonucleosides is further investigated by dispersing purified SWNTs with ribonucleoside's moieties; nucleobases and ribose sugar. Previous theoretical studies suggested that hydrophobic and heterocyclic ring of nucleobases play an important role to impart dispersion to nanotubes via π–π stacking. However, nucleobase/purified SWNTs dispersion showed very low UV-Vis-NIR absorption peaks (**Figure 6-12**).
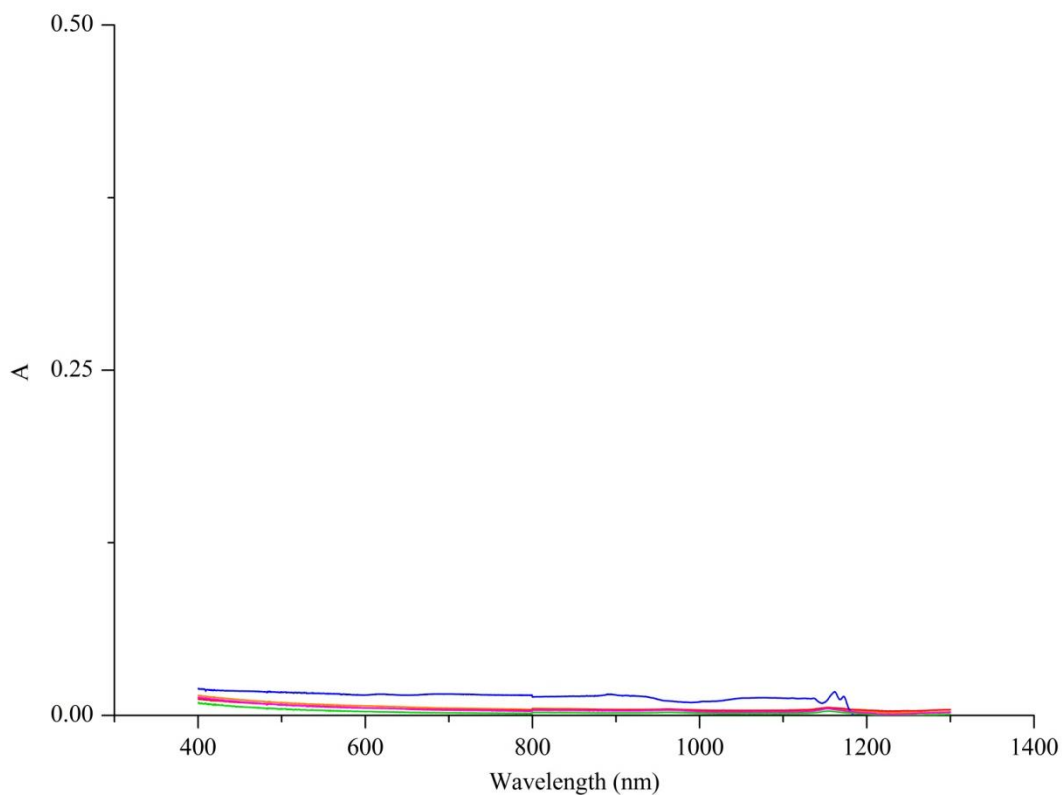
Figure 6-12: UV-Vis-NIR absorption spectra of dispersed purified SWNTs with nucleobases: **(Orange line)** adenine/purified SWNTs, (**Blue line**) guanine/purified SWNTs, (**Green line**) thymine/purified SWNTs, (**Red line**) cytosine/purified SWNTs, (**Pink line**) uracil/purified SWNTs.

This very low UV-Vis-NIR absorption intensity proves that the heterocyclic ring size of the nucleobases is not enough to have an efficient π–π stacking interaction with the hydrophobic surface of the purified SWNTs. Thus nucleobases dispersed a very small amount of purified SWNTs in water (**Table 6-2**).

Nucleobase	Conc. of Dispersed Purified SWNTs $\mu g \, mL^{-1}$
SDS (control)	196.4
Adenine	0.7
Guanine	2.0
Thymine	0.2
Cytosine	0.5
Uracil	0.5

Table 6-2: Concentration of purified SWNTs dispersed by nucleobases determined from UV-Vis-NIR absorption after sonication and centrifugation.

Similar results were found when purified SWNTs were dispersed with ribose sugar (4.2 $\mu g \, mL^{-1}$). These results indicate that there is only weak π–π stacking/hydrophobic interaction between nucleobase, ribose sugar, and the hydrophobic surface of purified SWNT. Thus they have weak dispersion ability towards nanotubes surface.

6.2.2.2. Dispersion of Oxidised SWNTs

The surface chemistry of SWNTs, in particular oxygen-containing functional groups such as OH and COOH, has considerable effects on the adsorption of organic molecules.[82,349,357] As discussed in (**Section 6.2.1**), more severe oxidation conditions introduces more oxygen-containing functional groups on the sidewalls of the nanotubes. The overall objective of this section was to investigate the nonhydrophobic interactions between ribonucleosides and SWNTs. In particular, to investigate how the combined effect of ribonucleoside substituent groups (oxygen and amino) and the oxygen-containing functional groups on SWNT surface might

affect adsorption. The oxidised nanotubes, 2 M and 8 M, were noncovalently functionalised with ribonucleosides following the same method used for the dispersion of purified SWNTs (**Section 6.2.2.1**). The supernatants colour intensity provides an initial qualitative estimation of nanotubes' amount in the dispersion. **Figure 6-13** shows ribonucleoside/oxidised SWNTs supernatants after sonication and centrifugation.
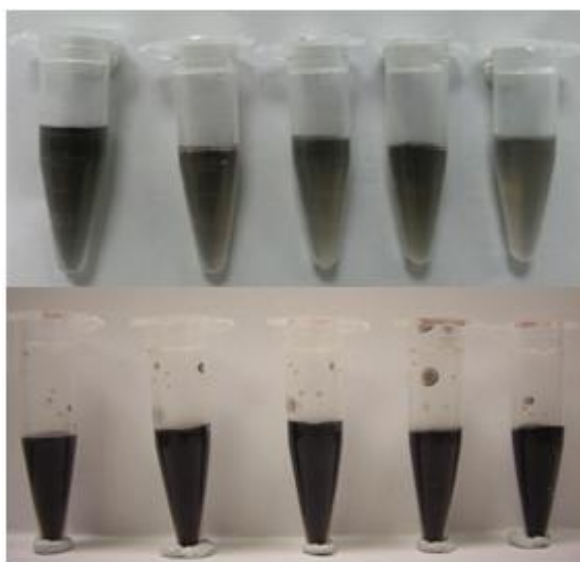
Figure 6-13: Ribonucleoside/oxidised SWNTs aqueous dispersions after sonication and centrifugation. Dispersion from left to right: (**Top**) adenosine/oxidised SWNTs (2 M), guanosine/oxidised SWNTs (2 M), thymidine/oxidised SWNTs (2 M), cytidine/oxidised SWNTs (2 M), uridine/oxidised SWNTs (2 M). (**Bottom**) adenosine/oxidised SWNTs (8 M), guanosine/oxidised SWNTs (8 M), thymidine/oxidised SWNTs (8 M), cytidine/oxidised SWNTs (8 M), uridine/oxidised SWNTs (8 M).

By comparing the ribonucleoside/oxidised SWNTs (2 M and 8 M) supernatant colour with ribonucleoside/purified SWNTs (**Section 6.2.2.1**), it is clear that oxygen-containing functional groups on nanotubes' surface have a significant influence on their interaction with ribonucleosides. Ribonucleoside/oxidised SWNTs (8 M) supernatant has a significantly darker colour than ribonucleoside/oxidised SWNTs (2 M). Knowing that 8 M oxidised nanotubes has a higher degree of oxidation than the

2 M oxidised nanotubes (**Section 6.2.1**). Thus, based on the supernatant colour intensity, it is thought that increasing the number of oxygen-containing functional groups on the nanotube surface resulted in a better interaction with ribonucleosides. The ribonucleoside/oxidised nanotube (2 M and 8 M) dispersion are characterised with UV-Vis-NIR spectroscopy to determine the relative amount of individual SWNTs versus ropes or bundles in the suspensions and also the net concentration of the dispersed nanotubes. **Figure 6-14**, and **Figure 6-15** show UV-Vis-NIR absorption spectra of ribonucleoside/oxidised SWNTs (8 M) and ribonucleoside/oxidised SWNTs (2 M) dispersions, respectively.
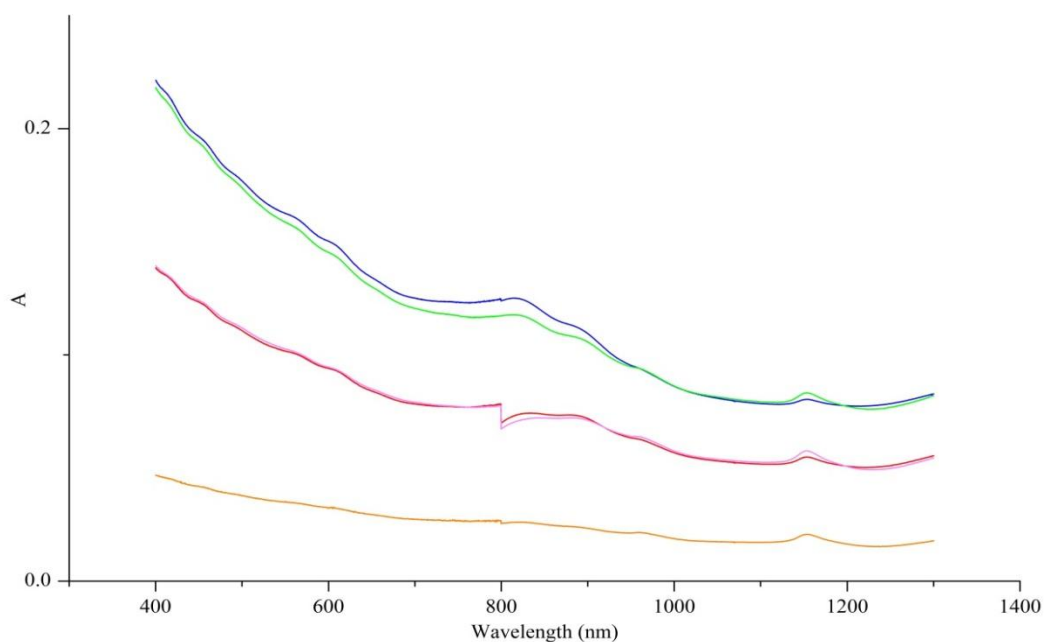
Figure 6-14: UV-Vis-NIR absorption spectra of ribonucleoside/oxidised SWNTs (8 M) aqueous dispersion. (**Blue line**) guanosine/oxidised SWNTs (8 M), (**Green line**) thymidine/oxidised SWNTs (8 M), (**Red line**) cytidine/oxidised SWNTs (8 M), (**Pink line**) uridine/oxidised SWNTs (8 M). (**Orange line**) adenosine/oxidised SWNTs (8 M).
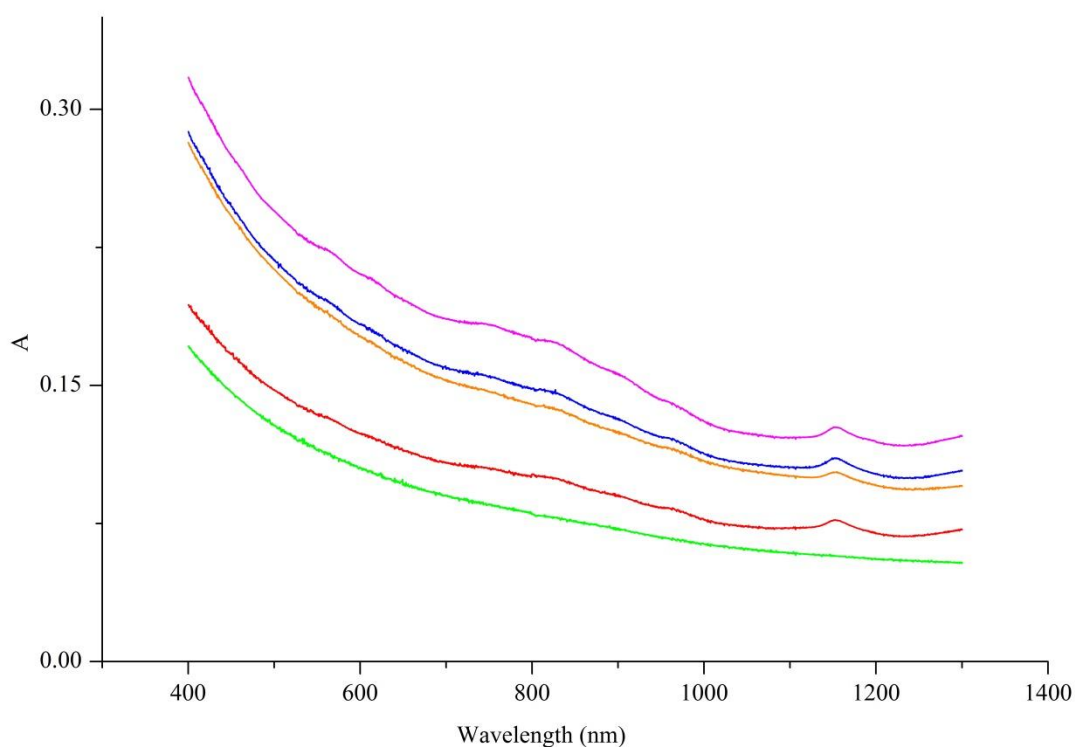
Figure 6-15: UV-Vis-NIR absorption spectra of dispersed SWNTs (2 M) with ribonucleosides: (**Pink line**) uridine/oxidised SWNTs (2 M), (**Blue line**) guanosine/oxidised SWNTs (2 M), (**Orange line**) adenosine/oxidised SWNTs (2 M), (**Red line**) cytidine/oxidised SWNTs (2 M), (**Green line**) thymidine/oxidised SWNTs (2 M).

The UV-Vis-NIR spectra of ribonucleoside/oxidised SWNTs (2 M) composites show low intensity and broad absorption peaks. The broad absorption peaks indicate that ribonucleosides dispersed the nanotubes in bundles or aggregates. Whereas, fine structure in the absorption peaks of ribonucleoside/oxidised SWNTs (8 M) indicate the presence of SWNTs as individuals or as very small bundles.[37] Additionally, the discrete peaks of ribonucleoside/oxidised SWNTs (2 M and 8 M) that extend throughout the metallic (440 − 645 nm) and semiconducting (830 − 1600 nm) indicate ribonucleosides act as a general dispersal agent and do not select for nanotubes of specific type (metallic or semiconducting).

The concentration of dispersed nanotubes in each supernatant after sonication, centrifugation was determined from optical absorption spectroscopy using the Beer-Lambert law and calculated extinction coefficient of 8 M and 2 M oxidised SWNTs at 700 nm (ε_{700} = 14.14, and 19.19 mL mg^{-1} cm^{-1}, respectively) (see **Appendix B**). **Table 6-3** shows the concentration of dispersed oxidised SWNTs (2 M and 8 M) by ribonucleosides.

Ribonucleoside	Conc. of Dispersed Oxidised SWNTs 2 M µg mL^{-1}	Conc. of Dispersed Oxidised SWNTs 8 M µg mL^{-1}
H$_2$O (control)	30	249.3
Adenosine	52.8	84.9
Guanosine	55.1	389.9
Thymidine	96.5	375.9
Cytidine	37.2	244.0
Uridine	37.3	246.2

Table 6-3: Concentration of dispersed oxidised SWNTs (2 M and 8 M) by ribonucleosides determined from UV-Vis-NIR absorption after sonication and centrifugation.

From the results obtained it can be seen that the concentration of dispersed oxidised SWNTs by both the water control and all of the ribonucleosides was greater than that of purified SWNTs (**Section 6.2.2.1**). This suggests that ribonucleosides are not engaging in a hydrophobic interaction with the carbon nanotube surface. It worth noting that when the concentration of oxidised SWNTs is changed from 2 M to 8 M the differences between the control dispersion (i.e. dispersion in just H$_2$O) and the ribonucleosides dispersions changes. When 2 M oxidised SWNTs are used all of the ribonucleosides give rise to a higher concentration of dispersed SWNT than the control (**Table 6-3**). However, when 8 M oxidised SWNTs were used adenosine,

(and to a lesser extent cytidine, and uridine) the concentration of the dispersed CNTs is less than that of the water control. The reason behind the differences observed in the dispersions at the two concentrations of oxidised SWNT used is not immediately apparent. Additionally, it should be noted that the concentration of dispersed 8 M oxidised SWNTs by all of the ribonucleosides is higher than corresponding 2 M oxidised SWNTs. This indicates that increasing the number of oxygen-containing functional groups increases sites for noncovalent integration with ribonucleosides, thus increases the concentration of dispersed nanotubes.

For further evaluation of the ribonucleoside/oxidised SWNTs (8 M) aqueous dispersion stabiliteis as a function of time, the concentraton of oxidised SWNTs (8 M) in the dispersion was checked with optical absorption measurements. **Table (6-4)** compares between the concentration of dispersed carbon nanotubes in each ribonucleoside/oxidised SWNTs (8 M) complex 4 weeks after the initial preparation of the solutions.

Ribonucleoside	Conc. of Dispersed Oxidised SWNTs 8 M $\mu g\ mL^{-1}$	Conc. of Dispersed Oxidised SWNTs 8 M After 4 Weeks $\mu g\ mL^{-1}$
Adenosine	84.9	56.9
Guanosine	389.9	363.1
Thymidine	375.9	356.1
Cytidine	244.0	228.4
Uridine	246.2	232.9

Table 6-4: A comparison between the concentration of dispersed oxidised SWNTs (8 M) by ribonucleosides after dispersion and 4 weeks.

The concentration of the oxidised SWNTs (8 M) recorded after 4 weeks reflects the high stability of these dispersions. This can be explained by a strong hydrogen bond between the ribonucleosides and oxygen-containing functional groups on carbon nanotube's surface.

In order to obtain a better understanding of the nature of this interaction addition of nucleobases with oxidised SWNTs (2 M and 8 M) was investigated. **Figure 6-16** shows the individual nucleobases used in the dispersion.
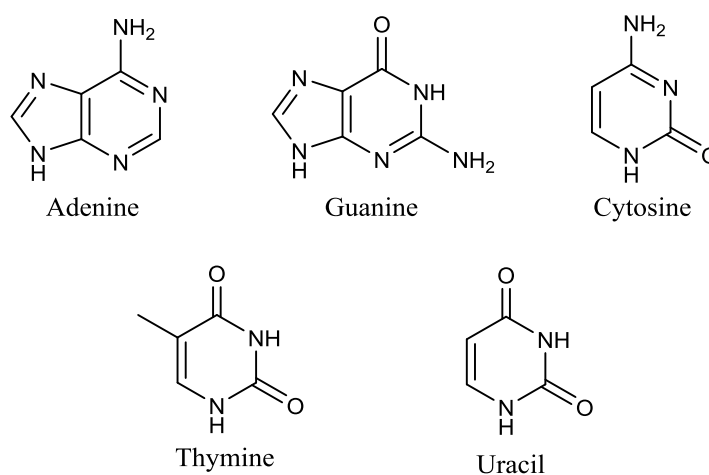
Figure 6-16: Nucleobases used in the dispersion of oxidised SWNTs.

The nucleobase/oxidised nanotubes (2 M and 8 M) composite dispersions were prepared in similar way to the ribonucleosides composites (**Section 6.2.2.1**). **Figure 6-17** shows the nucleobase/oxidised SWNTs (2 M) and nucleobase/oxidised SWNTs (8 M) dispersions supernatant after sonication and centrifugation.
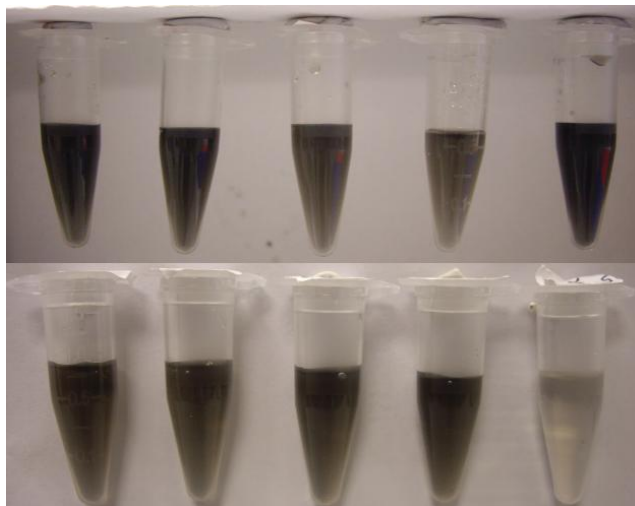
Figure 6-17: Nucleobase/oxidised nanotubes composites dispersion after sonication and centrifugation. Dispersion from left to right: (**Top**) adenosine/oxidised SWNTs (8 M), guanosine/oxidised SWNTs (8 M), thymidine/oxidised SWNTs (8 M), cytidine/oxidised SWNTs (8 M), and uridine/oxidised SWNTs (8 M). (**Bottom**) adenosine/oxidised SWNTs (2 M), cytidine/oxidised SWNTs (2 M), thymidine/oxidised SWNTs (2 M), uridine/oxidised SWNTs (2 M), and guanosine/oxidised SWNTs (2 M).

In comparison with purified SWNTs (**Section 6.2.2.1**), the nucleobase/oxidised SWNTs (2 M, and 8 M) produced a darker supernatant. In addition, the nucleobase/oxidised SWNTs (8 M) showed a darker supernatant colour compared to nucleobase/oxidised SWNTs (2 M). **Figure 6-18**, and **Figure 6-19** show the UV-Vis-NIR absorption spectra of nucleobase/oxidised SWNTs (8 M and 2 M) dispersion, respectively. It can be seen that the absorption intensity nucleobase/oxidised SWNTs (8 M) dispersion is higher than that of ribonucleoside/oxidised SWNTs (2 M).
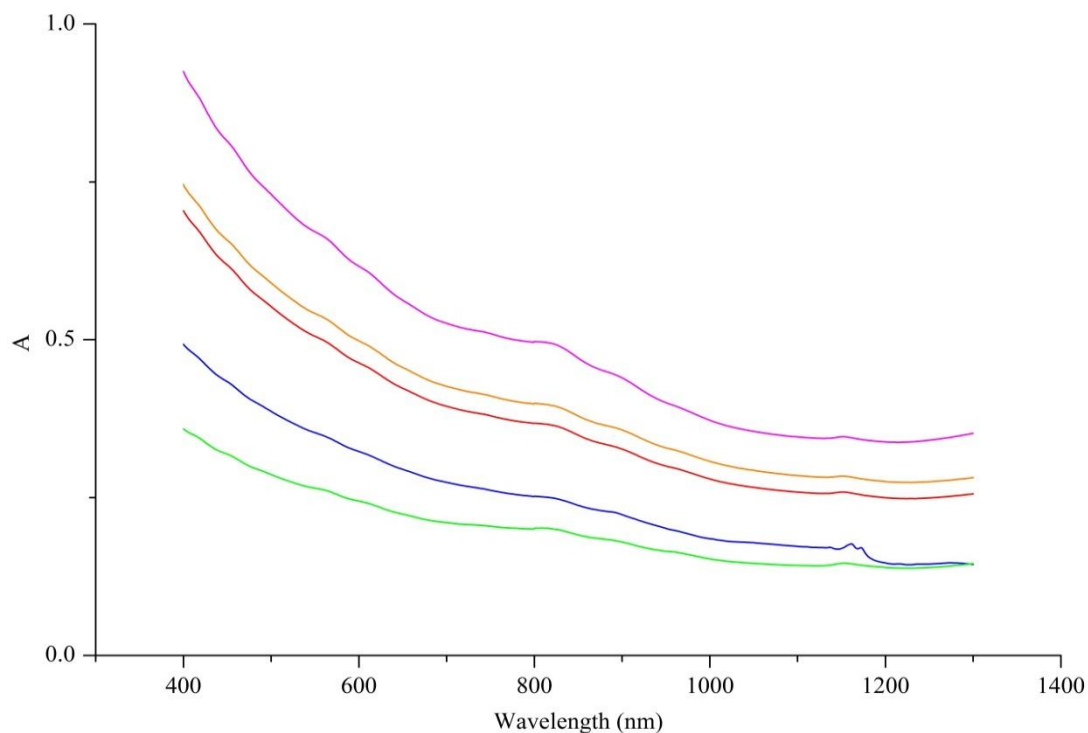
Figure 6-18: UV-Vis-NIR absorption spectra of 8 M oxidised dispersed with nucleobases. (**Pink line**) uracil/oxidised SWNTs (8 M), (**Orange line**) adenine/oxidised SWNTs (8 M), (**Red line**) cytosine/oxidised SWNTs (8 M), (**Blue line**) guanine/oxidised SWNTs (8 M), (**Green line**) thymine/oxidised SWNTs (8 M).
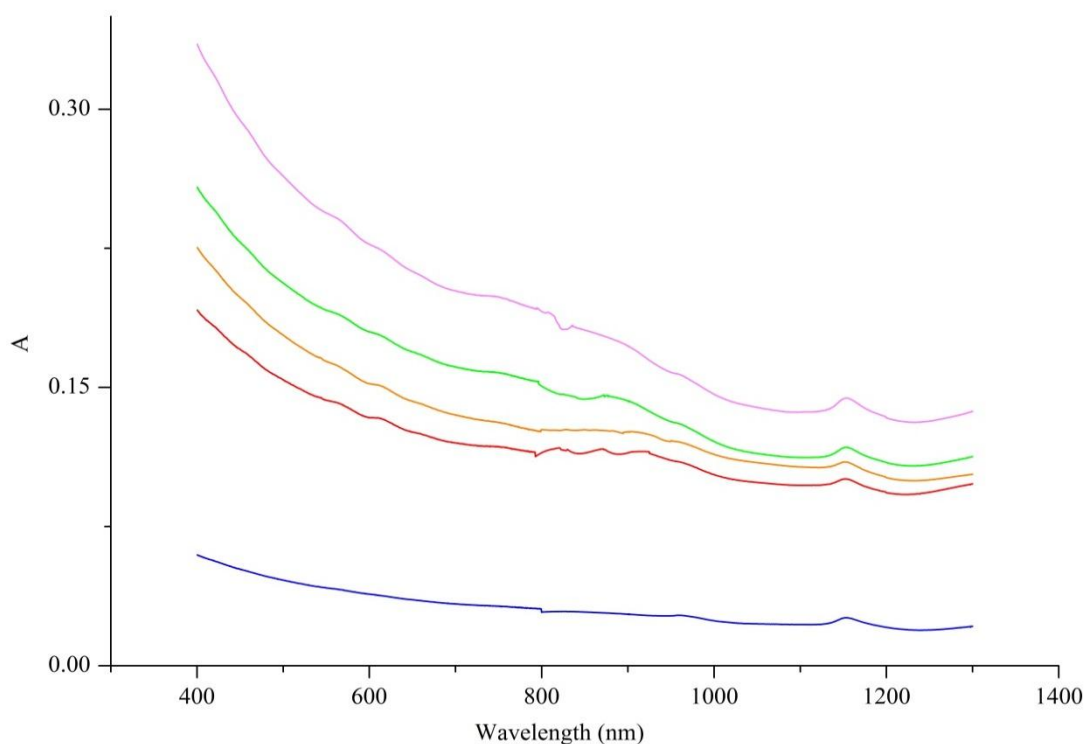
Figure 6-19: UV-Vis-NIR adsorption spectra of 2 M oxidised dispersed with nucleobases. (**Pink line**) uracil/oxidised SWNTs (2M), (**Green line**) thymine/oxidised SWNTs (2M), (**Orange line**) Adenine/oxidised SWNTs (2M), (**Red line**) Cytosine/oxidised SWNTs (2M),. (**Blue line**) Guanine/oxidised SWNTs (2M).

The results in **Table 6-4** show that the concentration of the nucleobase dispersed oxidised SWNTs (2 M and 8 M) are less than the ribonucleoside dispersed oxidised SWNTs (2 M and 8 M). However, they are higher than the concentration of nucleobase dispersed purified SWNTs (**Section 6.2.1**). The concentration of dispersed oxidised SWNTs by the nucleobase increases with increasing the number of oxygen functional groups on nanotube surface from 2 M oxidised SWNTs to 8 M oxidised SWNTs. However, it should be noted that at 8 M all of the nucleobases give rise to a lower concentration of disperse SWNTs compared to the water control. These results suggest that here the nucleobases are actually causing the SWNTs to aggregate and crash out of solution. Water can form H-bonds with oxygen-containing functional groups on the oxidised SWNTs. Thus, the overall decrease in the concentration of dispersed oxidised nanotubes using ribonucleosides and nucleobases compared their dispersion in water suggests that water molecules compete with the ribonucleosides and nucleobases over adsorption sites and/or form a 3D cluster around the oxygen-containing functional groups, and block the adsorption sites nearby.

Nucleobase	Conc. of Dispersed oxidised SWNTs 2 M $\mu g\ mL^{-1}$	Conc. of Dispersed oxidised SWNTs 8 M $\mu g\ mL^{-1}$
H_2O (control)	30	249.3
Adenine	46.7	147.6
Guanine	11.5	94.9
Thymine	55.7	72.8
Cytosine	41.5	136.7
Uracil	69.9	182.1

Table 6-5: Concentration of dispersed oxidised SWNTs by nucleobases determined for their UV-Vis-NIR absorption after sonication and centrifugation.

These results provide further evidence that the key dispersing interaction depends on the oxygen-containing functional groups on the surface of oxidised SWNTs. Furthermore, the variation in the concentration of dispersed oxidised carbon nanotubes by nucleobases suggests that they play a key role in ribonucleosides' dispersion affinity towards nanotubes. Nucleobases are known to have a very low solubility in water; however, ribonucleosides have slightly higher solubility in water. This is due to ribose moiety which interacts with water molecules, thus decreases the hydrophobicity of the nucleobase moiety. The interaction of the ribose sugar with SWNTs has been studied and its ability to disperse SWNTs is shown in **Table 6-5**.

Dispersant	Conc. of Dispersed Oxidised SWNTs 2 M $\mu g\ mL^{-1}$	Conc. of Dispersed Oxidised SWNTs 8 M $\mu g\ mL^{-1}$
H$_2$O (control)	30	249.3
Ribose	67.7	441.5

Table 6-6: Concentration of dispersed oxidised SWNTs by ribose sugar determined for UV-Vis-NIR absorption after sonication and centrifugation.

The concentration of dispersed nanotubes with oxidised SWNTs (2 M and 8 M) is higher than purified SWNTs (**6.2.2.1**). It was speculated that one of the ribose hydroxyl groups forms hydrogen bonds with the carboxylic groups on the surface of the oxidised SWNTs while the second interacts with water molecules therefore increasing the dispersibility of the nanotubes in water. **Figure 6-20** illustrates the ribose sugar's ability to individually debundle the 8 M oxidised SWNTs compared to the low adsorption intensity of the 2 M oxidised, which also shows the low amount of the bundled dispersion.
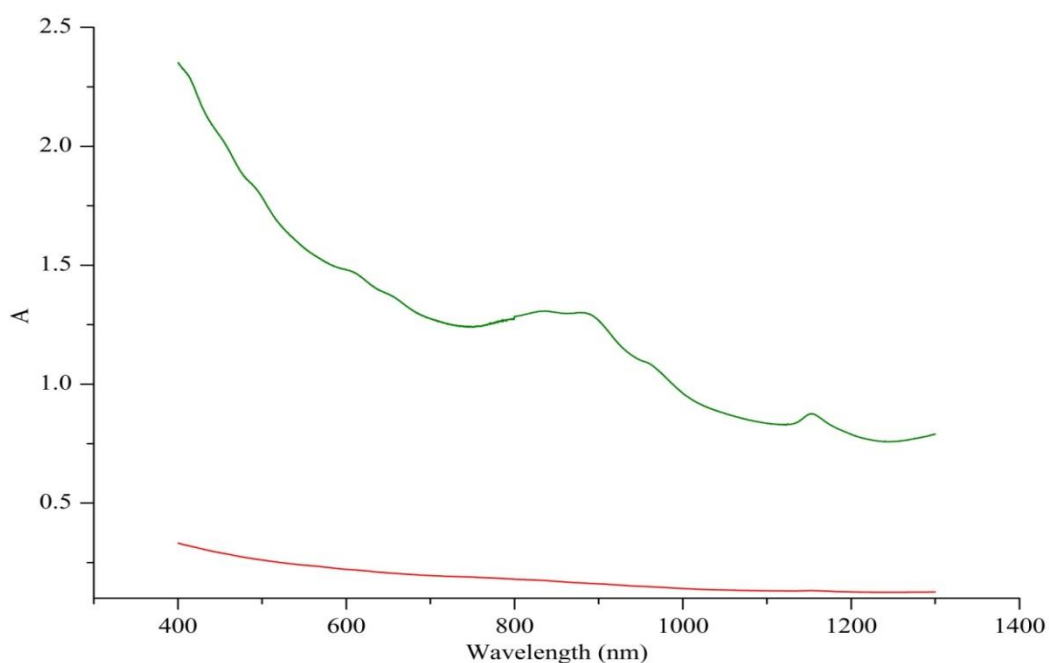
Figure 6-20: UV-Vis-NIR absorption spectra of purified and oxidised SWNTs with ribose sugar: (**Green line**) oxidised SWNTs (8 M), (**Red line**) oxidised SWNTs (2 M).

As all the ribonucleosides have the ribose moiety and vary in their nucleobase moiety, the above results imply that the variation in ribonucleosides' interaction affinity towards nanotubes depends on their nucleobase moiety only. Thus, it is thought that the nucleobase moiety in a ribonucleoside interacts with oxygen-containing functional groups on the carbon nanotube surface, while its ribose moiety interacts with solvent water molecules.

In order to further study the effect of the non-covalent interaction between the ribonucleosides and the oxidised SWNT's electronic properties, Raman spectra of oxidised SWNTs (8 M) (control) and ribonucleoside/oxidised SWNTs (8 M) composites have been measured. The Raman analyses were measured by drop casting each sample on a silicon substrate. **Figure 6-21** shows a representative

Raman spectra of ribonucleoside/oxidised SWNTs (8 M) composites along with oxidised SWNTs (8 M) as a reference.
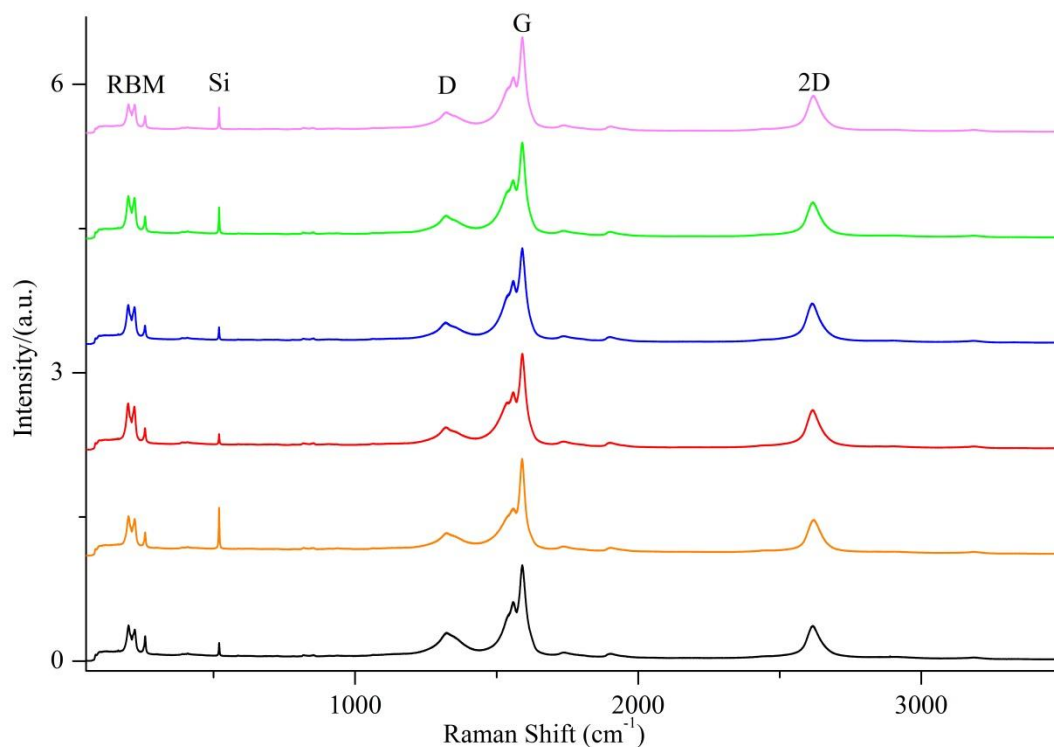
Figure 6-21: A representative Raman spectra (633 nm) of ribonucleoside/oxidised SWNTs (8 M) composites and oxidised SWNTs (8 M) as a control: (**Black line**) oxidised SWNTs (8 M) (control), (**Orange line**) adenosine/oxidised SWNTs (8 M), (**Red line**) cytidine/oxidised SWNTs (8 M), (**Blue line**) guanosine/oxidised SWNTs (8 M), (**Green line**) thymidine/oxidised SWNTs (8 M), (**Pink line**) uridine/oxidised SWNTs (8 M).

The Raman spectra of ribonucleoside/oxidised SWNT (8 M) composites and oxidised SWNTs (8 M) (control) show the characteristic SWNTs resonances; in particular, radial breathing modes (RBMs), D-band, G-band, and 2D-band. **Table 6-6** shows that the G-band of the composites does not show any considerable shift compared to the oxidised SWNTs (8 M) (control). This further suggests that the interaction between ribonucleosides interaction with nanotubes surface is a nonhydrophobic interaction.

Dispersion	G band cm^{-1}
Oxidised SWNTs (8 M) (control)	1589.2 ± 0.9
Adenosine/oxidised SWNTs (8 M)	1589.8 ± 0.3
Guanosine/oxidised SWNTs (8 M)	1590.8 ± 0.3
Thymidine/oxidised SWNTs (8 M)	1590.4 ± 0.2
Cytidine/oxidised SWNTs (8 M)	1590.9 ± 0.3
Uridine/oxidised SWNTs (8 M)	1590.2 ± 0.4

Table 6-7: Raman G band of purified SWNTs (control) and peptoids dispersed purified SWNTs.

The G-band split into G$^+$ and G$^-$ mode in both oxidised SWNTs (8 M) (control) and ribonucleoside/oxidised SWNTs (8 M) composites. This indicates that the dispersed nanotubes are a mixture of metallic and semiconducting nanotubes. The noncovalent interaction between ribonucleosides and oxidised SWNTs give rise to the change in the G$^+$ band compared the oxidised SWNTs (control). **Figure 6-22** show that the intensity of G$^+$ band of adenosine/oxidised SWNTs (8 M) is less than that of oxidised SWNTs (8 M) (control). While, guanosine/oxidised SWNTs (8 M) composite has a higher G$^+$ band than oxidised SWNTs (control). Previous researchers have claimed that the BWF line intensity for the G-mode of metallic tubes enhanced in individualised of nanotubes and can be decreased in a bundled one.[137,358] Thus, these results indicate that adenosine has a very weak interaction with the nanotubes, and the dispersed nanotubes are dispersed in bundles. On the other hand, guanosine/oxidised nanotube composite shows high intensity of comparing to oxidised SWNTs control sample and other ribonucleoside/oxidised nanotube composites. This indicates that oxidised SWNTs are individually dispersed by guanosine. These results agree with the UV-Vis-NIR absorption intensity of ribonucleoside/oxidised SWNTs (8 M) composites.
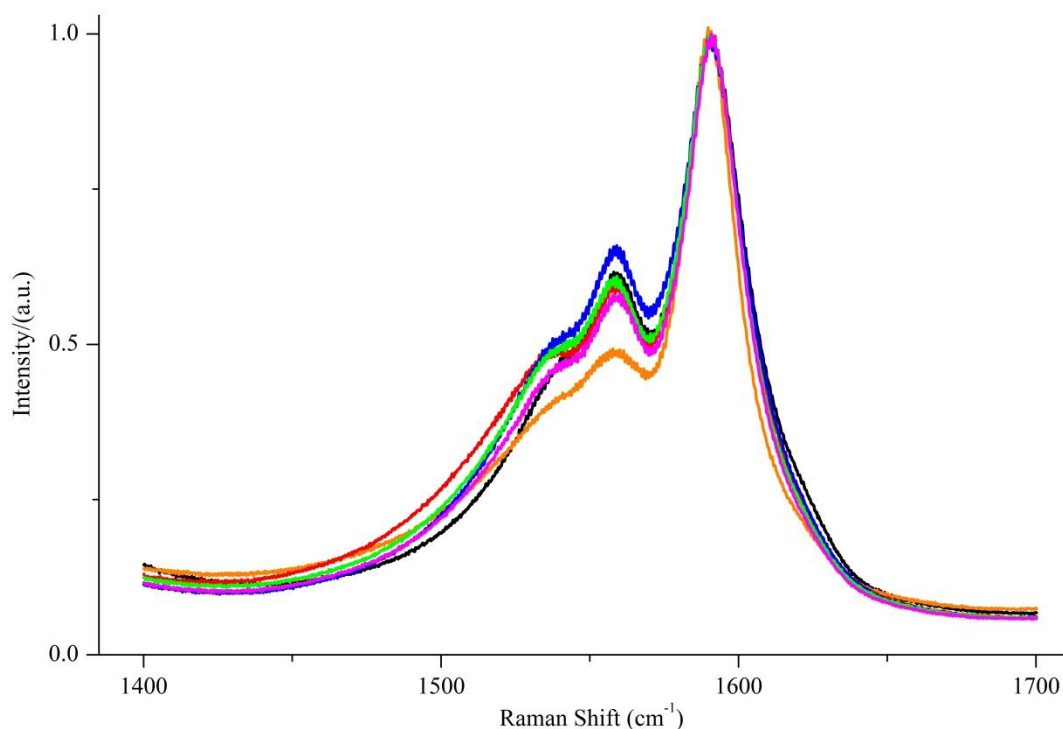
Figure 6-22: A representative Raman G-band spectra of ribonucleoside/oxidised SWNTs (8 M) composites and oxidised SWNTs (8 M) as a control: (**Orange line**) adenosine/oxidised SWNTs (8 M), (**Black line**) oxidised SWNTs (8 M) (control), (**Pink line**) uridine/oxidised SWNTs (8 M), (**Green line**) thymidine/oxidised SWNTs (8 M), (**Red line**) cytidine/oxidised SWNTs (8 M), (**Blue line**) guanosine/oxidised SWNTs (8 M),

6.2.2.2.1. Effect of pH on Dispersions

Several possible mechanisms can be used to explain the interaction between SWNTs and ribonucleosides. Hydrogen bonding between amine groups on nucleobases and oxygen functional groups (e.g., COOH) on SWNTs is not likely to be the primary force driving the interaction. This is mainly because if this were true, then the affinity of nitrogenous nucleobases to SWNTs would increase with decreasing pH, because as pH deceases, there is a transition from the COO$^-$ group to the COOH group on the surface of the SWNTs. Another possible electron donor acceptor (EDA) interaction is that the lone-pair electrons in the nucleobase can act as *n*–electron-

donors and might interacts through n–π EDA with the π–electron acceptor of carbon nanotubes. However, similar to π–π EDA, n–π EDA interactions usually enhanced at high pH, which was experimentally proved to completely impede the dispersion. However, experimentally it was found that at high pH the dispersion precipitated completely (**Table 6-7**).

Dispersion	pH	Conc. of Dispersed Oxidised SWNTs 2 M $\mu g \ mL^{-1}$	Conc. of Dispersed Oxidised SWNTs 8 M $\mu g \ mL^{-1}$
Adenosine/SWNTs	2	0	0
	12	0	0
Guanosine/SWNTs	2	0	0
	12	0	0

Table 6-8: Concentration of adenosine/SWNTs and guanosine/SWNTs dispersion at different pH.

It is thought that Lewis acid base interaction is the main mechanism controlling the interaction of nucleobases' moiety of a ribonucleoside with nanotubes. The NH_2 group in the nucleobases' moiety serves as the weak Lewis base and the oxygen-containing functional groups on carbon nanotubes serve as Lewis acids. As previously discussed, the adsorption of nucleobases onto oxidised nanotubes was stronger the same process with purified nanotubes. This can be explained explains by the fact that untreated nanotubes do not possess any oxygen-containing functionality and, thus, the Lewis acid base interaction cannot be in effect.

6.2.2.2.2. Watson Crick Base-Pairing Effect

It was found that the mixing two complementary ribonucleoside/oxidised SWNTs (8 M) composites leads to the precipitation of the SWNTs (**Figure 6-23**). It is thought that Watson Crick base-pairing occurs between ribonucleosides while still noncovalently bounded to a carbon nanotube side wall. Thus, mixing two complementary ribonucleoside/oxidised SWNTs composites (thymidine/oxidised SWNTs with adenosine/oxidised SWNTs) leads to aggregation of the carbon nanotubes and thus the sedimentation of the SWNT.
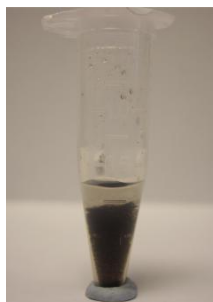
Figure 6-23: Sedimented SWNTs due to Watson Crick base-pairing between complementary ribonucleosides.

The same aggregation behavior was observed for guanosine/oxidised SWNTs with cytidine/oxidised SWNTs. In theory this pairing of ribonucleosides protocol could allow the recovery of SWNTs from aqueous dispersions. Such an H-bonding driven recognition process could be of use in a diverse range of methodologies for example in the recognition of organic molecules, metals and supramolecular molecules.[346,347]

6.3.   Conclusion

In this chapter, the noncovalent interaction of ribonucleosides, nucleobases, and ribose sugar with purified and oxidised SWNTs was studied. The lack of dispersion of purified SWNTs by ribonucleosides determined from their UV-Vis-NIR absorption indicate that the cyclic and aromatic ring of ribonucleosides, nucleobases are too small to disperse the hydrophobic nanotube surface by π–π stacking. On the other hand, the ribonucleosides vary in the dispersion ability toward nanotubes depends on the number of oxygen-containing functional groups on the nanotube's surface and the competition between water molecules which can from hydrogen bonds with oxidised nanotubes, with ribonucleosides and nucleobases over adsorption sites. Furthermore, ribonucleosides show different dispersion affinity towards oxidised nanotubes of similar number of oxygen-containing functional on their surface. Since the ribose moiety is present in all ribonucleosides, it demonstrates the important role of the nucleobase moiety in ribonucleoside in nanotube dispersion. Additionally, it was found that mixing two complementary ribonucleoside/oxidised SWNTs resulted in precipitation of the nanotube due to the Watson Crick pairing. These results suggest that the interaction depends on a nonhydrophobic interaction between the nucleobase moiety in a ribonucleoside interacts with oxygen functional groups on nanotube surface. While, its ribose sugar moiety interacts with water molecules.

7. COVALENT AND NONCOVALENT FUNCTIONALISATION OF

GRAPHENE BASED NANOMATERIALS WITH BIOMOLECULES

7.1. Introduction

7.1.1. Structure

Graphene is a single atomic layer of sp^2 two-dimensional (2D) hybridised carbon atoms arranged in a honeycomb structure.[359] As illustrated in **Figure 7-1**, the graphene sheet is a basic building block for graphitic materials of all other dimensionalities. The graphene planar sheet can be 'wrapped' into a 0D spherical C60 buckyball, 'rolled' into a 1D carbon nanotube, or 'stacked' into 3D graphite.
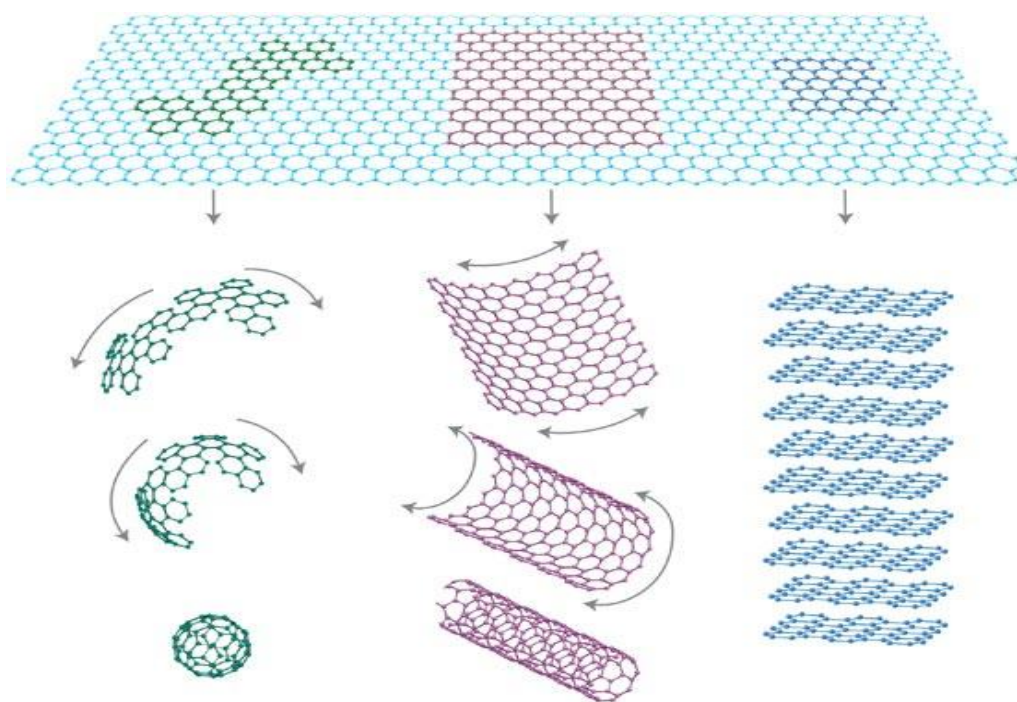
Figure 7-1: Mother of all graphitic forms. Graphene is a 2D building material for carbon materials of all other dimensionalities. It can be wrapped up into 0D buckyballs, rolled into 1D nanotubes or stacked into 3D graphite. Reprinted by permission from Macmillan Publishers Ltd: [Nature Materials] [359] copyright (2007).

At the molecular level, a single-layer graphene sheet has two different structural regions, basal plane and edge[360] (**Figure 7-2**). The graphene basal plane is enriched with π electrons where each carbon atoms bonded with three adjacent carbon atoms with sp^2 hybridised orbitals forming robust σ bonds, and the rest of the electrons in the p atomic orbitals are delocalised over the basal plane of the graphene sheet forming a π bond. Therefore, it is possible for the graphene to interact with the molecules through π–π stacking interaction.[361]
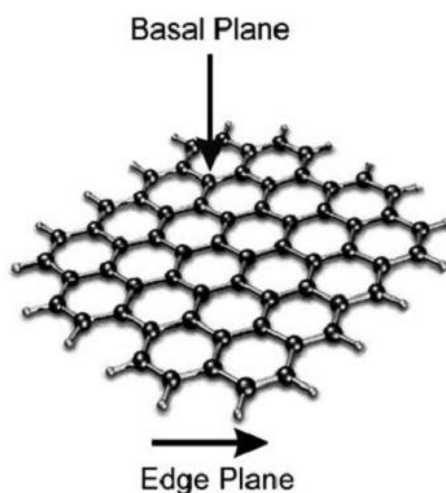
Figure 7-2: A conceptual schematic model of the structure of graphene-indicating its basal and edge plane like sites. Reproduced from [362] with permission of The Royal Society of Chemistry.

The edge plane graphite contains a variety of sites, often called "armchair" or "zig–zag" as shown in **Figure 7-3**.[360] The edge of the majority of synthesised graphene consists of a mixture of the two motifs. The two edge types leading to different electronic and magnetic properties.[363]
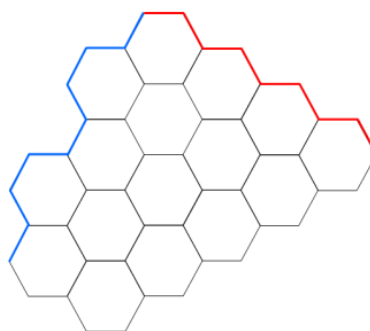
Figure 7-3: Edge states of a graphene sheet showing an armchair (**Blue**) and zigzag (**Red**) edge type.

Although the term graphene refers to a single two-dimensional hexagonal sheet of carbon atoms, it is usually stacked into bi- and few-layer graphene. In general few-layer graphene is defined as being less than ten carbon layers thick, as beyond this the electronic structure resembles that of graphite.[359,364] Therefore, graphene properties are sensitive to the number of layers, their stacking configuration and mis-orientation with respect to each other.[365,366] In bi- and few-layer graphene, Carbon atoms can be stacked in different ways, generating hexagonal or AA stacking, Bernal or AB stacking, and rhombohedral or ABC stacking, finally discernible stacking or turbostratic (**Figure 7-4**).[367] The interlayer spacing for turbostratic graphene (> 0.342 nm) has been found to be larger than that of crystalline graphene (0.335 nm), which is thought to enable rotation and translation of the graphene sheets due to the increased distance resulting in weaker inter-planar bonding.[132]
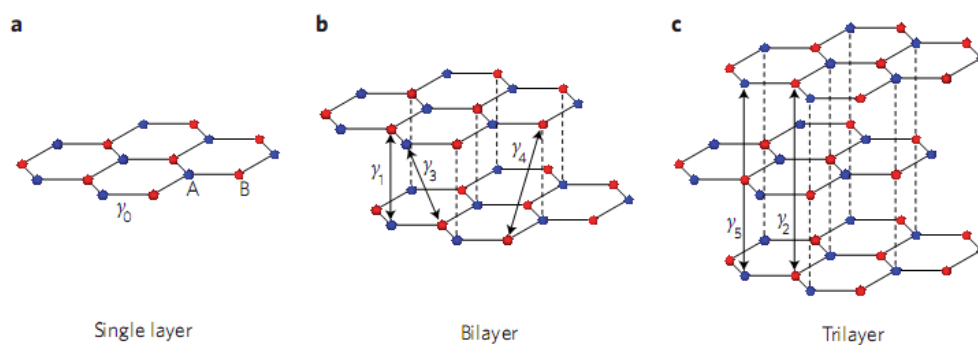
Figure 7-4: (**a**) Graphene structure of single two-dimensional hexagonal sheet of carbon atoms, (**b**) bilayer, and (**c**) tri (few)-layer stacking sequences. Reprinted by permission from Macmillan Publishers Ltd: [Nature Physics] [366], copyright (2011).

There is no chemical bond between the individual graphene layers in graphite; rather they are bonded to each other through weak van der Waals interactions which makes it easy to separate (exfoliate) them into individual graphene sheets.

7.1.2. Synthesis

Although graphene occurs naturally, graphene oxide does not, and its preparation relies on either top-down or bottom-up synthesis method (**Figure 7-5**).
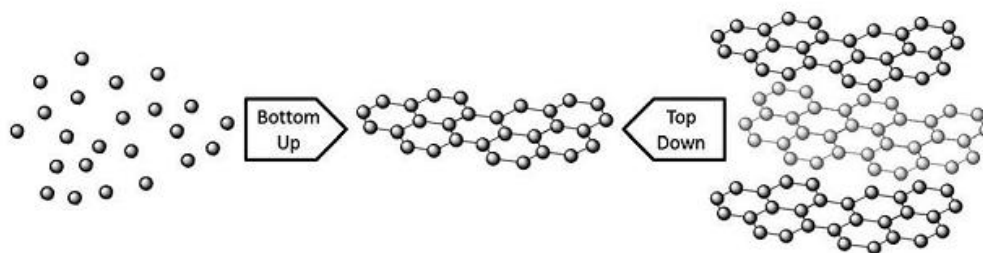
Figure 7-5: A schematic of top down and bottom up graphene synthesis. Reproduced from [368] with permission of The Royal Society of Chemistry.

163

Prior work has shown that the performance of graphene in many applications strongly depends on the preparation method, which has been a major topic of interest.

Many approaches have been successful in producing graphene. Top-down methods tend to use natural or synthetic graphite and in various ways to 'peel off' single graphene sheets. Methods such as the Scotch tape stripping, ion sputtering, pulsed laser deposition, ball milling and arc discharge are all examples of top-down approaches.[368] Bottom-up methods, on the other hand, usually make use of small carbon containing molecules or some other carbon source and build up graphene structures by joining carbon atoms together to grow up graphene. Synthetic routes such as chemical vapour deposition (CVD), wet chemistry or the so-called Fischer-Tropsch synthesis, ion implantation, pyrolysis can be regarded as examples of bottom-up approaches.[368,369] **Figure 7-6** summaries the synthesis methods of graphene oxide.
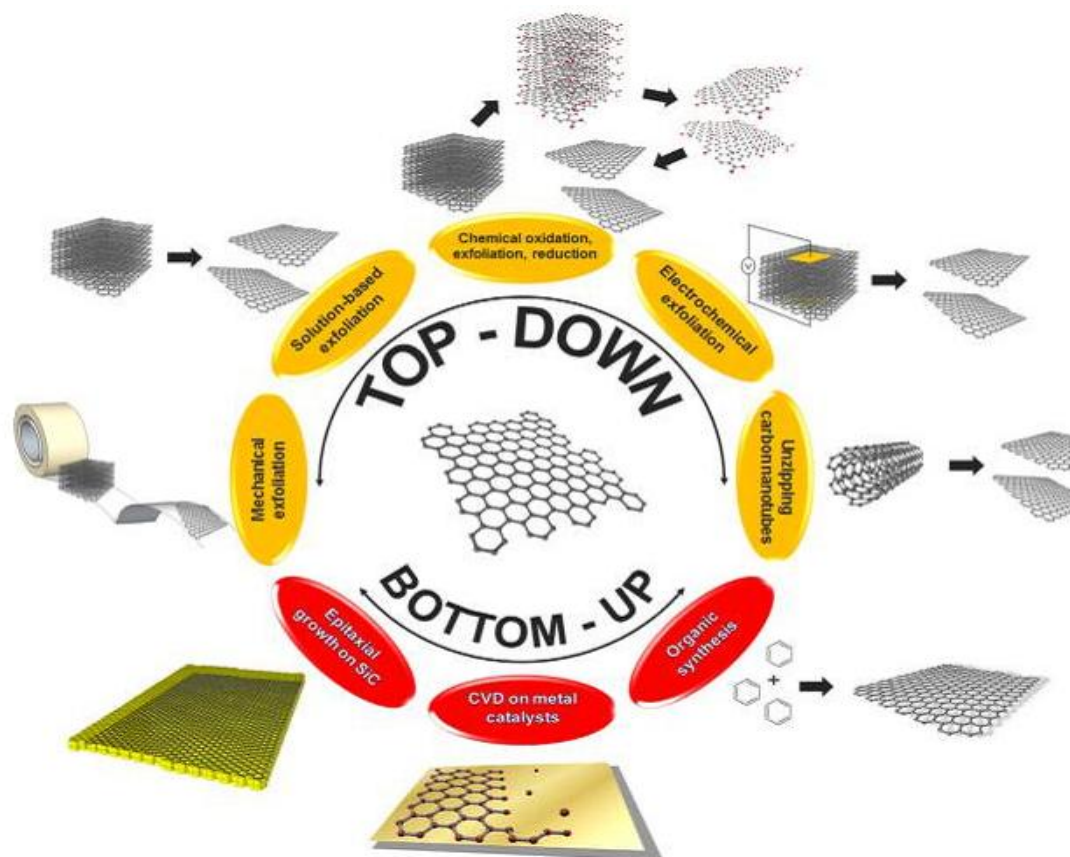
Figure 7-6: Illustration of the Preparation Methods for Graphene and Graphene-Related Materials. Reprinted from [370] with the permission with permission from the American Chemistry society.

7.1.3. Graphite Oxide and Graphene Oxide (GO)

Graphite oxide can be described as an atomically thin sheet of graphite with various organic functional groups covalently bonded to its basal plane and edges.[371] According to recent studies these include epoxy and hydroxyl moieties bonded to the basal plane and carbonyl, carboxylic acid and lactol groups on the edges.[166] The presence of these functionalities in random abundance makes graphite oxide a chemically complex, inhomogeneous system consisting of a hybrid sp^2/sp^3 domain. These functional groups provide reactive sites for a variety of surface-modification reactions to develop functionalised graphene base nanomaterials. When compared to

graphite, the presence of these functional groups between layers also results in the interlayer spacing of graphite oxide (6 – 12 Å depending on the amount of intercalated water) being larger than that of graphite (3.4 Å)).[372] However, due to the disruption of the conjugated electronic structure by these functional groups, graphene oxide is electrically insulating with irreversible defects and disorders.[373] Additionally, the presence of the oxygen-containing functional groups makes graphite oxide thermally unstable, as it undergoes pyrolysis at elevated temperatures.[166] The most important features of graphite oxide is that it is hydrophilic in nature and can be readily exfoliated via thermal treatments or sonication in water, to allow stable dispersion consisting mostly of single layered sheets which is known as graphene oxide (GO) (**Figure 7-7**).[80,374,375]
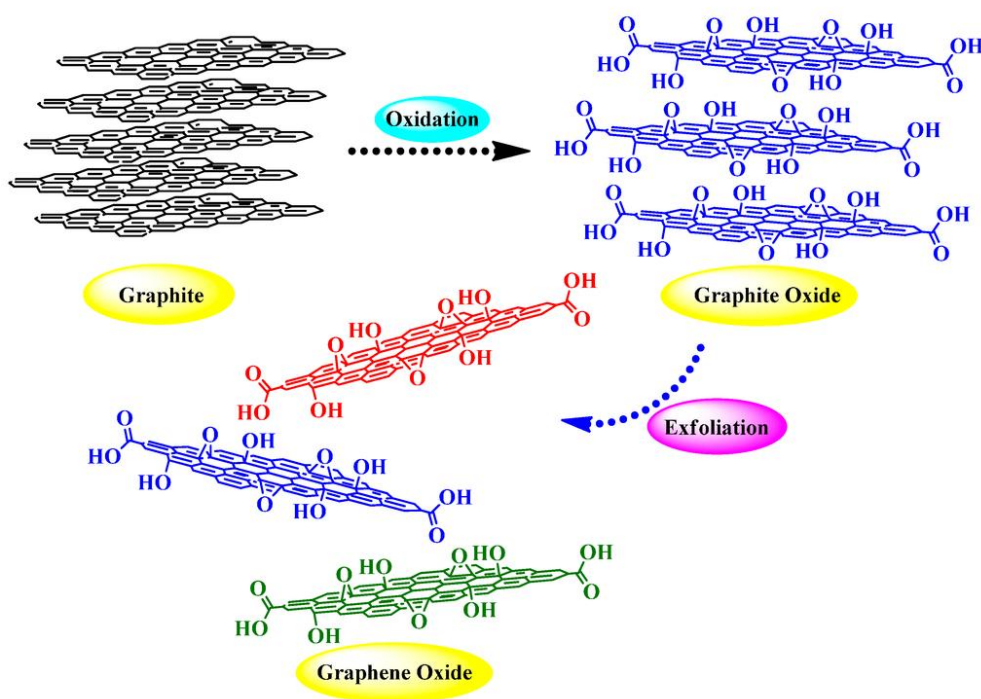
Figure 7-7: Production of GO dispersion from graphite oxide though oxidation and exfoliation. Reproduced with permission from [376]; published by [MDPI], [2014].

Graphite oxide can be synthesised through the oxidation of graphite using strong acids and oxidants. The first method was introduced in 1859 by Brodie.[377] This method involved several repeated oxidation cycles of graphite powder in a mixture of potassium chromate and fuming nitric acid producing a material that contained carbon, hydrogen and oxygen in a ratio of roughly 61:2:37. The Brodie method was later improved by Staudenmaier (1898),[378] and even further by Hofmann and König (1937).[379] However, the most significant paper on the synthesis of graphite oxide was published in 1958 by William Hummers and Richard Offeman,[380] which was later modified by Marcano *et al.*[381] The Hummers and Marcano methods involve the heating of graphite in sulphuric acid with the addition of potassium permanganate and sodium nitrate, which generates nitric acid in situ.

All of the above methods use strong oxidisers and harsh conditions to oxidise graphite flakes into graphene oxide. The harsh oxidation conditions results in a significant portion of double bonds of graphite sheet being broken and forming of various oxygen containing functional groups which decorate the surface and edges of the graphite sheets. Regardless of the oxidation method, the GO produced contains the same type of functional groups, but their relative and absolute abundance depends on the oxidation conditions, which play the key role in the formation of GO. For example, the carbon-to-oxygen elemental ratio (C/O), which is a measure of the degree of oxidation of GO, depends on the method used (i.e. nature of the oxidant), reaction time, the amount of oxidant, and reaction temperature. **Table 7-1** shows the effect of the difference in graphite oxidation condition on the C/O ratio in graphite oxide. Additionally, the starting material, especially graphite flake size, affects the efficiency of the oxidation.

Method	Oxidant	Reaction media	C/O ratio
Staudenmaier	$KClO_3$	Fuming HNO_3	1.17
Brodie	$KClO_3$	$HNO_3 + H_2SO_4$	-
Hofmann	$KClO_3$	Non-fuming HNO_3	1.15
Hummers	$KMnO_4 + NaNO_3$	Conc. H_2SO_4	0.84
Marcano	$KMnO_4$	$H_2SO_4 + H_3PO_4$	0.74

Table 7-1: Summary of the effect between graphite oxide synthetic methods on the degree of oxidation.

7.1.3.1.   Graphene Oxide Structure

Similar to synthetic methods, the structure of GO has also greatly evolved over time. The complexity associated with preferential oxidation of graphite oxide's aromatic domains, and the defects that accompany it makes predicting the oxidation mechanism of graphite oxide a challenging problem. In addition to this, the possible variability in graphite starting material and its highly amorphous structure makes predicting a structural formula for GO a difficult question to answer. **Figure 7-8** summarises several structural models that have been proposed, with the Lerf-Klinowski perhaps the most wildly accepted.
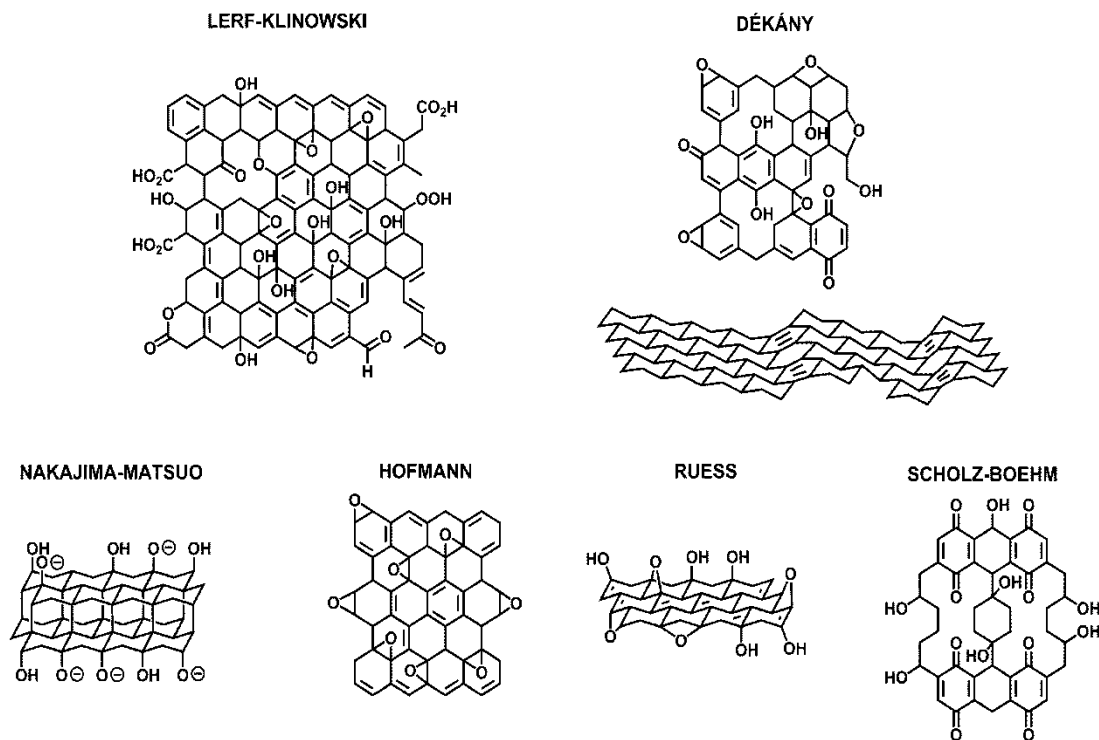
Figure 7-8: Summary of proposed structural models of GO. Reproduced from [382] with permission of The Royal Society of Chemistry.

7.1.4.   Reduction of Graphene Oxide

The main reason for GO's popularity, at least initially, was to synthesise single graphene sheet, due to the remarkable electronic and optical properties of graphene. As discussed earlier, the oxidation of GO destroys the planar sp^2 carbons of graphite and converts them to sp^3 carbons.[80,383] Therefore, the π-electronic conjugation of graphite is destroyed in GO, resulting in a significant decrease in electrical conductivity and makes GO thermally unstable at elevated temperatures.[384] The reduction reaction is utilised to restore or at least partially restore the GO's conjugated system and thus increases the electrical conductivity and thermal stability of GO close to the level of an exfoliated graphene sheet. However, reduced graphene oxide (rGO) does not quite resemble either graphene oxide or graphene but is something in between

these materials. It is moderately hydrophobic but can be dispersed in water to some extent, as well as in several organic solvents. It is a rather good electrical conductor but not as good as graphene. Its mechanical properties are closer to GO than pristine graphene. There are several methods used for the reduction of GO including chemical,[385] thermal,[386] electrochemical,[387] and photochemical methods.[388]

7.1.5.   Surface Functionalisation of Graphene Oxide

The majority of previous graphene based research concentrates on the electronic application of graphene; however, research on the biomedical applications of graphene nanomaterials are only now flourishing.[389,390] This is due to the graphene's high specific surface area which renders it an ideal substrate for high-density biofunctionalisation, facilitating the development of nanomaterial based biomedical applications.[391] However, because graphene based nanomaterials are derived from hydrophobic graphite through chemical or physical modification; their biological and biomedical applications have been hampered by their instability under physiological conditions.[392-396] Therefore, in order to exploit them in such applications, it is critical to establish versatile functionalisation method to provide high dispersion stability of graphene based nanomaterials with biomolecules or bioactive materials. To improve their solubility in physiological media, covalent and noncovalent functionalisation methods have been widely utilised for the preparation of biofunctionalised graphene based nanomaterials.[397]

7.1.5.1. Noncovalent Functionalisation

Pristine graphene sheets are hydrophobic in nature, so they are difficult to dissolve in polar solvents. This makes functionalisation of graphene sheets important for their future applications. The noncovalent interaction of biomolecules with carbon graphene based nanomaterials greatly enhances their structural functionality, making it possible for these hybrids to be used in biological processes. Noncovalent functionalisation of graphene based nanomaterial essentially relies on weak interactions, such as π–π stacking interactions, hydrophobic effects, van der Waals forces, and electrostatic interactions.[80] Thus, it preserves the π-system of graphene and thus its electronic properties. There are various adsorptive sites on graphene nanomaterials surface including flat π–networks, defects, and functional groups attached to the surfaces and edges. According to the Lerf-Klinowski model, the carbonyl and carboxylic groups remain attached to the edges of the GO sheet, while the hydroxyl and epoxy groups are found on the basal plane.[80,371,398] These groups render the GO sheets hydrophilic due to the H-bonding present between the carboxylic and hydroxyl groups. Additionally, they provide sites for noncovalent functionalising through hydrogen bonding with biomolecules. On the contrary, reduced graphene oxide sheets have a very limited number of oxygen-containing functional groups, and thus tend to from aggregates with poor dispersion stability under physiological conditions.[399] Although, rGO planar surface provides a high capacity for hydrophobic interactions with various biomolecules, it has a tendency to agglomerate irreversibly due to its strong hydrophobicity, or even to restack into graphite through van der Waals interactions in the absence of stabiliser.[166,400-405] Therefore, there is a great challenge for using rGO for biological and biomedical

applications. However, their surface modification with biomolecules has been used to stabilise and improve their utility under physiological conditions. Various biomolecules have been reported to be integrated with graphene based nanomaterials, such as proteins, nucleic acids, cells, bacteria, and so on, as illustrated in **Figure 7-9**.
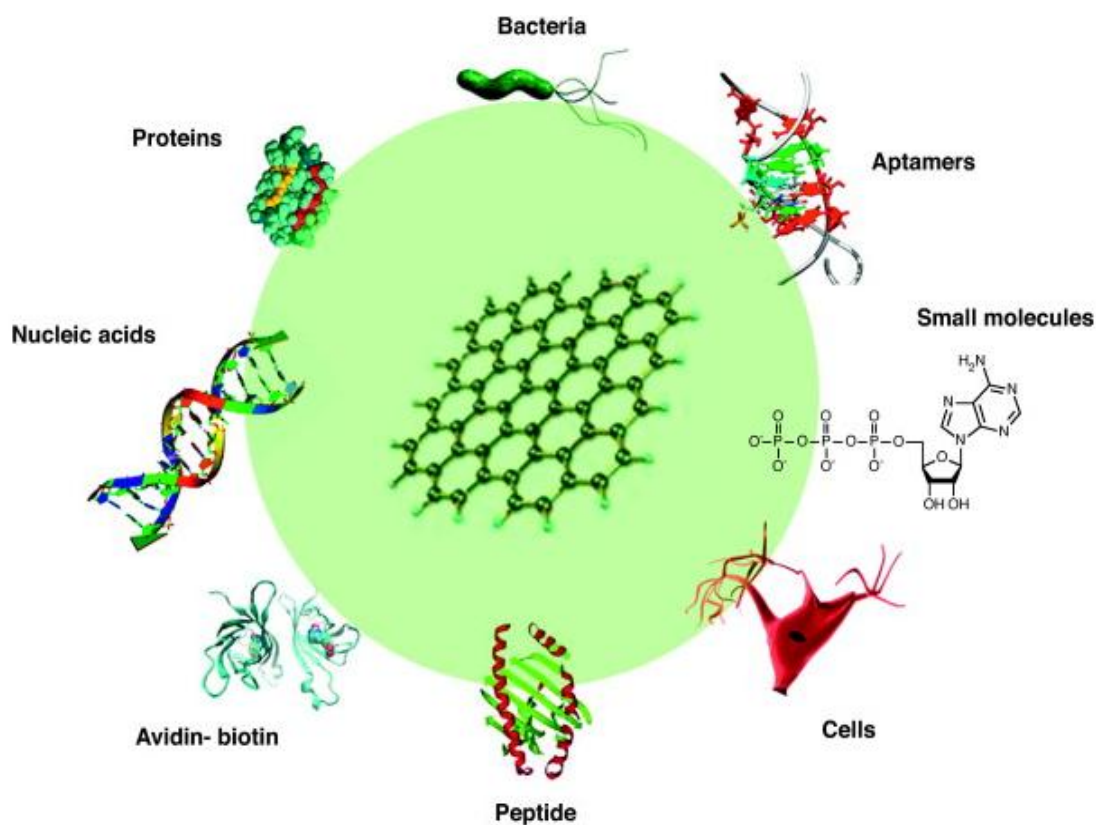
Figure 7-9: Biofunctionalisation of graphene based nanomaterials. Reprinted from [406], Copyright (2011), with permission from Elsevier.

7.1.5.1.1. Peptide and Protein

As a result of their varied surface functional groups and secondary structure, peptides and proteins can exfoliate and modify graphene based nanomaterials through physical adsorption. Amino acids,[407,408] peptides[409,410] and proteins[411] bind to the planar or edge of graphene via π–π stacking or electrostatic interactions. The

aromatic residue in amino acids, peptides or proteins can adsorb onto graphene and reduced graphene oxide (rGO) by π–π stacking. On the other hand, their noncovalent interaction with GO is based on the electrostatic interaction between charged or polar residues in amino acids, peptides and proteins with the oxygen containing groups of GO.

π–π stacking is an attractive interaction between aromatic rings, especially carbon nanomaterials and aromatic groups. A previous study investigated the interaction of aromatic amino acids (Phe, His, Tyr, and Trp) with graphene, suggested that the aromatic rings of the amino acids prefer to orient in parallel with respect to the plane of the graphene sheet, the so-called π–π interactions. Remarkably, the polarisability of the aromatic ring and the strength of the interaction are highly correlated: the higher the polarisability is, the greater the binding strength is, following the trend: His < Phe < Tyr < Trp. They also found that the binding strength with CNTs was weaker than that with the graphene sheet, which may be associated with the surface curvature.

Hydrophobic interactions are another important contribution to proteins and peptides interaction with graphene based nanomaterials. Hydrophobic interactions tend to minimise the non-polar surface, by clustering hydrophobic groups to avoid exposure to hydrophilic media. Since graphene based nanomaterials have large hydrophobic areas, they tend to bind to the partially exposed non-polar residues of proteins and peptide. For example, Kowalewski et al.[412] reported that on hydrophobic graphite surfaces, the Alzheimer's amyloid β-peptide (Aβ) forms uniform, elongated β-sheet, whereas less-ordered particulate aggregates appear both at hydrophilic mica and positively charged surfaces. Sheng et al.[413,414] used molecular dynamics simulations

(MD) to study the interaction between ionic complementary peptide EAK16-II (AEAEAKAKAEAEAKAK) on the hydrophobic surface of graphene. They found that the hydrophobic interaction is the main force to govern the peptide adsorption, and the inter-peptide electrostatic interaction affects the adsorption rate. Guo *et al.*[415] investigated by density functional theory the interaction between carbon nanostructures with tripeptide arginine-glycine-aspartic acid. Their results revealed that GO has a stronger interaction with tripeptide than the pristine and the defective graphene because of oxygen-containing functional. The oxygen-containing functional groups are able to form hydrogen bonds with the functional groups of tripeptide. The comparison of its interaction on the GO model with OH, epoxy, and mixed OH/epoxy groups reveals that different oxygen-containing functional groups have distinguishing binding ability with tripeptide. While Chen *et al.*[416] prepared biocompatible and stable rGO suspension by using L-lysine amino acid as a reducing agent and sodium cholate as a stabiliser.

The hydrophobic interaction between proteins and peptide with graphene based nanomaterials usually unfolds the protein's and peptides' native structure.[417-419] This is probably due to the fact that the hydrophobic graphene based nanomaterials bind more tightly with unfolded proteins, which have more hydrophobic residues exposed than the native proteins and peptides. Moreover, it was found that graphene may possess a higher capability than CNTs to break α-helices due to proteins and peptides are more favourable surface curvature.[309] Peptides adsorption on graphitic nanomaterials changes the physiochemical properties of both the proteins and the graphitic nanomaterials, leading to an alteration of their properties.[420] Peptides and proteins are more flexible than graphitic nanomaterials. During the interaction

process, graphitic nanomaterials surface disturbs the native structure of peptides and proteins as well as their self-assembly pathway.[421,422] Since peptides and proteins biological activity is influenced by their secondary structure, these conformational changes, could lead to the loss of function (e.g. enzyme activity). Therefore, resolving the peptide's structure upon their interaction with graphene like nanomaterials is fundamentally important for their application.[423] Molecular dynamics simulations has been used in elucidating the structure of adsorbed biopolymers at carbon nanomaterials surfaces, thereby enabling a deeper understanding of the connections between biopolymers' structure and carbon nanomaterial geometry. It is evident from the MD simulations on adsorption of peptides and proteins depend mainly upon the size, curvature and surface chemistry of CNTs and graphene oxides.[424,425] Zuo *et al.*[426] studied the adsorption of protein villin headpiece (HP35) on graphene using large scale molecular dynamics simulations (**Figure 7-10**). Their results indicated that the π–π stacking interactions between the graphene and HP35's aromatic residues play a key role in this adsorption.
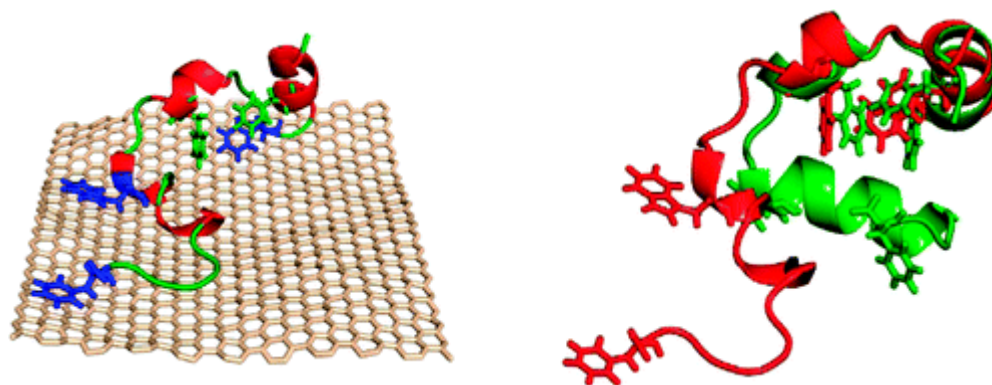
Figure 7-10: (**Left**) A typical structure of HP35 adsorbed on the graphene surface. Here, HP35 is shown as a cartoon with red helix and green loop, the graphene is shown as the cyan lines. (**Right**) The superposition of the adsorbed HP35 structure on graphene (red) with its native structure (green). Reprinted with permission from [426]. Copyright (2011) American Chemical Society.

Radic *et al.*[427] used rapid discrete-molecular-dynamics simulations to examine the binding of graphene and graphene oxide with peptides, fatty acids, and cellulose. Their simulations revealed that the amphiphilicity of cellulose, peptide and palmitic acid, owing to their differences in hydrocarbon content, conformational flexibility, and molecular geometry, displayed distinct binding affinities for the graphene derivatives. Katoch *et al.*[428] used atomic force microscopy (AFM), Raman spectroscopy, fourier transform infrared (FTIR) spectroscopy, and molecular dynamics simulations to investigate the dodecamer peptide (GAMHLPWHMGTL) binding behaviour to graphene and graphite (**Figure 7-11**). FTIR spectra of the adsorbed peptide on graphene indicate that the peptide's helical structure is disrupted upon the interaction with graphene surface.
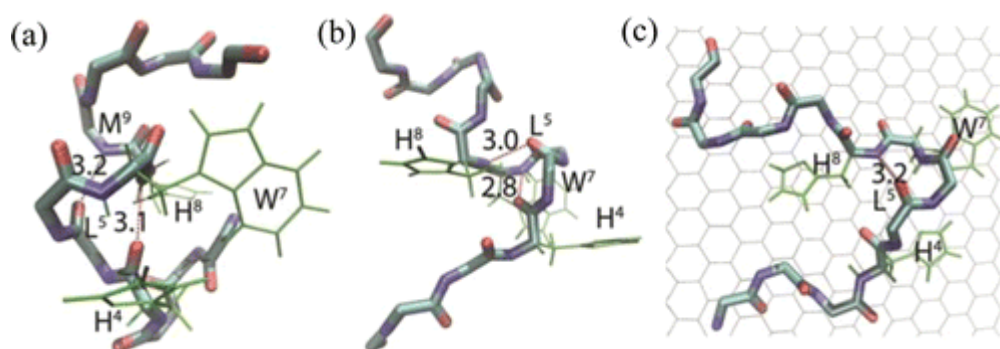
Figure 7-11: Molecular dynamics based structure of the dodecamer peptide (**a**) in vacuum, (**b**) in water, and (**c**) on a graphene sheet. Reprinted with permission from [428]. Copyright (2012) American Chemical Society.

Guo *et al.*[429] studied the effect of planarity of graphene on protein conformations. Their results indicate that β-sheet-rich proteins have almost no loss of secondary structures upon interaction with graphene, while α-helical proteins involves a partial loss of α-helices upon interaction.

7.1.5.1.2. Enzymes

Like proteins, enzymes are long, linear chains of amino acids that fold to 3D structures. Immobilisation of enzymes on certain solid substrate is an efficient way to improve their performance. Among a range of materials that have been employed as solid matrixes for enzyme immobilisation, graphene or GO seems to be an ideal choice with the unique 2D structure, flat plane, tunable functionalities, structural characteristics. GO used as a matrix for enzyme immobilisation was first reported by Zhang *et al.*[430,431] They studied the noncovalent interaction between horseradish peroxidase (HRP) and lysozyme molecules onto GO. By varying the immobilisation conditions for both HRP and lysozyme, they demonstrated that the HRP and lysozyme immobilisations on the GO were dominated by the electrostatic interaction between negatively charged GO sheets and enzyme molecules. Moreover, the flat surface of GO makes it possible to observe the native immobilised enzyme in situ with AFM, as shown in **Figure 7-12**.
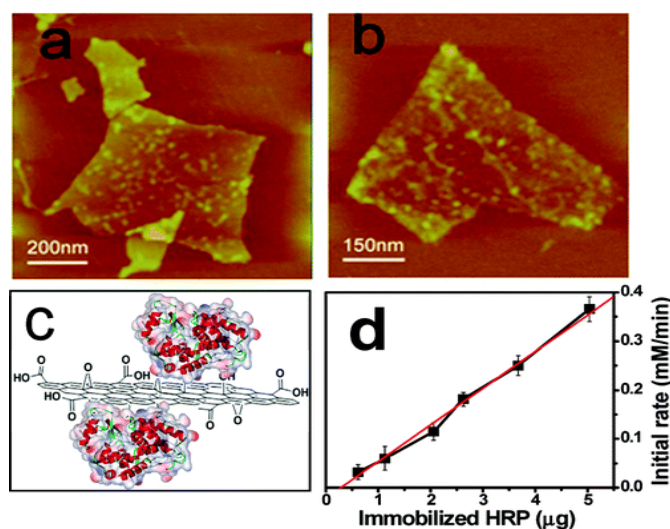
Figure 7-12: AFM images of the GO-bound HRP with (**A**) lower and (**B**) higher enzyme loadings acquired in a liquid cell. (**C**) Schematic model of the GO-bound HRP. (**D**) Initial reaction rates of GO-bound HRP vs. HRP concentration. Reprinted with permission from [430]. Copyright (2010) American Chemical Society.

The electrostatic interactions between enzyme molecules and GO are complicated because the charge status of the surface functional groups of the enzyme depends strongly on the environmental conditions. Additionally, surface density of the oxygen-containing functional groups on the GO are varied with the preparation procedure and storage conditions. Therefore, different enzymes could exhibit different enzyme loadings and stabilities on the GO.[361] Zhang *et al.*[432] studied the possibility of hydrophobic interactions between rGO and two model enzymes, HRP and oxalate oxidase (OxOx). Their result implied that the interaction between the enzymes and rGO is dominated by the hydrophobic interaction. Furthermore, the results indicate that the hydrophobic interaction between the enzymes and rGO is stronger than the electrostatic interaction between the enzymes and GO (**Figure 7-13**).
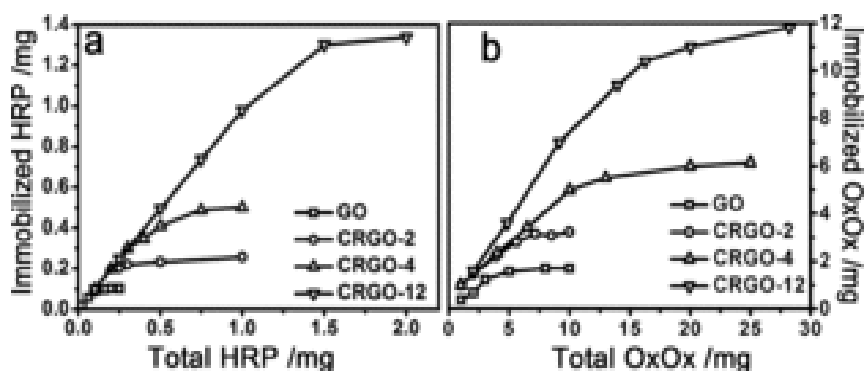
Figure 7-13: HRP (**A**) and OxOx (**B**) loadings on GO and CRGO as a function of the total amount of enzyme. GO and CRGO weights are all 1 mg. Reproduced from [432] with permission of John Wiley and Sons.

7.1.5.1.3. DNA

The large 2D aromatic surface of graphene makes it an ideal substrate for adsorption of DNA. The DNA molecule and graphene sheet are ideal nanostructures to fabricate novel nanobiohybrid materials to construct highly sensitive nanobioelectronic devices including sensors and chips.[433,434] Furthermore, the adsorption of DNA on an electrode surface may lead to new approaches to deliver drugs in DNA grooves.[435-437] Wu *et al.*[438] investigated the noncovalent interaction between GO and DNA. They found that the adsorption of DNA on GO is affected by several factors, such as cations, pH, organic solvent and temperature. Generally, shorter DNA binds to the surface with faster kinetics and higher adsorption efficiency. However, by adding c-DNA to form double-stranded (dsDNA) and increasing temperature, desorption can occur, as shown in **Figure 7-14**.
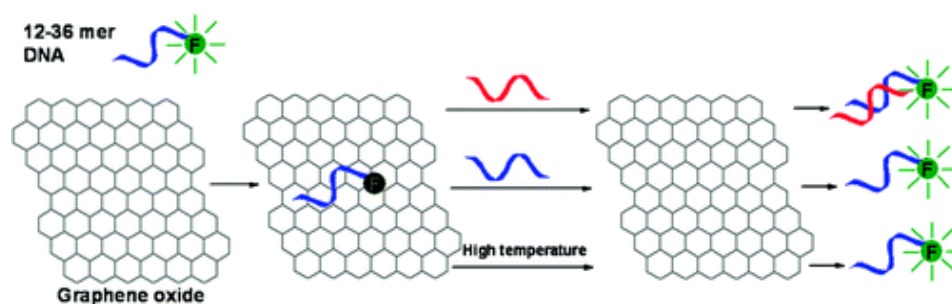
Figure 7-14: Dye labelled DNA adsorption and desorption on GO. Reprinted with permission from [438]. Copyright (2011) American Chemical Society.

Lu *et al.*[439] demonstrated the ability of water-soluble GO as a platform for the sensitive and selective detection of DNA and proteins. **Figure 7-15** shows a schematic representation of this detection platform.
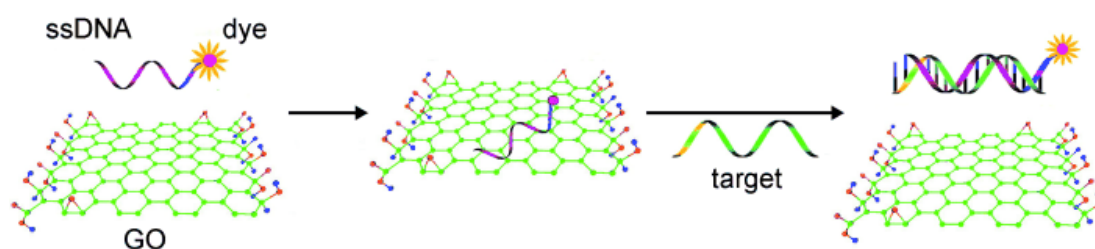
Figure 7-15: Schematic representation of the target-induced fluorescence change of the ssDNA-dye-GO complex. Reproduced from [439] with permission of John Wiley and Sons.

The fluorescence emission indicated that the GO noncovalent interaction with dye-labelled ssDNA completely quenches the fluorescence of the dye (**Figure 7-15**). However, in the presence of a target, the binding between the dye-labelled DNA and target molecule altered the conformation of dye-labelled DNA, and disturbed the interaction between the dye-labelled DNA and GO. This feature could result in a fluorescence-enhanced detection system that is sensitive and selective to the target molecule. On the other hand, GO scarcely interacts with the rigid structure of dsDNA probably due to the efficient shielding of nucleobases within the negatively charged phosphate backbone of dsDNA.[440] Thus, according to the fluorescence quenching of DNA-GO complex, Huang *et al.*[441] found that GO can selectively remove ssDNA from dsDNA with a simple mixing and centrifugation operation as shown in **Figure 7-16**.
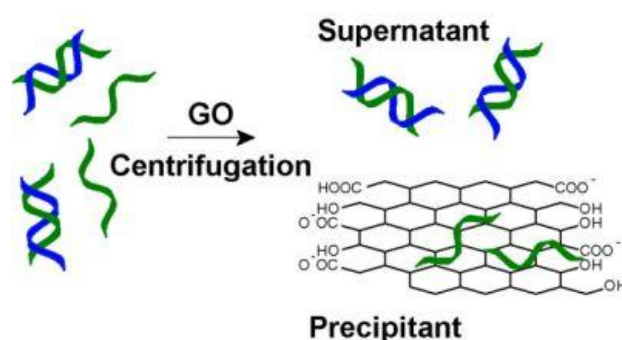
Figure 7-16: GO-based selective removal of ssDNA. Reprinted with permission from [441].

7.1.5.1.4. Small Molecules

The interaction of graphene with DNA, nucleobases, and nucleosides has potential medical and industrial applications. Several experimental and computational studies have focused on studying the binding of different nucleosides and their derivatives on graphene like materials. In computational studies, Antony et al.[442] calculated the interaction energy of DNA nucleobases with graphene with the dispersion-corrected density functional theory method and obtained the order guanine > adenine > thymine > cytosine. Vovusha et al.[443] studied the interaction of nucleobases and aromatic amino acids with graphene and graphene oxide (GO) by ab initio density functional theory. Their results indicated that GO complexes are stabilised by hydrogen bonding interactions whereas graphene complexes are stabilised by π–π interactions, leading to enhanced binding energies for GO complexes compared to G complexes (**Figure 7-17**). Similar observations were found by Xu et al.[444]
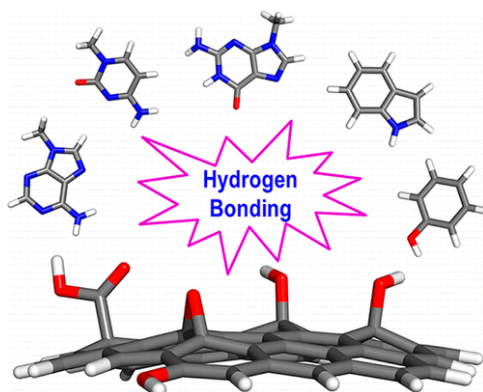
Figure 7-17: The hydrogen bonding between nucleobases and graphene based nanomaterials. Reprinted with permission from [443]. Copyright (2013) American Chemical Society.

Single solute adsorption isotherm study of DNA nucleobases at the graphite-water interface showed that the adsorption strength to vary guanine > adenine > thymine >

cytosine.[445] Similar calculations suggested that cytosine has a very weak interaction with graphene surfaces.[446] It is interesting to note that the majority of studies shown that nucleobases and nucleosides binding to graphene surface depend on π–π interactions. However, work by Spiwok *et al.*[447] showed that nucleobases interaction with graphene form hydrogen-bonded complexes in vacuum but prefer π–π stacking in partially and fully solvated systems as shown in **Figure 7-18**.
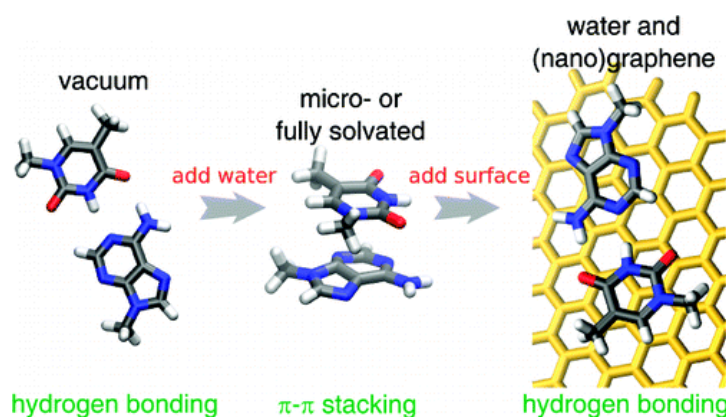
Figure 7-18: Interaction between nucleobases and nucleosides. Reprinted with permission from [447]. Copyright (2011) American Chemical Society.

Theoretical and AFM measurements show that nucleobases bind to graphene more strongly through π–π stacking as well as hydrogen bonding interaction.[448] Varghese *et al.*[329] carried out experimental investigation to study the binding of nucleobases and nucleosides with graphene using isothermal titration calorimetry (ITC). They found that the relative interaction energies of the nucleobases decrease in the order guanine > adenine > cytosine > thymine in aqueous solutions. The studies on the effect of carbon nanomaterials topography on the noncovalent interaction show that the curvature of the nanomaterial has a strong influence on their noncovalent interaction.[449,450] Umadevi *et al.*[330] studied interaction of graphene and CNTs of

different radius with the nucleobases using dispersion-corrected DFT based approach and observed that the binding energy depends on the curvature of the nanomaterial.

7.1.5.2. Covalent Functionalisation

Compared to the noncovalent modification of graphene, the covalent approach offers the advantage of achieving permanent stabilisation of the functionalised graphene sheets.[451] Furthermore, it provides the opportunity to impart aqueous solubility, processability, and biocompatibility to graphene.[452] However, the main drawback of this approach is that it is associated with destroying the sp^2 of the π network into a sp^3 configuration leading to a partial or total loss of π–π conjugation. As a consequence, the intrinsic physical, chemical and electronic properties could be altered considerably.

The covalent functionalisation of graphene oxide is the most exploited method for the connection of solubilising bioactive moieties to graphene surface. Therefore, lots of effort has been made towards constructing hybrids of biological and carbon nanocomposites due to their paramount importance in both biosensing and drug delivery.[453]

Because of the one-atom-thick flat sheet nature of graphene, the chemical reactivity of this carbon nanoform may occur on the π surface and/or on the edges.[454] On the basal plane, sp^2 hybridisation of carbon leads to a strong covalent bonding as well as to delocalisation of the π electrons. Therefore, the covalent interaction of the basal plane leads to modification of the π–π conjugation and thus the electron density

distribution and the physical and chemical properties. The carbon atoms in the basal plane are protected by their π–conjugation system.[453] Thus, during the covalent addition, the basal carbon has to protrude outward from the plane to adopt a tetrahedral sp^3 geometry, causing strain in the plane. Therefore, their covalent modification usually encounters large energy barriers.[455] On the other hand, the edge of graphene oxide can undergo reaction with low energy barriers as their sp^3 hybridisation have a tetrahedral geometry thus does not imply additional strain for the basal carbon atoms.[391,453,456] Therefore, edge carbon atoms are preferred in covalent addition reactions.

Different techniques have been explored for the covalent derivatisation of GO, but this section will concentrate in the covalent modification of GO related to the preparation of materials for biological purposes, which mainly involve esterification, and amidation of the carboxyl groups.[457,458] Addition of nucleophilic species, amines or hydroxyls, produce covalently attached functional groups to GO via the formation of amides or esters often require activation of the carboxylic acid group either by converting it to acid derivatives via the acyl chloride or by using coupling activators.[459-461] **Figure 7-19** shows the direct and indirect coupling leads to the formation of ester and amide bonds. In the indirect route for esterification and amidation that utilises $SOCl_2$, GO is typically exfoliated in relatively non-nucleophilic solvents and then refluxed with a large excess of the chlorinating agent, followed by the addition of a nucleophile. While the direct route involves utilising coupling agents, including such as 1-ethyl-3-(3-dimethylaminopropyl)- carbodiimide (EDC), *N,N′*-dicyclohexylcarbodiimide (DCC), or 2-(7-aza-1H-benzotriazole-1-yl)-1,1,3,3-tetramethyluronium hexafluorophosphate (HATU), GO is first exfoliated in a

polar solvent (typically DMF or NMP) and then treated with a catalytic amount of

N,N-dimethylaminopyridine (DMAP), N-hydroxysuccinimide (NHS), or another

carboxylic acid activator. Subsequent addition of nucleophilic species, such as

amines or hydroxyls, produce covalently attached functional groups to graphene

oxide platelets via the formation of amides or esters.[80]
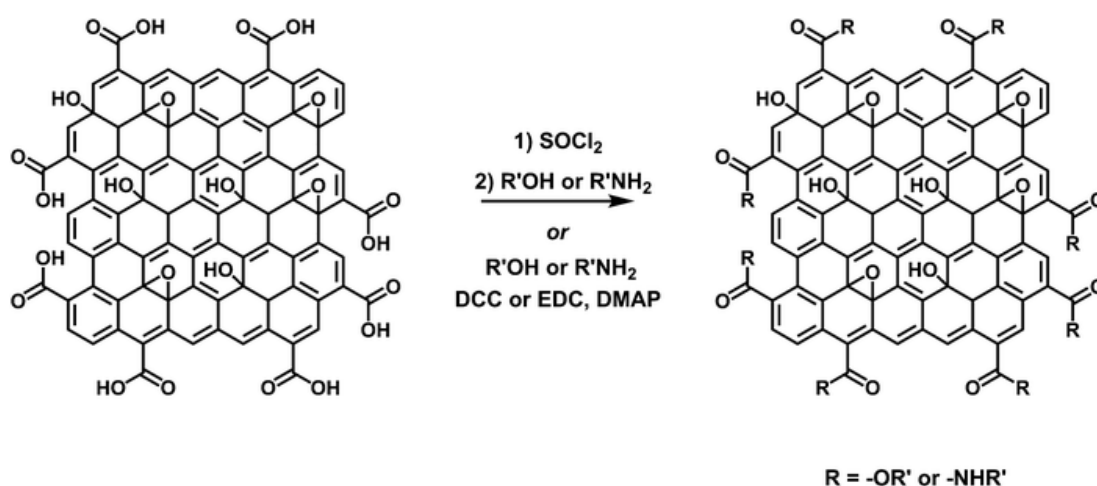
Figure 7-19: Activation of GO's peripheral carboxylic acid groups with either SOCl$_2$ or a coupling agents, and subsequent condensation with an alcohol or an amine. Reproduced from [382] with permission of The Royal Society of Chemistry.

7.1.5.2.1. Amidation

On GO, amidation proceeds mainly through the reaction between the -COOH group

native to GO and the -NH$_2$ group of the functional molecule, or vice versa. Various

NH$_2$ terminated functional groups have been anchored onto graphene. He *et al.*[462]

reported the synthesised GO-Fe$_3$O$_4$ hybrid in a two-step process. In the first, Fe$_3$O$_4$

was modified by tetraethyl orthosilicate and (3-aminopropyl) triethoxysilane to

introduce amino groups on its surface. Then, with the aid of N-hydroxysuccinnimide

(NHS) and 1-ethyl-3-(3-dimethyaminopropyl)carbodiimide (EDC), GO-Fe$_3$O$_4$ hybrid

was obtained from the condensation reaction between amino group of Fe$_3$O$_4$ and

carboxylic group of GO. The synthesis process of GO-Fe$_3$O$_4$ hybrid is schematically illustrated in **Figure 7-20**.
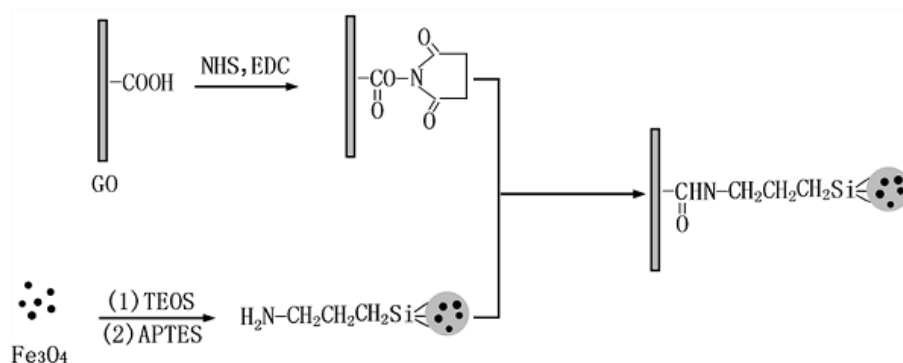
Figure 7-20: Schematic of the fabrication of GO-Fe$_3$O4 hybrid. Reprinted from [462], Copyright (2010), with permission from Elsevier.

The synthesised hybrids not only have great potential as an effective absorbent for removing cationic dyes in water, but also could be used to prepare rGO–Fe$_3$O$_4$ hybrids and magnetic GO films, which is suitable for many other applications such as fabrication of functional polymer composites, sensors, heterogeneous catalysts, and drug delivery.

Similarly, Shen *et al.*[461] studied the functionalisation of GO with biomaterials, including adenine, cystine, nicotamide and ovalbumin (OVA) through diimide-activated amidation. The process used in this study involved two steps, firstly carboxylic acid groups on GO were activated by N-ethyl-N′-(3-dimethylaminopropyl)carbodiimide hydrochloride (EDAC) with stable active ester formed by the addition of N-hydroxysuccinimide (NHS). Second, the active ester was reacted with the amine groups on biomaterials, forming an amide bond between GO and biomaterials (**Figure 7-21**).
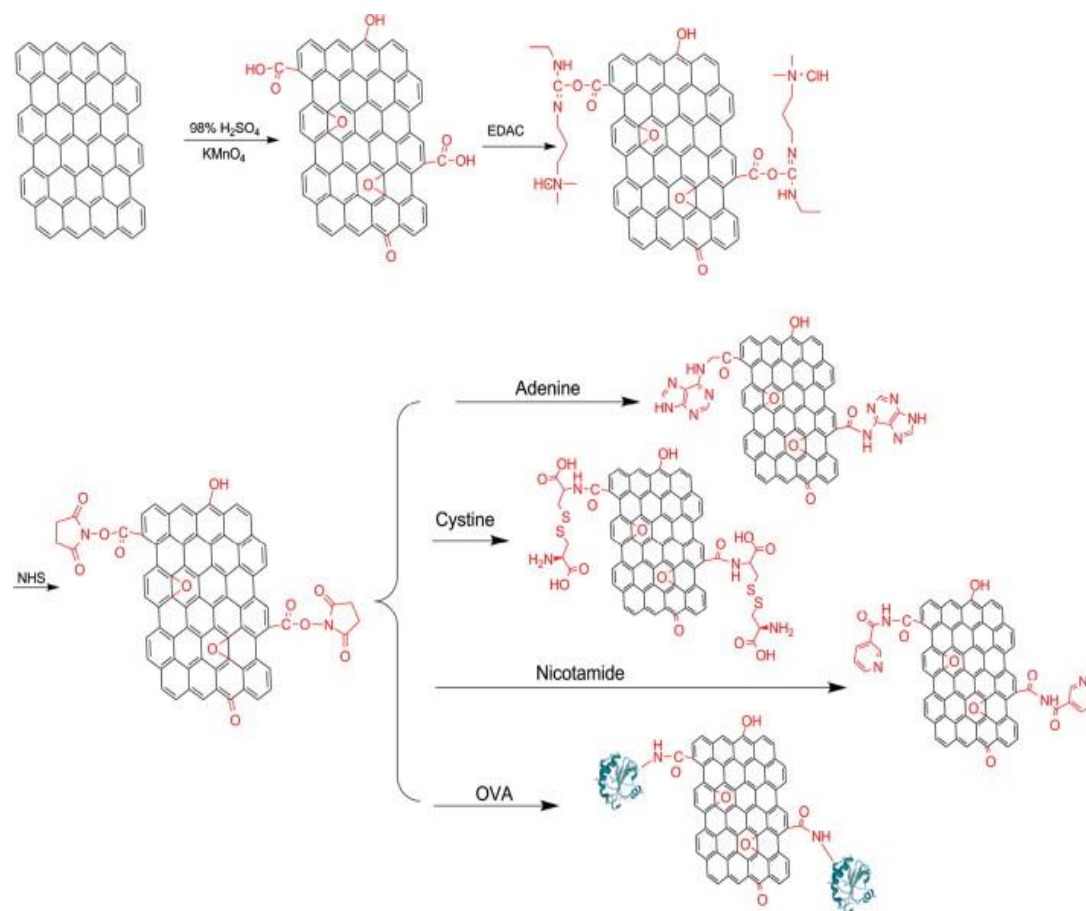
Figure 7-21: A Schematic diagram to produce GOS-based biocomposites. Reprinted from [461], Copyright (2011), with permission from Elsevier.

Mungse *et al*.[463] developed a chemical approach for selective inclusion of long alkyl chains on the edges and defects sites of reduced graphene oxide sheets through the amide linkage. The carboxylic functionalities, which were selectively introduced in the rGO by mild oxidation, were converted into acyl chlorides using thionyl chloride. Subsequently, the acylated-rGO sample was reacted with octadecylamine (ODA). Presence of long alkyl chains in the ODA-rGO sheets facilitated their stable dispersion in commercial engine oil, which is very important for their efficient tribological performance. Using the same amidation technique, Chu *et al*.[464] grafted CdTe nanorods on a GO surface through an amidation reaction between acyl

chlorides of GO and amino groups of the L-cysteine capped CdTe nanorods (**Figure 7-22**). The intrinsic optical properties of the GO–CdTe hybrid material may make a promising candidate for graphene- and GO-based materials in optoelectronic applications.
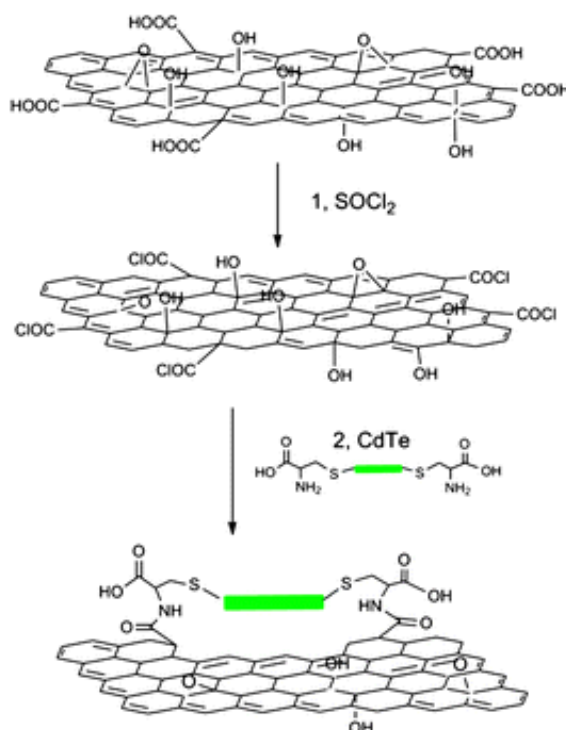
Figure 7-22: Synthesis procedure of GO–CdTe hybrid materials through the amidation reaction**. Reproduced from [464] with permission of The Royal Society of Chemistry.

Liu *et al*.[94] and Sun *et al*.[465] reported the synthesis of PEGylated nano-GO conjugate via carbodiimide catalysed amide formation for delivery of water-insoluble cancer drugs and found that the functionalised graphene sheets are biocompatible and stable in various biological solutions without obvious toxicity (**Figure 7-23**).
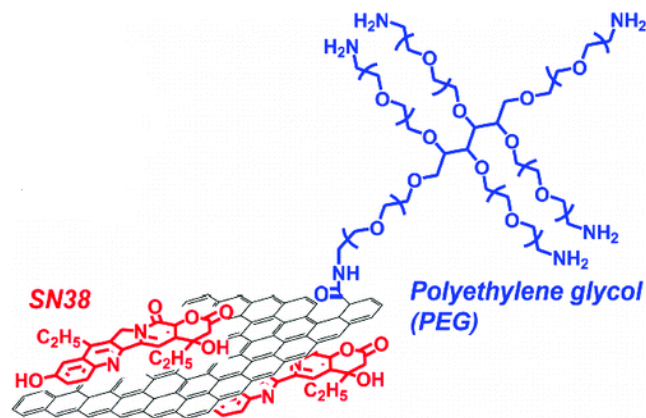
Figure 7-23: Schematic draw of cancer drug (SN38) loaded NGO-PEG. Reprinted with permission from [94]. Copyright (2008) American Chemical Society.

Sun *et al.*[465] explored first the properties of PEGylated NGO for cell imaging. Amine-terminated PEG stars (6-armed branched PEG molecules) were grafted onto NGO sheets via carbodiimide activation chemistry by formation of amide bonds. The resulting functionalised NGO exhibited intrinsic photoluminescence in the near-infrared range (NIR), providing a NIR probe for cellular imaging. They further conjugated PEG-NGO to a B-cell specific antibody, Rituximab, to selectively recognize and bind B-cell lymphoma, proving selective targeting (**Figure 7-24**).
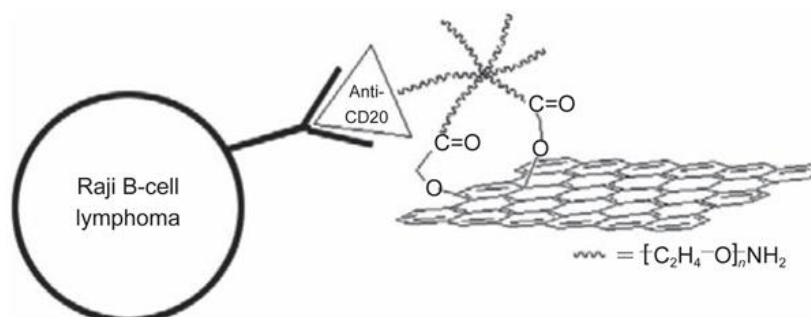
Figure 7-24: A schematic drawing illustrating the selective binding and cellular imaging of NGO–PEG conjugated with anti-CD20 antibody, Rituxan. Reprinted with permission from [465].

Later on, Yang *et al.*[466] investigated the in vivo behaviour of NGO by labelling PEG-NGO with Cy7, a commonly used NIR fluorescent probe, via amide bond. Their vivo fluorescence imaging revealed a remarkably high tumour uptake of NGO, and PEGylated NGO showed efficient tumour passive targeting and relatively low retention in the reticulo-endothelial system (RES). Irradiation of tumour-bearing mice with a low-power NIR laser led to complete ablation of the tumour (**Figure 7-25**) showing the potential of graphene derivatives for in vivo PTT.
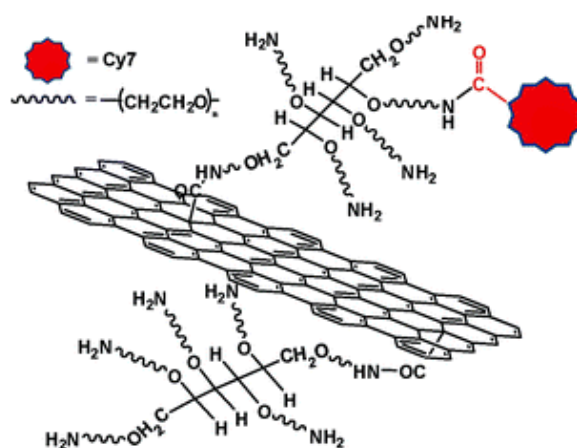
Figure 7-25: NGS with PEG functionalisation and labelled by Cy7. Reprinted with permission from [466]. Copyright (2010) American Chemical Society.

Ali *et al.*[467] combined between the direct and indirect amidation techniques for the synthesis of antiapolipoprotein B 100 functionalised-aminated reduced graphene oxide or detection of low density lipoprotein (LDL or lipid) cholesterol. In the first step, the carboxylic groups introduced to rGO were converted into acyl chlorides using thionyl chloride. Subsequently, acylated-rGO sample was reacted with ethyleendiamine (EDA). Then, the NH_2-rGO covalently functionalised with

antiapolipoprotein B 100 using EDC/NHS coupling chemistry detection of low

density lipoprotein (LDL or lipid) cholesterol (**Figure 7-26**).

Figure 7-26: Apo-lipoprotein B 100 functionalisation on an NH_2-rGO sheet for LDL detection. Reprinted with permission from [467]. Copyright (2014) American Chemical Society.

7.1.5.2.2. Esterification

The presence of -COOH groups native to graphene renders their functionalisation

with CH_2OH-terminated functional groups feasible, i.e., esterification. There are a

number of studies addressing this process.[459,468,469] Yang *et al.*[470] covalently grafted

polysaccharides (hydroxypropyl cellulose and chitosan) onto graphene oxide by

simple esterification reactions. The oxidation introduced carboxyl groups in

graphene oxide were then converted into acyl chloride with thionyl chloride ($SOCl_2$).

Subsequently, hydroxypropyl cellulose or chitosan was covalently grafted onto the

activated graphene oxide through esterification reactions. The polysaccharide-

functionalised graphenes have potential applications in biological and medical fields,

such as drug delivery, transplant device, and biosensors. Namvari *et al.*[471] synthesised a magnetic nanocomposite of citric-acid-functionalised GO which acts as an efficient adsorbent to remove methylene blue from (MB) contaminated water. The peripheral carboxylic acids of GO were converted into acyl chloride by treating GO with thionyl chloride. Citric acid (CA) was covalently grafted onto the GO through a simple esterification reaction. Then, Fe_3O_4 magnetic nanoparticles (MNPs) were chemically deposited onto the GO-CA hybrid. The hybrid surface was negatively charged, thus the nanocomposite had a high adsorption capacity with the cationic MB. The high adsorption capacity accompanied by the ease of separation by an external magnetic field makes the synthesised nanocomposite a powerful separation tool to be utilised in wastewater treatment. Salavagione *et al.*[472] employed two synthetic strategies for grafting poly(vinyl alcohol) (PVA) on G, as shown in **Figure 7-27**. The first involves the direct esterification of GO in presence of the N,N′-dicyclohexylcarbodiimide (DCC) and 4-dimethylaminopyridine (DMAP) catalyst, while the second goes through converting GO into acid chloride by reacting with $SOCl_2$, followed by coupling with hydroxyl group of PVA. They found that covalent linkages between the GO and the PVA are responsible for remarkably altering the crystallinity and thermal stability.
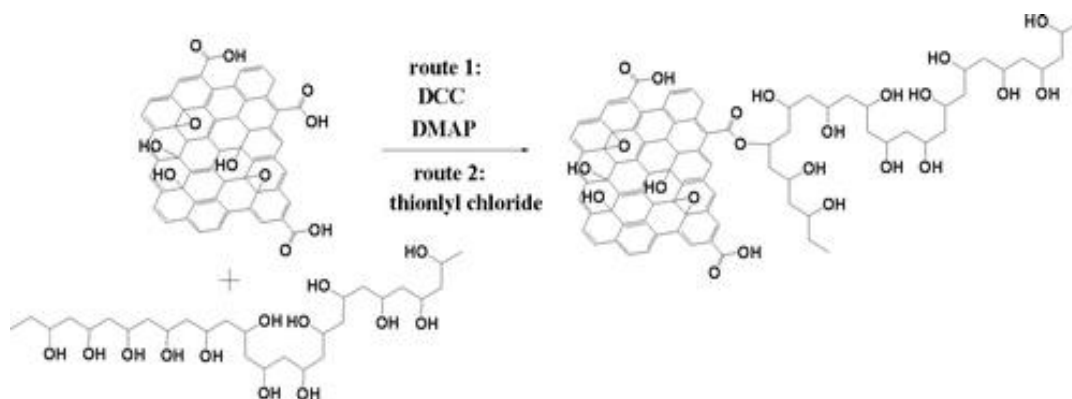
Figure 7-27: Esterification of Graphite Oxide with PVA. Reprinted with permission from [472]. Copyright (2009) American Chemical Society.

Yu *et al.*[473] reported functionalisation of GO with $-CH_2OH$ terminated regioregular poly(3-hexylthiophene) (P3HT) through the formation of ester bonds with the carboxyl groups of GO nanoplatelets. The resultant P3HT-grafted GO sheets (G-P3HT) possess good solubility in common organic solvents.

Recently, Liu *et al.*[458] reported the grafting of hydroxypropyl cellulose (HPC) on GO through the esterification reaction in the presence of EDC-HCl and DMAP. HPC-based materials are useful in removing dyes from aqueous solutions. However, one of the main limitations in the practical use of HPC hydrogel is their relatively small adsorption capacity. Results shows that the incorporation of GO into HPC hydrogel exhibited shows a higher adsorption capacity toward methylene blue compared with pure HPC hydrogel.

7.2. **Results and Discussion**

The objective of the present study is to study the covalent and noncovalent functionalisation of rGO with biomolecules, specifically peptide, peptoid, and ribonucleosides. The noncovalent functionalisation of rGO investigates the impact of the difference in secondary structure of biopolymers (peptides and peptoids) on their interaction with rGO. The covalent functionalisation sections studies the functionalisation of rGO with cell penetrating peptoid and ribonucleosides to improve its solubility in water.

7.2.1. **Noncovalent Functionalisation of Reduced Graphene Oxide (rGO) with Nano-1 Peptides**

The presence of a large number of hydrophilic oxygen-containing functional groups allows GO sheets to readily form stable suspensions in water for several weeks without any visible precipitation.[383] However, the dispersibility of rGO is very low and it tends to agglomerate and sediment, therefore hampering further processing of the material.[474]

To better exploit bio-nanotechnology applications it is necessary to gain greater understanding of the structure-property relationships of biomolecules at graphitic surfaces. The main objective of this section is to study the interaction between rGO and helical nano-1 peptides to study the effect of a peptide's aromatic content on rGO dispersion in water.

7.2.1.1.   Synthesis of Graphene Oxide and Reduced Graphene Oxide

In order to study the interaction of nano-1 peptides with rGO, graphite oxide was first synthesised by the Hummers method.[380] The graphite oxide was probe sonicated for 40 min in an ice bath to exfoliated it and afford GO. Reduced graphene oxide (rGO) was formed by reduction with hydrazine monohydrate ($N_2H_4. H_2O$), which generates reduced graphene oxide (rGO). GO and rGO were characterised by Raman spectroscopy, and TGA (**Appendix D**).

7.2.1.2.   Synthesis of Nano-1 Peptides

The degree of folding of a peptide designed to form a helical structure depends on its sequence and length.[191,206] Therefore, in order to investigate the role of peptide aromatic content on rGO dispersion, two versions of nano-1 peptide have been synthesised (see **Chapter 4**, **Section 4.2.1**). The two versions of nano-1 peptide vary in the number of aromatic residues on the hydrophobic surface of the helix, and have a different helicity.[120] **Table 7-2** shows the nano-1 peptides sequence used in the dispersion of rGO.

Peptide	Sequence
Nano-1 (**4**)	Ac-NH-EVEAFEKKVAAFESK VQAFEKKVEAFEHG-CONH$_2$
Short Nano-1 (**6**)	Ac-NH-EVEAFEKKY- CONH$_2$

Table 7-2: Nano-1 peptides sequence.

7.2.1.3. Dispersion of Reduced Graphene Oxide with Nano-1 Peptides

This section aims to compare the quality of rGO dispersion where two versions of nano-1 peptide are used as a dispersant. To make such a comparison all dispersions have been processed at identical concentrations. In all cases the peptide dispersed rGO solutions were mixed by probe sonicating the peptide solution (1.0 mL, 1.0 mM) with rGO (1.0 mg). During the sonication, the provided mechanical energy overcomes the van der Waals interactions between rGO sheets and leads to rGO sheet exfoliation, whereas at the same time the peptide molecules adsorb onto the rGO surface, inhibiting their reaggregation. As this process continues, eventually the rGO sheets are exfoliated and become coated by peptide. Any uncoated rGO sheets reaggregate and are expected to be heavier than exfoliated sheets, thus having a faster sedimentation rate. Thus upon mixing rGO with the peptide, the solution contains both well dispersed and sedimented rGO. The centrifugation process accelerates the separation of inefficiently dispersed and sedimented rGO from stable and well dispersed rGO. Thus, the supernatant phase contains the well-dispersed and mostly exfoliated rGO which is then taken for UV-Vis-NIR absorbance measurement to determine the concentration of rGO present in solution in each case. **Figure 7-28** shows an image of rGO dispersions after sonication and centrifugation with the two versions of nano-1 peptide in water, together with unmodified rGO as a reference. As the carbon nanomaterials disperse, the solution will becomes darker. Therefore, solely based on the supernatant color intensity of unmodified rGO (clear), short nano-1(**6**)/rGO (gray), and nano-1(**4**)/rGO (dark gray), it can be indicated that the amount of solubilised rGO appears to have increased with an increasing number of aromatic amino acids in the peptide sequence.
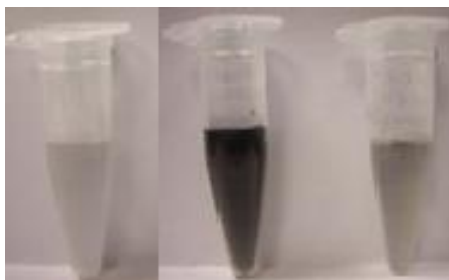
Figure 7-28: A visual comparison of the aqueous supernatant of rGO dispersion with nano-1 peptides. Dispersion from left to right: H$_2$O/rGO (control), nano-1(**4**)/rGO, short nano-1(**6**)/rGO.

Then UV-Vis-NIR absorption spectroscopy was employed to gain further insight into the capability of these peptides to disperse rGO. **Figure 7-29** shows UV-Vis-NIR absorption spectra for the two peptides with rGO dispersions in water, together with the spectrum from the dispersion of unmodified rGO as a control. The absorption spectra were obtained under identical conditions.
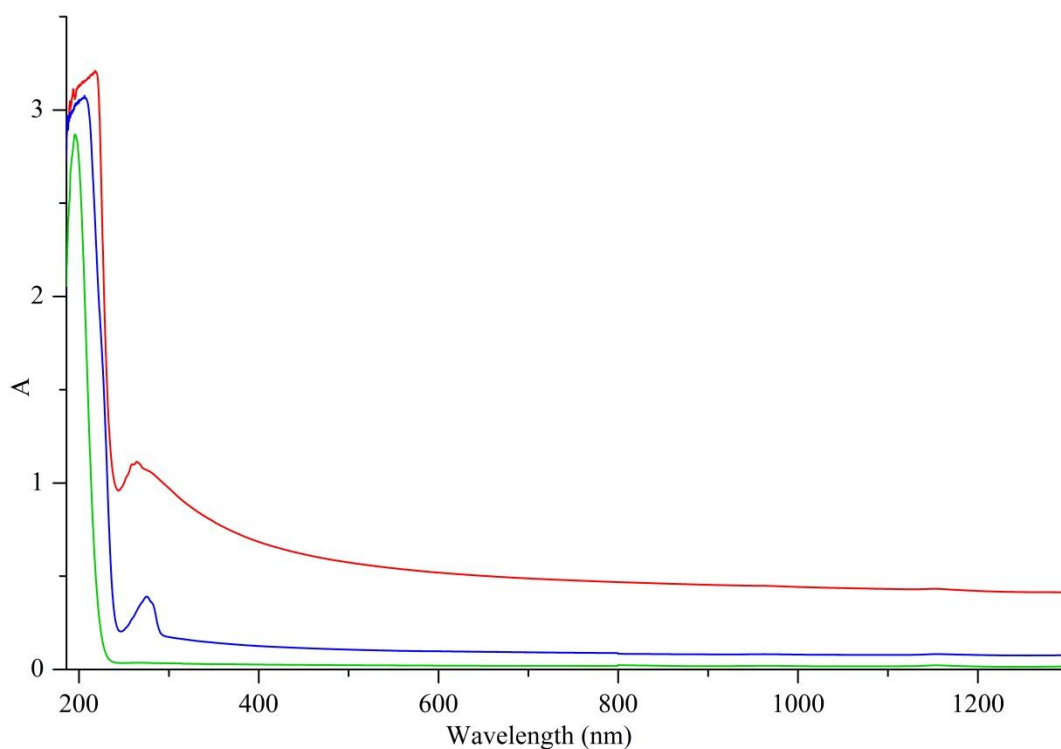
Figure 7-29: UV-Vis-NIR absorption spectra of rGO and nano-1 peptides dispersed rGO. (**Green line**) rGO, (**Blue line**) short nano-1(**6**)/rGO, (**Red line**) nano-1(**4**)/rGO.

The matching absorption spectral traces of the nano-1(**4**)/rGO and short nano-1(**6**)/rGO samples, shown in **Figure 7-29**, indicate that both peptides are capable of dispersing rGO. However, nano-1 (**4**)/rGO dispersion a displays higher absorption compared to that of the short nano-1 (**6**)/rGO dispersion. In contrast, as expected the unmodified reference rGO sample disperse displays a negligible amount as compared to the peptides. The concentration of dispersed rGO in these dispersions was estimated from their absorbance at 660 nm by using the extinction coefficient of rGO. The extinction coefficient of rGO was determined experimentally at 660 nm in 1 % SDS solution ($\epsilon_{660} = 38.7$ mL mg^{-1} cm^{-1}, see **Appendix B**), which agrees with the reported value using similar conditions. According to the Lambert Beer law, the concentration of rGO in these dispersions is shown in **Table 7-3**.

Dispersant	Conc. of Dispersed rGO. µg mL^{-1}
H$_2$O (control)	2.6
Short Nano-1(**6**)	12.1
Nano-1 (**4**)	64.3

Table 7-3: Concentration of dispersed rGO by two versions of nano-1 peptide determined from UV-Vis-NIR absorption after sonication and centrifugation.

Both visual inspection and UV-Vis-NIR absorption spectroscopy indicated that rGO dispersion with longer peptide chains give a better dispersion than short ones in water. This result can be explained in terms of the difference in the number of the hydrophobic residues in the sequence between the two peptides. Nano-1 peptide displayed the highest capability in dispersing rGO, with more than twice the absorbance as measured for the short nano-1(**6**) dispersion. This suggests that increasing the number of hydrophobic residues (phenylalanine, and valine) in the

peptide's sequence increases the amount of rGO that is dispersed. It has previously been shown that a peptide' sequence with more hydrophobic residues to interact with the nanomaterials surface allow for increased π–π stacking interactions, thereby enhancing the dispersion. Therefore, it is believed that this noncovalent dispersion depends on the adsorption of the hydrophobic face of the amphiphilic nano-1 peptide on the hydrophobic surface of rGO sheet. As a consequence, the presence of more hydrophobic residues in a peptide's chain increases adsorption to rGO, and thus the amount of dispersed rGO. Similar results were found using the same peptides to disperse purified SWNTs (**Chapter 4**).

Earlier theoretical studies have found that planar graphene sheet significantly disrupts the helical structure when compared to CNTs. Therefore, the expectation was that a helical peptide, represented here by nano-1 peptide (**4**), would disperse less rGO than purified SWNTs. Indeed, by comparing the dispersion results shown in **Table 7-4** it can be seen that the nano-1 peptide (**4**) shows better dispersion affinity towards purified SWNTs than rGO. A similar dispersion profile can be seen (below) when short nano-1 peptide (**6**) is used in the dispersion of purified SWNTs and rGO.

Peptide	Conc. of Dispersed rGO $\mu g\ mL^{-1}$	Conc. of Dispersed Purified SWNTs $\mu g\ mL^{-1}$
Nano-1(**4**)	64.3	586.9
Short nano-1 (**6**)	12.1	167.9

Table 7-4: Concentrations of dispersed rGO and purified SWNTs using the two versions of nano-1 peptide determined from UV-Vis-NIR absorption after sonication and centrifugation.

This dispersion affinity can be explained in terms of both the curvature of the nanomaterials surface and the helicity of the peptide. Since the same peptides and dispersion conditions have been used in the dispersion of both rGO and purified

SWNTs, it is obvious that the difference in curvature (planarity) of the surface between rGO and SWNTs is primarily responsible for difference in the amount of dispersed nanomaterial. Additionally, the amphiphilicity of a dispersant peptide plays a key role in the dispersion of carbon nanomaterials. Usually a peptide shows its maximum amphiphilicity when forming an α-helix. Therefore, how it adjusts its secondary structure (helicity) will affect the amphiphilicity and its stability at the water/hydrophobic nanomaterial interface. Therefore, when the nano-1 peptide interacts with SWNT, it matches its hydrophobic face against the curved surface of SWNT by curving around it without disturbing its helical structure and achieving its maximum amphiphilicity. However, this is not possible in rGO because of its rigid planner geometry. During nano-1 interaction with rGO, the peptide is thought to adjust its conformation by unfolding its helicity to permit the matching of its hydrophobic face to the hydrophobic and flat rigid rGO surface. This conformational adjustment disrupts the peptide's helical structure and thus minimises its dispersion ability when compared to SWNTs. Therefore, nano-1 (**4**) was less able to disperse rGO (64.3 μg mL^{-1}), while the same peptide dispersed (586.9 μg mL^{-1}) of purified SWNTs. In a peptide α-helix, the linear translation is a rise of 5.4 A˚ per turn of the helix, which is equal to the product of the translation (1.5 A˚) and circular rotation of 3.6 residues per turn.[191,475] Additionally, literature on the helical structures shows that the average length of helix is 12 residues. Previous theoretical research on nano-1 peptide revealed that its helix structure is a seven residue repeating sequence, which completes approximately two turns of the helix. Since short nano-1 peptide (**6**) is one heptad sequence, thus it is expected to show a minimum ability to fold into a helix, which previously has been proven by Zorbas *et al*.[120] Short nano-1 peptide (**6**) affinity to interact with rGO and SWNTs followed nano-1 peptide's behaviour

towards them, as it dispersed only 12.1 μg mL^{-1} of rGO while the same peptide dispersed 167.9 μg mL^{-1} of SWNTs. A Raman spectrum is used to obtain the structural information of rGO sheets in their nano-1 peptides composite. Raman spectra of rGO (control) and nano-1 peptides/rGO composite have been measured by drop casting each sample's aqueous dispersion on silicon substrate and left to dry in air.

Raman spectra of rGO (control) and nano-1 peptides/rGO composite have been measured by drop casting each sample's aqueous dispersion on silicon substrate and left to dry in air. Raman analyses were repeated ten times at different areas of each sample. **Figure 7-30** shows a representative G band normalised Raman spectra of nano-1(**4**)/rGO, short nano-1 (**6**)/rGO along with rGO as a reference.
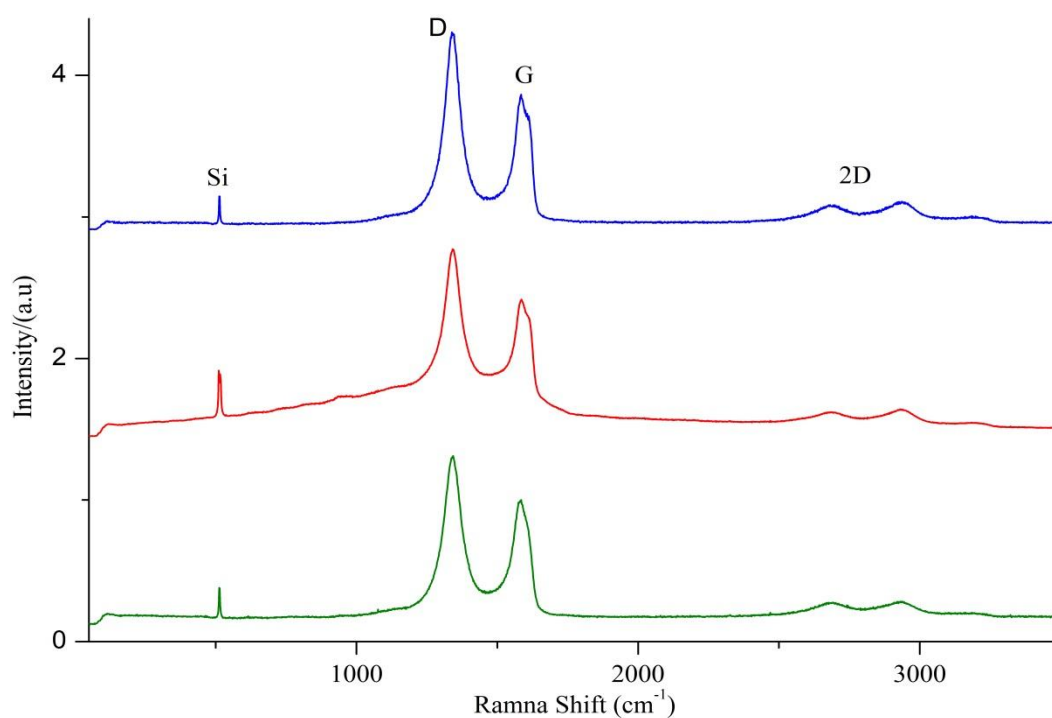
Figure 7-30: A representative Raman spectra (532 nm) of rGO (control) and nano-1peptides/rGO composites. (**Green line**) rGO, (**Red line**) nano-1(**4**)/rGO, (**Blue line**) short nano-1(**6**)/rGO.

All the Raman spectra exhibit two prominent peaks of the D band and G band as well as a very weak 2D band, which is typical characteristic of graphene based nanomaterials. Considering that the G-band of carbon nanomaterials is highly sensitive to the electronic effects,[476,477] the change in the G-band position of rGO upon its the interaction with nano-1 peptides was investigated. **Figure 7-31** compares the G mode feature for rGO (control) and peptide/rGO composites.
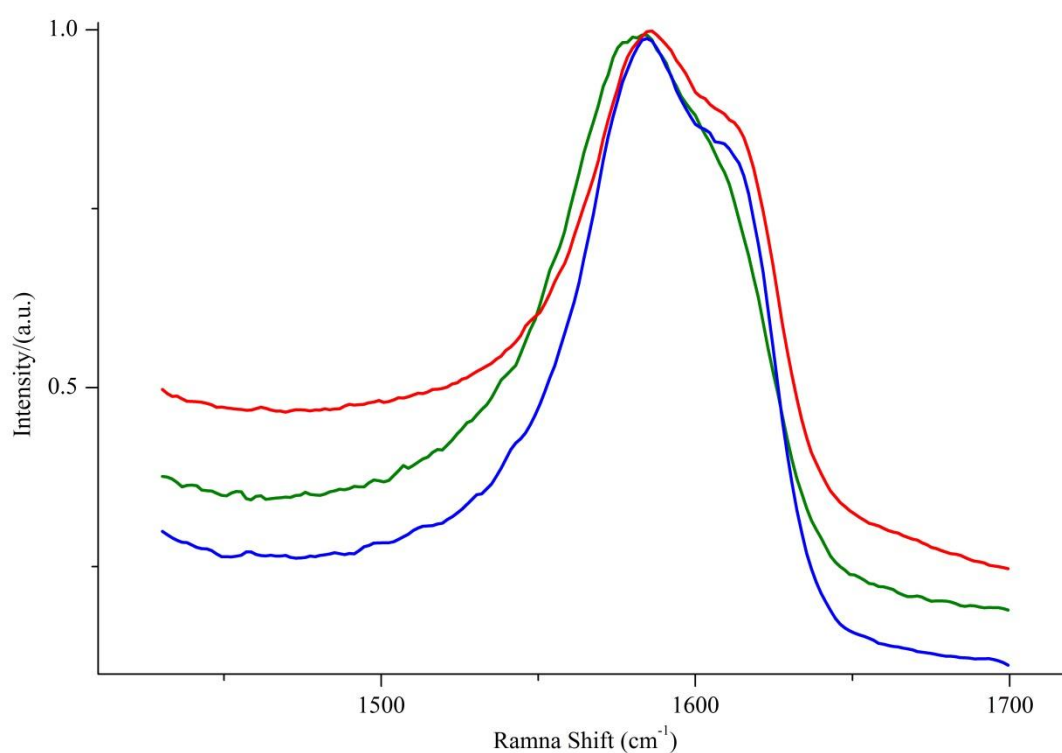
Figure 7-31: A representative Raman spectra of the tangential mode features for rGO and peptide/rGO composites. (**Green line**) rGO, (**Red line**) nano-1(**4**)/rGO and (**Blue line**) short nano-1(**6**)/rGO.

By comparing the G bands of nano-1(**4**)/rGO and short nano-1(**6**)/rGO with rGO, it can be seen that the G band of rGO is up shifted in its nano-1(**4**) and short nano-1 (**6**) composites. **Table 7-5** summaries the G peak position and shift of peptide/rGO and rGO as a control.

Sample	G band cm^{-1}	Up Shift cm^{-1}
rGO (control)	1581.3 ± 0.7	-
Nano-1(**4**)/rGO	1583.8 ± 0.7	2.5 ± 0.9
Short nano-1(**6**)/rGO	1584.0 ± 0.7	2.7 ± 0.9

Table 7-5: A comparison between the G band of rGO and peptide dispersed rGO.

This upshift supports the proposed interaction mechanism between nano-1 (**4**) and short nano-1 (**6**) and rGO that peptides' aromatic residues interact via π–π stacking with the rGO surface. Furthermore, it supplies an evidence for a weak charge transfer between rGO and nano-1 peptides which is in agreement with previous reports.[253,478-482]

7.2.2. Noncovalent Functionalisation of Reduced Graphene Oxide with (*N*lys*N*spe*N*spe)$_6$ Peptoid

There have been extensive studies on the adsorption of peptides and proteins onto nanomaterials which, it has been shown, can affect both the structure and function of these biomolecules. The adsorption of peptides and proteins on the surface of carbon nanomaterials is often accompanied with the loss of proteins' native conformation, and this is a major concern in the development of the potential of nanomaterials in various applications. Among carbon nanomaterials, the CNTs and graphene-based nanomaterials have the capability to disrupt the α-helical structures of short peptides, and due to its low surface curvature, graphene possesses the additional capability to distort α-helical conformations.

Peptides have been used to disperse graphene-like materials, as they have the ability to interact with the graphene surface. Although graphene-like materials' flat surface could be ideal for π–π stacking interaction with the aromatic residues in the peptide chain, however the results discussed in (**Section 7.2.1**) suggest that the rGO's flat rigid surface might disrupt the helical conformation of the peptide upon binding and hence disperse only a limited amount of rGO. Compared to peptides the absence of hydrogen-bond donors in the peptoid's backbone leads to a greater chain flexibility and prevents intra- and inter-chain hydrogen bonding. The rigidity of peptide's backbone decrease its adsorption onto SWNTs.[418] Whereas, compared to peptides the absence of hydrogen-bond donors in peptoid's backbone leads to a greater chain flexibility and prevents intra- and inter-chain hydrogen bonding which is thought to help them to fold around the curved surface of the side walls of SWNTs. In a previous chapter (see **Chapter 5**) it was concluded that due to the peptoids' backbone flexibility they showed a better ability, compared to nano-1 peptides, to curl around the curved SWNTs to disperse them in water. The 18 residue peptoid (*N*lys*N*spe*N*spe)$_6$ (**17**) dispersed 672.0 μg mL^{-1} of purified SWNTs, while nano-1 peptide (**4**) dispersed 586.9 μg mL^{-1}. Therefore; it is thought that the flexible backbone of the peptoid will allow a better noncovalent interaction of the peptoid's hydrophobic face with the flat rGO surface than the peptide.

7.2.2.1.   Synthesis of (*N*lys*N*spe*N*spe)$_6$ Peptoid

Among the tested peptoids and peptides for the dispersion of purified SWNTs, 18 residue peptoid (**17**) had high dispersion affinity toward the nanotubes (see **Chapter**

5). Therefore, 18 residue peptoid (**17**) was chosen to study impact of the dispersant chain flexibility on their ability to disperse the rGO. Peptoid **17** contain six repeating motif of three residues with the repeating subunit structure: (*N*lys*N*spe*N*spe)$_6$. **Figure 7-32** show the 18 residue peptoid (**17**) motif.
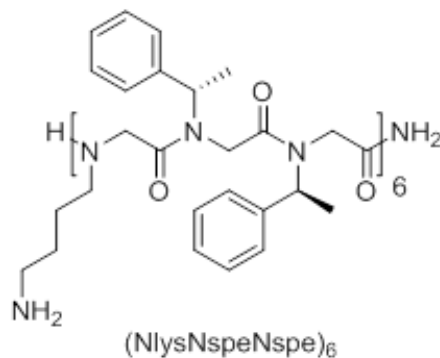
Figure 7-32: Synthesised peptoid (**17**) repeating unit.

The peptoids were routinely synthesised on Rink amide linker-derivatised solid supports using the submonomer synthesis method developed by Zuckermann.[284] The peptoid **17** has an amphiphilic nature; the two hydrophobic chiral aromatic residues (*N*spe) induce a repeated *cis* amide bond conformation and handedness of helical structure along the peptoid backbone. While the hydrophilic lysine-type side chain (*N*lys) residue aids the water solubility of the peptoid and encourages the formation of an amphiphilic helix in solution, and peptoid (**17**) showed a strong helicity CD spectrum (see **Chapter 5**).

7.2.2.2.   Dispersion of Reduced Graphene Oxide (rGO) with Peptoids

1.0 mg mL^{-1} of rGO was noncovalently functionalised by dispersion in 1.0 mM aqueous solution of 18 residue peptoid (**17**) (see **Chapter 5**) via probe ultra-sonication for 20 min in an ice bath. The concentration of **17** is set to 1.0 mM to ensure assembly of the peptoid on the rGO surface. Then, the (*N*lys*N*spe*N*spe)$_6$ (**17**)/rGO dispersion was centrifuged to accelerate the removal of suspended rGO that were not efficiently solubilised and thus aggregates, leaving the black-coloured supernatant aqueous solution which contains the stable and well-dispersed rGO. **Figure 7-33** shows rGO dispersion by **17** after sonication and centrifugation, and rGO dispersion in water as a control.
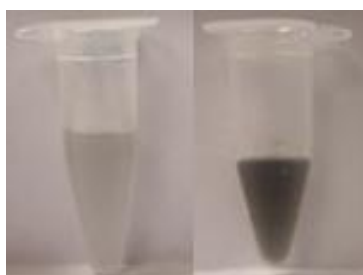
Figure 7-33: Visual comparison of rGO aqueous supernatant after sonication and centrifugation. Dispersion from left to right: rGO (control), (*N*lys*N*spe*N*spe)$_6$ (**17**)/rGO.

rGO sonication in water is carried out as a control; rGO sedimentation immediately and irreversibly after the centrifugation to give a clear supernatant. By contrast, the addition of **17** to the rGO suspension in water prevented rGO sheet agglomeration and leads to a visually homogeneous black dispersion.

The (*N*lys*N*spe*N*spe)$_6$ (**17**)/rGO complex supernatant was further characterised by UV-Vis-NIR spectroscopy. The UV-Vis-NIR spectra of rGO (control) and peptoid (**17**)/rGO dispersion solutions are shown in **Figure 7-34**. Due to rGO's (control) very

limited dispersion in water its UV-Vis-NIR spectra did not exhibit a well-defined absorption peak. As expected, the peptoid **17** coated rGO sample showed a much higher absorbance compared to rGO (control). The peptoid works as a surfactant through its noncovalent interaction with the hydrophobic surface of rGO. Therefore, (*N*lys*N*spe*N*spe)$_6$ (**17**)/rGO complex shows a strong UV-Vis-NIR absorbance corresponding to π–π* transitions of C-C bonds of rGO. Additionally, this significant increase in the absorbance of (*N*lys*N*spe*N*spe)$_6$ (**17**)/rGO corresponds to a darkening of the solution which could clearly be seen with the eye (**Figure 7-33**) and indicated that more rGO is dispersed in the supernatant.
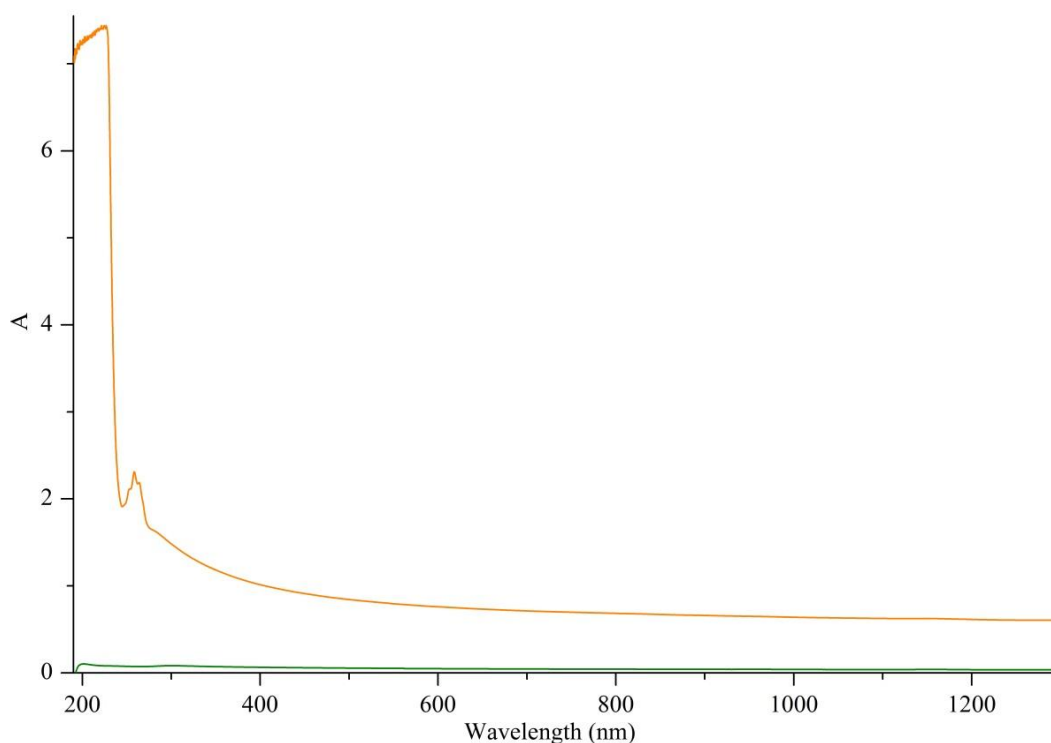
Figure 7-34: UV-Vis-NIR spectra of (*N*lys*N*spe*N*spe)$_6$ (**17**)/rGO composite (**Orange line**) and rGO (control) (**Green line**).

The amount of rGO retained in the supernatant after sonication and centrifugation was taken as a relative measure of the ability of the peptoid to disperse rGO in water. Such an amount was estimated by determining the absorbance of the peptoid (**17**)/rGO complex at a wavelength of 660 nm. Although rGO is known to exhibit a well-defined absorption peak at 268 – 270 nm (provided that the sheets have been well reduced), the latter wavelength was not used in the present measurements. This is because many peptoid displayed a strong absorbance in the 200 – 300 nm wavelength range, which could not be compensated for in the double-beam spectrophotometer. However, the peptoid **17** did not exhibit absorption at wavelengths above 400 nm. Thus, any absorbance measured at a given wavelength above 400 nm could be safely related to the amount of dispersed rGO according to the Beer-Lambert law and the determined extinction coefficient (see **Appendix B**), as shown in **Table 7-6**.

Dispersant	Conc. of Dispersed rGO $\mu g \ mL^{-1}$
H$_2$O (control)	2.6
(*N*lys*N*spe*N*spe)$_6$ (**17**)	93.8
Nano-1 (**4**)	64.3

Table 7-6: Concentration of dispersed rGO by nano-1 peptide (**4**) and (*N*lys*N*spe*N*spe)$_6$ (**17**) determined from UV-Vis-NIR after sonication and centrifugation.

The concentration of rGO dispersed in the supernatant after centrifugation was greater in the peptoid dispersed rGO then nano-1 (**4**) dispersed rGO (64.3 $\mu g \ mL^{-1}$, see **Section 7.2.1**). This is likely to arise from the flexibility of the peptoid's backbone compared to the peptide's backbone, which allows assembly on the flat rigid surface of the rGO sheets without disrupting the peptoid's helicity. The flexible

backbone of the peptoids allows assembly on the flat rigid surface of the rGO sheets, leading it to disperse more rGO than the nano-1 helical peptide.

The rGO (control) and (*N*lys*N*spe*N*spe)$_6$ (**17**)/rGO aqueous dispersions were drop casted to silicon wafer substrate and left to dry in air for Raman measurements. Their Raman spectra are normalised to G band and is repeated at least ten times from different areas of the sample. **Figure 7-35** shows a representative Raman spectra of rGO (control), and (*N*lys*N*spe*N*spe)$_6$ (**17**)/rGO complex.
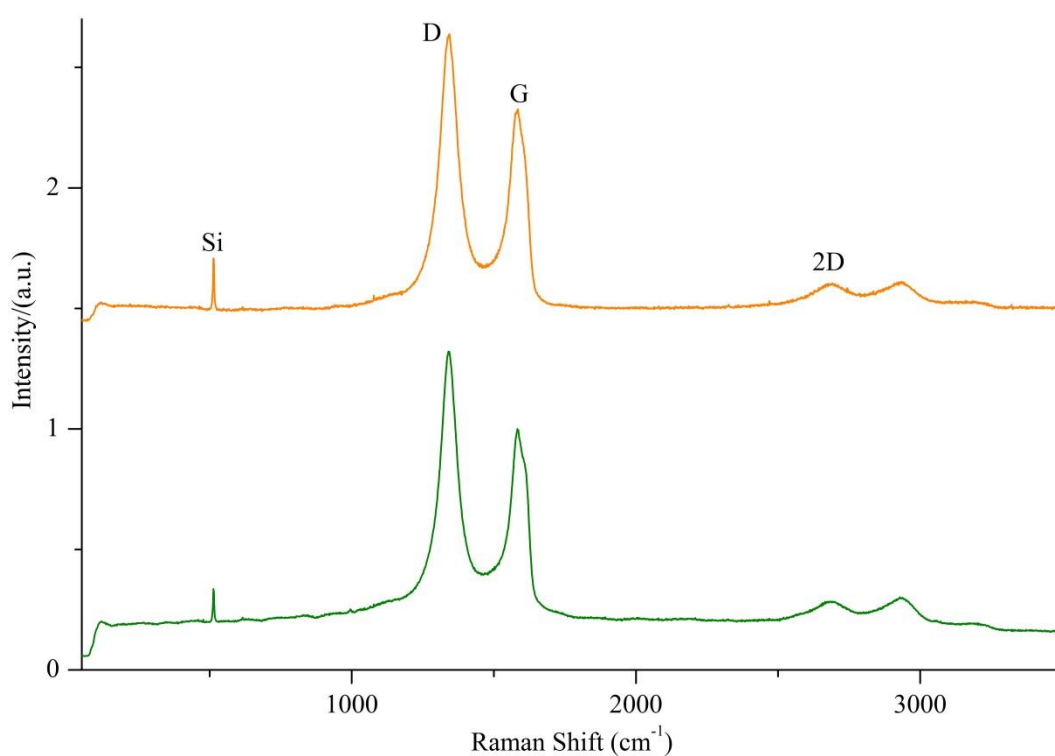
Figure 7-35: A representative normalised Raman spectra (532 nm) of rGO and peptoid dispersed rGO: (**Green line**) rGO (control), (**Orange line**) (*N*lys*N*spe*N*spe)$_6$ (**17**)/rGO.

The Raman spectra of both samples exhibit characteristic Raman bands of graphene based nanomaterials, namely D, G and weak 2D band. However, the G band of (*N*lys*N*spe*N*spe)$_6$ (**17**)/rGO appears at 1583.3 ± 0.9 cm^{-1}, while it is appears at 1581.3

± 0.7 cm^{-1} for rGO (control), **Figure 7-36**. The (*N*lys*N*spe*N*spe)$_6$ (**17**)/rGO G band upshift of 2.1 ± 1.1 cm^{-1} comparing to the control rGO sample indicates that there is a π–π stacking interaction between peptoid's aromatic residue interacts and rGO surface. Moreover, this upshift suggests a weak charge transfer between the rGO and the peptoid. These shifts are similar to those reported by in which carbon nanomaterials were noncovalently dispersed with aromatic molecules.[318]
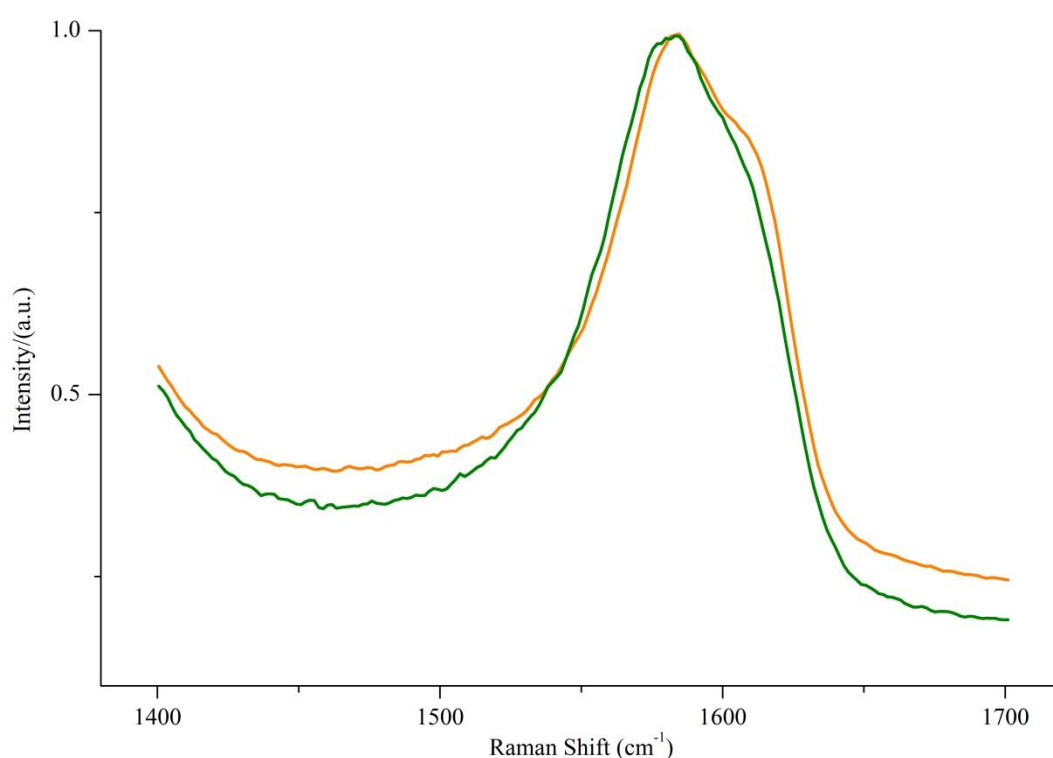
Figure 7-36: A representative Raman spectra of the tangential mode features for rGO and peptoid/rGO composite: (**Green line**) rGO, (**Orange line**) (*N*lys*N*spe*N*spe)$_6$ (**17**)/rGO.

7.2.3. Noncovalent Functionalisation of Reduced Graphene Oxide with Ribonucleosides

Most previous investigations carried out to study the interaction of DNA nucleobases and nucleosides with graphene were based on theoretical approaches. Therefore, this

section experimentally investigates a noncovalent functionalisation of reduced graphene oxide (rGO) with ribonucleosides (adenosine, cytidine, guanidine, thymidine, and uridine) and its nucleobases.

The desired aqueous ribonucleoside solution to disperse rGO was prepared by diluting a stock solution (2.0 mg 10 mL^{-1}). To prepare ribonucleoside/rGO complex dispersion, 1.0 mg mL^{-1} of rGO was added to 1.0 mM of each ribonucleoside aqueous solution. The ribonucleoside/rGO solution was probe sonicated for 20 min in an ice bath, and then centrifuged to remove inefficiently dispersed and sedimented rGO from stable and well dispersed rGO. Thus, the supernatant phase contains the well dispersed and mostly exfoliated rGO. Visual observation suggested uridine appears to have the highest dispersion affinity towards rGO necessary to suspend rGO in water compared to other tested ribonucleosides. **Figure 7-37** shows rGO dispersions after sonication and centrifugation for the ribonucleosides series.

Figure 7-37: A visual comparison between rGO aqueous supernatant with a series of ribonucleosides after sonication and centrifugation. Dispersion from left to right; adenosine/rGO, cytidine/rGO, guanidine/rGO, thymidine/rGO and uridine/rGO.

This observation was confirmed by UV-Vis-NIR absorption spectroscopy, as shown in **Figure 7-38**. The UV-Vis-NIR spectra of rGO (control) exhibited an absorption band correspond to π–π* electronic transition, indicating that most of oxygen-containing functional groups on the GO surface are removed and the conjugated

structure is restored. However, due to rGO hydrophobic nature and the absence of a surfactant, this peak was very weak, which indicates that the reduction removed most of the oxygen-containing functional groups on the GO. On the other hand, comparing to absorption of rGO, ribonucleoside/rGO complexes had higher absorption intensity due to the noncovalent interaction between rGO and the ribonucleoside.
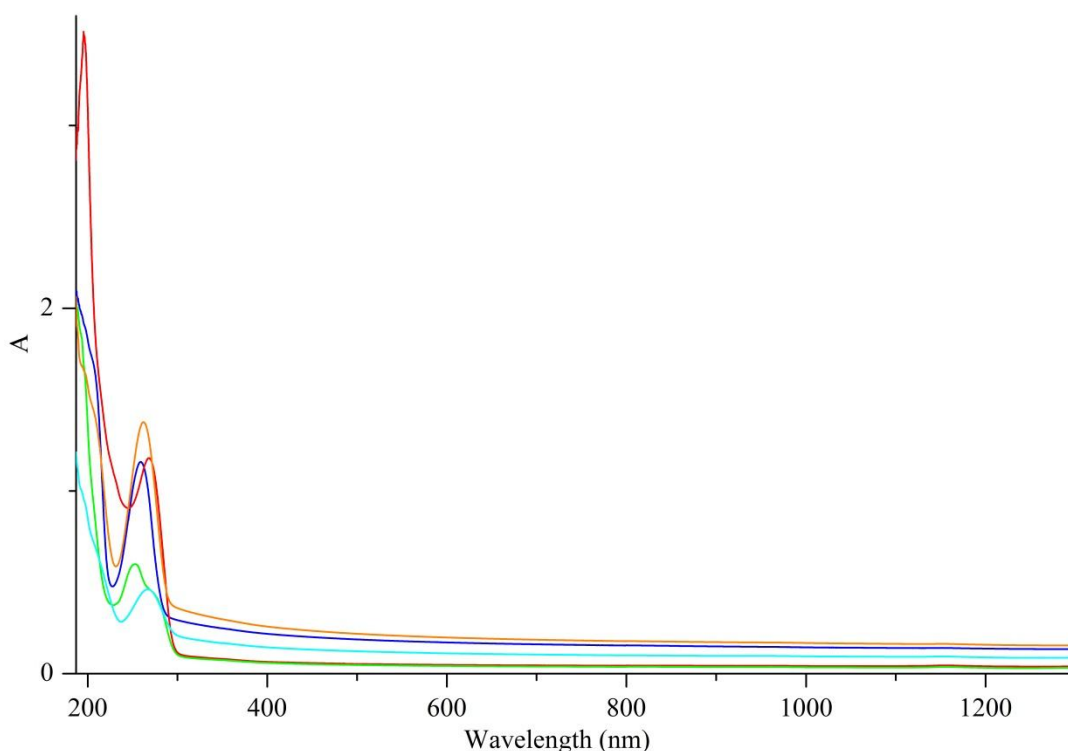
Figure 7-38: UV-Vis-NIR spectra of ribonucleoside/rGO complexes aqueous supernatant**:** (**Blue line**) Adenosine/rGO, (**Red line**) cytidine/rGO, (**Green line**) guanidine/rGO, (**Cyan line**) thymidine/rGO and (**Orange line**) uridine/rGO.

rGO's UV-Vis-NIR absorption is proportional to its concentration dispersed in solution. Thus, dispersion rGO's concentration in the ribonucleoside/rGO supernatant was determined from their absorbance at 660 nm using Beer-Lambert law and calculated extinction coefficient of rGO at 660 nm (**Appendix B**). **Table 7-7** shows the concentration of rGO in ribonucleoside/rGO supernatant determined using

UV-Vis-NIR absorption. The UV-Vis-NIR absorbance intensity of uridine/rGO complex shows higher absorption intensity comparing to other complexes and rGO (control) at 660 nm, indicating that an increasing amount of rGO was in the uridine/rGO complex dispersed solution.

Ribonucleoside	Conc. of Dispersed rGO $\mu g\ mL^{-1}$
H_2O (control)	2.6
Adenosine	21.1
Cytidine	5.9
Guanidine	5.1
Thymidine	13.7
Uridine	24.4

Table 7-7: Concentration of dispersed rGO with series of ribonucleosides determined from their UV-Vis-NIR adsorption after sonication and centrifugation.

Among the five tested ribonucleosides, uridine shows the highest interaction affinity towards rGO and guanidine shows the lowest, which is in agreement with its dark supernatant colour shown in **Figure 7-37**. The low concentration of dispersed rGO by the ribonucleosides suggests that there is a weak binding energy with rGO surface, which parallels with what has been theoretically predicted by Antony *et al.*[442] and Varghese *et al.*[329] The low amount of dispersed rGO by these ribonucleosides is thought to be due to the small ring (cyclic and aromatic) of these ribonucleosides, thus their ability to disperse rGO in the aqueous solution is quite limited.

The concentration of dispersed rGO by ribose sugar alone is 22.4 $\mu g\ mL^{-1}$, which is less than the concentration of dispersed rGO by uridine. **Figure 7-39** shows the UV-

Vis-NIR of ribose/rGO supernatant. This indicates that the interaction between ribose and rGO is a nonhydrophobic interaction as the limited number of oxygen-containing functional groups on rGO surfaces resulted in a very weak interaction between ribose and rGO's hydrophobic surface.
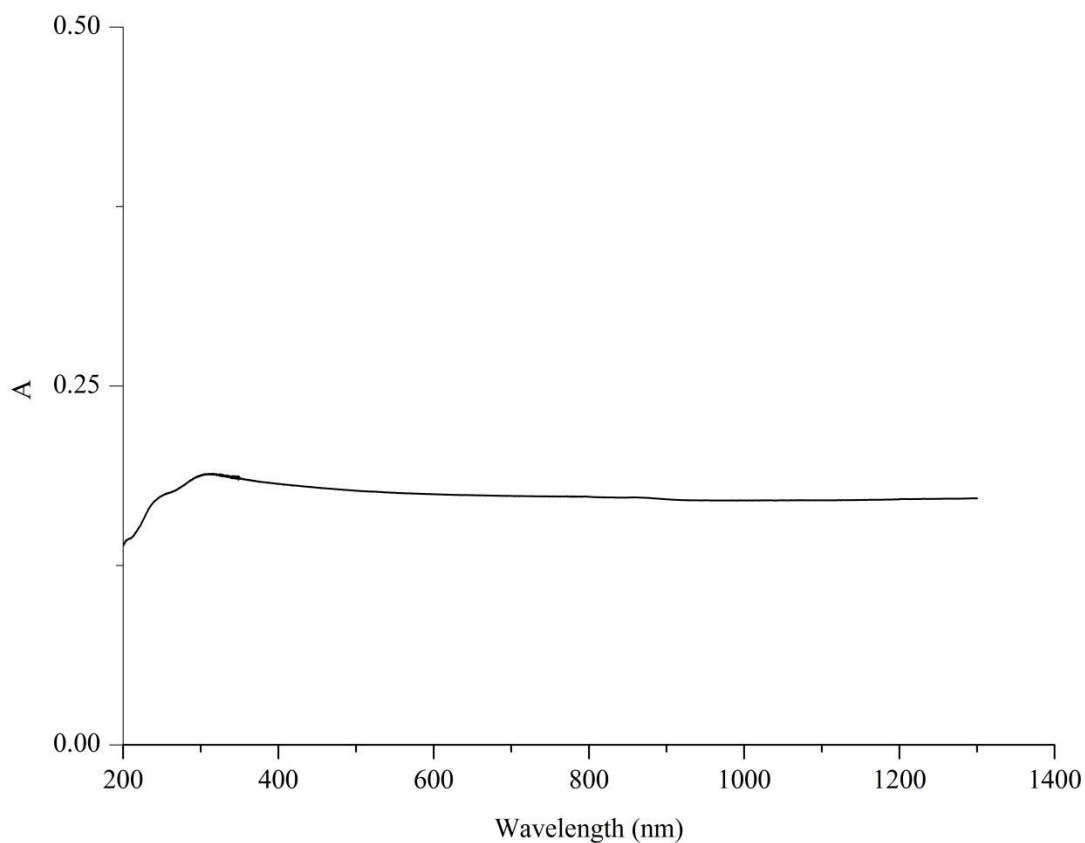
Figure 7-39: UV-Vis-NIR of ribose/rGO after sonication and centrifugation.

To investigate the effect of nucleobase moieties in ribonucleoside interaction with rGO, the rGO dispersion with the aid of series of nucleobases; cytosine, guanine, adenine, thymine, and uracil, were studied. The nucleobase/rGO complexes were prepared following the same dispersion method used for the preparation of ribonucleoside/rGO complexes. The faint grey colour of nucleobase/rGO complexes supernatant after the sonication and centrifugation shown in **Figure 7-40** suggest that

the nucleobases have a very limited ability to disperse rGO compared to ribonucleosides (**Figure 7-37**).
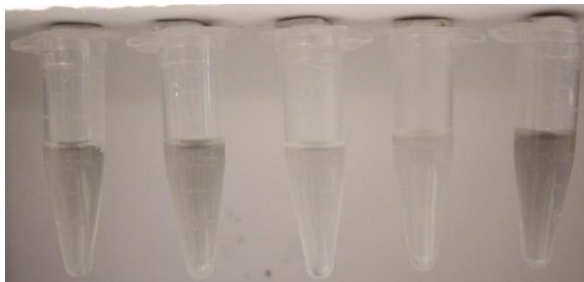
Figure 7-40: A Visual comparison between rGO aqueous dispersion supernatant with a series of nucleobases after sonication and centrifugation. Dispersion from left to right: cytosine/rGO, adenine/rGO, guanine/rGO, uracil/rGO.

The rGO dispersion solution colour is proportional with its quantity in the solution. Therefore, Based on the above visual comparison in **Figure 7-40** of nucleobases interaction with rGO in water, it is thought that uracil dispersed higher quantity of rGO than the rest of nucleobases.

The noncovalent interaction between nucleobases and rGO was monitored by UV-Vis-NIR spectroscopy. As shown in **Figure 7-41**, nucleobases/rGO complexes dispersion supernatant exhibited a characteristic rGO absorption peak attributed to the π–π* electronic transitions of sp^2 C–C bonds in rGO.
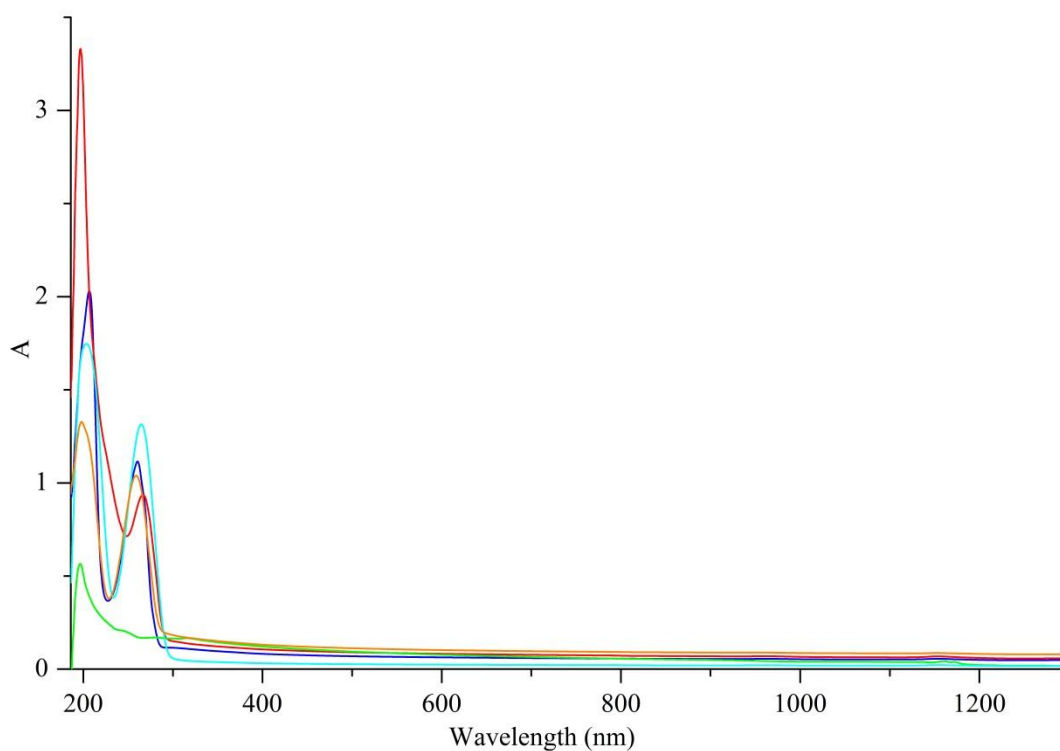
Figure 7-41: UV-Vis-NIR spectra of nucleobases/rGO complexes supernatant: (**Blue line)** adenine/rGO, (**Red line**) cytosine/rGO, (**Green line**) guanine/rGO, (**Cyan line**) thymine/rGO and (**Orange line**) uracil/rGO.

The low absorption intensity spectrum of nucleobases/rGO complexes suggests that the nucleobases noncovalent interaction of nucleobases' ring (cyclic and aromatic) with rGO was not effective in dispersing rGO in water. Additionally, UV-Vis-NIR absorption spectra of nucleobases/rGO complexes were used to evaluate the concentration of the dispersed rGO in nucleobases/rGO complex supernatant. The rGO concentration in the nucleobases/rGO complexes supernatant after sonication and centrifugation calculated from the rGO absorbance at 660 nm using Beer-Lambert law and calculated extinction coefficient of rGO (see **Appendix B**). **Table 7-8** shows the concentration of rGO in nucleobase/rGO complexes supernatant determined using UV-Vis-NIR absorption.

Nucleobase	Conc. of Dispersed rGO $\mu g\ mL^{-1}$
H$_2$O (control)	2.6
Adenine	7.8
Cytosine	10.2
Guanine	9.0
Thymine	2.9
Uracil	12.7

Table 7-8: Concentration of dispersed rGO with a series of nucleobases determined from their UV-Vis-NIR absorption after sonication and centrifugation.

As can be seen from **Table 7-8** the low amount of dispersed rGO by nucleobases indicates that nucleobases have a very limited dispersion efficacy towards rGO. This indicates that there is a very weak noncovalent interaction, although, the planar surface of rGO is presented as an ideal system for π–π interaction with the planar ring of nucleobases and ribonucleosides. However, the low amount of dispersed rGO by nucleobases shown in **Table 7-8** indicate that the small purine's and pyrimidine's ring (aromatic ring in adenosine and guanosine purine ribonucleosides and cyclic ring in cytosine, thymidine, and uracil pyrimidine ribonucleosides) has a limited interaction efficiency towards rGO. Therefore, it is thought that there is a very weak π-π stacking interaction between the nucleobases and the hydrophobic surface of the rGO, due to the small ring size of the nucleobases. Similar results were found when ribonucleosides were used in dispersing purified SWNTs (**Chapter 6**), indicating that π–π interaction probably is not the main interaction driving SWNTs dispersion in water. Thus, it is thought that the high dispersion affinity of ribonucleosides towards oxidised SWNTs (**Chapter 6**, **Section 6.2.2.2**) is due to the nonhydrophobic interaction.

Pervious theoretical studies have shown that the size and curvature of carbon nanomaterials play an important role in their non-bonded interactions. Although, the above experimental results suggests that ribonucleosides have limited dispersion efficiency towards the hydrophobic surface of both rGO and SWNTs. It also indicated that ribonucleosides had higher dispersion affinity towards rGO then purified SWNTs, as uridine dispersed 24.4 µg mL^{-1} of rGO, while it dispensed 0.2 µg mL^{-1} of purified SWNTs. This is probably is due topological difference between rGO and SWNTs. Since the ribonucleosides tend to have π–π stacking type of interactions with the hydrophobic surface of rGO and purified SWNTs, thus as the curvature decreases, there will be more efficient stacking between the rGO and the ribonucleoside surface. These results parallel with pervious theoretical studies which show that molecules binding energy increases as the curvature decreases and reaches the maximum for graphene.[420,449]

Raman spectroscopy was also used to probe the ribonucleoside's impact on the electronic structure of the rGO. The Raman analyses were measured by drop casting each sample's aqueous dispersion on silicon substrate left to dry in air. The Raman analyses were repeated ten times at different areas of the sample. **Figure 7-42** shows representative Raman spectra of rGO (control) and ribonucleoside/rGO normalised to G band.
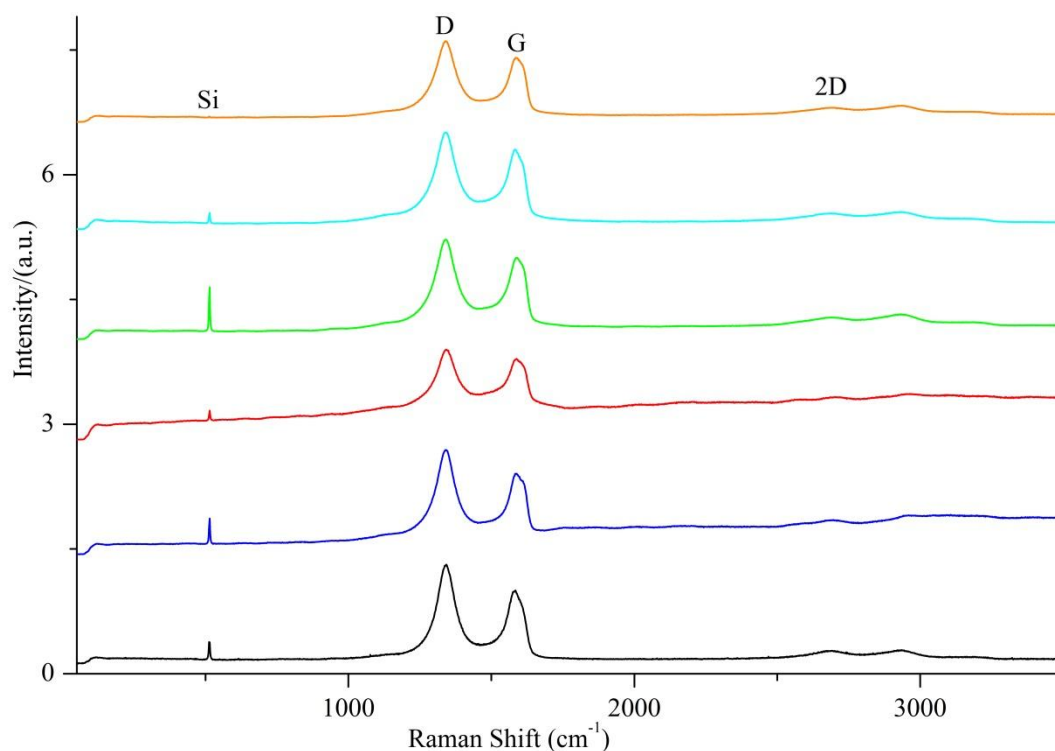
Figure 7-42: A representivtive Raman spectra (532 nm) of rGO and ribonucleoside/rGO complexes**: (Blue line)** Adenosine/rGO, (**Red line**) cytidine/rGO, (**Green line**) guanidine/rGO, (**Cyan line**) thymidine/rGO, (**Orange line**) uridine/rGO and (**Black line**) rGO (control).

Raman spectra of rGO and its ribonucleoside composites show the characteristic G and D band of graphene base nanomaterials at $1581 - 1588$ and $1338 - 1350$ cm^{-1}, respectively. Previous studies have demonstrated that the tangential vibrational modes for carbon nanomaterials are sensitive to doping. Specifically, the G band peak was shown to shift to lower frequencies for electron donor dopants and to higher frequencies for electron acceptor dopants. The G band peak of all ribonucleoside/rGO dispersions are up shifted with respect to that of rGO (control). **Figure 7-43** compares the G mode feature for rGO (control) and ribonucleoside/rGO composites.
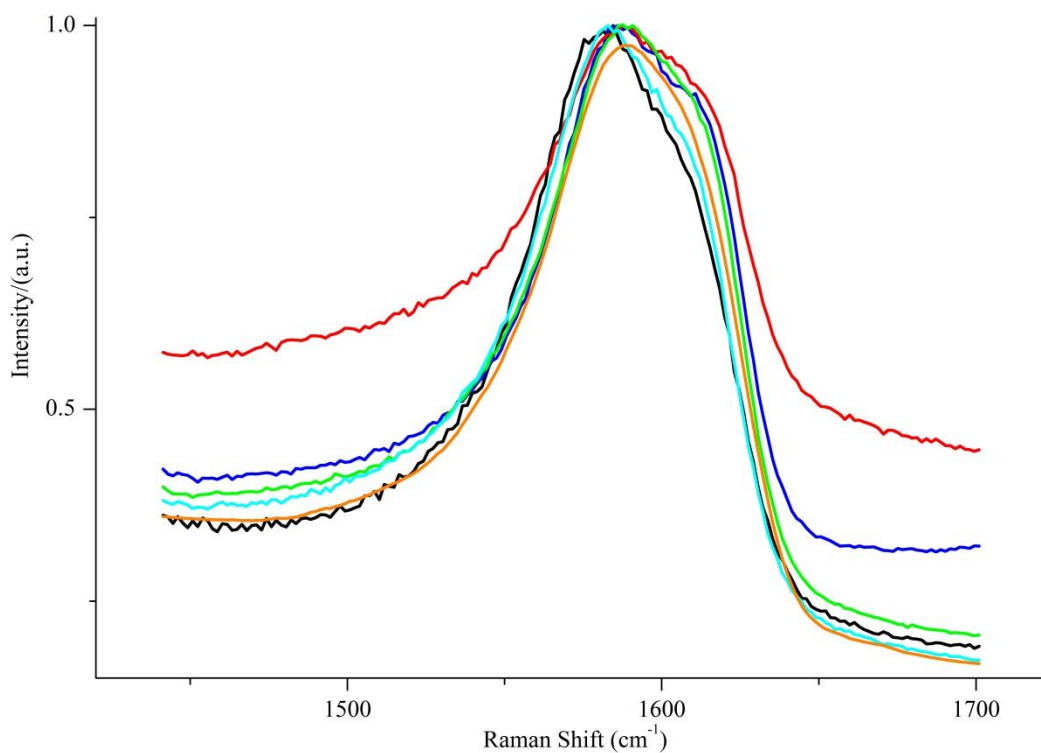
Figure 7-43: A representivtive Raman spectra showing the tangential mode features for rGO and ribonucleoside/rGO complexes: (**Blue line)** Adenosine/rGO, (**Red line**) cytidine/rGO, (**Green line**) guanidine/rGO, (**Cyan line**) thymidine/rGO, (**Orange line**) uridine/rGO and (**Black line**) rGO (control).

The small G band upshift of ribonucleoside/rGO composite comparing to rGO are summarised in **Table 7-9**.

Dispersion	G band (cm^{-1})	G band Upshift cm^{-1}
rGO (control)	1581.3 ± 0.7	-
Adenosine/rGO	1589.0 ± 1.2	7.7 ± 1.4
Cytidine/rGO	1589.8 ± 1.9	8.5 ± 2.0
Guanidine/rGO	1588.4 ± 0.9	7.1 ± 1.1
Thymidine/rGO	1586.2 ± 0.8	4.9 ± 1.1
Uridine/rGO	1587.2 ± 1.2	5.9 ± 1.4

Table 7-9: A summary of tangential mode features for rGO and ribonucleoside/rGO complexes.

These shifts suggest that there is a weak charge transfer between the rGO and ribonucleosides. Thus, it suggests that there is weak hydrophobic interaction in between ribonucleosides and rGO.

7.2.4. Covalent Functionalisation of Reduced Graphene Oxide with Cell Penetrating Peptoid (Ac-*N*glu-*N*lys-*N*lys-Nlys-*N*phe)

GO and rGO has been considered to be a potential carrier for drug delivery system,[483,484] because their 2D structural feature has a large surface area. As a result, drugs can be loaded onto both sides of the graphene sheet. For the practical application high dispersion stability of graphene based nanomaterials has to be provided through biofunctionalisation process, mainly through π–π stacking, covalent binding, hydrophobic and electrostatic interaction.[389] Although noncovalent chemistry is attractive because of the preservation of the conjugated π system, however, adsorption of water insoluble drugs (such as peptide, protein, and DNA) on planar graphene depends mainly on weak hydrophobic interactions, resulting in a lower drug loading ratio.[485] Therefore, covalent functionalisation methods have been widely utilised for the preparation of biofunctionalised GO or rGO.[486-488]

The cellular uptake of free biomolecules in general and peptides in particular is extremely poor; therefore conjugation of these molecules onto carbon nanomaterials surfaces may allow improvements in the delivery of such biological molecules.[489] However, cell penetrating peptides (CPPs) often display an inefficient bioavailability due to their proteolysis and opsonisation in the presence of serum.[490] Unlike CPPs, cell penetrating peptoids (CPPos) are highly stable against enzymatic degradation

and less toxic mimetics of CPPs.[491-493] Although CPPos do not always resemble the conformational constraints of the respective peptides, as the chirality of the α-carbon is lost, they can be modified by a large variety of functional side chains offering a toolkit for the development of artificial cell penetrating moieties. The cellular uptake mechanism is not yet revealed in all details; however, it is found that the polycationic character is a very important feature of CPPos. It is assumed that the positive charges allow the CPPos to interact strongly with the negatively charged structures and the head groups of membrane phospholipids on the extracellular side of the plasma membrane.[494] A peptoid (**17**) was previously used for the noncovalent functionalisation of rGO and showed limited dispersion ability (93.8 μg mL^{-1}). Thus, the main focus of this section is to study the covalent functionalisation of CPPos with rGO not only to improve the solubility of rGO in water but also to bring a biological function to it.

7.2.4.1.   Synthesis of Cell Penetrating Peptoid (CPPo)

The chosen CPPo sequence, shown in **Figure 7-44**, was previously reported by Kölmel *et al.*[490] to have an efficient entry into human cells by endocytosis with subsequent endosomal release. The hydrophilic side chain (*N*lys) is critical for the CPPo's hydrophilicity and the ability to dissolve in biological fluids. The hydrophobic side chain (*N*phe) is included in the sequence to support the passage through the lipid bilayer cell membrane. The charged residues (*N*lys) play an important role in the CPPo (**18**) ability to penetrate the cell membrane.[490] Thus, in order to preserve the *N*lys residues in **18**, glutamic acid residue (*N*glu) has been

added to the original CPPo's sequence. One of the carboxylic groups has been acetylated, while the second one left free to react with amino group on the amidated rGO.
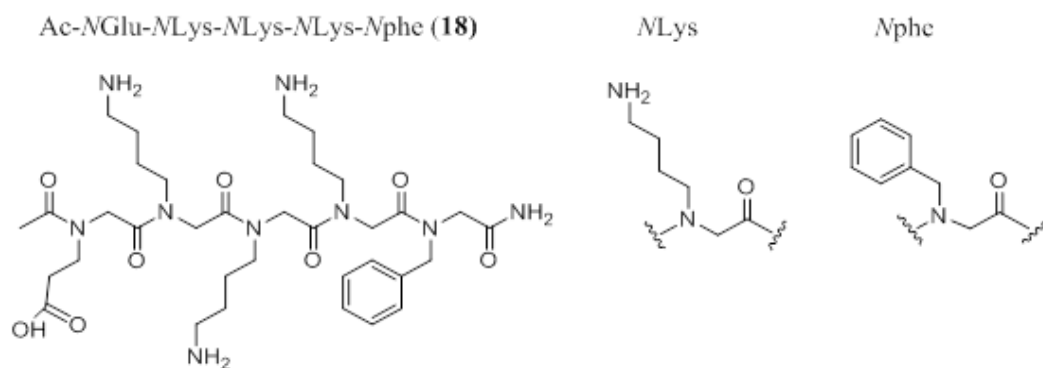
Figure 7-44: The structure of CPPo (**18**) and its monomers.

The CPPo was synthesised by Hannah L. Bolt (Cobb group) on Rink amide linker-derivatised solid supports using the submonomer synthesis method developed by Zuckermann.[284] The synthesis of **18** was achieved following the same methods used for the synthesis of peptoids previously mentioned in (**Chapter 5**). Following the synthesis of the peptoids, pure samples were obtained following RP-HPLC and confirmed using ESI-MS (**Figure 7-45**).
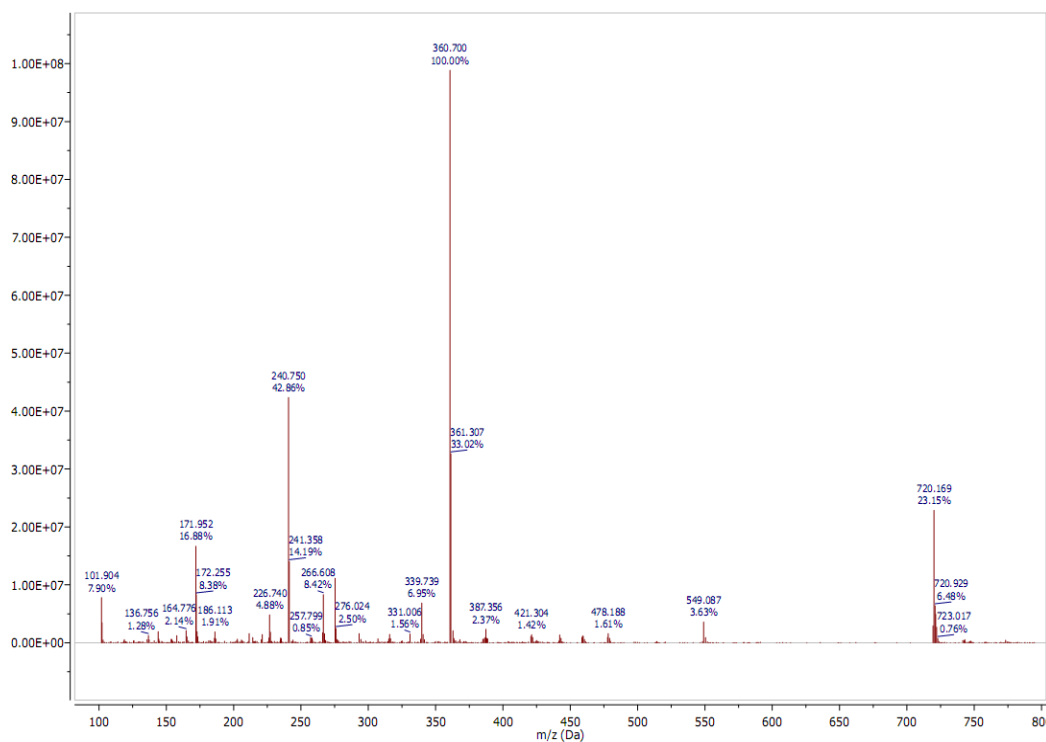
Figure 7-45: LC-MS of purified CPPo (**18**).

7.2.4.2.   Synthesis of Amidated Reduced Graphene Oxide (Am-rGO)

For medical and biological applications, rGO sheets should be thoroughly dispersed in the water. Hence, the first step is to generate the active sites in rGO, where the chemical moieties of the CPPo (**18**) can be introduced to facilitate their dispersion in the water. In order to prepare amidated rGO (Am-rGO), carboxylic acid groups as active sites were introduced at edges and defect sites of rGO sheets by oxidation using (8 M) nitric acid reflux for 24 h at 100℃. The oxidised rGO (Oxi-rGO) has higher water dispersion than the hydrophobic rGO, due to introduction of oxygen functional groups to the rGO sheet. The concentration of dispersed oxidised-rGO in water is 86.7 μg mL^{-1}, while dispersed rGO control concentration is 2.6 μg mL^{-1}. The

thermal decomposition properties of Oxi-rGO were probed using TGA (**Figure 7-46**).
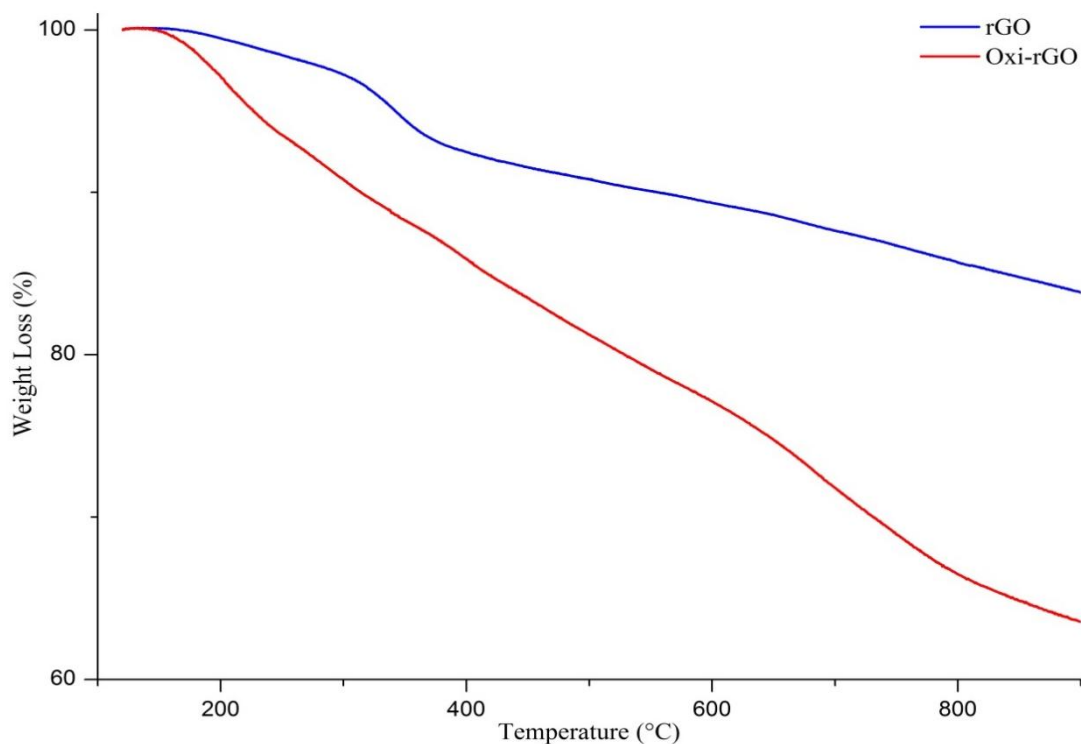
Figure 7-46: TGA of Oxi-rGO and rGO under N_2.

The TGA profile of rGO shows a high thermal stability, which indicates a low amount of oxygen-containing groups on its surface. TGA curve of rGO show a 2.8 % loss at 200 °C which is assigned to the decomposition of the residual oxygen containing groups, and a 10.5 % loss from 440 to 590 °C which is associated with the pyrolysis of the carbon skeleton of rGO.[495] The oxidation of rGO introduces carboxylic groups at the defect sites and edges of rGO, thus, shows a higher weight loss as seen in Oxi-rGO. Whereas rGO lost 16.2 % of its dry mass at 900 °C Oxi-rGO lost 36.5 %, this indicates that in Oxi-rGO there are more functional groups

present, hence the higher mass loss, and so the material has successfully been oxidised.

The second step is the formation of amino-terminated rGO by amidation of Oxi-rGO. Ethylenediamine (EDA) coupled with the carboxylic groups of Oxi-rGO to synthesise amidated rGO. This approach involves first transformation of the oxidatively introduced carboxyl groups in Oxi-rGO to rGO-COCl by refluxing with an excess of thionyl chloride (SOCl$_2$) in the presence of a small amount of *N,N*-dimethylformamide (DMF). Excess thionyl chloride was removed by filtration, and then acylated-rGO product was washed with anhydrous DMF to remove from the traces of residual thionyl chloride (**Scheme 7-1**).
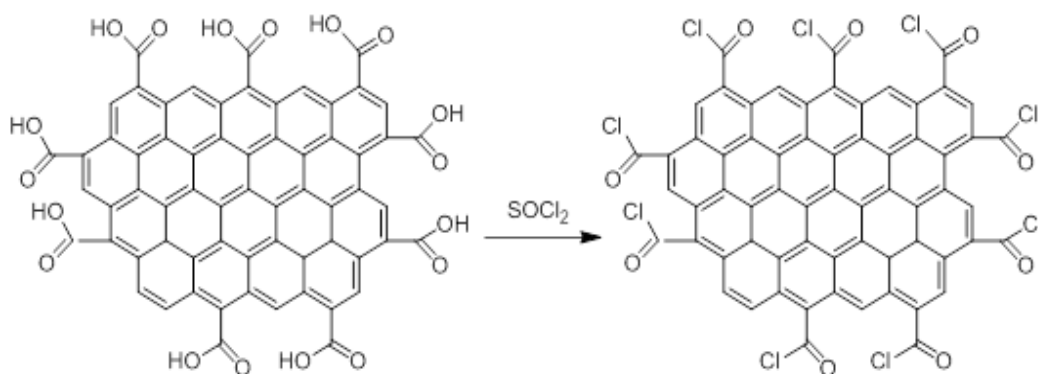
Scheme 7-1: Acetylation of Oxi-rGO with thionyl chloride (SOCl$_2$).

Subsequently, the acylated sample was reacted with excess EDA in the presence of *N,N*-Dimethylformamide (DMF) as a catalyst at room temperature for 24 hours under nitrogen atmosphere. Loading of EDA molecules on rGO-COCl through amide linkage afforded the EDA-rGO, which was washed several times with ethanol to remove residual EDA. As can be seen in **Scheme 7-2**, this approach has its own

downside represented by inter and intra crosslinking between the amidated rGO, which may lead to aggregated and/or minimise the available free amino groups to react with CPPo.
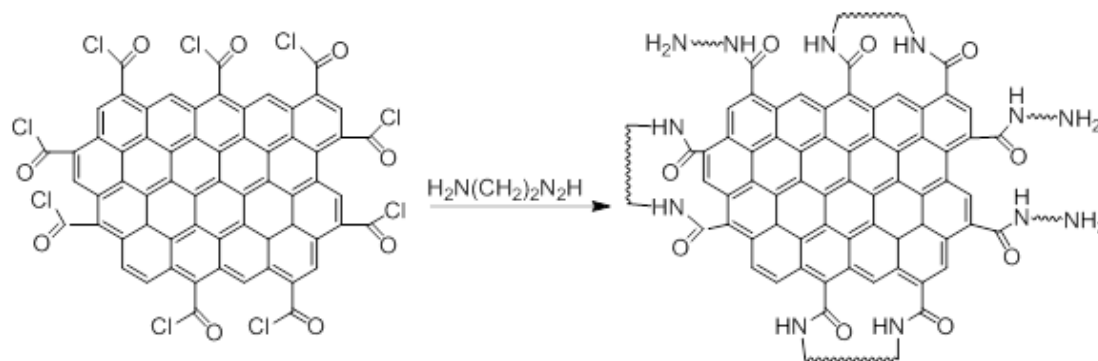
Scheme 7-2: Amidation of rGO-COCl with ethylenediamine.

7.2.4.3. Covalent Functionalisation of Am-rGO with CPPo

In order to prepare the CPPo functionalised rGO (CPPo-rGO), the CPPo's (**18**) carboxylic acid is activated using benzotriazol-1-yl-oxytripyrrolidinophosphonium hexafluorophosphate (PyBOP®) in anhydrous DMF which form of the active-OAt ester, which then reacts with the amino group of the EDA-rGO. In order to enhance the activation of carboxyl group, DIEA has been used. After 15 min of activation, the EDA-rGO dispersion/DMF was added to the CPPo (**18**) mixture, and then stirred for 4 hours at 40°C. The CPPo-rGO was the vacuum-filtered and washed extensively with excess methanol, and then dried in a vacuum oven at 60°C for 8 hours. **Scheme 7-3** illustrates the proposed covalent functionalisation route of rGO with the synthesised CPPo (**18**).
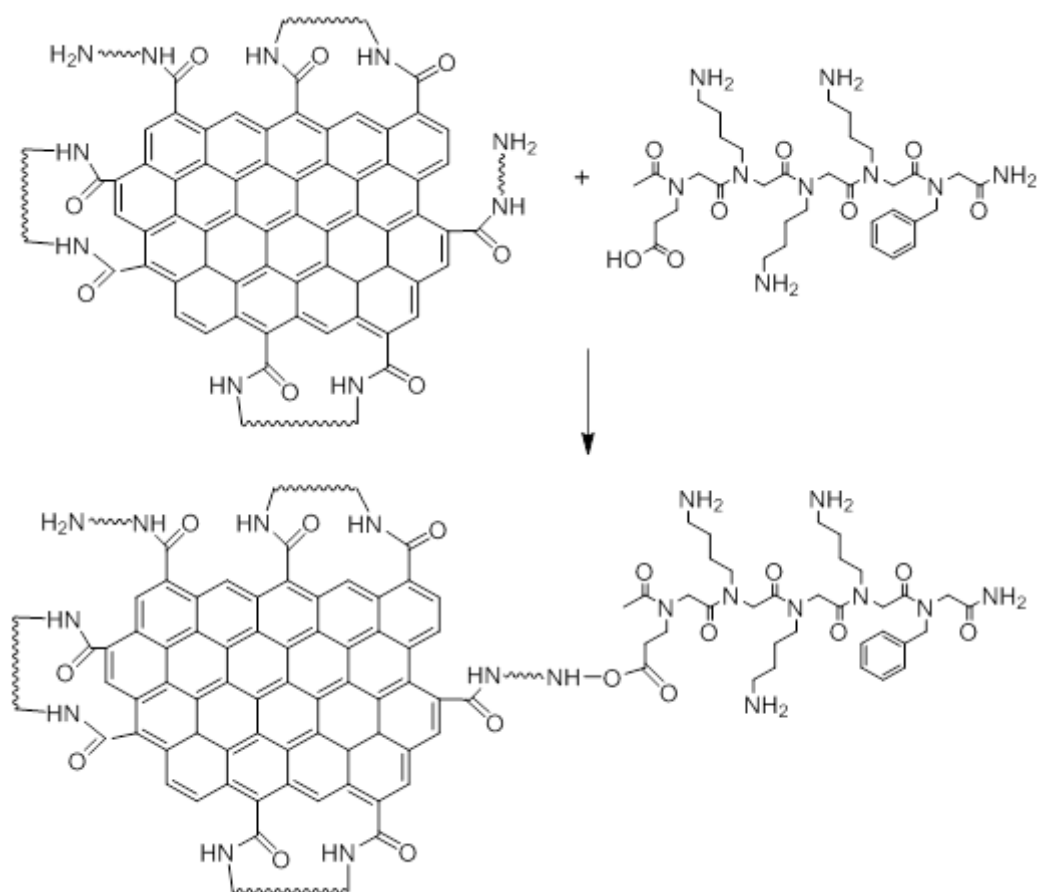
Scheme 7-3: Covalent functionalisation of CPPo (**18**) with EDA-rGO.

The aqueous dispersion of EDA-rGO and CPPo-rGO was prepared by probe sonication for 20 min in an ice bath, 1.0 mg of each sample in 1.0 mL of deionised water. The sonication was followed by centrifugation and separating the supernatant from aggregated material. **Figure 7-47** compares between the samples supernatant after sonication and centrifugation.
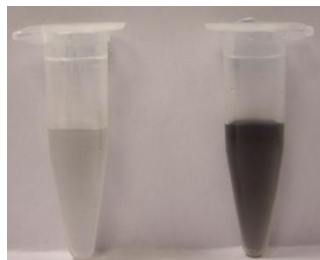
Figure 7-47: A visual comparison between aqueous supernatant of EDA-rGO (control) and CPPo modified rGO supernatant after sonication and centrifugation. Dispersion from left to right: CPPo-rGO, EDA-rGO (**19**).

The light grey colour of CPPo-rGO's supernatant compared to EA-rGO indicates that a limited amount of CPPo-rGO has been dispersed. As expected the dispersion of rGO in water (control) gave a clear solution. The dispersions are further characterised with UV-Vis-NIR spectroscopy to determine concentration of the dispersed rGO in each sample. The dispersed rGO concentration in each composite's supernatant was determined from optical absorption spectroscopy using the Beer-Lambert law and the calculated rGO extinction coefficient of 38.7 mL mg^{-1} cm^{-1} and absorption values at 660 nm (see **Appendix B**). **Table 7-10** shows the concentration of rGO in each supernatant.

Sample	Conc. of Dispersed rGO µg.mL^{-1}
H$_2$O	2.6
EDA-rGO	40.2
CPPo-rGO	21.2

Table 7-10 : Concentration of dispersed rGO in the supernatant of the aqueous dispersion of rGO (control), EDA-rGO and CPPo-rGO after sonication and centrifugation.

The UV-Vis-NIR absorption spectra of rGO (control), EDA-rGO and CPPo-rGO dispersion in water are shown in **Figure 7-48**. The absorption spectra of EDA-rGO supernatant shows a strong absorption peak at 231 nm which is almost overlapping with a small shoulder at 300 nm, which corresponded to the π–π* transitions of the aromatic C=C bond and the n–π* transition of the C=O bond, which is arising from the conjugated system of GO. However, the absorption spectrum of CPPo-rGO has a weak absorption peak at 231 nm indicating that a limited amount of EDA-rGO has been covalently grafted with CPPo (**18**). The control sample, rGO dispersion in water, does not show any absorption peak.
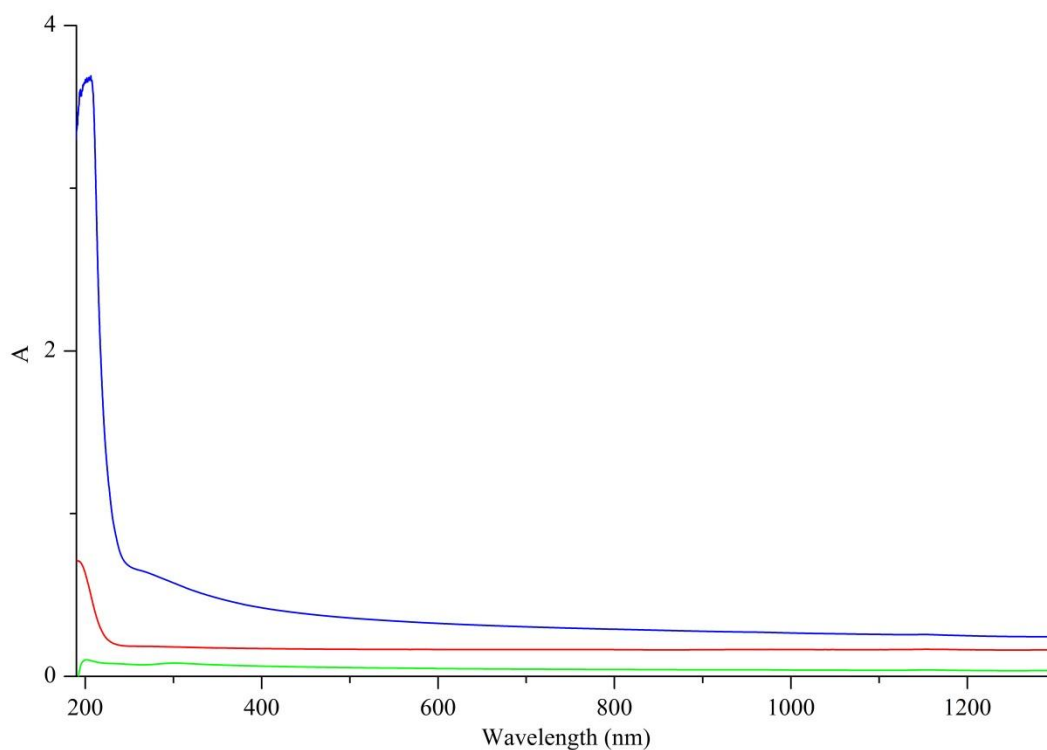
Figure 7-48: UV-Vis-NIR spectra of rGO (control) (**Green line**), EDA-rGO (**Blue line**) and CPPo-rGO (**Red line**).

The limited dispersion of EDA-rGO in water indicates that the chlorine atom has been substituted not only by the amide group of the EDA, but also that other reactions may have occurred which link the rGO sheets together to make big poorly dispersed aggregates. Additionally, the very low dispersion CPPo-rGO in water supports the assumption that a crosslinking reaction occurs between EDA-rGO. This results in limited number of free amino group for amidation reaction with the carboxylic group of CPPo (**18**). Therefore, only the EDA-rGO with a free amine group would react with the carboxylic group of CPPo (**18**). As a consequence, the limited number of CPPo is grafted on reduced graphene sheet, thus only 21.2 μg mL^{-1} of rGO is dispersed in water. Similar results have been found from comparing the thermal gravimetric analysis (TGA) under N$_2$ of CPPo-rGO with EDA-rGO (**Figure 7-49**).
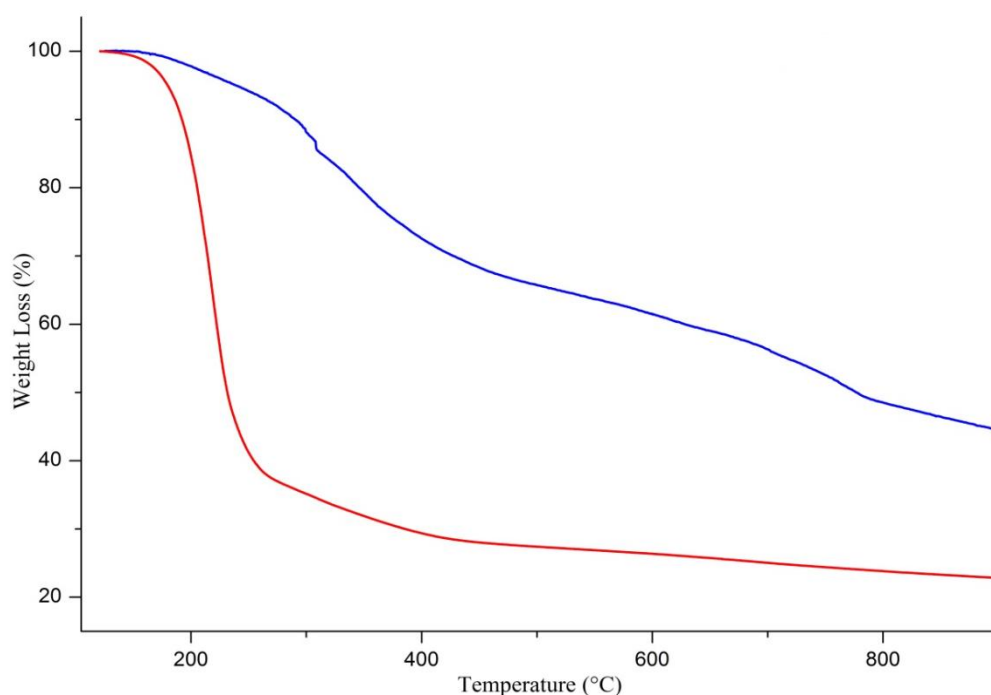
Figure 7-49: TGA of EDA-rGO (**Red line**) and CPPo-rGO (**Blue line**) under N$_2$.

The TGA of EDA-rGO under nitrogen reveals a major mass loss of about 61.2 % in the temperature range of $160 - 260$ °C. By comparison, the TGA of the CPPo-rGO shows a slight weight loss of about 55.5 % until the temperature reaches 900 °C while EDA-rGO lost 77.1 % at the same temperature. These results indicate that the amino groups in rGO have formed heat-stable structures via covalent bonding with the CPPo (**18**). Raman spectroscopy is an efficacious tool to probe the structural characteristics and properties of graphene-based materials. **Figure 7-50** shows a representative of G normalised Raman spectrum of rGO (control) and CPPo-rGO. The samples are drop casted on a silicon wafer and left to dry in air. The measurement repeated 10 times at different areas of the sample.
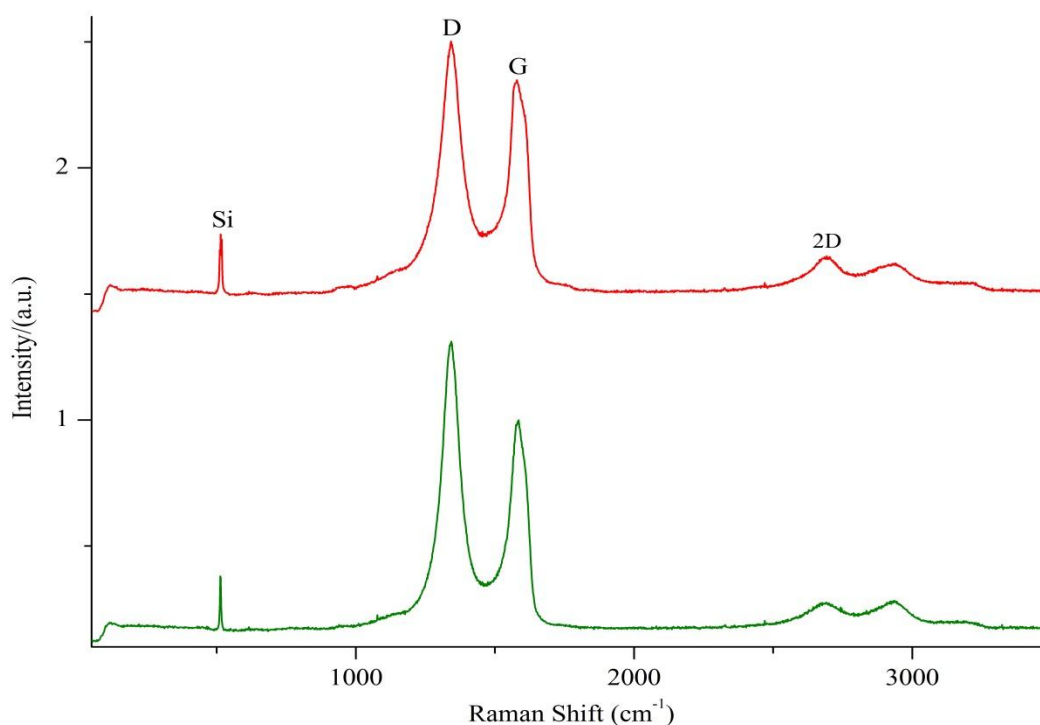
Figure 7-50: A representative normalised Raman spectra (532 nm) of rGO (**Green line**), and CPPo-rGO (**Red line**).

In the spectrum of rGO, the peak at 1581.3 ± 0.7 cm^{-1} (G-band) corresponds to an E_{2g} mode of graphite and is related to the vibration of sp^2-bonded carbon atoms in a 2D hexagonal lattice. The peak at 1338.6 ± 0.7 cm^{-1} (D-band, the breathing mode of A_{1g} symmetry) is associated with vibrations of carbon atoms with dangling bonds in plane terminations of disordered graphite. The Raman I_D/I_G ratio is widely used to evaluate the quality of graphene and graphene-based materials. The ratio is a measure of the disorder in the sample, which can be edges, ripples, or any other defects, such as doping organic functions in graphene. From the Raman spectrum obtained of CPPo-rGO, a I_D/I_G of 1.4 ± 0.02 can be calculated, compared with I_D/I_G of rGO which is about 1.3. The I_D/I_G ratio of CPPo-rGO increases in comparison with that of starting material, implying the functionalisation process of graphene skeleton has introduced an amount of structural disorder in the graphene lattice, which also demonstrates that rGO has been chemically modified with CPPo molecules.

7.2.5. Covalent Functionalisation of Graphene Oxide with Thymidine and Adenosine

The discussed results in (**Section 7.2.3**) suggest that there was a very weak noncovalent interaction between nucleobases and ribonucleosides with reduced graphene oxide (rGO). Therefore, this section studied the covalent functionalisation of rGO with ribonucleosides to improve its dispersion in water.

GO was prepared by a Hummers method using graphite as precursor. As-synthesised graphite oxide (50 mg) was exfoliated with deionised water to a concentration of 1.0

mg mL^{-1} by probe sonication for 40 min in an ice bath to produce graphene oxide (GO). The acetylation of the freeze dried GO (50 mg) was refluxed in an excess amount of thionyl chloride (SOCl$_2$) (20 mL) in the presence of anhydrous *N,N*-dimethylformaide (DMF) at 80℃ for 24 h to yield acyl chloride-bound GO (GO-COCl). The product was vacuum-filtered and washed with anhydrous DMF. The GO-COCl powder was collected immediately and divided into two, then separately reacted with a ribonucleoside solution (adenosine, and thymidine) in DMF in the presence of catalytic amounts of triethylamine (Et$_3$N) at 130 °C for 72 hours under a nitrogen atmosphere. The acetyl chloride reaction with amine group forms hydrogen chloride (HCl), which protonates the amine, making it less nucleophilic. Therefore, the Et$_3$N is added to neutralise the acid by forming triethylamine hydrochloride salt, thus freeing the amine for attack on the acid chloride and allows the reactions to proceed to completion. Finally, both of the ribonucleoside/GO composites (adenosine/GO, thymidine/GO) were washed with HCl solution (0.5 mM L^{-1}) to remove any adsorbed ribonucleoside on rGO surface, then and washed with deionised water and dried in a vacuum oven at 45 °C. The synthetic route for preparation of water-dispersible ribonucleoside/GO composites is illustrated in **Scheme 7-4**.
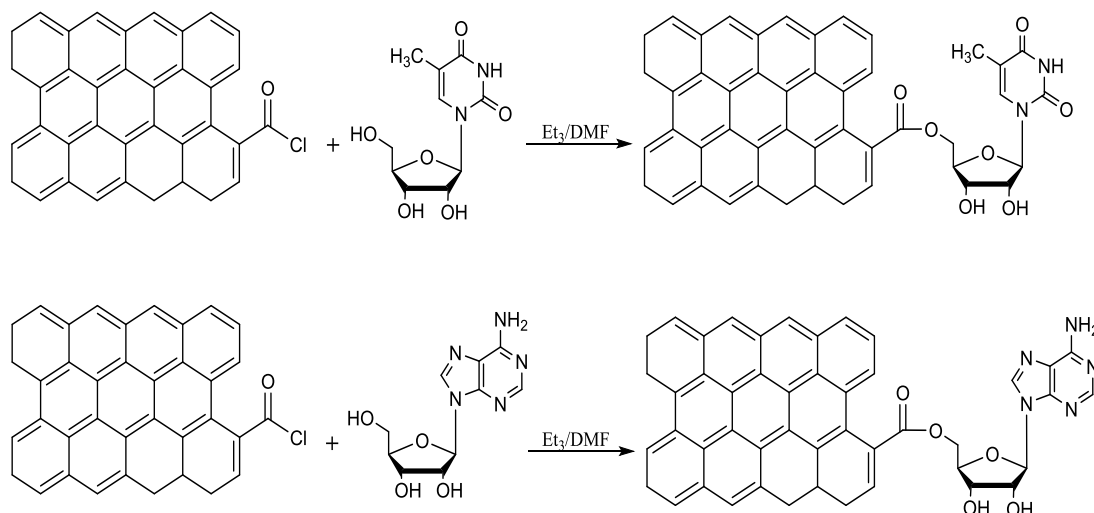
Scheme 7-4: The synthesis route of ribonucloside/GO composite.

To examine the dispersion ability of the prepared ribonucleoside/GO composites, 1.0 mg of each composite was dispersed in deionised water to make a 1.0 mg mL^{-1} solution by probe sonication for 20 min in an ice bath. The image shown in **Figure 7-51** provides a visual observation on the dispersion states of each sample.
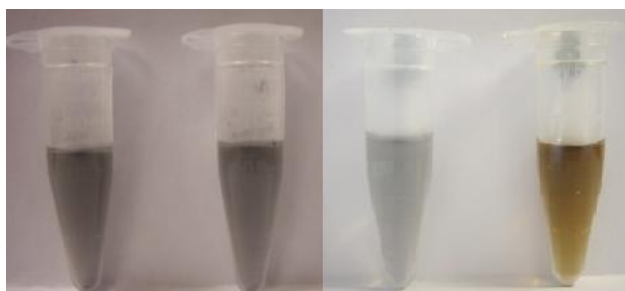
Figure 7-51: Visual comparison between the aqueous supernatant after sonication and centrifugation. Dispersion from left to right: adenosine-GO, thymidine-GO, rGO, and GO (control).

In comparison to rGO, GO showed a better water dispersion stability due to the presence of covalently bonded oxygen containing groups on the surface. However, GO tends to form irreversible agglomerates into multilayeric graphite via strong π–π stacking and van der Waals interaction, indicated by the existence of a solid at the

bottom of the vial. In contrast, the color of adenosine/GO and thymidine/GO supernatant indicates good dispersion efficiency in water. The aqueous dispersions of the composites were stable for at least 2 weeks without aggregates. The presence of the ribose fragment in the nucleoside moiety covalently grafted to the GO sheet, allows the dispersion of the different ribonucleoside/GO complex (i.e. adenosine/GO, and thymidine/GO) in water.

UV-Vis-NIR absorption was used for a direct measurement of the concentration of dispersed ribonucleoside/GO supernatant in aqueous supernatant via the Beer-Lambert law and estimated extinction coefficient of rGO at 660 nm (ϵ_{660} = 38.7 mL mg^{-1} m^{-1}) (**Appendix B**). The concentration of ribonucleoside/GO complexes dispersed in water is shown in **Table 7-11**.

Composite	Conc. of Dispersed rGO. µg mL^{-1}
Adenosine/GO	20.8
Thymidine/GO	22.5

Table 7-11: Concentration of dispersed ribonucleoside/GO composite in the supernatant determined from their UV-Vis-NIR absorption after sonication and centrifugation.

The concentration of thymidine/GO in the supernatant after centrifugation was greater than the adenosine/GO. This indicates that the covalent grafting of thymidine on graphene was more successful that adenosine. **Figure 7-52** illustrates the UV-Vis-NIR absorption spectra of adenosine/GO, thymidine/GO, GO, adenine, and thymidine in water. Both of the ribonucleosides, adenine and thymidine, show a sharp peak centred at ~ 260 nm, which is due to the π–π* transition of conjugated electrons of the ribonucleoside ring.[496] While, adenosine/GO and thymidine/GO

complexes exhibited a broad peak at around 280 nm and strong peak at ~ 200 nm.
These results indicate that the utilised high temperature reaction condition resulted in
a covalent attachment of these ribonucleosides to GO and also a reduction of the GO
to rGO. However, due to attachment of these groups on GO the resulting composite
had good dispersion efficiency in water compared to rGO.
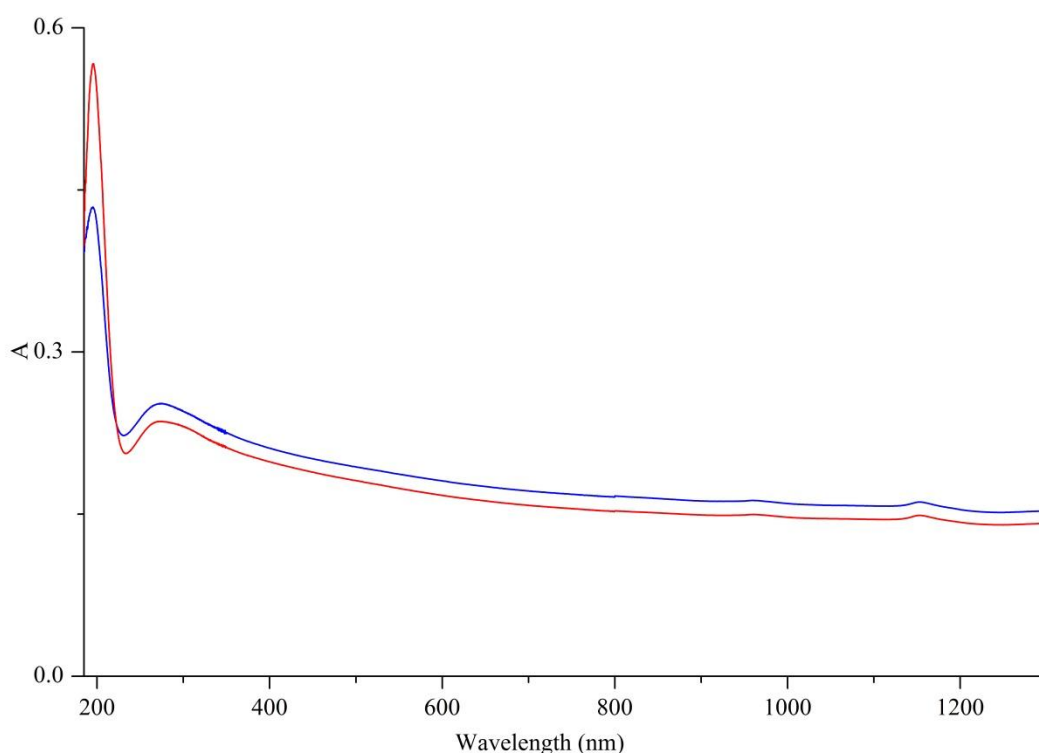
Figure 7-52: UV-Vis-NIR absorption spectra of the dispersion supernatant of (**Red line**)
adenosine/GO, and (**Blue line**) thymidine/GO.

The attachment of each ribonucleoside to the graphene sheets was further analysed
using TGA by heating under a nitrogen atmosphere to 900 °C at a rate of 10 °C.
min^{-1}. **Figure 7-53** shows the thermogravimetric profiles of adenosine/GO,
thymidine/GO, GO. The TGA of GO reveals a major weight loss of about 30 % in
the temperature range of 200 – 240 °C corresponding to the decomposition of labile

oxygen-containing groups and illustrating its thermally instability. Grafting of a ribonucleoside on the graphene sheet in adenosine/GO and thymidine/GO may increase the thermal stability of GO leads to low weight loss. While GO lost 65 % at 350 °C adenosine/GO and thymidine/GO showed a lower weight lost. These results indicate that the oxygen-based groups in GO have formed heat-stable structures via covalent bonding with the thymidine and adenosine moieties. Additionally, the difference in the amount of weight loss between the two composites suggested that thymidine the covalent attachment of was more successful than the adenosine.
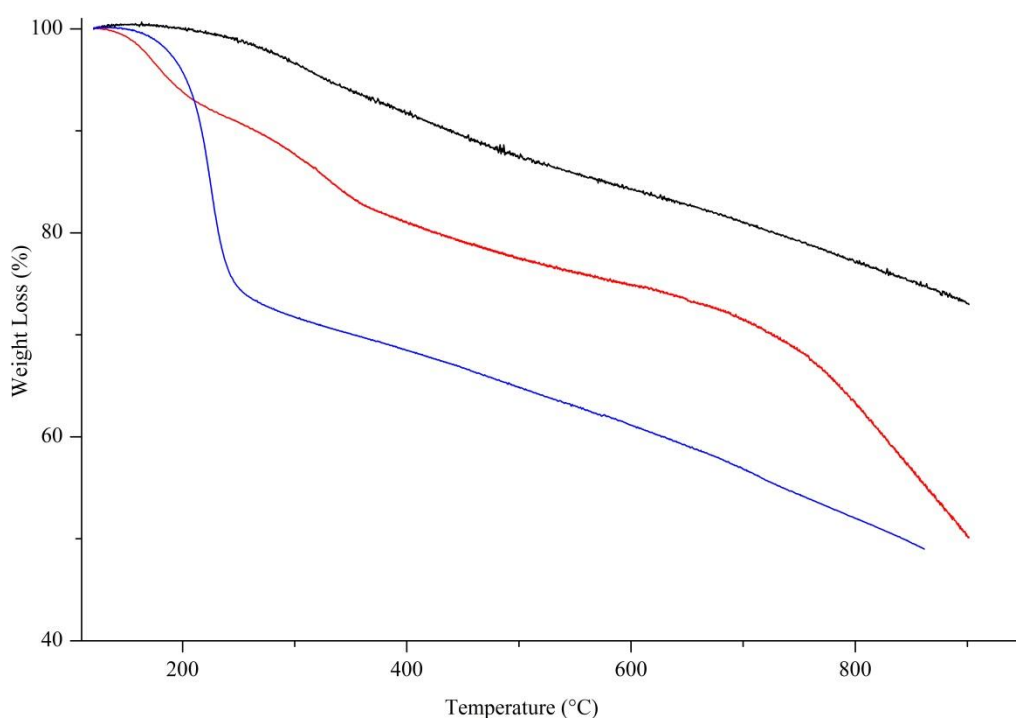
Figure 7-53: TGA of (**Blue line**) GO, (**Red line**) thymidine/G, (**Black line**) adenosine/GO under N_2.

To verify the selective molecular recognition by the complementary ribonucleosides; thymidine and adenosine on GO, the aqueous dispersion of adenosine/GO, and

thymidine/GO composites were shaken for 2 min. immediately after that the mixture

start to precipitate was formed as shown in **Figure 7-54**.

Figure 7-54: The mixture of aqueous dispersion of adenosine/GO and thymidine/GO after 2 min shaking.

The presence of complementary hydrogen bonding arrays, i.e. donor sites comprising

the NH amide and NH amine, and acceptor sites comprising the O and N

functionalities, allow ribonucleosides to oligomerise via hydrogen bonding.[497] Thus,

the interaction between ribonucleoside groups attached to GO shown in **Scheme 7-5**

affects the dispersibility behaviour of ribonucleoside-rGO in H_2O as polar solvents

able to interact via H-bonds with the complementary sites of ribonucleoside.
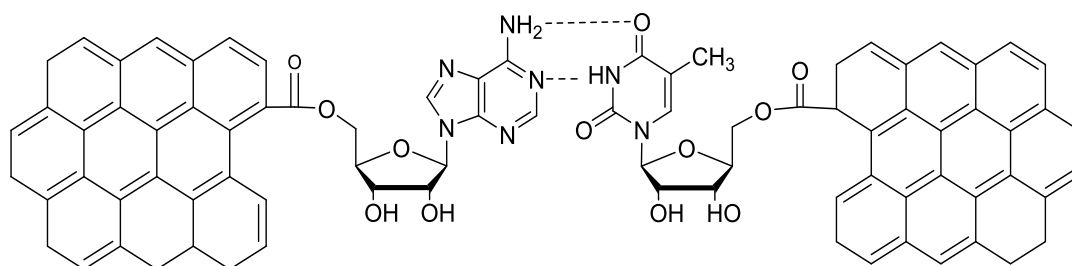
Scheme 7-5: Schematic representation of the recognition processes between complementary base pairs, adenosine-GO/thymidine-GO.

The changes of structure from GO to ribonucleoside grafted GO are also reflected in

the Raman spectroscopy. The Raman spectra of adenosine/GO and thymidine/GO are

compared with GO, thymidine and adenosine in **Figure 7-55**.sipersions were drop

casted on silicon wafer and left to dry in air , their Raman were repeated at less 10 times at different areas of the sample.
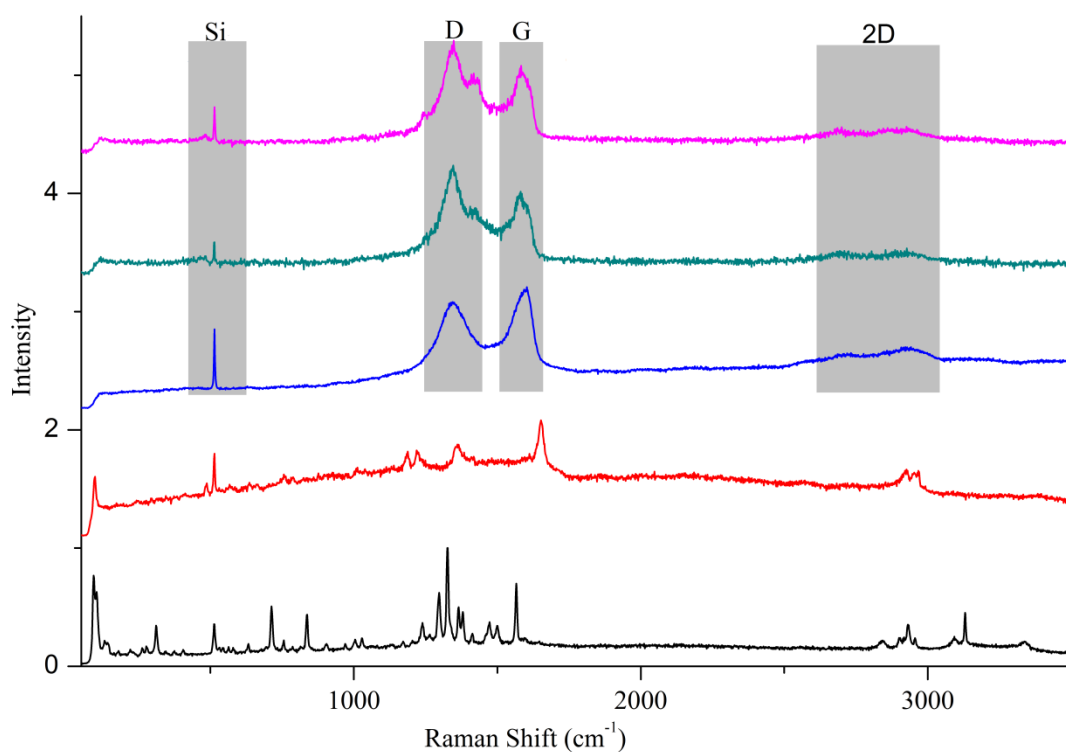
Figure 7-55: A representative Raman spectra (532 nm) of adenosine (**Black line**), thymidine (**Red line**), GO (**Blue line**), adenosine/GO (**Green line**), thymidine/GO (**Pink line**).

The Raman spectrum of GO displays broadened G band at 1597.6 ± 1.5 cm^{-1} and D band at 1344.0 ± 1.7 cm^{-1}. Similar bands are seen in the Raman spectra of adenosine/GO and thymidine/GO. However, both composites show an additional band fused into their D band. This additional peak is assigned to presence of ribonucleosides.

7.3.   Conclusion

In this chapter, rGO was covalently and noncovalently functionalised with a series of biomolecules. It was found that nano-1 peptide had the highest capability in dispersing rGO compared to its short version, short nano-1 peptide. This suggests that increasing the number of hydrophobic residues (Phe, and Val) in the peptide's sequence increases the amount of rGO that is dispersed. Thus, it is believed that this noncovalent dispersion depends on the adsorption of the hydrophobic face of the amphiphilic nano-1 peptide on the hydrophobic surface of a rGO sheet. However, the concentration of dispersed rGO by these peptides was found to less than that of purified SWNTs (**Chapter 4**). This is thought to be due the planarity of rGO surface and the helicity of the peptide. It was believed that the interaction of biomolecules with higher backbone flexibility can show a higher dispersion affinity towards rGO. Thus, a peptoid with an 18 residues was used in the dispersion of rGO. It was found that the concentration of rGO dispersed by the peptoid was higher than that of nano-1 peptides. This shows that the flexibility of the peptoid's backbone compared to the peptide's backbone allows it to assembly on the flat rigid surface of the rGO sheets without disrupting the peptoid's helicity.

In a similar context, rGO was noncovalently functionalised with ribonucleosides, nucleobases, and ribose. The optical absorption of these composites indicated that ribonucleosides and its nucleases, and ribose moieties have very limited dispersion affinity towards rGO. Thus, it was that thought that there is a very weak π–π stacking interaction between the ribonucleosides and the hydrophobic surface of the rGO; due to the small ring size of the ribonucleosides they show very dispersion affinity towards rGO. However, they dispersion ability is still higher than nucleobases. This

is thought to be due the presence of the ribose moiety in ribonucleosides, which decreases its hydrophobicity and thus increases its solubility in water. In all pervious dispersions, the Raman spectroscopy of dispersion of rGO composites showed a shift in its G band comparing to rGO (control). This up shift provides evidence that the interaction mechanism between these biomolecules and rGO depends on the biomolecule's aromatic residues via π stacking with the rGO surface. Furthermore, it supplies an evidence for a weak charge transfer between them.

This chapter also studied the covalent functionalisation of rGO with a cell penetrating peptoid (CPPo), thymidine, and adenosine. In both cases, the rGO was converted to its acetylated form then reacted with the biomolecules. The concentration of the aqueous dispersion of CPPo/rGO, thymidine/rGO, and adenosine/rGO found to higher than the unmodified rGO. Furthermore, The TGA analysis of the covalently functionalised rGO with these biomolecules showed a higher weight loss than the unmodified rGO. This provided is further evidence for the covalent grafting of rGO with biomolecules. The Raman spectra of the covalent rGO composites shows increases in the I_D/I_G comparison with that of starting material, implying the functionalisation process of graphene skeleton has introduced an amount of structural disorder in the graphene lattice.

.

.

8.   Thesis Conclusion

The focus of this thesis has been the exploration SWNTs and rGO covalent and noncovalent functionalisation with peptides, peptoids, and ribonucleosides in water to gain a better understanding on the factors that controls the dispersion of nanomaterials with biomolecules.

The results in **Chapter 4** showed that peptide N-terminus acetylation has a greater effect on short sequence peptide ability to disperse SWNTs compared to long sequence peptide. It was found that acetyled short nano-1 had a better tendency to disperse the purified SWNTs than its free N-terminus version. While N-terminus acetylation of long sequence nano-1 peptide did not a significant effect on their ability to disperse purified SWNTs.

Additionally, the ^{19}F NMR signal of fluorinated nano-1 peptide used to study the interaction between the peptide with the side wall of purified SWNTs disappeared from the spectra after its interaction with the nanotubes. This is thought to be due to peptide's noncovalent bonding to the nanotube side wall. However, the signal did not appear after the sedimentation of nanotubes. This is thought to be due to the fact that the peptide has sedimented from the dispersion while still noncovently attached to the SWNTs.

Finally, this chapter investigated the enzymatic degradation of peptide/SWNTs composite. It was found that when Ac nano-1 (**6**) was non-covalently mixed with SWNTs that it was enzymatically digested more slowly than short Ac nano-1 peptide (**4**) by trypsin. This thought to be due to the more rapid exchange that short Ac nano-

1 peptide (**6**) will have between its SWNT bound and unbound forms compared to to full length Ac nano-1 (**4**)

In **Chapter 5** a series of chiral amphiphilic peptoids which vary in the number of aromatic residues on the hydrophobic surface of the helix yet have the same hydrophilic/hydrophobic ratio were synthesised. The absorption spectra of the peptoid/SWNTs dispersions revealed that the peptoids ability to disperse individual SWNTs increases with increasing the number of aromatic residues in the peptoid. Also the stability of these dispersions with respect to time has been studied. It was found that peptoid/purified SWNTs dispersion stability increased with increasing the number of residues in the peptoid. The Raman G band peak shift to higher frequencies suggested that peptoid acts as an electron acceptor and the SWNT acts as an electron donor (charge-transfer interaction). Altogether, these results suggest that the noncovalent peptoid/SWNT interaction does not perturb the electronic structure of SWNTs. In this context, designed peptoid may provide an accessible means to incorporate the desired electrical properties of SWNTs into biocompatible nanoscale electronic devices. TEM and AFM measurements reveal that the chosen peptoids are capable of fully coating the SWNT surface and dispersing individual SWNTs and will facilitate many applications of SWNTs to medical problems; such as artificial muscles or biomedical sensors that can be placed inside the human body. Hybrids of biomolecules and nanomaterials are promising candidates in the development of novel therapeutics and electronic devices. Since peptoids are known for their potential application as a drug due to their resistance to proteases and long life in the human body. The next step for this work would be to study the toxicity, cell penetration, and cellar uptake of the biological active peptoid/SWNT composite.

These biological tests will test the possibility of improving the biological activity of peptoids upon their interaction with CNTs. This will open the possibility of using peptoid/CNTs composites in biological and medical applications

The noncovalent interaction of ribonucleosides, nucleobases, and ribose sugar with purified and oxidised SWNTs was investigated in **Chapter 6**. The results indicated the interaction of these biomolecules with oxidised SWNTs vary in the dispersion ability toward nanotubes depends on the number of oxygen-containing functional groups on the nanotube's surface and the competition between water molecules which can from hydrogen bonds with oxidised nanotubes, with ribonucleosides and nucleobases over adsorption sites. Additionally, it was found that mixing two complementary ribonucleoside/oxidised SWNTs resulted in precipitation of the nanotube due to the Watson Crick pairing. These results suggest that the interaction depends on a nonhydrophobic interaction between the nucleobase moiety in a ribonucleoside interacts with oxygen functional groups on nanotube surface. While, its ribose sugar moiety interacts with water molecules. This interaction will undoubtedly provide a new and exciting playground in the ribonucleosides self-assembly for the development of novel make functional architectures.

Finally, in **Chapter 7** the noncovalent and noncovalent functionalisation of rGO with series of biomolecules including peptide, peptoid, and ribonucleosides has been studied.

The aqueous dispersion of rGO with peptides and peptoids indicated that the interaction of rGO with biomolecules with higher backbone flexibility can show higher dispersion affinity towards rGO. Thus, the concentration of rGO dispersed by

the peptoid was higher than that of nano-1 peptides. This shows that the flexibility of the peptoid's backbone compared to the peptide's backbone allows it to assembly on the flat rigid surface of the rGO sheets without disrupting the peptoid's helicity.

In a similar context, rGO noncovalently functionalised with ribonucleosides, nucleobases, and ribose was studied. The optical absorption of these composites indicated that ribonucleosides and its nucleases, and ribose moieties have very limited dispersion affinity towards rGO. Thus, it was that thought that there is a very weak π-π stacking interaction between the ribonucleosides and the hydrophobic surface of the rGO; due to the small ring size of the ribonucleosides they show very dispersion affinity towards rGO. However, they dispersion ability is still higher than nucleobases. This is thought to be due the presence of the ribose moiety in ribonucleosides, which decreases its hydrophobicity and thus increases its solubility in water. The Raman G band peak up shift provides evidence that the interaction mechanism between these biomolecules and rGO depended on the biomolecule's aromatic residues via π stacking with the rGO surface. Furthermore, it supplies an evidence for a weak charge transfer between them.

Finally this chapter studied the covalent functionalisation of rGO with a cell penetrating peptoid (CPPo), thymidine, and adenosine. In functionalisations, the rGO was converted to its acetylated form then reacted with the biomolecules. Although the concentration of the aqueous dispersion of CPPo/rGO, thymidine/rGO, and adenosine/rGO was very limited, it was higher than the concentration of unmodified rGO in water.

9. EXPERIMENTAL SECTION

9.1. Materials and Reagents

All reagents used in this project were purchased from Sigma Aldrich and used without further purification unless otherwise specified. Peptide synthesis grade DMF was obtained from AGTC Bioproducts (Hessle, UK), PyBOP from Apollo Scientific (Stockport, UK) and NMR solvents which were purchased from Cambridge Isotopes Inc., supplied by Goss Scientific (Crewe, UK). All resins were purchased from Novabiochem (Darmstadt, Germany). These chemicals were used without further purification and stored under appropriate conditions, as detailed in the manufacturer's instructions. Solvents were removed under reduced pressure using a Büchi Rotavapor R11. The following centrifuges were used: an Eppendorf centrifuge 5415D (for 1.5 mL tubes). Aqueous solutions were lyophilised using a Christ Alpha 1-2 LD Plus freeze-drier.

9.2.   Equipment Methodology

9.2.1.   Raman Spectroscopy

Raman spectra were recorded using a Horiba Jobin Yvon LabRam Evolution HR spectrometer in a back scattered confocal configuration using a Nd:YAG laser (532 nm, 2.33 eV.) for graphene based nanomateriales and He:Ne Laser (633 nm, 1.96 eV.) for carbon nanotube samples. The spectrometer was equipped with a CCD detector. The samples were prepared by drop casting them onto silicon slides then left to dry in air before analysing. All spectra were referenced to the position of the A_{1g} Raman active mode of Silicon at 520 cm^{-1}. All spectra were nomliaed to the G band. Analysis of the data was performed using the proprietary Labspec 6 data, where peak fits were obtained using classical least square (CLS) fitting with lineshapes that were permitted to have asymmetric, Gaussian and Lortenzian character.

9.2.2.   Ultraviolet-Visible-Near Infrared (UV-Vis-NIR) Spectroscopy

UV-vis spectroscopy was performed on a Perkin Elmer Lambda 900 UV/Vis/NIR spectrometer over a wavelength range of 200 – 1300 nm. Where necessary the samples were diluted prior to measurement, such that the absorbance of the sample remained below 2.5, and the absorbance of the original solution was found by multiplying the obtained value by the dilution factor. Measurements were taken using 0.2 cm paired quartz cuvettes for the sample and the blank.

9.2.3. Sonication of Carbon Nanomaterials

Dispersions of graphitic material were prepared by probe sonicating (probe model: Cole Parmer Ultrasonic Processor (750 W), ¾" probe tip) 1 mg of the sample in 1 mL of selected solvent for 15 min for CNTs and 20 min for graphene nanomaterials (30 % amplitude, pulse 5 sec on: 5 sec off (total time 30 min and 40 min, respectively)). External ice baths was used to cool the mixture during sonication. Then the dispersion is centrifuged at 6.000 rpm for 90 sec.

9.2.4. Atomic Force Microscopy (AFM)

Analyses were carried out in Tapping-Mode (TM-AFM), in air at r.t., using a using a Nanoscope IV scanning probe microscop. The surfaces for AFM analyses were prepared as follows: the carbon nanomaterial dispersion was drop casted on a freshly cleaved mica surfaces. Then they left to dry in air. Surfaces were imaged with nitride -doped silicon tips (cantilever: thickness = 25 μm, length = 25 μm, frequency f0 = 70 kHz, force constant k = 0.4 N/m; Veeco). Analysis of the AFM images was carried out using Nanscope analysis 1.5 software.

9.2.5. Transmission electron microscopy (TEM)

Microscopy was conducted on a JOEL-2100 FEG TEM operated at 80 kV under high vacuum conditions. Samples for TEM were prepared by drop depositing onto holey carbon TEM grids (Cu, 300 mesh, SPI Supplies) a dispersion of the nanomaterial.

Samples were left to dry in air before imaging and then loaded into the TEM using a Gatan model 914 single tilt holder. HRTEM images were collected on a Gatan Orius camera. Data analysis was conducted using the proprietary Digital Micrograph software.

9.2.6. Thermogravimetric Analysis (TGA)

TGA was carried out using a Perkin Elmer Pyris I. Carbon samples (1 − 10 mg) were heated in a ceramic boat from 30 − 120 °C/10 °C per min, the temperature was then held at 120 °C for 30 min to remove any residual solvent. After this the sample was heated under compressed air in a ceramic pan from room temperature to 900 °C at a rate of 10 °C per min.

9.2.7. Thermogravimetric Analysis – Mass Spectrometry (TGA-MS)

TGA− MS was performed on a Perkin-Elmer Pyris 1 TGA in a helium atmosphere. The TGA was coupled to a HIDEN HPR20 mass spectrometer which used evolved gas analysis to determine the released species. Carbon samples (1 − 3 mg) were heated in a ceramic boat from 30 − 120 °C/10 °C per min, the temperature was then held at 120 °C for 30 min, and then heated to 900 °C at a rate of 10 °C per min.

.

9.2.8.   Mass Spectroscopy (MS) Liquid Chromatography Electrospray Ionisation Mass Spectrometry (LC-MS)

Analytical LC– MS data were obtained using a triple quadrupole mass spectrometer equipped with an Acquity UPLC (Waters Ltd, UK) and a photodiode array detector. Samples were injected onto the Acquity UPLC BEH C8 column 1.7 μm (2.1 mm × 50 mm) with a flow rate of 0.6 mL min^{-1} and a linear gradient of 5–95 % of solvent B over 3.8min (A = 0.1 % formic acid in H$_2$O, B = 0.1 % formic acid in MeCN). The flow was introduced into the electrospray ion source of the Aquity TQD mass spectrometer.

9.2.9.   Matrix Assisted Laser Desorption/Ionisation-Time of Flight Mass Spectrometry (MALDI-TOF MS)

MALDI-ToF mass spectra were obtained using an Autoflex II ToF/ToF mass spectrometer with a 337 nm nitrogen laser (Bruker Daltonik GmBH) operating in positive mode. Samples were dissolved in 1:1 deionised water (0.1 % TFA)/MeCN. The sample solution (1mg mL^{-1}) was mixed with the matrix solution (an α-cyano-4-hydroxycinnamic acid matrix) in a ratio of 1:9 and 1 μL of this was spotted onto a metal target and placed into the MALDI ion source.

9.2.10.   Circular Dichroism Spectroscopy (CD)

Circular dichroism measurements were conducted using a Jasco Model J-1500 spectropolarimeter fitted with a Jasco J815 MCB-100 mini circulation bath. All measurements were carried out using 0.1 cm path length and 500 μL quartz cuvette. The peptoid and peptide concentration are based on their dry weight after lyophilisation. Samples were made to 1 mM in distilled water, and then diluted to 50 μM for the peptoid and 100 μM for the peptide in a phosphate buffered solution (PBS). 300 μL of this solution was transferred to a cuvette for the measurements. All data collection was taken at room temperature and data was collected as an accumulation of 10 measurements, adjusted by the background spectrum of the PBS buffer. Scans were conducted at 50 nm/min between 260 – 190 nm, 1 nm data pitch, 5 mdeg sensitivity and a 2 sec response.

Mean residue molar ellipticity [θ] was obtained using the equation:

$$[\theta] = (100 \ x \ \theta obs \ x \ M \ )/(n \ x \ 1 \ x \ C)$$

Where θobs is measured ellipticity (degrees), M is the molecular weight (g mol^{-1}), n is the number of residues, l is path length (cm), and c is the concentration of biomolecule (mg mL^{-1}).

9.2.11.   High Performance Liquid Chromatography (HPLC)

Crude biomolecules (peptides, and peptoids) were purified by reversed-phase high-performance liquid chromatography (RP-HPLC) using a Speck and Burke Analytical

C-18 column (5.0 μm, 10.0 x 250 mm) attached to a PerkinElmer Series 200 LC Pump and 785A UV/Vis Detector. For preparative runs, concentrations up to 30 mg mL^{-1} (1.0 mL) were injected and peak fractions of interest pooled and lyophilised. All samples were prepared by dissolving their crude powder in H_2O/acetonitrile then centrifuged before injection to remove undissolved material. A flow rate of 2 mL min^{-1} was used for all separations. The aqueous phase (solvent A) consisted of a mixture (*v/v*) 95 % H_2O/5% CH_3CN with 0.1 % TFA while the organic phase (solvent B) consisted of a mixture (*v/v*) 5 % H_2O/95 % CH_3CN with 0.1 % TFA. Initial injections of each biomolecule sample were set to 45 to 90 min for linear gradients of 0-100 % of solvent B to detect different compound peaks, and either shorter times or shorter gradients (from solvent A to B) applied for subsequent injections depending on each peptide sequence. A UV-Vis lamp was used as detector and 280 nm was the wavelength selected in all cases to monitor and detect the chromophore of the aromatic residue–which was part of the synthesised peptides and peptoids sequence.

9.2.12. Nuclear Magnetic Resonance (NMR)

^{1}H, ^{13}C, ^{19}F NMR spectra were obtained on the following machines; Varian Mercury-400 and 700 MHz, Varian VNMRS-600 MHz and Bruker Avance-400 and 700 MHz spectrometers. Chemical shifts are reported in parts per million (δ ppm) and are referenced to residual solvent peaks. J couplings are reported in megahertz (MHz). Multiplicities: s = singlet, d = doublet, dd = doublet of doublets, ddd = doublet of doublet of doublets, dt, doublet of triplets, m = multiplet, t = triplet, q =

quartet, bd = broad doublet, bs = broad singlet, app s = apparent singlet, app d = apparent doublet, app t = apparent triplet, app td = apparent triplet doublet. All organic synthesis reactions were monitored by TLC using Merck precoated silica gel plates.

9.3. General experimental procedures

9.3.1. Negishi Chemistry

Acid washed zinc dust (4.00 eq.) was placed in a pyrex test tube flask fitted with a screw top that could b opened when chemicals were added at the time that vacuum or argon were applied. The reaction flask was evacuated under heating at 100 ˚C for at least 30 minutes with vigorous stirring. After this the reaction mixture was cooled to 70 ˚C and vacuum line stopped, then placed under a positive pressure of argon. Then anhydrous DMF (0.5 mL) and I_2 (0.015 g) were added and the light grey suspension stirred for a further 20 min. The reaction mixture was then cooled to 50 ˚C followed by the addition of the corresponding iodoalanine (1.00 eq.) in anhydrous DMF (0.5 mL). After stirring for 20 minutes under argon, addition of the catalyst $Pd(dba)_2$ (0.03 eq.), the 2-dicyclohexylphosphino-2',6'-dimethoxybiphenyl (SPhos) (0.010 eq.) and the relevant aryl halide (1 eq.) were added and the resulting black mixture stirred at 50 ˚C under argon for a minimum of 5 hours. The reaction mixture was sealed to keep in the Argon and cooled to room temperature whilst stirring overnight. The cooled reaction mixture was purified *via* column chromatography without work-up (SiO_2; 80/20 hexane/EtOAc → 100 % EtOAc and if impure a second column was run using SiO_2; 100 % CH_2Cl_2).

9.3.2. Fmoc-SPPS Peptide Synthesis

9.3.2.1. Microwave Assisted Automated Fmoc-SPPS

Peptide syntheses were undertaken on a CEM Liberty microwave peptide synthesiser fitted with a Discover microwave unit and a 30 mL PTFE reaction vessel. Pre-synthesis swelling of the resin was carried out in DMF for 1 h at room temperature. Microwave assisted coupling cycles were carried out for 10 min at 75 °C (25 W) with amino acid (5.0 eq.), TBTU (5.0 eq.) and DIPEA (10.0 eq.). In the case of double couplings, the vessel was drained after the first cycle and coupling cycle was repeated with fresh reagents. The Fmoc deprotection step was carried out for 10 min at 75 °C (45 W) with a solution of 20 % piperidine in DMF.

9.3.2.2. Manual Fmoc-SPPS

Manual SPPS was carried out at room temperature for 2 hours with amino acid (4.0 eq.), TBTU (5.0 eq.) and DIPEA (10.0 eq.) in a fritted polypropene vessel. For successive couplings the vessel was drained after the each coupling cycle and the coupling cycle was repeated with fresh reagents. The Fmoc deprotection step was carried out for 15 min with a solution of 20 % piperidine in DMF, followed by a further treatment for 15 min with a fresh solution of 20 % piperidine in DMF. In all steps agitation was provided by rolling.

9.3.2.3. Peptide Cleavage

Pre-cleavage the peptide-resins, in a fritted polypropene vessel, were washed with DCM (x 3) and ether (x 3) and left to air dry for 5 min. Subsequently the peptide-resins were treated with a (4 mL per 0.1 mmol of resin) solution of 2.5 % TIPS and 2.5 % H_2O in TFA for 4 h at room temperature. The resin was then removed by filtration and the filtrate was added dropwise to ice-cold diethyl ether. After centrifugation the supernatant was removed and the pellets suspended in fresh ether and centrifuged again. Following further centrifugation, the supernatant was discarded. The resulting solid peptide was dissolved in deionised water and lyophilised.

9.3.2.4. Peptide Sequences Capping

Acetylation of the peptide N-terminus was accomplished by suspending the peptide-resin in a 20 % (v/v) solution of acetic anhydride in DMF in a fritted polypropene vessel for 45 min. For successive acetylation the vessel was drained after the acetylation reaction was repeated with fresh reagents.

9.3.3. Synthesis of Peptoids (Carried out by Hannah L. Bolt, Cobb Group)

Fmoc-protected Rink Amide resin (normally 100 – 300 mg, 0.1 – 0.3 mmol) was swollen in DMF (minimum 1 h, room temperature, overnight preferred) and deprotected with piperidine (20 % in DMF v/v, 2 x 20 min). After DMF washing, the

resin was treated with bromoacetic acid (8 eq. wrt. resin, 2 M in DMF) and DIC (8 eq. wrt. resin, 2 M in DMF) for 15 min at 50 ˚C on a heated shaker with a metal block (400 rpm). The resin was washed three times with DMF, before the desired amine submonomer was added (4 eq. wrt. resin, 1 M in DMF) and allowed to react for 15 min at 50 ˚C. The resin was washed three times with DMF again. The bromoacetylation and amine displacement steps were repeated until the final submonomer had been added and the desired peptoid sequence had been obtained. Cleavage was performed with TFA (95 %), TIPS (2.5 %) and H_2O (2.5 %) for 90 min at room temperature. The cleavage cocktail was collected in a 50 ml falcon tube and precipitated with 50 mL diethyl ether. The solution was centrifuged for 15 min at 5,000 rpm. Afterwards, the ether phase was decanted. The crude was dissolved in acidified H_2O (with 0.1 % TFA) or a mixture of acidified H_2O and MeCN, and lyophilized. The crude products were redissolved in acidified H_2O (with 0.1 % TFA) or a mixture of acidified H_2O and MeCN, and purified by RP-HPLC. A typical method used for the purification was 0 – 50 % B over 60 min then 50 – 100 % B over 15 minutes (A = 0.1 % TFA in 95 % H_2O and 5 % MeCN, B = 0.1 % TFA in 5 % H_2O and 95 % MeCN) at 250 nm wavelength. Relevant fractions were collected, lyophilised and analysed by LC-MS and MALDI-TOF.

9.4. Peptide Synthesis

9.4.1. Synthesis of Nano-1 First Section (1)

General procedure for microwave assisted automated Fmoc-SPPS synthesis outlined in **Section 9.3.2.1** was followed on a 0.10 mmol scale with rink amide resin (0.77 mmol g^{-1}). Fmoc-His(Trt)-OH double coupling was carried out at a reduced temperature (10 min at 50 °C (25 W). The peptide left on resin. The MALDI-MS m/z [M + H]$^+$ = 1962.8.

9.4.2. Synthesis of Nano-1 peptide (2)

The synthesised first section of nano1- peptide (**1**) was reloaded into CEM and the automated Fmoc-SPPS synthesis (**Section 9.3.2.1**) was continued to from nano-1 peptide (**2**). A small amount of the synthesised peptide was cleaved for characterisation (MALDI-MS [M + H]$^+$ = 3312.8).

9.4.3. Synthesis of Free N-terminus Nano-1 (3)

Half of the synthesised nano-1 peptide (**2**) manually cleaved form the resin (**Section 9.3.2.3**), purified by HPLC (**Section 9.2.11**). Maldi TOF MS proves the formation of the acetylated nano-1,**3**, MALDI [M + H]$^+$ = 3312.8.

9.4.4. Synthesis of Acetylated N-terminus Nano-1 Peptide (4)

The second half of nano-1 peptide (**2**) was acetylated following the method outlined in **Section 9.3.2.4**. Finally the peptide cleaved from the resin (**Section 9.3.2.3**) and purified by RP-HPLC (**Section 9.2.11**). MALDI confirms the formation of the acetylated nano-1, **4**, m/z $[M + H]^+ = 3353.4$

9.4.5. Synthesis of Free N-terminus Short Nano-1 Peptide (5)

The synthesis of short nano-1 peptide was carried out using the automated Fmoc-SPPS synthesis (**Section 9.3.2.1**) on 0.05 mmol scale with rink amide resin (0.77 mmol g^{-1}). MALDI proves the successful synthesis of free-N terminus short nano-1 peptide, **3**, *m/z* $[M + H]^+ = 1141.6$.

9.4.6. Synthesis of Acetylated Short Nano-1 Peptide (6)

Acetyled short nano-1 peptide (**6**) synthesised following the general Fmoc-SPPS synthesis on a 0.05 mmol scale with rink amide resin (0.77 mmol g^{-1}). Then N terminus of the peptide was acetylated by method outlined in **Section 9.3.2.4**. Finally, it is cleaved from the resin using the procedure outlined in **Section 9.3.2.3.** The peptide was purified by RP-HPLC (**Section 9.2.11**). Acetylated N-terminus short nano-1 peptide MALDI, **6**, *m/z* $[M + Na]^+ = 1205$.

9.4.7. Synthesis of Fluorinated Nano-1 Peptide (13)
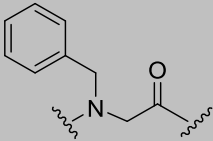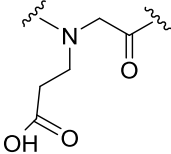
The resin attached first section nano-1 (**1**) was manually double coupled to the synthesised fluorinated amino acid (**12**) following the general manual peptide synthesis outlined in **Section 9.3.2.2**. A small amount of the peptide was cleaved for characterization (MALDI-MS m/z [M^+ + H] =2203.2 confirmed that product. Then the peptide-resin was reloaded into CEM and the automated Fmoc-SPPS synthesis (**Section 9.3.2.1**) was continued to from fluorinated amino acid (**12**). Finally, the peptide was cleaved from the resin using the procedure outlined in **Section 9.3.2.3**. The peptide was purified by RP-HPLC (**Section 9.2.11**).

9.5. Synthesis of Peptoids

The following table shows the amine sub-monomers used to synthesise peptoids. All peptoids were synthesised (**Section 9.5**), cleaved from the resin and purified by RP-HPLC.

Monomer	Chemical Structure	Amine Sub-monomer
*N*lys N-(4-aminobutyl) glycine		N-Boc-1,4-diaminobutane
*N*spe N(S-phenylethyl) glycine		(S)-(−)-α- Methylbenzylamine

*N*phe		Benzylamine
N-(phenylmethyl) glycine		

*N*glu	
N-(2-carboxyethyl) glycine	

Table1: Monomers and sub-monomer precursors used for peptoid synthesis.

Sequence	LC-MS m/z = [M+H]⁺ *m/z = [M+2H]²⁺		Accurate Mass m/z = [M+2H]²⁺		RP-HPLC Elution
	Calculated	*Observed*	*Calculated*	*Observed*	*(% MeCN)*
(*N*lys*N*spe*N*spe)₂ (**14**)	917.55	917.58	459.7842	459.7801	34%
(*N*lys*N*spe*N*spe)₃ (**15**)	1368.82	1368.26	684.9157	684.9142	35%
(*N*lys*N*spe*N*spe)₄ (**16**)	1819.08	1818.97	910.0473	910.0494	40%
(*N*lys*N*spe*N*spe)₆ (**17**)	*1360.30	*1360.73	1360.8119	1360.8058	47%
(Ac-*N*glu-*N*lys-*N*lys-*N*lys-*N*phe) (**18**)	719.43	720.17	-	-	45%

Table 2: Analysis data for synthesised peptoids

9.6. Synthesis of Small Organic Molecules

9.6.1. (*S*)-tert-butyl-2-((((9H-fluoren-9-yl)methoxy)carbonylamino)-3-hydroxypropanoate (9)
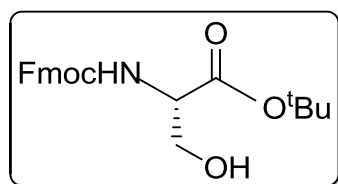
t-Bu-2,2,2,-trichloroacetimidate (2.03 g, 9.29 mmol) in EtOAc (20 ml) was added to a stirred solution of Fmoc-Ser-OH, **8** (2.0 g, 6.14 mmol) and the resulting solution was left to stir overnight. Solvent was removed under reduced pressure and the crude product obtained was purified via column chromatography (Hex-EtOAc, 80:20) to yield the desired product, **9** (1.50 g, 63 %) as a white solid. m.p: 130 °C; ¹H-NMR δ$_H$ (400 MHz; CDCl₃), 1.49 (s, 9H, CO₂^{t}Bu), 3.92 (dd, 2H, *J* = 11.0 β-CH₂), 4.23 (m, 1H, *J* = 7.5 Fmoc-CHCH₂), 4.32 (m, 1H, *J* = 7.6, α-CH), 4.41 (d, 2H, *J* = 7.1, Fmoc-CHCH₂), 5.68 (d, 1H, *J* = 6.8, NH), 7.30 to 7.33 (appt, 2H, Fmoc-

ArH), 7.38 to 7.42 (appt, 2H, Fmoc-ArH), 7.60 (d, 2H, J = 7.2, Fmoc-ArH), 7.78 (d,

2H, J = 7.3, Fmoc-ArH); Spectral data obtained matched that previously

reported[241,498]. ^{1}H-NMR analysis of the product after column purification showed a

minor impurity. The impurity was removed by re-dissolving the product in ether (20

ml) and washing with water (3× 10 ml).

9.6.2. (*R*)-tert-butyl-2-((((9H-fluoren-9-yl)methoxy)carbonylamino)-3-iodo-propanoate (10)
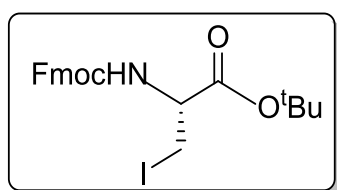
PPh$_3$ (0.99 g, 3.78 mmol), imidazole (0.25 g, 3.78 mmol) and iodine (0.96 g, 3.78 mmol) were added sequentially to a stirred solution of **9** (1.50 g, 3.91 mmol) in DCM (20 ml) and the reaction mixture as left to stir at rt for 16 h. Removal of the solvent under reduced pressure provided the crude product which was purified *via* column chromatography (Hex-EtOAc, 90:10) to afford **10** (1.00 g, 68%) as a thick yellow oil. ^{1}H-NMR (400 MHz; CDCl$_3$), 1.51 (s, 9H, CO$_2$^{t}Bu), 3.59 (dd, 2H, J = 3.3, 2.0 Hz, β-CH$_2$), 4.23 (t, 1H, J = 7.2 Hz, Fmoc-CHCH$_2$), 4.33 (dd, 1H, J = 10.4, 7.2 Hz, α-CH), 4.44 − 4.37 (m, 2H, Fmoc-CHCH$_2$), 5.66 (d, 1H, J = 6.7 Hz, NH), 7.75 (d, 2H, J = 7.5 Hz, Fmoc-ArH), 7.60 (d, 2H, J = 7.4 Hz, Fmoc-ArH), 7.39 (appt, 2H, J = 7.2 Hz, Fmoc-ArH), 7.31 (m, 2H, J = 7.5, 2.6, 1.0 Hz, Fmoc-ArH); MS (ESI +ve) *m/z* 516.3 [M + Na]$^+$. Spectral data obtained for **10** matched that previously reported.[499,500]

9.6.3. (S)-tert-butyl-2-(((9H-fluoren-9-yl)methoxy)carbonylamino)-3-(trifluoromethyl)phenyl)propanoate (11).
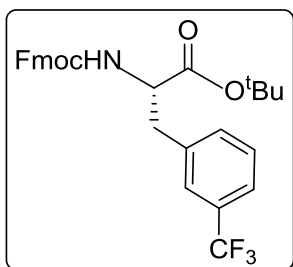
The synthesis of the amino acid was performed using the Negishi reaction outlined in **Section 6.2.1.** After finishing the reaction, the solvent was removed under reduced pressure provided the crude product which was purified via column chromatography (Hex-EtOAc, 70:30) to afford the purified product **11** (0.29 g, 65%) as a white solid. v_{max} (solid)/cm^{-1} 2979 (w, C-H), 2239.7 (w, C≡N), 1719.6 (s , bd C=O amide), 1500.6 (m, bd N-H), 1450.2 and 1369.5 (m, C-H), 1318.5 (m, C-N), 1286.5 and 1258.4 (C-O ester), 1176.6 and 1136.7 (s, bd C-F), 1050 (C-O ester), 794 and 740 (m, bd C-H); ^{1}H-NMR (400 MHz; CDCl$_3$), 1.39 (9H, s, CO$_2{}^t$Bu), 3.19 (dd, 2H, J = 10.8, 6.3, β-CH$_2$), 4.18 (t, 1H, J = 6.8, Fmoc-CHCH$_2$), 4.41-4.35 (m, 1H, α-CH), 4.50 (dd, 2H, J = 19.1, Fmoc-CHCH$_2$,), 5.33 (d, 1H, J = 7.6, NH), 7.30 (appt, 2H, Fmoc-ArH), 7.39 (m, 2H, Fmoc-ArH), 7.56 (m, 2H, Fmoc-ArH), 7.71 (m, 1H, ArH), 7.76 (d, 2H, ArH) 7.90 (m, 1H, ArH), 7.99 (m, 2H, ArH), 8.01 (m, 1H, ArH); ^{13}C-NMR δ$_C$ (100 MHz; CDCl$_3$) 169.5, 155.5, 143.5 (d, 1C, J = 12.5), 142.4 (d, 1C, J = 38.5), 141.3 (d, 1C, J = 5.2), 135.7, 134.6, 133.3, 130.0, 127.8, 127.0 (d, 1C, J = 3.1), 125.6 (m, 1C, CF$_3$), 125.5 (d, 1C, J = 10.2), 120.0 (d, 1C, J = 3.6), 115.3, 114.7, 108.63, 83.5, 66.9, 54.6, 47.3, 38.3, 27.9 (d, J = 7.0 Hz) ; F-NMR δ$_F$ (376 MHz; CDCl$_3$) -62.84 (bs, 2F, Ar-CF$_3$), -62.97 (bs, 1F, Ar-CF$_3$); MS (ESI +ve) m/z 537.1999 [M + H]$^+$.

9.6.4. (S)-tert-butyl-2-((((9H-fluoren-9-yl)methoxy)carbonylamino)-3-(trifluoromethyl)phenyl)propanoic acid (12)
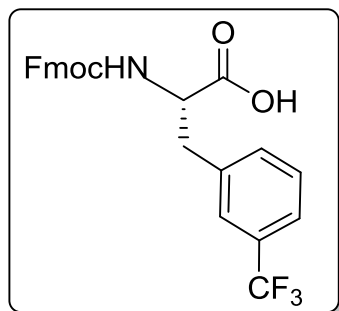
Trifluoroacetic acid (4 ml) was added dropwise to a solution of **11** (0.29 g, 0.54 mmol) in DCM (4 ml). The resulting solution was stirred at room temperature for 5h. Removal of the solvent under reduced pressure and the residue washed and concentrated twice with ether (10 ml). This yielded the product 76%. ^{1}H-NMR δ_H (400 MHz, CDCl$_3$), δ_H 3.33 (dd, 1H, J = 13.8, 5.6 Hz, β-CH$_2$, 3.17 (dd, 1H, J = 14.0, 5.2 Hz, β-CH$_2$), 4.16 (appt, 1H, J = 6.2 Hz, Fmoc CHCH$_2$), 4.51–4.37 (m, 2H, Fmoc CHCH$_2$), 4.67 (d, 1H, J = 6.5 Hz, α-CH), 5.27 (d, 1H, J = 7.3 Hz, NH), 7.28 (m, 2H, J = 7.4, Fmoc-ArH), 7.35 (m, 2H, J = 7.4, Fmoc-ArH),7.39 (m, 1H, J = 7.6, ArH), 7.50 to 7.55 (m, 2H, Fmoc-ArH), 7.69 (m, 1H, ArH), 7.75 (appd, 1H, ArH,), 7.90 (appd, 1H, J = 8.4, ArH), 8.00 (appt, 2H, J = 7.6, Fmoc-ArH), 12.89 (1H, s, CO$_2$H).

Chapter 9

9.7. Preparation of CNTs

9.7.1. Purification of SWNTs

As-synthesised SWNTs produced by the HiPco method and supplied by Unidym, USA (6 wt % Iron impurities, 35 wt % Ash impurities) were purified by heating in air at 400 °C for 30 min, then soaking in 6.0 M HCl at rt. overnight. They were then filtrated over a polycarbonate membrane (0.45 μm), and washed with copious amounts of high-purity water until pH-neutral. Finally, the nanotubes were dispersed in ethanol, filtered, removed from the membrane and allowed to dry in vacuum oven overnight at 60 °C.

9.7.2. Oxidation of SWNTs

Two batches of oxidised HiPco SWNTs were prepared. Purified HiPco SWNTs (100 mg) were refluxed in 100 mL nitric acid (2 M, and 8 M) for 4 h at 120 °C to yield 2 M and 8 M oxidised HiPco SWNTs, respectively. Following the reflux, both samples were treated similarly: after the sample had cooled it was filtered over a polycarbonate membrane (0.45 μm), and then rinsed with water, until the filtrate was colourless and reached the pH of the distilled water. The sample was then washed with 500 mL of sodium hydroxide (NaOH, 0.05 M), producing a yellow/brown filtrate. The base washing was continued until the filtrate is colourless. The resulting nanotubes were then washed with distilled water until neutral. Finally, the product was washed with hydrochloric acid (HCl, 0.05 M, 500 mL) and again returned to neutral with distilled water. Finally, the oxidised nanotubes were dried in a vacuum oven at 60 °C for 24 h.

Chapter 9

9.8. Preparation of Graphene Based Nanomaterials

9.8.1. Synthesis of Graphene Oxide

Graphene oxide was synthesised using Hummer's method[380] as shown **Figure** 1:
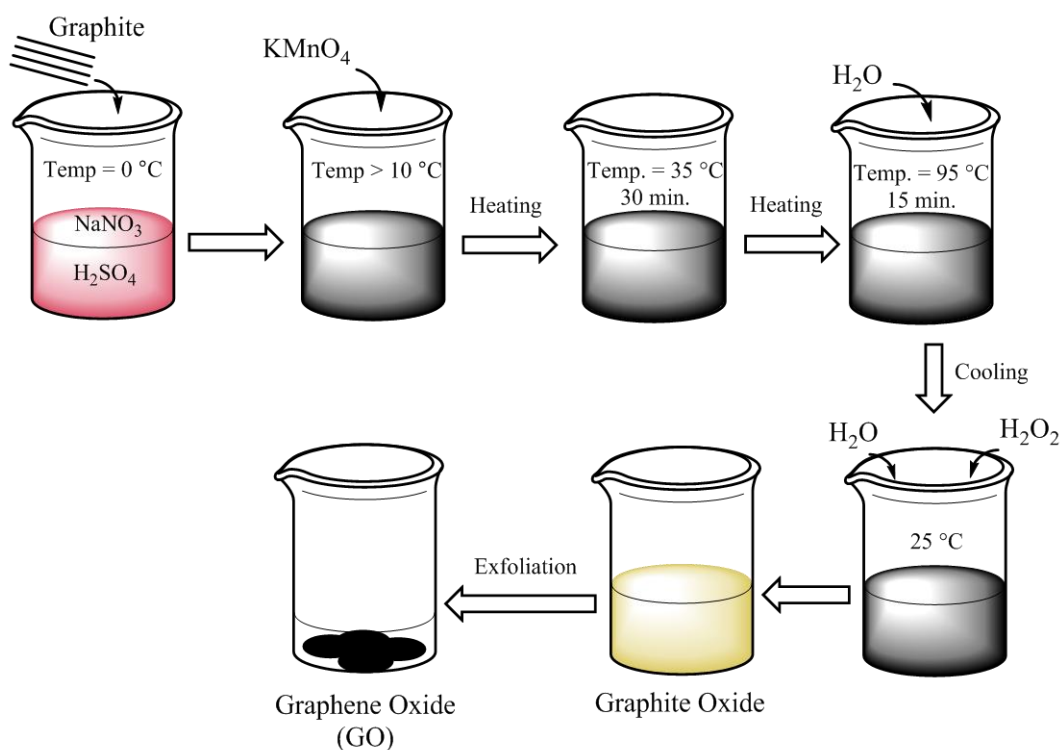
Figure 1: Synthesis of GO by Hummer's method.

Firstly, graphite powder (1.0 g, 1.0 eq. wt.) and sodium nitrate (NaNO$_3$, 0.5 g, 0.5 eq. wt.) were dispersed by stirring in concentrated sulphuric acid (H$_2$SO$_4$, 23 mL, S.G. 1.83, 1 eq. wt.) at 0 °C using a Grant LTD6G recalculating cooler. Then potassium permanganate (KMnO$_4$, 3 g, 3.0 eq. wt.) was slowly added to the suspension, ensuring that the reaction temperature did not rise above 10 °C. Then the reaction was heated to 35 °C in a water bath for 30 min, during this time the viscosity of the reaction mixture increased greatly and it becomes difficult to stir. High purity water (46 mL, 2.0 eq. vol.) was then added causing an exothermic reaction to occur. This

increase in temperature was supplemented with external heating and the reaction was heated to 95 °C for 15 min. Following this, the reaction was cooled to room temperature and decanted into 140 ml (6.1 eq. vol.) of high purity water. The remaining active manganese species were quenched by the addition of H_2O_2 (1 mL, 30 %) over a period 15 min. The colour of the suspension changed to bright yellow. Secondly, several workups were followed to isolate and purify the graphite oxide produced by the reaction; centrifugation and washing with high purity water until neutral. Finally, graphite oxide samples were exfoliated to form GO by probe sonication. Samples were dispersed in high purity water at concentrations of 1.0 mg ml^{-1} and probe sonicated for a total of 40 min (**Section 9.2.3**).

9.8.2. Synthesis of Reduced Graphene Oxide (rGO)

Exfoliated GO at a concentration of 1.0 mg mL^{-1} in high purity water was added to hydrazine monohydrate (N_2H_4. H_2O, 1.0 μL per 3 mg of GO) and refluxed at 80 °C for 24 h. The solution quickly changed from a dark brown to a black colour, indicative of the formation of rGO. Then the reaction was cooled to room temperature and the rGO produced was isolated via vacuum filtration over a polycarbonate membrane (pore size 0.25 μ).

9.8.3. Synthesis of Oxidised rGO (Oxi-rGO)

(100 mg) of rGO was refluxed in 100 mL of 8 M HNO_3 for 24 h at 100 °C. The oxidised rGO was collected via vacuum filtration over a polycarbonate membrane (0.25 μ), then rinsed with deionised water, dried in vacuum at 60 °C overnight.

9.8.4. Synthesis of Synthesis of Acylated-rGO (rGO-COCl)

The oxidised rGO (100 mg) was refluxed in a mixture of thionyl chloride ($SOCl_2$, 5 mL) and dimethylformamide (DMF, 20 mL) at 80 °C overnight. Then filtered via vacuum filtration over a polycarbonate membrane (pore size 0.45 μm), and washed with dry DMF.

9.8.5. Synthesis of EDA-rGO

(100 mg) of acylated-rGO (rGO-COCl) was stirred in 10 mL of 50:50 mixture of ethylene diamine (EDA) and dimethylformamide (DMF) under nitrogen atmosphere at rt. over night. Then washed with ethanol several times and dried at 60 °C overnight in vacuum.

9.8.6. Synthesis of CPPo-rGO

A mixture of 15.0 mg CPPo (**18**), 8.0 mg PyBOP, 10.0 ml DIEA in 3 ml anhydrous DMF was prepared in order to enhance activation of carboxyl groups by DIEA. After 15 min of activation, EDA-rGO (10.0 mg) dispersed in anhydrous DMF (15 mL) were added to the mixture. The obtained mixture was then sonicated for 4 h at 40 °C. The product was then diluted with 300 mL of methanol and vacuum-filtered using a polycarbonate membrane (0.05 mm pore size), after which the filtranate was washed extensively with excess methanol. Finally, CPPo-rGO was dried in a vacuum oven at 60 °C for 8 h.

9.8.7. Synthesis of of Thymidine/GO and Adensine/rGO Composites

Freeze dried GO (50 mg) was acetylated by refluxing it in an excess amount of thionyl chloride ($SOCl_2$, 20 mL) in the presence of anhydrous *N,N*-dimethylformamide (DMF, 5 mL) at 80 ℃ for 24 h to yield GO-COCl. The GO-COCl powder was collected immediately by distillation and washed with anhydrous DMF. Then divided into two, and then separately reacted with a 125 mg ribonucleoside solution (adenosine, and thymidine) in 10 mL of DMF in the presence of 0.5 mL of triethylamine at 130 °C for 72 h in nitrogen atmosphere. The produced adenosine/rGO was further washed with HCl solution (0.5 mMol) once and deionised water three times and dried at vacuum oven at 45 °C for 8 h

References

1.   H. W. Kroto, J. R. Heath, S. C. O'Brien, R. F. Curl and R. E. Smalley, *Nature*, 1985, 318, 162-163.

2.   S. Iijima, *Nature*, 1991, 354, 56-58.

3.   S. Iijima and T. Ichihashi, *Nature*, 1993, 363, 603-605.

4.   D. S. Bethune, C. H. Klang, M. S. de Vries, G. Gorman, R. Savoy, J. Vazquez and R. Beyers, *Nature*, 1993, 363, 605-607.

5.   H. Jie, in *Carbon Nanotubes*, ed. M. Meyyappan, CRC Press, New York, 2004, ch.1, pp. 2-104.

6.   D. B. Zhang, E. Akatyeva and T. Dumitrica, *Phys. Rev. Lett.*, 2011, 106, 2555031-2555034.

7.   N. K. Mehra, V. Mishra and N. K. Jain, *Biomaterials*, 2014, 35, 1267-1283.

8.   M. Monthioux and V. L. Kuznetsov, *Carbon*, 2006, 44, 1621-1623.

9.   P. M. Ajayan, *Chem. Rev.*, 1999, 99, 1787-1800.

10.   W. Zhang, Z. Zhang and Y. Zhang, *Nanoscale Res. Lett.*, 2011, 6, 555-555.

11.   M. S. Dresselhaus, G. Dresselhaus, J. C. Charlier and E. Hernandez, *Philos. T. R. Soc. A*, 2004, 362, 2065-2098.

References

12. A. Thess, R. Lee, P. Nikolaev, H. J. Dai, P. Petit, J. Robert, C. H. Xu, Y. H. Lee, S. G. Kim, A. G. Rinzler, D. T. Colbert, G. E. Scuseria, D. Tomanek, J. E. Fischer and R. E. Smalley, *Science*, 1996, 273, 483-487.

13. A. Krueger, in *Carbon Materials and Nanotechnology*, Wiley-VCH Verlag GmbH & Co. KGaA, Germany, 2010,.ch.3, pp. 123-281.

14. T. W. Odom, J. L. Huang, P. Kim and C. M. Lieber, *J. Phys. Chem. B*, 2000, 104, 2794-2809.

15. M. S. Dresselhaus, G. Dresselhaus, R. Saito and A. Jorio, *Phys. Rep.*, 2005, 409, 47-99.

16. E. T. Thostenson, Z. Ren and T.-W. Chou, *Composites Sci. Technol.*, 2001, 61, 1899-1912.

17. S. A. Hodge, M. K. Bayazit, K. S. Coleman and M. S. P. Shaffer, *Chem. Soc. Rev.*, 2012, 41, 4409-4429.

18. R. Saito, M. Fujita, G. Dresselhaus and M. S. Dresselhaus, *Appl. Phys. Lett.*, 1992, 60, 2204-2206.

19. C. Liu and H.-M. Cheng, *Mater. Today*, 2013, 16, 19-28.

20. C. A. Dyke and J. M. Tour, *J. Phys. Chem. A*, 2004, 108, 11151-11159.

21. W. Kratschmer, L. D. Lamb, K. Fostiropoulos and D. R. Huffman, *Nature*, 1990, 347, 354-358.

22. C. Journet and P. Bernier, *Appl. Phys. A: Mater. Sci. Process*, 1998, 67, 1-9.

References

23.   D. M. Guldi and N. Martín, *Carbon Nanotubes and Related Structures: Synthesis, Characterization, Functionalization, and Applications*, Wiley-VCH Verlag GmbH & Co. KGaA, Germany, 2010.

24.   S S. Yahachi, O. Mitsumasa, F. Naoya, Y. Tadanobu, T. Masato and H. Takayoshi, *Jpn. J. Appl. Phys.*, 1994, 33, L526-L529.

25.   C. Journet, W. K. Maser, P. Bernier, A. Loiseau, M. L. de la Chapelle, S. Lefrant, P. Deniard, R. Lee and J. E. Fischer, *Nature*, 1997, 388, 756-758.

26.   I. Hinkov, S. Farhat and C. D. Scott, *Carbon*, 2005, 43, 2453-2462.

27.   T. Guo, P. Nikolaev, A. Thess, D. T. Colbert and R. E. Smalley, *Chem. Phys. Lett.*, 1995, 243, 49-54.

28.   T. Guo, P. Nikolaev, A. G. Rinzler, D. Tomanek, D. T. Colbert and R. E. Smalley, *J. Phys. Chem.*, 1995, 99, 10694-10697.

29.   R. T. K. Baker, *Carbon*, 1989, 27, 315-323.

30.   S. N. Marinkovic, *J. Serb. Chem. Soc.*, 2008, 73, 891-913.

31.   J. Mohsen and K. Asieh Dehghani, in *Syntheses and Applications of Carbon Nanotubes and Their Composites*, ed. Satoru Suzuki, InTech, 2013, ch.4, pp. 54-76.

32.   V. N. Popov, *Mater. Sci. Engin. R*, 2004, 43, 61-102.

33.   J. Kong, A. M. Cassell and H. J. Dai, *Chem. Phys. Lett.*, 1998, 292, 567-574.

References

34. J. Kong, H. T. Soh, A. M. Cassell, C. F. Quate and H. Dai, *Nature*, 1998, 395, 878-881.

35. M. J. Bronikowski, P. A. Willis, D. T. Colbert, K. A. Smith and R. E. Smalley, *J. Vac. Sci. Technol. A*, 2001, 19, 1800-1805.

36. P. Nikolaev, M. J. Bronikowski, R. K. Bradley, F. Rohmund, D. T. Colbert, K. A. Smith and R. E. Smalley, *Chem. Phys. Lett.*, 1999, 313, 91-97.

37. I. W. Chiang, B. E. Brinson, A. Y. Huang, P. A. Willis, M. J. Bronikowski, J. L. Margrave, R. E. Smalley and R. H. Hauge, *J. Phys. Chem. B*, 2001, 105, 8297-8301.

38. S. Cataldo, P. Salice, E. Menna and B. Pignataro, *Energy Environ. Sci.*, 2012, 5, 5919-5940.

39. T.-J. Park, S. Banerjee, T. Hemraj-Benny and S. S. Wong, *J. Mater. Chem.*, 2006, 16, 141-154.

40. R. C. Haddon, *Science*, 1993, 261, 1545-1550.

41. M. A. Hamon, M. E. Itkis, S. Niyogi, T. Alvaraez, C. Kuper, M. Menon and R. C. Haddon, *J. Am. Chem. Soc.*, 2001, 123, 11292-11293.

42. D. Srivastava, D. W. Brenner, J. D. Schall, K. D. Ausman, M. F. Yu and R. S. Ruoff, *J. Phys. Chem. B*, 1999, 103, 4330-4337.

43. S. Niyogi, M. A. Hamon, H. Hu, B. Zhao, P. Bhowmik, R. Sen, M. E. Itkis and R. C. Haddon, *Acc. Chem. Res.*, 2002, 35, 1105-1113.

References

44. R. C. Haddon, *J. Am. Chem. Soc.*, 1990, 112, 3385-3389.

45. R. C. Haddon, *Acc. Chem. Res.*, 1988, 21, 243-249.

46. D. A. Britz and A. N. Khlobystov, *Chem. Soc. Rev.*, 2006, 35, 637-659.

47. Y. Chen, R. C. Haddon, S. Fang, A. M. Rao, W. H. Lee, E. C. Dickey, E. A. Grulke, J. C. Pendergrass, A. Chavan, B. E. Haley and R. E. Smalley, *J. Mater. Res.*, 1998, 13, 2423-2431.

48. Y. Miyata, T. Kawai, Y. Miyamoto, K. Yanagi, Y. Maniwa and H. Kataura, *J. Phys. Chem. C*, 2007, 111, 9671-9677.

49. A. A. Balandin, *Nat. Mater.*, 2011, 10, 569-581.

50. S. Berber, Y.-K. Kwon and D. Tománek, *Phys. Rev. Lett.*, 2000, 84, 4613-4616.

51. M. S. Dresselhaus, G. Dresselhaus and A. Jorio, *Annu. Rev. Mater. Res.*, 2004, 34, 247-278.

52. J. Hone, M. C. Llaguno, N. M. Nemes, A. T. Johnson, J. E. Fischer, D. A. Walters, M. J. Casavant, J. Schmidt and R. E. Smalley, *Appl. Phys. Lett.*, 2000, 77, 666-668.

53. J. P. Lu, *Phys. Rev. Lett.*, 1997, 79, 1297-1300.

54. J. N. Coleman, U. Khan, W. J. Blau and Y. K. Gun'ko, *Carbon*, 2006, 44, 1624-1652.

References

55.   D. Tomanek, A. Jorio, M. S. Dresselhaus and G. Dresselhaus, *Top Appl. Phys.*, 2008, 111, 1-12.

56.   A. Peigney, C. Laurent, E. Flahaut, R. R. Bacsa and A. Rousset, *Carbon*, 2001, 39, 507-514.

57.   C. H. Sun, L. C. Yin, F. Li, G. Q. Lu and H. M. Cheng, *Chem. Phys. Lett.*, 2005, 403, 343-346.

58.   L. A. Girifalco, M. Hodak and R. S. Lee, *Phys. Rev. B*, 2000, 62, 13104-13110.

59.   P. Singh, S. Campidelli, S. Giordani, D. Bonifazi, A. Bianco and M. Prato, *Chem. Soc. Rev.*, 2009, 38, 2214-2230.

60.   K. L. Lu, R. M. Lago, Y. K. Chen, M. L. H. Green, P. J. F. Harris and S. C. Tsang, *Carbon*, 1996, 34, 814-816.

61.   Q. H. Cheng, S. Debnath, E. Gregan and H. J. Byrne, *J. Phys. Chem. C*, 2010, 114, 8821-8827.

62.   A. Hirsch, *Angew. Chem., Int. Ed.*, 2002, 41, 1853-1859.

63.   G. Jia, H. Wang, L. Yan, X. Wang, R. Pei, T. Yan, Y. Zhao and X. Guo, *Environ. Sci. Technol.*, 2005, 39, 1378-1383.

64.   G. Tobias, E. Mendoza and B. Ballesteros, in *Encyclopedia of Nanotechnology*, ed. B. Bhushan, Springer Netherlands, 2nd end., 2015, ch. 48-2, pp. 1-12.

References

65.   D. Tasis, N. Tagmatarchis, A. Bianco and M. Prato, *Chem. Rev.*, 2006, 106, 1105-1136.

66.   J. Zhang, H. L. Zou, Q. Qing, Y. L. Yang, Q. W. Li, Z. F. Liu, X. Y. Guo and Z. L. Du, *J. Phys. Chem. B*, 2003, 107, 3712-3718.

67.   L. J. Meng, C. L. Fu and Q. H. Lu, *Prog. Nat. Sci.*, 2009, 19, 801-810.

68.   J. L. Bahr, J. Yang, D. V. Kosynkin, M. J. Bronikowski, R. E. Smalley and J. M. Tour, *J. Am. Chem. Soc.*, 2001, 123, 6536-6542.

69.   C. A. Dyke and J. M. Tour, *Nano Lett.*, 2003, 3, 1215-1218.

70.   J. L. Bahr and J. M. Tour, *Chem. Mater.*, 2001, 13, 3823-3824.

71.   C. A. Dyke and J. M. Tour, *J. Am. Chem. Soc.*, 2003, 125, 1156-1157.

72.   E. T. Mickelson, C. B. Huffman, A. G. Rinzler, R. E. Smalley, R. H. Hauge and J. L. Margrave, *Chem. Phys. Lett.*, 1998, 296, 188-194.

73.   Y. Ying, R. K. Saini, F. Liang, A. K. Sadana and W. E. Billups, *Org. Lett.*, 2003, 5, 1471-1473.

74.   M. Holzinger, J. Abraham, P. Whelan, R. Graupner, L. Ley, F. Hennrich, M. Kappes and A. Hirsch, *J. Am. Chem. Soc.*, 2003, 125, 8566-8580.

75.   K. S. Coleman, S. R. Bailey, S. Fogden and M. L. H. Green, *J. Am. Chem. Soc.*, 2003, 125, 8722-8723.

References

76. K. Kamaras, M. E. Itkis, H. Hu, B. Zhao and R. C. Haddon, *Science*, 2003, 301, 1501-1501.

77. T. Nakamura, M. Ishihara, T. Ohana, A. Tanaka and Y. Koga, *Chem. Commun.*, 2004, 1336-1337.

78. S. Qin, D. Qin, W. T. Ford, J. E. Herrera, D. E. Resasco, S. M. Bachilo and R. B. Weisman, *Macromolecules*, 2004, 37, 3965-3967.

79. S. Banerjee, T. Hemraj-Benny and S. S. Wong, *Adv. Mater.*, 2005, 17, 17-29.

80. D. R. Dreyer, S. Park, C. W. Bielawski and R. S. Ruoff, *Chem. Soc. Rev.*, 2010, 39, 228-240.

81. M. J. O'Connell, P. Boul, L. M. Ericson, C. Huffman, Y. H. Wang, E. Haroz, C. Kuper, J. Tour, K. D. Ausman and R. E. Smalley, *Chem. Phys. Lett.*, 2001, 342, 265-271.

82. L. Y. Piao, Q. R. Liu, Y. D. Li and C. Wang, *J. Phys. Chem. C*, 2008, 112, 2857-2863.

83. M. Vizuete, M. Barrejón, M. J. Gómez-Escalonilla and F. Langa, *Nanoscale*, 2012, 4, 4370–4381.

84. Wei Yana,Dai-Wen Panga, Sheng-Fu Wanga and Yuan-Di Zhaoa, *Fuller. Nanotub. Carb. N.*, 2005, 13, 309.

85. H. Wang, *Curr. Opin. Colloid Interface Sci.*, 2009, 14, 364-371.

References

86.   T. Wei, M. A. Carignano and I. Szleifer, *J. Phys. Chem. B*, 2012, 116, 10189-10194.

87.   S. M. Tomasio and T. R. Walsh, *J. Phys. Chem. C*, 2009, 113, 8778-8785.

88.   C. Y. Hu, Y. J. Xu, S. W. Duo, R. F. Zhang and M. S. Li, *J. Chin. Chem. Soc.*, 2009, 56, 234-239.

89.   N. Nakashima, S. Okuzono, H. Murakami, T. Nakai and K. Yoshikawa, *Chem. Lett.*, 2003, 32, 456-457.

90.   N. Hadidi, F. Kobarfard, N. Nafissi-Varcheh and R. Aboofazeli, *Int. J. Nanomedicine*, 2011, 6.

91.   G. Prencipe, S. M. Tabakman, K. Welsher, Z. Liu, A. P. Goodwin, L. Zhang, J. Henry and H. J. Dai, *J. Am. Chem. Soc.*, 2009, 131, 4783-4787.

92.   N. Nakayama-Ratchford, S. Bangsaruntip, X. Sun, K. Welsher and H. Dai, *J. Am. Chem. Soc.*, 2007, 129, 2448-2449.

93.   J. Chattopadhyay, F. de Jesus Cortez, S. Chakraborty, N. K. H. Slater and W. E. Billups, *Chem. Mater.*, 2006, 18, 5864-5868.

94.   R. J. Liu Z, Sun X, Dai H. , *J. Am. Chem. Soc.*, 2008, 130, 10876–10877.

95.   K. Kostarelos, A. Bianco and M. Prato, *Nat. Nano*, 2009, 4, 627-633.

96.   P. Randhawa, J. S. Park, S. Sharma, P. Kumar, M. S. Shin and S. S. Sekhon, *J. Nanoelectron. Optoelectron.*, 2012, 7, 279-286.

References

97.   J. C. Goak, S. H. Lee, J. H. Han, S. H. Jang, K. B. Kim, Y. Seo, Y. S. Seo and N. Lee, *Carbon*, 2011, 49, 4301-4313.

98.   L. Vaisman, H. D. Wagner and G. Marom, *Adv. Colloid Interface Sci.*, 2006, 128–130, 37-46.

99.   A. J. Blanch, C. E. Lenehan and J. S. Quinton, *J. Phys. Chem. B*, 2010, 114, 9805-9811.

100.   V. C. Moore, M. S. Strano, E. H. Haroz, R. H. Hauge, R. E. Smalley, J. Schmidt and Y. Talmon, *Nano Lett.*, 2003, 3, 1379-1382.

101.   Y. Q. Tan and D. E. Resasco, *J. Phys. Chem. B*, 2005, 109, 14454-14460.

102.   H. S. Kim, W. I. Park, M. Kang and H. J. Jin, *J. Phys. Chem. Solids*, 2008, 69, 1209-1212.

103.   M. F. Islam, E. Rojas, D. M. Bergey, A. T. Johnson and A. G. Yodh, *Nano Lett.*, 2003, 3, 269-273.

104.   R. Rastogi, R. Kaushal, S. K. Tripathi, A. L. Sharma, I. Kaur and L. M. Bharadwaj, *J. Colloid Interface Sci.*, 2008, 328, 421-428.

105.   C. C. Ge, J. F. Du, L. N. Zhao, L. M. Wang, Y. Liu, D. H. Li, Y. L. Yang, R. H. Zhou, Y. L. Zhao, Z. F. Chai and C. Y. Chen, *Proc. Natl. Acad. Sci. U. S. A.*, 2011, 108, 16968-16973.

106.   S. Marchesan and M. Prato, *Chem. Commun.*, 2015, 51, 4347-4359.

107.   N. Saifuddin, A. Z. Raziah and A. R. Junizah, *J. Chem.*, 2013, 2013, 1-18.

References

108.   Y. X. Wang and H. Q. Ai, *J. Phys. Chem. B*, 2009, 113, 9620-9627.

109.   Y. Lin, S. Taylor, H. P. Li, K. A. S. Fernando, L. W. Qu, W. Wang, L. R. Gu, B. Zhou and Y. P. Sun, *J. Mater. Chem.*, 2004, 14, 527-541.

110.   Z. Su, K. Mui, E. Daub, T. Leung and J. Honek, *J. Phys. Chem. B*, 2007, 111, 14411-14417.

111.   K. Kurppa, H. Jiang, G. R. Szilvay, A. G. Nasibulin, E. I. Kauppinen and M. B. Linder, *Angew. Chem. Int. Ed.*, 2007, 46, 6446-6449.

112.   D. Nepal and K. E. Geckeler, *Small*, 2007, 3, 1259-1265.

113.   N. W. S. Kam and H. Dai, *J. Am. Chem. Soc.*, 2005, 127, 6021-6026.

114.   K. Matsuura, T. Saito, T. Okazaki, S. Ohshima, M. Yumura and S. Iijima, *Chem. Phys. Lett.*, 2006, 429, 497-502.

115.   R. J. Chen, Y. Zhang, D. Wang and H. Dai, *J. Am. Chem. Soc.*, 2001, 123, 3838-3839.

116.   S. C. Tsang, J. J. Davis, M. L. H. Green, H. A. O. Hill, Y. C. Leung and P. J. Sadler, *J. Chem. Soc., Chem. Commun.*, 1995, 17, 1803–1804.

117.   Y. Kang, Q. Wang, Y. C. Liu, J. W. Shen and T. Wu, *J. Phys. Chem. B*, 2010, 114, 2869-2875.

References

118. M. Sheikholeslam, M. Pritzker and P. Chen, *Langmuir*, 2012, 28, 12550-12556.

119. Siqun Wang1, Elen S. Humphreys, Sung-Yoon Chung, Daniel F. Delduco, Steven R. Lustig, Hong Wang, Kimberley N. Parker, Nancy W. Rizzo, Shekhar Subramoney, Yet-Ming Chiang and Anand Jagota, *Nat. Mater.*, 2003, 2, 196 - 200

120. V. Zorbas, A. L. Smith, H. Xie, A. Ortiz-Acevedo, A. B. Dalton, G. R. Dieckmann, R. K. Draper, R. H. Baughman and I. H. Musselman, *J. Am. Chem. Soc.*, 2005, 127, 12323-12328.

121. S.-F. Chin, R. H. Baughman, A. B. Dalton, G. R. Dieckmann, R. K. Draper, C. Mikoryak, I. H. Musselman, V. Z. Poenitzsch, H. Xie and P. Pantano, *Exp. Biol. Med.*, 2007, 232, 1236-1244.

122. W. Y. Chen, L. S. Wang, H. T. Chiu, Y. C. Chen and C. Y. Lee, *J. Am. Soc. Mass Spectrom.*, 2004, 15, 1629-1635.

123. C. G. Salzmann, M. A. H. Ward, R. M. J. Jacobs, G. Tobias and M. L. H. Green, *J. Phys. Chem. C*, 2007, 111, 18520-18524.

124. G. R. Dieckmann, A. B. Dalton, P. A. Johnson, J. Razal, J. Chen, G. M. Giordano, E. Muñoz, I. H. Musselman, R. H. Baughman and R. K. Draper, *J. Am. Chem. Soc.*, 2003, 125, 1770-1777.

References

125. S. Wang, E. S. Humphreys, S.-Y. Chung, D. F. Delduco, S. R. Lustig, H. Wang, K. N. Parker, N. W. Rizzo, S. Subramoney, Y.-M. Chiang and A. Jagota, *Nat Mater*, 2003, 2, 196-200.

126. X. Li, W. Chen, Q. Zhan, L. Dai, L. Sowards, M. Pender and R. R. Naik, *J. Phys. Chem. B*, 2006, 110, 12621-12625.

127. M. S. Arnold, M. O. Guler, M. C. Hersam and S. I. Stupp, *Langmuir*, 2005, 21, 4705-4709.

128. J. M. Brown, *Molecular Spectroscopy*, Oxford University Press, Oxford, 1998.

129. S. Arepalli, S. W. Freiman, S. A. Hooker, and K. D. Migler, Measurement issues in single-wall carbon nanotubes, National Institute of Standards and Technology, Gaithersburg, 2008.

130. R. S. Das and Y. K. Agrawal, *Vib. Spectrosc.*, 2011, 57, 163-176.

131. F. Tuinstra and J. L. Koenig, *J. Chem. Phys*, 1970, 53, 1126-1130.

132. L. M. Malard, M. A. Pimenta, G. Dresselhaus and M. S. Dresselhaus, *Phys. Rep.*, 2009, 473, 51-87.

133. U. J. Kim, C. A. Furtado, X. Liu, G. Chen and P. C. Eklund, *J. Am. Chem. Soc.*, 2005, 127, 15437-15445.

134. M. S. Dresselhaus, A. Jorio and R. Saito, *Annu. Rev, Condens. Matter. Phys.,* 2010, 1, 89-108.

References

135.   A. C. Ferrari and J. Robertson, *Phil. Trans. R. Soc. Lond*. A, 2004, 362, 2477-
         2512.

136.   A. C. Ferrari and J. Robertson, *Phys. Rev. B*, 2000, 61, 14095-14107.

137.   F. Hennrich, R. Krupke, S. Lebedkin, K. Arnold, R. Fischer, D. E. Resasco
         and M. M. Kappes, *J. Phys. Chem. B*, 2005, 109, 10567-10573.

138.   A. Jorio, C. Fantini, M. S. S. Dantas, M. A. Pimenta, A. G. Souza Filho, G.
         G. Samsonidze, V. W. Brar, G. Dresselhaus, M. S. Dresselhaus, A. K. Swan,
         M. S. Ünlü, B. B. Goldberg and R. Saito, *Phys. Rev. B*, 2002, 66, 115411.

139.   A. M. Rao, E. Richter, S. Bandow, B. Chase, P. C. Eklund, K. A. Williams,
         S. Fang, K. R. Subbaswamy, M. Menon, A. Thess, R. E. Smalley, G.
         Dresselhaus and M. S. Dresselhaus, *Science*, 1997, 275, 187-191.

140.   A. Jorio, A. G. Souza Filho, G. Dresselhaus, M. S. Dresselhaus, A. K. Swan,
         M. S. Ünlü, B. B. Goldberg, M. A. Pimenta, J. H. Hafner, C. M. Lieber and
         R. Saito, *Phys. Rev. B*, 2002, 65, 155412.

141.   A. Jorio, M. A. Pimenta, A. G. S. Filho, R. Saito, G. Dresselhaus and M. S.
         Dresselhaus, *New J. Phys.*, 2003, 5, 139, 139.1-139.17.

142.   J. L. Hughes and E. Krausz, in *Encyclopedia of Inorganic and Bioinorganic
         Chemistry*, Wiley, New Jersey, 2011.

143.   C. Backes, in *Noncovalent Functionalization of Carbon Nanotubes*, Springer,
         Berlin, 2012, ch. 1, pp. 1-37.

References

144. J. S. Lauret, C. Voisin, G. Cassabois, P. Roussignol, C. Delalande, A. Filoramo, L. Capes, E. Valentin and O. Jost, *Physica E*, 2004, 21, 1057-1060.

145. F. Wang, Y. B. Zhang, C. S. Tian, C. Girit, A. Zettl, M. Crommie and Y. R. Shen, *Science*, 2008, 320, 206-209.

146. J. Hone, B. Batlogg, Z. Benes, A. T. Johnson and J. E. Fischer, *Science*, 2000, 289, 1730-1733.

147. L. Vanhove, *Phys. Rev.*, 1953, 89, 1189-1193.

148. G. A. Rance, D. H. Marsh, R. J. Nicholas and A. N. Khlobystov, *Chem. Phys. Lett.*, 2010, 493, 19-23.

149. D. Wunderlich, F. Hauke and A. Hirsch, *J. Mater. Chem.*, 2008, 18, 1493-1497.

150. B. Wu, D. C. Geng and Y. Q. Liu, *Nanoscale*, 2011, 3, 2074-2085.

151. S. M. Bachilo, M. S. Strano, C. Kittrell, R. H. Hauge, R. E. Smalley and R. B. Weisman, *Science*, 2002, 298, 2361-2366.

152. G. A. Rance, D. H. Marsh, R. J. Nicholas and A. N. Khlobystov, *Chem. Phys. Lett.*, 2010, 493, 19-23.

153. M. E. Itkis, D. E. Perea, R. Jung, S. Niyogi and R. C. Haddon, *J. Am. Chem. Soc.*, 2005, 127, 3439-3448.

154. R. Sen, S. M. Rickard, M. E. Itkis and R. C. Haddon, *Chem. Mater.*, 2003, 15, 4273-4279.

References

155. M. E. Itkis, D. E. Perea, S. Niyogi, S. M. Rickard, M. A. Hamon, H. Hu, B. Zhao and R. C. Haddon, *Nano Lett.*, 2003, 3, 309-314.

156. M. C. Hersam, *Nat. Nano*, 2008, 3, 387-394.

157. S. H. Jeong, K. K. Kim, S. J. Jeong, K. H. An, S. H. Lee and Y. H. Lee, *Synth. Met.*, 2007, 157, 570-574.

158. J. L. Bahr, E. T. Mickelson, M. J. Bronikowski, R. E. Smalley and J. M. Tour, *Chem. Commun.*, 2001, 193-194.

159. B. J. Landi, H. J. Ruf, J. J. Worman and R. P. Raffaelle, *J. Phys. Chem. B*, 2004, 108, 17089-17095.

160. S. Kumar, I. Kaur, N. Kumari, S. Jain, K. Dharamveer, V. K. Jindal, N. K. Verma and L. Bharadwaj, *Appl. Nanosci.*, 2014, 4, 19-26.

161. M. A. Novak, S. Surwade, J. Prokop, K. Bolotin, J. Hone, L. Brus, C. Nuckolls and H. Liu, *J. Am. Chem. Soc.*, 2014, 136, 8536-8539.

162. M.-F. Yu, M. J. Dyer and R. S. Ruoff, *J. Appl. Phys.*, 2001, 89, 4554-4557.

163. A. Vilalta-Clemente, *Phys. Adv. Mater.,* 2008, pp. 1-10.

164. B. Cappella and G. Dietler, *Surf. Sci. Rep.*, 1999, 34, 1-104.

165. S. Magonov and N. Yerina, in *Handbook of Microscopy for Nanotechnology*, eds. N. Yao and Z. Wang, ed. N. Yao and Z. L. Wang, Springer US, New York, 2005, ch. 4, pp. 113-155.

References

166.   S. Stankovich, D. A. Dikin, R. D. Piner, K. A. Kohlhaas, A. Kleinhammes, Y. Jia, Y. Wu, S. T. Nguyen and R. S. Ruoff, *Carbon*, 2007, 45, 1558-1565.

167.   S. Bellucci, G. Gaggiotti, M. Marchetti, F. Micciulla, R. Mucciato and M. Regi, *J. Phys. Conf. Ser.*, 2007, 61, 99-104.

168.   A. Suresh, in *Metallic Nanocrystallites and their Interaction with Microbial Systems*, Springer, Netherlands, 2012, ch. 1, pp. 1-23.

169.   J. F. Mongillo, *Nanotechnology 101*, ABC-CLIO, London, 2007.

170.   J. C. H. Spence, *Experimental high-resolution electron microscopy*, Oxford University Press, 1988.

171.   S. Pekker, J. P. Salvetat, E. Jakab, J. M. Bonard and L. Forró, *J. Phys. Chem. B*, 2001, 105, 7938-7943.

172.   D. Bom, R. Andrews, D. Jacques, J. Anthony, B. Chen, M. S. Meier and J. P. Selegue, *Nano Lett.*, 2002, 2, 615-619.

173.   E. Mansfield, A. Kar and S. A. Hooker, *Anal. Bioanal. Chem.*, 2010, 396, 1071-1077.

174.   S. Arepalli, P. Nikolaev, O. Gorelik, V. G. Hadjiev, H. A. Bradlev, W. Holmes, B. Files and L. Yowell, *Carbon*, 2004, 42, 1783-1791.

175.   M. Reichenbächer and J. Popp, *Challenges in Molecular Structure Determination*, Springer, Berlin, 2012.

References

176. Matthias Mann, Ronald C. Hendrickson and A. Pandey, *Annu. Rev. Biochem.*, 2001, 70, 437-473.

177. D. Gilg, B. Riedl, A. Zier and M. F. Zimmermann, *Pharm. Acta. Helv.*, 1996, 71, 383-394.

178. W. M. A. Niessen and D. Falck, in *Analyzing Biomolecular Interactions by Mass Spectrometry*, J. Kool, W. M. A. Niessen, Wiley-VCH Verlag GmbH & Co. KGaA, Germany, 2015,.ch1, pp. 1-54.

179. N. J. Greenfield, *Anal. Biochem.*, 1996, 235, 1-10.

180. S. M. Kelly and N. C. Price, *Curr. Protein Pept. Sci.*, 2000, 1, 349-384.

181. R. Gopal, J. S. Park, C. H. Seo and Y. Park, *Int. J. Mol. Sci.*, 2012, 13, 3229-3244.

182. B. M. Bulheller, A. Rodger and J. D. Hirst, *PCCP*, 2007, 9, 2020-2035.

183. S. M. Kelly, T. J. Jess and N. C. Price, *Biochim. Biophys. Acta*, 2005, 1751, 119-139.

184. B. A. Wallace and R. W. Janes, *Curr. Opin. Chem. Biol.*, 2001, 5, 567-571.

185. N. Berova, K. Nakanishi and R. Woody, *Circular Dichroism: Principles and Applications*, Wiley, USA, 2000.

186. S. Brahms and J. Brahms, *J. Mol. Biol.*, 1980, 138, 149-178.

187. A. L. Rucker and T. P. Creamer, *Protein Sci.,* 2002, 11, 980-985.

References

188.   I. Gokce, R. W. Woody, G. Anderluh and J. H. Lakey, *J. Am. Chem. Soc.*, 2005, 127, 9700-9701.

189.   A. J. Miles and B. A. Wallace, *Chem. Soc. Rev.*, 2006, 35, 39-51.

190.   B. Ranjbar and P. Gill, *Chem. Biol. Drug Des.*, 2009, 74, 101-120.

191.   A. J. Doig, *Prog. Mol. Biol. Transl. Sci.,* 2008, 83, pp. 1-52.

192.   C. Richard, F. Balavoine, P. Schultz, T. W. Ebbesen and C. Mioskowski, *Science*, 2003, 300, 775-778.

193.   Y. Kang and T. A. Taton, *J. Am. Chem. Soc.*, 2003, 125, 5650-5651.

194.   G. von Maltzahn, S. Vauthey, S. Santoso and S. U. Zhang, *Langmuir*, 2003, 19, 4332-4337.

195.   N. M. B. Cogan, C. J. Bowerman, L. J. Nogaj, B. L. Nilsson and T. D. Krauss, *J. Phys. Chem. C*, 2014, 118, 5935-5944.

196.   S. R. Friling, R. Notman and T. R. Walsh, *Nanoscale*, 2010, 2, 98-106.

197.   C. C. Chiu, M. C. Maher, G. R. Dieckmann and S. O. Nielsen, *ACS Nano*, 2010, 4, 2539-2546.

198.   A. S. Klimenko and G. R. Dieckmann, in *Peptide Materials*, ed. C. Alemán, A. Bianco and M. Venanzi, John Wiley & Sons, UK, 2013,.ch. 8, pp. 217-245.

199.   T. R. Walsh and S. M. Tomasio, *Mol. Biosyst.*, 2010, 6, 1707-1718.

References

200.   S. Q. Wang, E. S. Humphreys, S. Y. Chung, D. F. Delduco, S. R. Lustig, H. Wang, K. N. Parker, N. W. Rizzo, S. Subramoney, Y. M. Chiang and A. Jagota, *Nat. Mater.*, 2003, 2, 196-200.

201.   W. J. Jeong and Y. B. Lim, *Macromol. Biosci.*, 2012, 12, 49-54.

202.   Y. Hashida, T. Umeyama, J. Mihara, H. Imahori, M. Tsujimoto, S. Isoda, M. Takano and M. Hashida, *J. Pharm. Sci.*, 2012, 101, 3398-3412.

203.   E. L. Bakota, L. Aulisa, D. A. Tsyboulski, R. B. Weisman and J. D. Hartgerink, *Biomacromolecules*, 2009, 10, 2201-2206.

204.   D. A. Tsyboulski, E. L. Bakota, L. S. Witus, J.-D. R. Rocha, J. D. Hartgerink and R. B. Weisman, *J. Am. Chem. Soc.*, 2008, 130, 17134-17140.

205.   Z. Fu, Y. Luo, P. Derreumaux and G. Wei, *Biophys. J.*, 2009, 97, 1795-1803.

206.   E. P. O'Brien, G. Stan, D. Thirumalai and B. R. Brooks, *Nano Lett.*, 2008, 8, 3702-3708.

207.   L. F. Zheng, D. Jain and P. Burke, *J. Phys. Chem. C*, 2009, 113, 3978-3985.

208.   D. Kase, J. L. Kulp, M. Yudasaka, J. S. Evans, S. Iijima and K. Shiba, *Langmuir*, 2004, 20, 8939-8941.

209.   V. Zorbas, A. Ortiz-Acevedo, A. B. Dalton, M. M. Yoshida, G. R. Dieckmann, R. K. Draper, R. H. Baughman, M. Jose-Yacaman and I. H. Musselman, *J. Am. Chem. Soc.*, 2004, 126, 7222-7227.

References

210. C.-c. Chiu, G. R. Dieckmann and S. O. Nielsen, *Pept. Sci.*, 2009, 92, 156-163.

211. C. Rajesh, C. Majumder, H. Mizuseki and Y. Kawazoe, *J. Chem Phys.*, 2009, 130, 124911.

212. Z. D. Su, T. Leung and J. F. Honek, *J. Phys. Chem. B*, 2006, 110, 23623-23627.

213. H. Xie, E. J. Becraft, R. H. Baughman, A. B. Dalton and G. R. Dieckmann, *J. Pept. Sci.*, 2008, 14, 139-151.

214. C. G. Salzmann, G. K. C. Lee, M. A. H. Ward, B. T. T. Chu and M. L. H. Green, *J. Mater. Chem.*, 2008, 18, 1977-1983.

215. E. J. Wallace, R. S. G. D'Rozario, B. M. Sanchez and M. S. P. Sansom, *Nanoscale*, 2010, 2, 967-975.

216. C.-c. Chiu, G. R. Dieckmann and S. O. Nielsen, *J. Phys. Chem. B*, 2008, 112, 16326-16333.

217. M. G. Rüther, F. Frehill, J. E. O'Brien, A. I. Minett, W. J. Blau, J. G. Vos and M. in het Panhuis, *J. Phys. Chem. B*, 2004, 108, 9665-9668.

218. P. J. Ren, A. M. Zheng, X. L. Pan, X. W. Han and X. H. Bao, *J. Phys. Chem. C*, 2013, 117, 23418-23424.

References

219.   A. Kitaygorodskiy, W. Wang, S.-Y. Xie, Y. Lin, K. A. Shiral Fernando, X. Wang, L. Qu, B. Chen and Y.-P. Sun, *J. Am. Chem. Soc.*, 2005, 127, 7517-7520.

220.   C. Engtrakul, M. F. Davis, K. Mistry, B. A. Larsen, A. C. Dillon, M. J. Heben and J. L. Blackburn, *J. Am. Chem. Soc.*, 2010, 132, 9956-9957.

221.   D. J. Nelson, H. Rhoads and C. Brammer, *J. Phys. Chem. C*, 2007, 111, 17872-17878.

222.   D. J. Nelson and R. Kumar, *J. Phys. Chem. C*, 2013, 117, 14812-14823.

223.   R. Marega, V. Aroulmoji, F. Dinon, L. Vaccari, S. Giordani, A. Bianco, E. Murano and M. Prato, *J. Am. Chem. Soc.*, 2009, 131, 9086-9093.

224.   R. Prakash, S. Washburn, R. Superfine, R. E. Cheney and M. R. Falvo, *Appl. Phys. Lett.*, 2003, 83, 1219-1221.

225.   S. L. Grage, U. H. N. Duerr, S. Afonin, P. K. Mikhailiuk, I. V. Komarov and A. S. Ulrich, *J. Magn. Reson.*, 2008, 191, 16-23.

226.   M. Holzinger, O. Vostrowsky, A. Hirsch, F. Hennrich, M. Kappes, R. Weiss and F. Jellen, *Angew. Chem. Int. Ed.*, 2001, 40, 4002-4005.

227.   A. Kumari and K. Dorai, *J. Phys. Chem. A*, 2011, 115, 6543-6550.

228.   L. Kiss, E. Forro, S. Fustero and F. Fulop, *Org. Biomol. Chem.*, 2011, 9, 6528-6534.

References

229. T. Vagt, E. Nyakatura, M. Salwiczek, C. Jackel and B. Koksch, *Org. Biomol. Chem.*, 2010, 8, 1382-1386.

230. A. Sutherland and C. L. Willis, *Nat. Prod. Rep.*, 2000, 17, 621-631.

231. Y. Tang, G. Ghirlanda, N. Vaidehi, J. Kua, D. T. Mainz, W. A. Goddard, W. F. DeGrado and D. A. Tirrell, *Biochem.*, 2001, 40, 2790-2796.

232. L. Hunter, S. Butler and S. B. Ludbrook, *Org. Biomol. Chem.*, 2012, 10, 8911-8918.

233. N. L. Ogihara, M. S. Weiss, D. Eisenberg and W. F. Degrado, *Protein Sci.*, 1997, 6, 80-88.

234. Ricardo M. F. Fernandes, Bárbara Abreu, Bárbara Claro, Matat Buzaglo, Oren Regev, István Furó, and Eduardo F. Marques, *Langmuir*, 2015, 31, 10955-10965.

235. K. R. Shoemaker, P. S. Kim, E. J. York, J. M. Stewart and R. L. Baldwin, *Nature*, 1987, 326, 563-567.

236. F. A. Quiocho, J. S. Sack and N. K. Vyas, *Nature*, 1987, 329, 561-564.

237. N. J. Greenfield, W. E. Stafford and S. E. Hitchcock-Degregori, *Protein Sci.*, 1994, 3, 402-410.

238. B. Forood, E. J. Feliciano and K. P. Nambiar, *PNAS*, 1993, 90, 838-842.

239. C. S. Dexter, R. F. W. Jackson and J. Elliott, *J. Org. Chem.*, 1999, 64, 7579-7585.

References

240.   M. Kruppa, G. Imperato and B. Konig, *Tetrahedron*, 2006, 62, 1360-1364.

241.   L. Le Corre, C. Gravier-Pelletier and Y. Le Merrer, *Eur. J. Org. Chem.*, 2007, 2007, 5386-5394.

242.   S. van Zutphen, E. A. Stone, S. van Rijt, M. S. Robillard, G. A. van der Marel, H. S. Overkleeft, H. den Dulk, J. Brouwer and J. Reedijk, *J. Inorg. Biochem.*, 2005, 99, 2032-2038.

243.   S. Kotha, K. Lahiri and D. Kashinath, *Tetrahedron*, 2002, 58, 9633-9695.

244.   J. Zhou and G. C. Fu, *J. Am. Chem. Soc.*, 2003, 125, 12527-12530.

245.   S. E. Denmark and M. H. Ober, *Adv. Synth. Catal.*, 2004, 346, 1703-1714.

246.   J. A. Casares, P. Espinet, B. Fuentes and G. Salas, *J. Am. Chem. Soc.*, 2007, 129, 3508-3509.

247.   N. Wang, *Chin. J. Org. Chem.*, 2011, 31, 1319-1323.

248.   X.-F. Wu, J. Schranck, H. Neumann and M. Beller, *Chem. Asian J.*, 2012, 7, 40-44.

249.   K. C. Nicolaou, P. G. Bulger and D. Sarlah, *Angew. Chem., Int. Ed.*, 2005, 44, 4442-4489.

250.   A. N. Tkachenko, D. S. Radchenko, P. K. Mykhailiuk, S. Afonin, A. S. Ulrich and I. V. Komarov, *Angew. Chem. Int. Edit.*, 52, 6504-6507.

References

251. S. L. Grage, U. H. N. Duerr, S. Afonin, P. K. Mikhailiuk, I. V. Komarov and A. S. Ulrich, *J. Magn. Reson.*, 2008, 191, 16-23.

252. H. Xie, A. Ortiz-Acevedo, V. Zorbas, R. H. Baughman, R. K. Draper, I. H. Musselman, A. B. Dalton and G. R. Dieckmann, *J. Mater. Chem.*, 2005, 15, 1734-1741.

253. V. Z. Poenitzsch, D. C. Winters, H. Xie, G. R. Dieckmann, A. B. Dalton and I. H. Musselman, *J. Am. Chem. Soc.*, 2007, 129, 14724-14732.

254. A. Chakrabartty, A. J. Doig and R. L. Baldwin, *PNAS*, 1993, 90, 11332-11336.

255. M. A. Kubasik, E. Daly and A. Blom, *Chembiochem*, 2006, 7, 1056-1061.

256. F. Evanics, J. L. Kitevski, I. Bezsonova, J. Forman-Kay and R. S. Prosser, *BB-Gen. Sub.,* 2007, 1770, 221-230.

257. A. Bianco, K. Kostarelos and M. Prato, *Curr. Opin. Chem. Biol.*, 2005, 9, 674-679.

258. R. G. Mendes, A. Bachmatiuk, B. Buchner, G. Cuniberti and M. H. Rummeli, *J. Mater. Chem. B*, 2013, 1, 401-428.

259. D. Pantarotto, J.-P. Briand, M. Prato and A. Bianco, *Chem. Commun.*, 2004, 16-17.

260. C. Klumpp, K. Kostarelos, M. Prato and A. Bianco, *Biochim. Biophys. Acta.*, 2006, 1758, 404-412.

References

261. K. Ajima, M. Yudasaka, T. Murakami, A. Maigne, K. Shiba and S. Ijima, *Mol. Pharm.*, 2005, 2, 475-480.

262. D. Pantarotto, C. D. Partidos, R. Graff, J. Hoebeke, J. P. Briand, M. Prato and A. Bianco, *J. Am. Chem. Soc.*, 2003, 125, 6160-6164.

263. D. Pantarotto, C. D. Partidos, J. Hoebeke, F. Brown, E. Kramer, J. P. Briand, S. Muller, M. Prato and A. Bianco, *Chem. Biol.*, 2003, 10, 961-966.

264. J. Svenson, W. Stensen, B.-O. Brandsdal, B. E. Haug, J. Monrad and J. S. Svendsen, *Biochem.*, 2008, 47, 3777-3788.

265. M. Werle and A. Bernkop-Schnürch, *Amino Acids*, 2006, 30, 351-367.

266. J. V. Olsen, S.-E. Ong and M. Mann, *Mol. Cell. Proteomics*, 2004, 3, 608-614.

267. R. Haggenmueller, S. S. Rahatekar, J. A. Fagan, J. Chun, M. L. Becker, R. R. Naik, T. Krauss, L. Carlson, J. F. Kadla, P. C. Trulove, D. F. Fox, H. C. DeLong, Z. Fang, S. O. Kelley and J. W. Gilman, *Langmuir*, 2008, 24, 5070-5078.

268. K. Jiang, L. S. Schadler, R. W. Siegel, X. Zhang, H. Zhang and M. Terrones, *J. Mater. Chem.*, 2004, 14, 37-39.

269. V. Georgakilas, N. Tagmatarchis, D. Pantarotto, A. Bianco, J.-P. Briand and M. Prato, *Chem. Commun.*, 2002, 3050-3051.

References

270.   A. de Leon, A. F. Jalbout and V. A. Basiuk, *Chem. Phys. Lett.*, 2008, 457, 185-190.

271.   F. Bomboi, A. Bonincontro, C. La Mesa and F. Tardani, *J. Colloid Interface Sci.*, 2011, 355, 342-347.

272.   Z. T. Xiao, X. Wang, X. Xu, H. Zhang, Y. Li and Y. H. Wang, *J. Phys. Chem. C*, 2011, 115, 21546-21558.

273.   N. Nakashima, S. Okuzono, H. Murakami, T. Nakai and K. Yoshikawa, *Chem. Lett.*, 2003, 32, 782-782.

274.   S. E. Baker, W. Cai, T. L. Lasseter, K. P. Weidkamp and R. J. Hamers, *Nano Lett.*, 2002, 2, 1413-1417.

275.   P. J. Halling, *J. Chem. Technol. Biotechnol.*, 1995, 62, 105-105.

276.   Y.-L. Zhao and J. F. Stoddart, *Acc. Chem. Res.*, 2009, 42, 1161-1171.

277.   M. Naito, K. Nobusawa, H. Onouchi, M. Nakamura, K. Yasui, A. Ikeda and M. Fujiki, *J. Am. Chem. Soc.*, 2008, 130, 16697-16703.

278.   S. Hanessian, X. Luo and R. Schaum, *Tetrahedron Lett.*, 1999, 40, 4925-4929.

279.   D. H. Appella, L. A. Christianson, I. L. Karle, D. R. Powell and S. H. Gellman, *J. Am. Chem. Soc.*, 1996, 118, 13071-13072.

280.   P. S. Farmer and E. J. Ariëns, *Trends Pharmacol. Sci.*, 1982, 3, 362-365.

References

281. R. N. Zuckermann, *Biopolymers*, 2011, 96, 545-555.

282. R. M. J. Liskamp, D. T. S. Rijkers, J. A. W. Kruijtzer and J. Kemmink, *ChemBioChem*, 2011, 12, 1626-1653.

283. D. Zhang, S. H. Lahasky, L. Guo, C.-U. Lee and M. Lavan, *Macromolecules*, 2012, 45, 5833-5841.

284. R. J. Simon, R. S. Kania, R. N. Zuckermann, V. D. Huebner, D. A. Jewell, S. Banville, S. Ng, L. Wang, S. Rosenberg and C. K. Marlowe, *PNAS*, 1992, 89, 9367-9371.

285. H. J. Olivos, P. G. Alluri, M. M. Reddy, D. Salony and T. Kodadek, *Org. Lett.*, 2002, 4, 4057-4059.

286. B. C. Gorske, S. A. Jewell, E. J. Guerard and H. E. Blackwell, *Org. Lett.*, 2005, 7, 1521-1524.

287. P. Armand, K. Kirshenbaum, A. Falicov, R. L. Dunbrack Jr, K. A. Dill, R. N. Zuckermann and F. E. Cohen, *Fold Des.*, 1997, 2, 369-375.

288. T. S. Burkoth, E. Beausoleil, S. Kaur, D. Tang, F. E. Cohen and R. N. Zuckermann, *Chem. Biol.*, 2002, 9, 647-654.

289. B. Carsten, G. Robert and H. Hans-Jörg, *Phys. Biol.*, 2006, 3, S1-S9.

290. R. S. Spolar, J. H. Ha and M. T. Record, *PNAS*, 1989, 86, 8382-8385.

291. N. T. Southall, K. A. Dill and A. D. J. Haymet, *J. Phys. Chem. B*, 2002, 106, 521-533.

References

292. R. Montserret, M. J. McLeish, A. Böckmann, C. Geourjon and F. Penin, *Biochem.*, 2000, 39, 8362-8373.

293. S. Kumar and R. Nussinov, *ChemBioChem*, 2002, 3, 604-617.

294. M. Meot-Ner, *Chem. Rev.*, 2005, 105, 213-284.

295. M. L. Waters, *Curr. Opin. Chem. Biol.*, 2002, 6, 736-741.

296. M. L. Waters, *Pept. Sci.*, 2004, 76, 435-445.

297. C. W. Wu, K. Kirshenbaum, T. J. Sanborn, J. A. Patch, K. Huang, K. A. Dill, R. N. Zuckermann and A. E. Barron, *J. Am. Chem. Soc.*, 2003, 125, 13525-13530.

298. E. J. Robertson, G. K. Olivier, M. Qian, C. Proulx, R. N. Zuckermann and G. L. Richmond, *PNAS*, 2014, 111, 13284-13289.

299. J. K. Pokorski, L. M. Miller Jenkins, H. Feng, S. R. Durell, Y. Bai and D. H. Appella, *Org. Lett.*, 2007, 9, 2381-2383.

300. B. C. Gorske, B. L. Bastian, G. D. Geske and H. E. Blackwell, *J. Am. Chem. Soc.*, 2007, 129, 8928-8929.

301. P. Armand, K. Kirshenbaum, R. A. Goldsmith, S. Farr-Jones, A. E. Barron, K. T. V. Truong, K. A. Dill, D. F. Mierke, F. E. Cohen, R. N. Zuckermann and E. K. Bradley, *PNAS*, 1998, 95, 4309-4314.

302. K. Kirshenbaum, A. E. Barron, R. A. Goldsmith, P. Armand, E. K. Bradley, K. T. V. Truong, K. A. Dill, F. E. Cohen and R. N. Zuckermann, *PNAS*, 1998, 95, 4303-4308.

References

303. J. Seo, A. E. Barron and R. N. Zuckermann, *Org. Lett.*, 2010, 12, 492-495.

304. C. W. Wu, T. J. Sanborn, K. Huang, R. N. Zuckermann and A. E. Barron, *J. Am. Chem. Soc.*, 2001, 123, 6778-6784.

305. C. W. Wu, T. J. Sanborn, R. N. Zuckermann and A. E. Barron, *J. Am. Chem. Soc.*, 2001, 123, 2958-2963.

306. R. C. N. C.B Gorske, Z.S. Bowden, T.A Kufe, and A.M. Childs, *J. Org. Chem.*, 2013, 78, 11172 - 11183.

307. S. A. Fowler and H. E. Blackwell, *Org. Biomol. Chem.*, 2009, 7, 1508-1524.

308. K. Huang, C. W. Wu, T. J. Sanborn, J. A. Patch, K. Kirshenbaum, R. N. Zuckermann, A. E. Barron and I. Radhakrishnan, *J. Am. Chem. Soc.*, 2006, 128, 1733-1738.

309. K. Balamurugan, E. R. A. Singam and V. Subramanian, *J. Phys. Chem. C*, 2011, 115, 8886-8892.

310. N. P. Chongsiriwatana, J. A. Patch, A. M. Czyzewski, M. T. Dohm, A. Ivankin, D. Gidalevitz, R. N. Zuckermann and A. E. Barron, *PNAS*, 2008, 105, 2794-2799.

311. Z. L. Yao, N. Braidy, G. A. Botton and A. Adronov, *J. Am. Chem. Soc.*, 2003, 125, 16015-16024.

312. Z. Li, T. Kameda, T. Isoshima, E. Kobatake, T. Tanaka, Y. Ito and M. Kawamoto, *Langmuir*, 2015, 31, 3482-3488.

References

313. A. L. Alpatova, W. Q. Shan, P. Babica, B. L. Upham, A. R. Rogensues, S. J. Masten, E. Drown, A. K. Mohanty, E. C. Alocilja and V. V. Tarabara, *Water Res.*, 2010, 44, 505-520.

314. C. Roquelet, J.-S. Lauret, V. Alain-Rizzo, C. Voisin, R. Fleurier, M. Delarue, D. Garrot, A. Loiseau, P. Roussignol, J. A. Delaire and E. Deleporte, *Chemphyschem*, 2010, 11, 1667-1672.

315. R. Anjana, M. K. Vaishnavi, D. Sherlin, S. P. Kumar, K. Naveen, P. S. Kanth and K. Sekar, *Bioinformation*, 2012, 8, 1220-1224.

316. C.-S. Park, C. J. Lee and E. K. Kim, *PCCP*, 2015, 17, 16243-16245.

317. R. Podila, P. Vedantam, P. C. Ke, J. M. Brown and A. M. Rao, *J. Phys. Chem. C*, 2012, 116, 22098-22103.

318. H. J. Shin, S. M. Kim, S. M. Yoon, A. Benayad, K. K. Kim, S. J. Kim, H. K. Park, J. Y. Choi and Y. H. Lee, *J. Am. Chem. Soc.*, 2008, 130, 2062-2066.

319. C. N. R. Rao and R. Voggu, *Mater. Today*, 2010, 13, 34-40.

320. A. B. Dalton, A. Ortiz-Acevedo, V. Zorbas, E. Brunner, W. M. Sampson, S. Collins, J. M. Razal, M. Miki Yoshida, R. H. Baughman, R. K. Draper, I. H. Musselman, M. Jose-Yacaman and G. R. Dieckmann, *Adv. Funct. Mater.*, 2004, 14, 1147-1151.

321. J. A. Patch and A. E. Barron, *J. Am. Chem. Soc.*, 2003, 125, 12092-12093.

References

322. S. C. Tsang, Z. Guo, Y. K. Chen, M. L. H. Green, H. A. O. Hill, T. W. Hambley and P. J. Sadler, *Angew. Chem. Int. Edit. Engl.*, 1997, 36, 2198-2200.

323. Z. J. Guo, P. J. Sadler and S. C. Tsang, *Adv. Mater.*, 1998, 10, 701-703.

324. D. A. Heller, E. S. Jeng, T.-K. Yeung, B. M. Martinez, A. E. Moll, J. B. Gastala and M. S. Strano, *Science*, 2006, 311, 508-511.

325. S. Meng, P. Maragakis, C. Papaloukas and E. Kaxiras, *Nano Lett.*, 2007, 7, 45-50.

326. H. Wang and A. Ceulemans, *Phys. Rev. B*, 2009, 79, 1954191- 1954196.

327. V. Verdolino, R. Cammi, B. H. Munk and H. B. Schlegel, *J. Phys. Chem. B*, 2008, 112, 16860-16873.

328. A. Das, A. K. Sood, P. K. Maiti, M. Das, R. Varadarajan and C. N. R. Rao, *Chem. Phys. Lett.*, 2008, 453, 266-273.

329. N. Varghese, U. Mogera, A. Govindaraj, A. Das, P. K. Maiti, A. K. Sood and C. N. R. Rao, *Chemphyschem*, 2009, 10, 206-210.

330. D. Umadevi and G. N. Sastry, *J. Phys. Chem. Lett.*, 2011, 2, 1572-1576.

331. A. L. Frischknecht and M. G. Martin, *J. Phys. Chem. C*, 2008, 112, 6271-6278.

332. V. A. Karachevtsev, A. M. Plokhotnichenko, M. V. Karachevtsev and V. S. Leontiev, *Carbon*, 2010, 48, 3682-3691.

References

333.   M. Hazani, R. Naaman, F. Hennrich and M. M. Kappes, *Nano Lett.*, 2003, 3, 153-155.

334.   R. R. Johnson, A. Kohlmeyer, A. T. C. Johnson and M. L. Klein, *Nano Lett.*, 2009, 9, 537-541.

335.   B. Maji, S. K. Samanta and S. Bhattacharya, *Nanoscale*, 2014, 6, 3721-3730.

336.   E. S. Jeng, A. E. Moll, A. C. Roy, J. B. Gastala and M. S. Strano, *Nano Lett.*, 2006, 6, 371-375.

337.   J. H. Kim, M. Kataoka, D. Shimamoto, H. Muramatsu, Y. C. Jung, T. Tojo, T. Hayashi, Y. A. Kim, M. Endo, M. Terrones and M. S. Dresselhaus, *Chemphyschem*, 2009, 10, 2414-2417.

338.   D. Roxbury, X. M. Tu, M. Zheng and A. Jagota, *Langmuir*, 2011, 27, 8282-8293.

339.   M. Zheng, A. Jagota, E. D. Semke, B. A. Diner, R. S. Mclean, S. R. Lustig, R. E. Richardson and N. G. Tassi, *Nat. Mater.*, 2003, 2, 338-342.

340.   M. Zheng, A. Jagota, M. S. Strano, A. P. Santos, P. Barone, S. G. Chou, B. A. Diner, M. S. Dresselhaus, R. S. Mclean, G. B. Onoa, G. G. Samsonidze, E. D. Semke, M. Usrey and D. J. Walls, *Science*, 2003, 302, 1545-1548.

341.   A. Ikeda, T. Hamano, K. Hayashi and J.-i. Kikuchi, *Org. Lett.*, 2006, 8, 1153-1156.

342.   X. Tu, S. Manohar, A. Jagota and M. Zheng, *Nature*, 2009, 460, 250-253.

References

343.   C. Y. Khripin, S. Manohar, M. Zheng and A. Jagota, *J. Phys. Chem. C*, 2009, 113, 13616-13621.

344.   R. R. Johnson, A. T. C. Johnson and M. L. Klein, *Small*, 2010, 6, 31-34.

345.   D. Chris, G. Martin, F. Michael, W. Sean, S. Richard and E. Dorothy, *Nanotechnol.*, 2002, 13, 601-604.

346.   A. Micoli, M. Quintana and M. Prato, *Supramol. Chem.*, 2013, 25, 567-573.

347.   A. Micoli, A. Turco, E. Araujo-Palomo, A. Encinas, M. Quintana and M. Prato, *Chem. Eur. J.*, 2014, 20, 5397-5402.

348.   S. Boncel, M. Brzeziński, J. Mrowiec-Białoń, D. Janas, K. K. K. Koziol and K. Z. Walczak, *Mater. Lett.*, 2013, 91, 50-54.

349.   W. Chen, L. Duan, L. Wang and D. Zhu, *Environ. Sci. Technol.*, 2008, 42, 6862-6868.

350.   B. Pan, D. Lin, H. Mashayekhi and B. Xing, *Environ. Sci. Technol.*, 2008, 42, 5480-5485.

351.   K. Yang, L. Zhu and B. Xing, *Environ. Sci. Technol.*, 2006, 40, 1855-1861.

352.   Z. Jijun, B. Alper, H. Jie and L. Jian Ping, *Nanotechnol.*, 2002, 13, 195-200.

353.   S. Zhang, T. Shao, S. S. K. Bekaroglu and T. Karanfil, *Environ. Sci. Technol.*, 2009, 43, 5719-5725.

References

354. H. Kataura, Y. Kumazawa, Y. Maniwa, I. Umezu, S. Suzuki, Y. Ohtsuka and Y. Achiba, *Synth. Met.*, 1999, 103, 2555-2558.

355. J. L. Bahr and J. M. Tour, *J. Mater. Chem.*, 2002, 12, 1952-1958.

356. M. S. Dresselhaus, A. Jorio, M. Hofmann, G. Dresselhaus and R. Saito, *Nano Lett.*, 10, 751-758.

357. B. Pan and B. Xing, *Environ. Sci. Technol.*, 2008, 42, 9005-9013.

358. C. Jiang, K. Kempa, J. Zhao, U. Schlecht, U. Kolb, T. Basché, M. Burghard and A. Mews, *Phys. Rev. B*, 2002, 66, 161404-161444.

359. A. K. Geim and K. S. Novoselov, *Nat. Mater.*, 2007, 6, 183-191.

360. R. L. McCreery, *Chem. Rev.*, 2008, 108, 2646-2687.

361. Y. Zhang, C. Y. Wu, S. W. Guo and J. Y. Zhang, *Nanotechnol. Rev.*, 2013, 2, 27-45.

362. D. A. C. Brownson and C. E. Banks, *Analyst*, 2010, 135, 2768-2778.

363. C. N. R. Rao, K. Biswas, K. S. Subrahmanyam and A. Govindaraj, *J. Mater. Chem.*, 2009, 19, 2457-2469.

364. K. S. Novoselov, A. K. Geim, S. V. Morozov, D. Jiang, Y. Zhang, S. V. Dubonos, I. V. Grigorieva and A. A. Firsov, *Science*, 2004, 306, 666-669.

365. B. Partoens and F. M. Peeters, *Phys. Rev. B*, 2006, 74, 0754041- 07540411.

366. M. Freitag, *Nat. Phys.*, 2011, 7, 596-597.

References

367. J. Hass, W. A. de Heer and E. H. Conrad, *J. Phys-Condens. Mat.*, 2008, 20. 323202.

368. R. S. Edwards and K. S. Coleman, *Nanoscale*, 2013, 5, 38-51.

369. K. T. H. Bonex W Mwakikunga, in *Graphene - Synthesis, Characterization, Properties and Applications*, ed. P. J. Gong, InTech, 2011, ch. 5, pp. 59-78.

370. A. Ambrosi, C. K. Chua, A. Bonanni and M. Pumera, *Chem. Rev.*, 2014, 114, 7150-7188.

371. A. Lerf, H. Y. He, M. Forster and J. Klinowski, *J. Phys. Chem. B*, 1998, 102, 4477-4482.

372. A. Buchsteiner, A. Lerf and J. Pieper, *J. Phys. Chem. B*, 2006, 110, 22328-22338.

373. A A. Mathkar, D. Tozier, P. Cox, P. J. Ong, C. Galande, K. Balakrishnan, A. L. M. Reddy and P. M. Ajayan, *J. Phys. Chem. Lett.*, 2012, 3, 986-991.

374. M. Lotya, Y. Hernandez, P. J. King, R. J. Smith, V. Nicolosi, L. S. Karlsson, F. M. Blighe, S. De, Z. M. Wang, I. T. McGovern, G. S. Duesberg and J. N. Coleman, *J. Am. Chem. Soc.*, 2009, 131, 3611-3620.

375. Y. Hernandez, V. Nicolosi, M. Lotya, F. M. Blighe, Z. Y. Sun, S. De, I. T. McGovern, B. Holland, M. Byrne, Y. K. Gun'ko, J. J. Boland, P. Niraj, G. Duesberg, S. Krishnamurthy, R. Goodhue, J. Hutchison, V. Scardaci, A. C. Ferrari and J. N. Coleman, *Nat. Nanotechnol.*, 2008, 3, 563-568.

References

376. B. Garg, T. Bisht and Y. C. Ling, *Molecules*, 2014, 19, 14582-14614.

377. B. C. Brodie, *Philos. Trans. R. Soc. Lond.*, 1859, 149, 249-259.

378. L. Staudenmaier, *Ber. Dtsch. Chem. Ges.,* 1898, 31, 1481-1487.

379. U. Hofmann and E. König, *Z. Anorg. Allg. Chem.*, 1937, 234, 311-336.

380. W. S. Hummers and R. E. Offeman, *J. Am. Chem. Soc.*, 1958, 80, 1339-1339.

381. D. C. Marcano, D. V. Kosynkin, J. M. Berlin, A. Sinitskii, Z. Z. Sun, A. Slesarev, L. B. Alemany, W. Lu and J. M. Tour, *ACS Nano*, 2010, 4, 4806-4814.

382. D. R. Dreyer, A. D. Todd and C. W. Bielawski, *Chem. Soc. Rev.*, 2014, 43, 5288-5301.

383. J. I. Paredes, S. Villar-Rodil, A. Martinez-Alonso and J. M. D. Tascon, *Langmuir*, 2008, 24, 10560-10564.

384. T. Kuila, A. K. Mishra, P. Khanra, N. H. Kim and J. H. Lee, *Nanoscale*, 2013, 5, 52-71.

385. Q. Tang, Z. Zhou and Z. F. Chen, *Nanoscale*, 2013, 5, 4541-4583.

386. X. F. Gao, J. Jang and S. Nagase, *J. Phys. Chem. C*, 2010, 114, 832-842.

387. Y. Y. Shao, J. Wang, M. Engelhard, C. M. Wang and Y. H. Lin, *J. Mater. Chem.*, 2010, 20, 743-748.

References

388. A. L. Stroyuk, N. S. Andryushina, N. D. Shcherban', V. G. Il'in, V. S. Efanov, I. B. Yanchuk, S. Y. Kuchmii and V. D. Pokhodenko, *Theor. Exp. Chem.*, 2012, 48, 2-13.

389. V. C. Sanchez, A. Jachak, R. H. Hurt and A. B. Kane, *Chem. Res. Toxicol.*, 2012, 25, 15-34.

390. Y. Zhang, T. R. Nayak, H. Hong and W. B. Cai, *Nanoscale*, 2012, 4, 3833-3842.

391. C. Spinato, C. Ménard-Moyon and A. Bianco, in *Functionalization of Graphene*, ed. V. Georgakilas, Wiley-VCH Verlag GmbH & Co. KGaA, Germany, 2014, ch4, pp. 95-138.

392. M. C. Duch, G. R. S. Budinger, Y. T. Liang, S. Soberanes, D. Urich, S. E. Chiarella, L. A. Campochiaro, A. Gonzalez, N. S. Chandel, M. C. Hersam and G. M. Mutlu, *Nano Lett.*, 2011, 11, 5201-5207.

393. H. Ali-Boucetta, D. Bitounis, R. Raveendran-Nair, A. Servant, J. Van den Bossche and K. Kostarelos, *Adv. Healthcare Mater.*, 2013, 2, 433-441.

394. H. Y. Mao, S. Laurent, W. Chen, O. Akhavan, M. Imani, A. A. Ashkarran and M. Mahmoudi, *Chem. Rev.*, 2013, 113, 3407-3424.

395. B. J. Hong, O. C. Compton, Z. An, I. Eryazici and S. T. Nguyen, *ACS Nano*, 2012, 6, 63-73.

396. M. Lotya, P. J. King, U. Khan, S. De and J. N. Coleman, *ACS Nano*, 2010, 4, 3155-3162.

References

397. I. V. Pavlidis, M. Patila, U. T. Bornscheuer, D. Gournis and H. Stamatis, *Trends Biotechnol.*, 2014, 32, 312-320.

398. H. Y. He, J. Klinowski, M. Forster and A. Lerf, *Chem. Phys. Lett.*, 1998, 287, 53-56.

399. C. Hou, H. Quan, Y. Duan, Q. Zhang, H. Wang and Y. Li, *Nanoscale*, 2013, 5, 1227-1232.

400. X. Y. Qi, K. Y. Pu, X. Z. Zhou, H. Li, B. Liu, F. Boey, W. Huang and H. Zhang, *Small*, 2010, 6, 663-669.

401. P. Laaksonen, A. Walther, J. M. Malho, M. Kainlauri, O. Ikkala and M. B. Linder, *Angew. Chem., Int. Ed.*, 2011, 50, 8688-8691.

402. L. Q. Xu, W. J. Yang, K. G. Neoh, E. T. Kang and G. D. Fu, *Macromolecules*, 2010, 43, 8336-8339.

403. G. X. Wang, X. P. Shen, B. Wang, J. Yao and J. Park, *Carbon*, 2009, 47, 1359-1364.

404. L. J. Cote, F. Kim and J. Huang, *J. Am. Chem. Soc.*, 2009, 131, 1043-1049.

405. M. J. Fernández-Merino, J. I. Paredes, S. Villar-Rodil, L. Guardia, P. Solís-Fernández, D. Salinas-Torres, D. Cazorla-Amorós, E. Morallón, A. Martínez-Alonso and J. M. D. Tascón, *Carbon*, 2012, 50, 3184-3194.

406. Y. Wang, Z. H. Li, J. Wang, J. H. Li and Y. H. Lin, *Trends. Biotechnol.*, 2011, 29, 205-212.

407. Y. Z. Hu, J. F. Shen, N. Li, M. Shi, H. W. Ma, B. Yan, W. B. Wang, W. S. Huang and M. X. Ye, *Polym. Compos.*, 2010, 31, 1987-1994.

408. T. A. Pham, J. S. Kim, B. G. Cho, S. M. Son and Y. T. Jeong, *Synth. React. Inorg. M.*, 2011, 41, 1257-1262.

409. G. Shim, J. Lee, J. Kim, H. J. Lee, Y. B. Kim and Y. K. Oh, *RSC Adv.*, 2015, 5, 49905-49913.

410. S. N. Kim, Z. F. Kuang, J. M. Slocik, S. E. Jones, Y. Cui, B. L. Farmer, M. C. McAlpine and R. R. Naik, *J. Am. Chem. Soc.*, 2011, 133, 14480-14483.

411. V. K. Kodali, J. Scrimgeour, S. Kim, J. H. Hankinson, K. M. Carroll, W. A. de Heer, C. Berger and J. E. Curtis, *Langmuir*, 2011, 27, 863-865.

412. T. Kowalewski and D. M. Holtzman, *PNAS*, 1999, 96, 3688-3693.

413. Y. B. Sheng, W. Wang and P. Chen, *Protein Sci.*, 2010, 19, 1639-1648.

414. Y. B. Sheng, W. Wang and P. Chen, *J. Phys. Chem. C*, 2010, 114, 454-459.

415. Y. N. Guo, X. Lu, J. Weng and Y. Leng, *J. Phys. Chem. C*, 2013, 117, 5708-5717.

416. C. B. Chen, J. Li, R. Li, G. Y. Xiao and D. Y. Yan, *New J. Chem.*, 2013, 37, 2778-2783.

417. L. Ou, Y. Luo and G. Wei, *J. Phys. Chem. B*, 2011, 115, 9813-9822.

References

418. K. Balamurugan, R. Gopalakrishnan, S. S. Raman and V. Subramanian, *J. Phys. Chem. B*, 2010, 114, 14048-14058.

419. Z. L. Gu, Z. X. Yang, Y. Chong, C. C. Ge, J. K. Weber, D. R. Bell and R. H. Zhou, *Sci. Rep.*, 2015, 5, 9.

420. T T. Mesaric, L. Baweja, B. Drasler, D. Drobne, D. Makovec, P. Dusak, A. Dhawan and K. Sepcic, *Carbon*, 2013, 62, 222-232.

421. M. Stefani, *Int. J. Mol. Sci.*, 2008, 9, 2515-2542.

422. M. Stefani, *Neuroscientist*, 2007, 13, 519-531.

423. B. Akdim, R. Pachter, S. S. Kim, R. R. Naik, T. R. Walsh, S. Trohalaki, G. Y. Hong, Z. F. Kuang and B. L. Farmer, *Acs. Appl. Mater. Interfaces*, 2013, 5, 7470-7477.

424. G. Raffaini and F. Ganazzoli, *Langmuir*, 2013, 29, 4883-4893.

425. C. E. Giacomelli and W. Norde, *Biomacromolecules*, 2003, 4, 1719-1726.

426. G. Zuo, X. Zhou, Q. Huang, H. P. Fang and R. H. Zhou, *J. Phys. Chem. C*, 2011, 115, 23323-23328.

427. S. Radic, N. K. Geitner, R. Podila, A. Kakinen, P. Y. Chen, P. C. Ke and F. Ding, *Sci. Rep.*, 2013, 3, 1-8.

428. J. Katoch, S. N. Kim, Z. F. Kuang, B. L. Farmer, R. R. Nalk, S. A. Tatulian and M. Ishigami, *Nano Lett.*, 2012, 12, 2342-2346.

References

429. J. Guo, X. Yao, L. Ning, Q. Wang and H. Liu, *RSC Advances*, 2014, 4, 9953-9962.

430. J. Zhang, F. Zhang, H. Yang, X. Huang, H. Liu, J. Zhang and S. Guo, *Langmuir*, 2010, 26, 6083-6085.

431. F. Zhang, B. Zheng, J. L. Zhang, X. L. Huang, H. Liu, S. W. Guo and J. Y. Zhang, *J. Phys. Chem. C*, 2010, 114, 8469-8473.

432. Y. Zhang, J. Y. Zhang, X. L. Huang, X. J. Zhou, H. X. Wu and S. W. Guo, *Small*, 2012, 8, 154-159.

433. T. Premkumar and K. E. Geckeler, *Prog. Polym. Sci.*, 2012, 37, 515-529.

434. M. Liu, Q. A. Zhang, H. M. Zhao, S. Chen, H. T. Yu, Y. B. Zhang and X. Quan, *Chem. Commun.*, 2011, 47, 4084-4086.

435. M. H. Alshehri, B. J. Cox and J. M. Hill, *Eur. Phys. J. D*, 2013, 67, 226-275.

436. A. M. O. Brett and A. M. Chiorcea, *Langmuir*, 2003, 19, 3830-3839.

437. N. S. Green and M. L. Norton, *Anal. Chim. Acta*, 2015, 853, 127-142.

438. M. Wu, R. Kempaiah, P.-J. J. Huang, V. Maheshwari and J. Liu, *Langmuir*, 2011, 27, 2731-2738.

439. C. H. Lu, H. H. Yang, C. L. Zhu, X. Chen and G. N. Chen, *Angew. Chem., Int. Ed.*, 2009, 48, 4785-4787.

440. E. Morales-Narvaez and A. Merkoci, *Adv. Mater.*, 2012, 24, 3298-3308.

References

441. P. J. J. Huang and J. W. Liu, *Nanomaterials*, 2013, 3, 221-228.

442. J. Antony and S. Grimme, *PCCP*, 2008, 10, 2722-2729.

443. H. Vovusha, S. Sanyal and B. Sanyal, *J. Phys. Chem. Lett.*, 2013, 4, 3710-3718.

444. Z Z. Xu, B. R. Meher, D. Eustache and Y. Wang, *J. Mol. Graphics Model.*, 2014, 47, 8-17.

445. S. J. Sowerby, C. A. Cohn, W. M. Heckl and N. G. Holm, *PNAS*, 2001, 98, 820-822.

446. Y.-H. Zhang, K.-G. Zhou, K.-F. Xie, C.-H. Liu, H.-L. Zhang, Y. Peng and Y.-Q. Xiong, *J. Nanosci.*, 2009, 08, 5-8.

447. V. Spiwok, P. Hobza and J. Rezac, *J. Phys. Chem. C*, 2011, 115, 19455-19462.

448. S. Panigrahi, A. Bhattacharya, S. Banerjee and D. Bhattacharyya, *J. Phys. Chem. C*, 2012, 116, 4374-4379.

449. D. Umadevi and G. N. Sastry, *Chemphyschem*, 2013, 14, 2570-2578.

450. Y. X. Wang and Y. X. Bu, *J. Phys. Chem. B*, 2007, 111, 6520-6526.

451. K. P. Loh, Q. Bao, P. K. Ang and J. Yang, *J. Mater. Chem.*, 2010, 20, 2277-2289.

452. A. Hirsch, J. M. Englert and F. Hauke, *Acc. Chem. Res.*, 2013, 46, 87-96.

References

453.   L. Yan, Y. B. Zheng, F. Zhao, S. J. Li, X. F. Gao, B. Q. Xu, P. S. Weiss and Y. L. Zhao, *Chem. Soc. Rev.*, 2012, 41, 97-114.

454.   L. Rodriguez-Perez, M. A. Herranz and N. Martin, *Chem. Commun.*, 2013, 49, 3721-3735.

455.   X. F. Gao, Y. Wang, X. Liu, T. L. Chan, S. Irle, Y. L. Zhao and S. B. B. Zhang, *PCCP*, 2011, 13, 19449-19453.

456.   M. Quintana, E. Vazquez and M. Prato, *Acc. Chem. Res.*, 2013, 46, 138-148.

457.   S. K. Singh, M. K. Singh, P. P. Kulkarni, V. K. Sonkar, J. J. A. Grácio and D. Dash, *ACS Nano*, 2012, 6, 2731-2740.

458.   X. Y. Liu, Y. F. Zhou, W. Y. Nie, L. Y. Song and P. P. Chen, *J. Mater. Sci.*, 2015, 50, 6113-6123.

459.   M. Namvari and H. Namazi, *J. Mater. Sci.*, 2015, 50, 5348-5361.

460.   A. A. Arbuzov, V. E. Muradyan, B. P. Tarasov, and E. A. Sokolov, *Nanomaterials*, 2013, 3, 3-39.

461.   J. F. Shen, B. Yan, M. Shi, H. W. Ma, N. Li and M. X. Ye, *J. Colloid Interface Sci.*, 2011, 356, 543-549.

462.   F. A. He, J. T. Fan, D. Ma, L. M. Zhang, C. Leung and H. L. Chan, *Carbon*, 2010, 48, 3139-3144.

463.   H. P. Mungse and O. P. Khatri, *J. Phys. Chem. C*, 2014, 118, 14394-14402.

References

464. J. Chu, X. Li and P. Xu, *J. Mater. Chem.*, 2011, 21, 11283-11287.

465. X. M. Sun, Z. Liu, K. Welsher, J. T. Robinson, A. Goodwin, S. Zaric and H. J. Dai, *Nano Res.*, 2008, 1, 203-212.

466. K. Yang, S. A. Zhang, G. X. Zhang, X. M. Sun, S. T. Lee and Z. A. Liu, *Nano Lett.*, 2010, 10, 3318-3323.

467. M. A. Ali, K. Kamil Reza, S. Srivastava, V. V. Agrawal, R. John and B. D. Malhotra, *Langmuir*, 2014, 30, 4192-4201.

468. Y. Jiang, Z. J. Jiang, S. Cheng and M. L. Liu, *Electrochim. Acta*, 2014, 146, 437-446.

469. M. Namvari and H. Namazi, *Carbohydr. Res.*, 2014, 396, 1-8.

470. Q. Yang, X. J. Pan, K. Clarke and K. C. Li, *Ind. Eng. Chem. Res.*, 2012, 51, 310-317.

471. M. Namvari and H. Namazi, *Polym. Int.*, 2014, 63, 1881-1888.

472. H. J. Salavagione, M. A. Gomez and G. Martinez, *Macromolecules*, 2009, 42, 6331-6334.

473. D. Yu, Y. Yang, M. Durstock, J.-B. Baek and L. Dai, *ACS Nano*, 2010, 4, 5633-5640.

474. D. Luo, G. Zhang, J. Liu and X. Sun, *J. Phys. Chem. C*, 2011, 115, 11327-11335.

References

475. B. Apostolovic, M. Danial and H. A. Klok, *Chem. Soc. Rev.*, 2010, 39, 3541-3575.

476. G. L. C. Paulus, Q. H. Wang and M. S. Strano, *Acc. Chem. Res.*, 2013, 46, 160-170.

477. A. C. Ferrari, *Solid State Commun.*, 2007, 143, 47-57.

478. M. Jana, S. Saha, P. Khanra, P. Samanta, H. Koo, N. C. Murmu and T. Kuila, *J. Mater. Chem. A*, 2015, 3, 7323-7331.

479. E. Y. Choi, T. H. Han, J. H. Hong, J. E. Kim, S. H. Lee, H. W. Kim and S. O. Kim, *J. Mater. Chem.*, 2010, 20, 1907-1912.

480. K. S. Kim, Y. M. Um, J.-r. Jang, W.-S. Choe and P. J. Yoo, *Acs. Appl. Mater. Interfaces*, 2013, 5, 3591-3598.

481. A. Ghosh, K. V. Rao, S. J. George and C. N. R. Rao, *Chem. Eur. J.*, 2010, 16, 2700-2704.

482. H. Q. Li, L. N. Han, J. J. Cooper-White and I. Kim, *Nanoscale*, 2012, 4, 1355-1361.

483. G. C. Wei, R. H. Dong, D. Wang, L. Feng, S. L. Dong, A. X. Song and J. C. Hao, *New J. Chem.*, 2014, 38, 140-145.

484. Y. H. Park, S. Y. Park and I. In, *J. Ind. Eng. Chem.*, 2015, 30, 190–196.

485. G. C. Wei, M. M. Yan, R. H. Dong, D. Wang, X. Z. Zhou, J. F. Chen and J. C. Hao, *Chem. Eur. J.*, 2012, 18, 14708-14716.

References

486. R. Kanchanapally, B. P. Viraka Nellore, S. S. Sinha, F. Pedraza, S. J. Jones, A. Pramanik, S. R. Chavva, C. Tchounwou, Y. Shi, A. Vangara, D. Sardar and P. C. Ray, *RSC Adv.*, 2015, 5, 18881-18887.

487. H. Wang, Q. Zhang, X. Chu, T. Chen, J. Ge and R. Yu, *Angew. Chem. Int. Ed.*, 2011, 50, 7065-7069.

488. S. Goenka, V. Sant and S. Sant, *J. Controlled Release*, 2014, 173, 75-88.

489. L. Lacerda, S. Raffa, M. Prato, A. Bianco and K. Kostarelos, *Nano Today*, 2007, 2, 38-43.

490. D. Kölmel, D. Fürniss, S. Susanto, A. Lauer, C. Grabher, S. Bräse and U. Schepers, *Pharmaceuticals*, 2012, 5, 1265-1281.

491. J. E. Murphy, T. Uno, J. D. Hamer, F. E. Cohen, V. Dwarki and R. N. Zuckermann, *PNAS*, 1998, 95, 1517-1522.

492. P. A. Wender, D. J. Mitchell, K. Pattabiraman, E. T. Pelkey, L. Steinman and J. B. Rothbard, *PNAS*, 2000, 97, 13003-13008.

493. T. Schroder, K. Schmitz, N. Niemeier, T. S. Balaban, H. F. Krug, U. Schepers and S. Brase, *Bioconj. Chem.*, 2007, 18, 342-354.

494. W. Huang, J. Seo, J. S. Lin and A. E. Barron, *Mol. Biosyst.*, 2012, 8, 2626-2628.

495. J. Q. Liu, L. Tao, W. R. Yang, D. Li, C. Boyer, R. Wuhrer, F. Braet and T. P. Davis, *Langmuir*, 2010, 26, 10068-10075.

References

496. B. Wozniak and J. Dera, in *Light Absorption in Sea Water*, Springer, New York, 2007, ch.2, pp 11-81.

497. S. Sivakova and S. J. Rowan, *Chem. Soc. Rev.*, 2005, 34, 9-21.

498. M. Ginisty, C. Gravier-Pelletier and Y. Le Merrer, *Tetrahedron: Asymmetry*, 2006, 17, 142-150.

499. T. Yajima, T. Tonoi, H. Nagano, Y. Tomita and K. Mikami, *Eur. J. Org. Chem.*, 2010, 2461-2464.

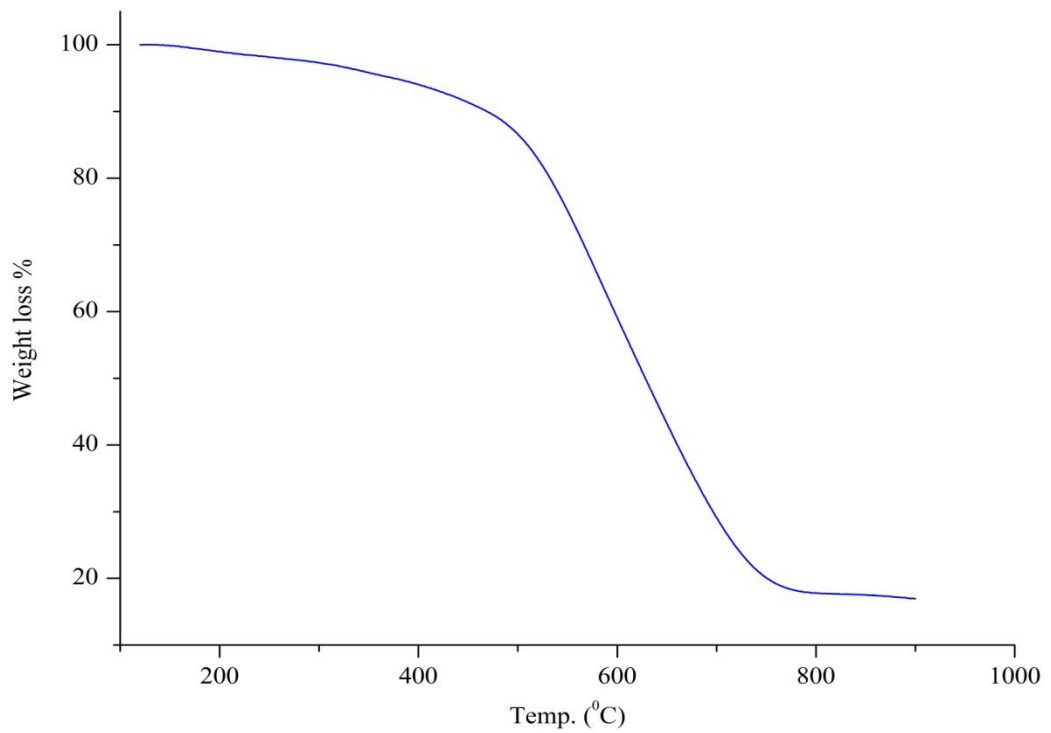500. L. Jobron and G. Hummel, *Org. Lett.*, 2000, 2, 2265-2267.

Appendix A: Characterisation of Purified SWNTs
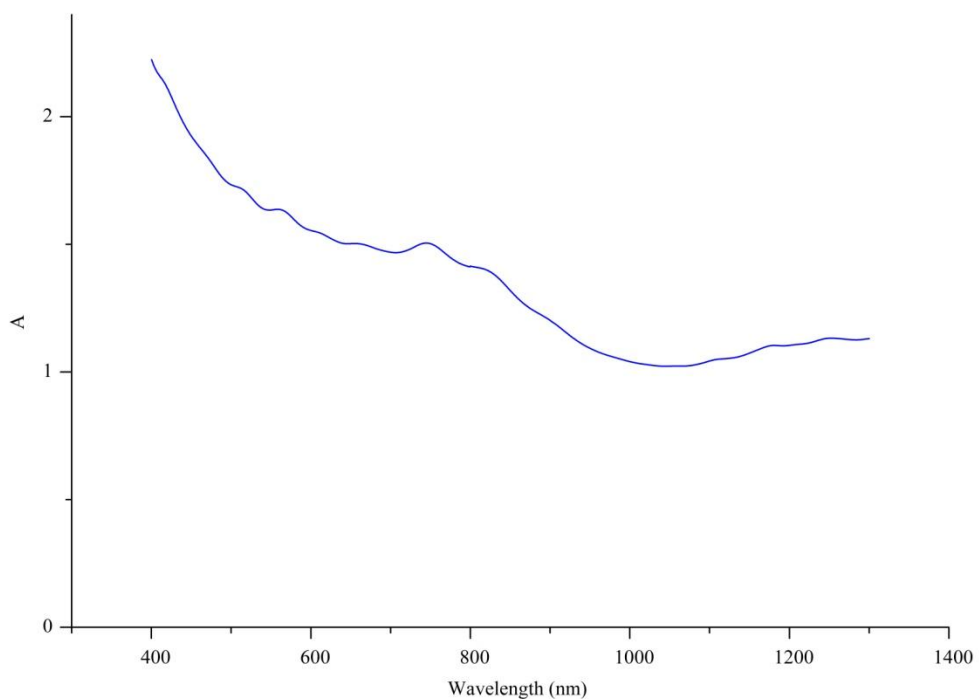
Figure 1: UV-Vis-NIR absorption of purified SWNTs in 1% SDS after sonication and centrifugation.
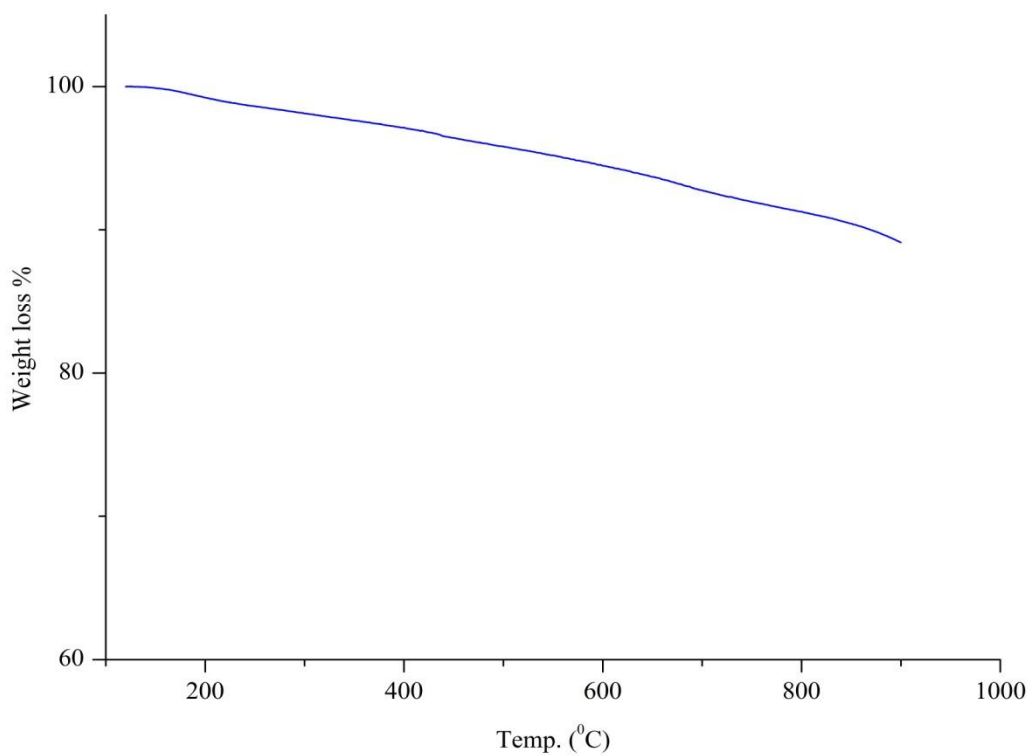
Figure 2: TGA-Ms of purified SWNTs under N_2 atmosphere.

Figure 3: TGA-Ms of purified SWNTs under air atmosphere.
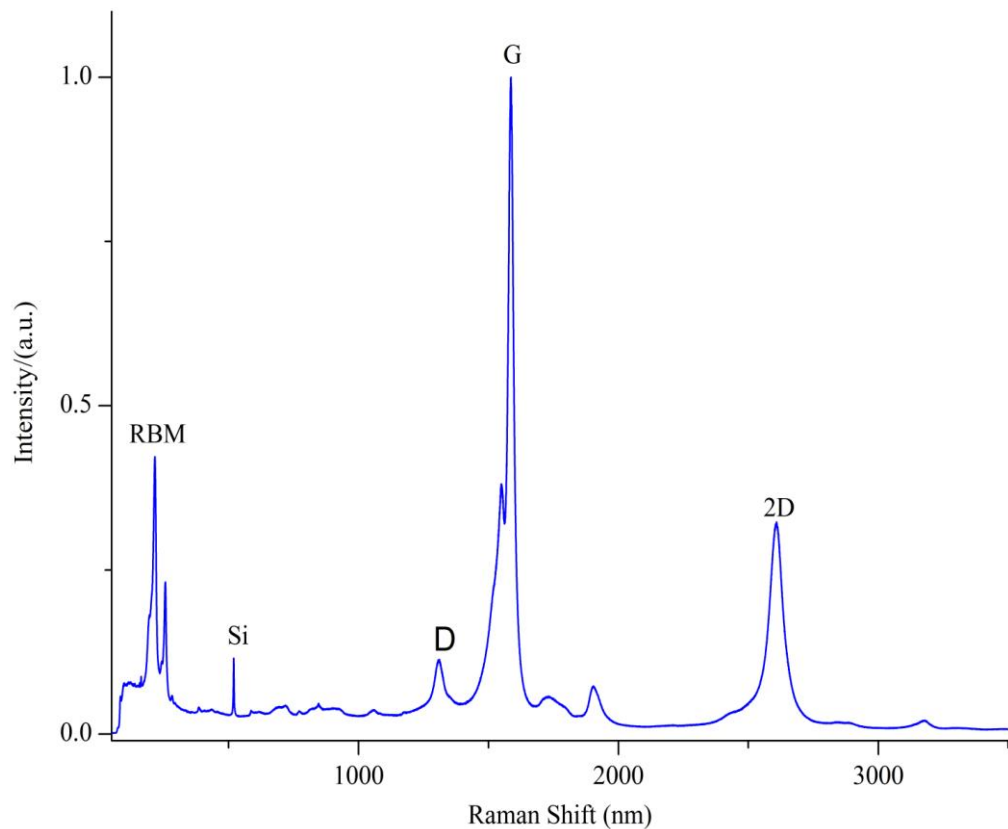
Figure 4: A representative Raman spectra (633 nm) of purified SWNTs normalised to the G band.

Appendix B: Extinction Coefficient of Carbon Nanomaterials

1. Extinction Coefficient of Purified SWNTs:
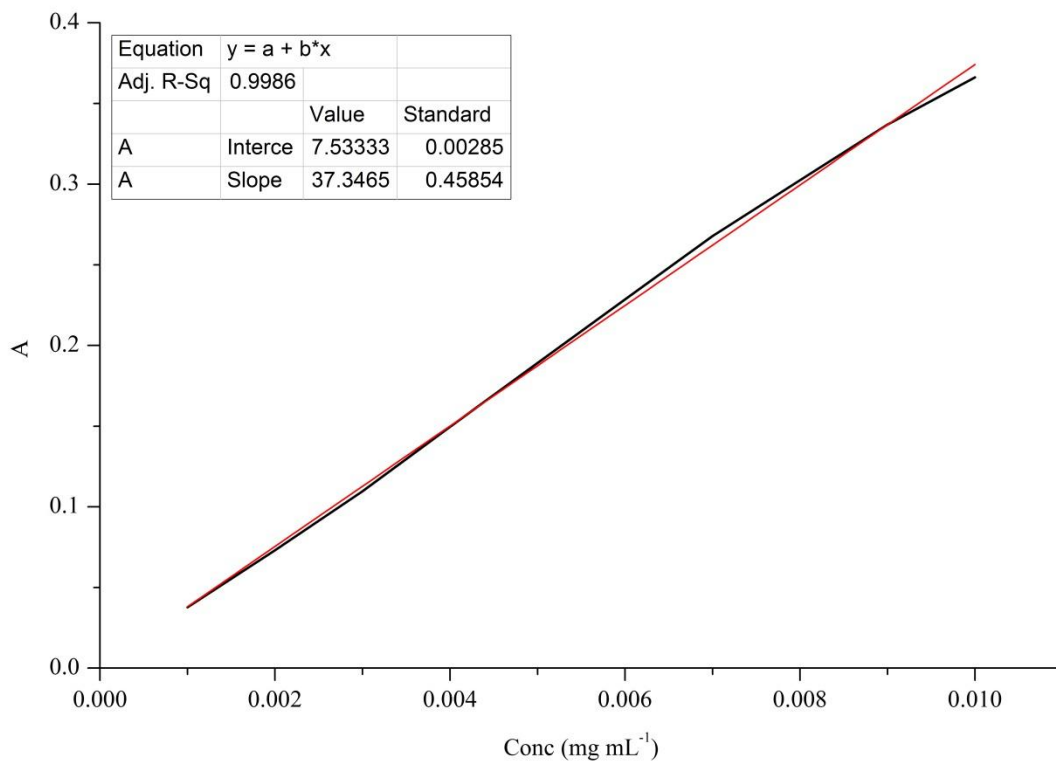
Figure 5: UV-Vis-NIR absorption of purified SWNTs at different concentrations in water.

2. Extinction Coefficient of 2 M Oxidised SWNTs
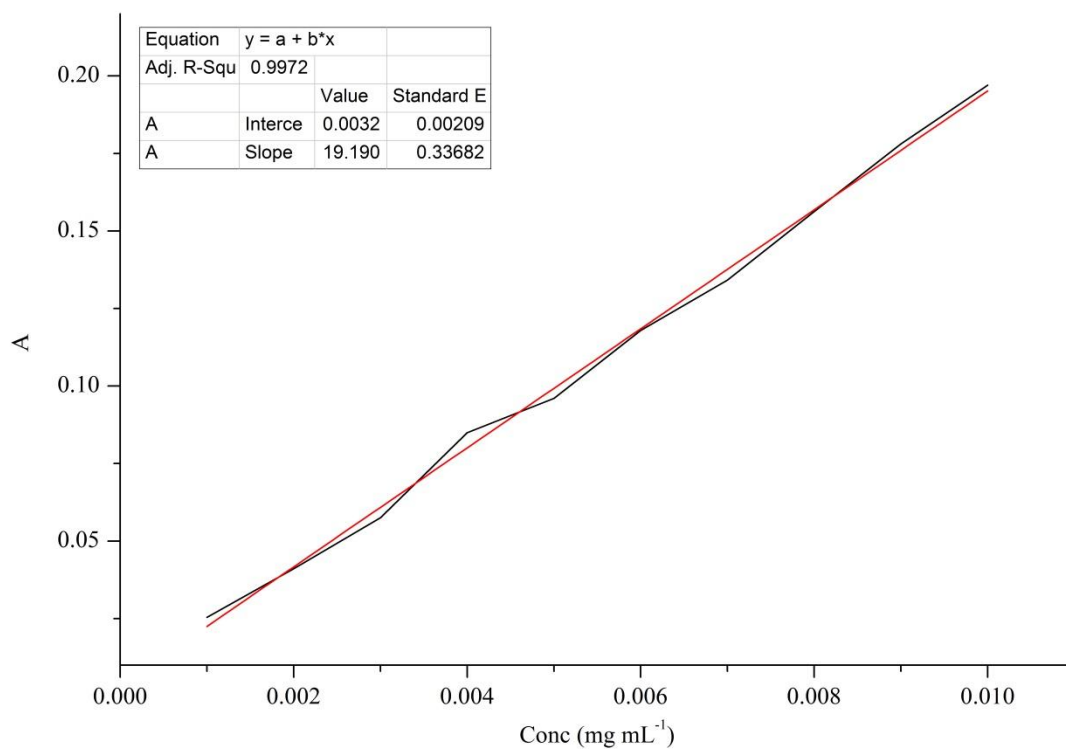
**Figure 6**: UV-Vis-NIR absorption of oxidised SWNTs (2 M) at different concentrations in water.

3. Extinction Coefficient of 8 M Oxidised SWNTs

Equation	y = a + b*x		
Adj. R-S	0.993		
		Value	Standard
Absorpti	Interce	-7.6333	0.00236
Absorpti	Slope	14.4403	0.38025
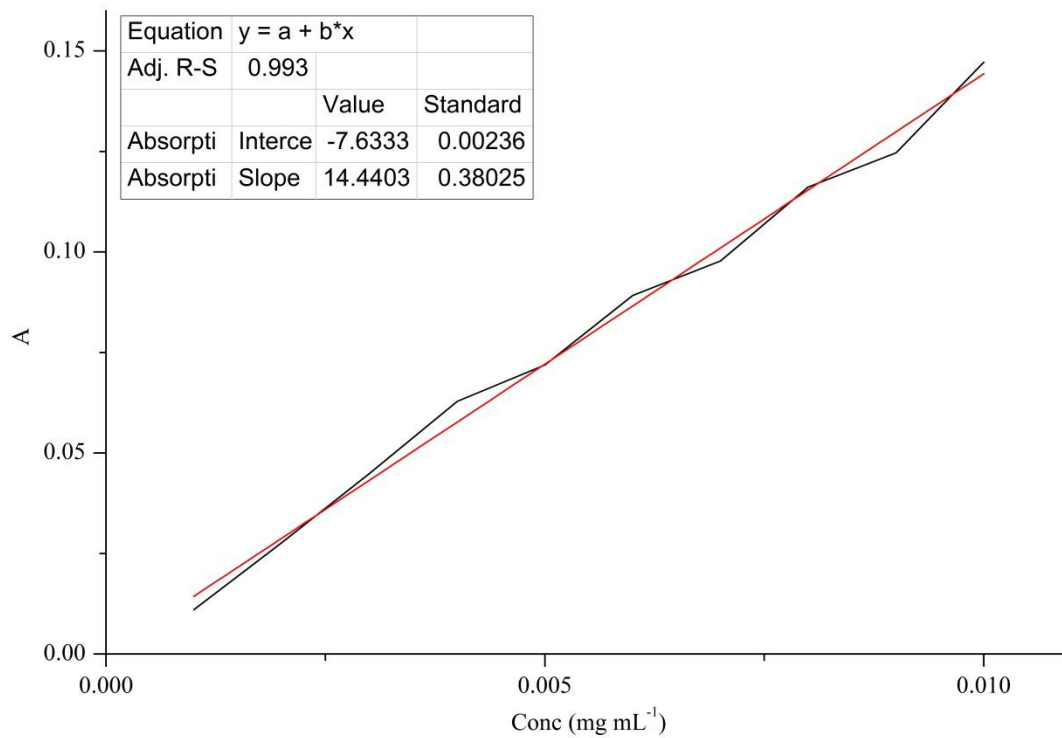
Figure 7: UV-VIS-NIR absorption of oxidised SWNTs (8 M) at different concentrations in water.

4. Extinction Coefficient of Reduced Graphene Oxide (rGO)
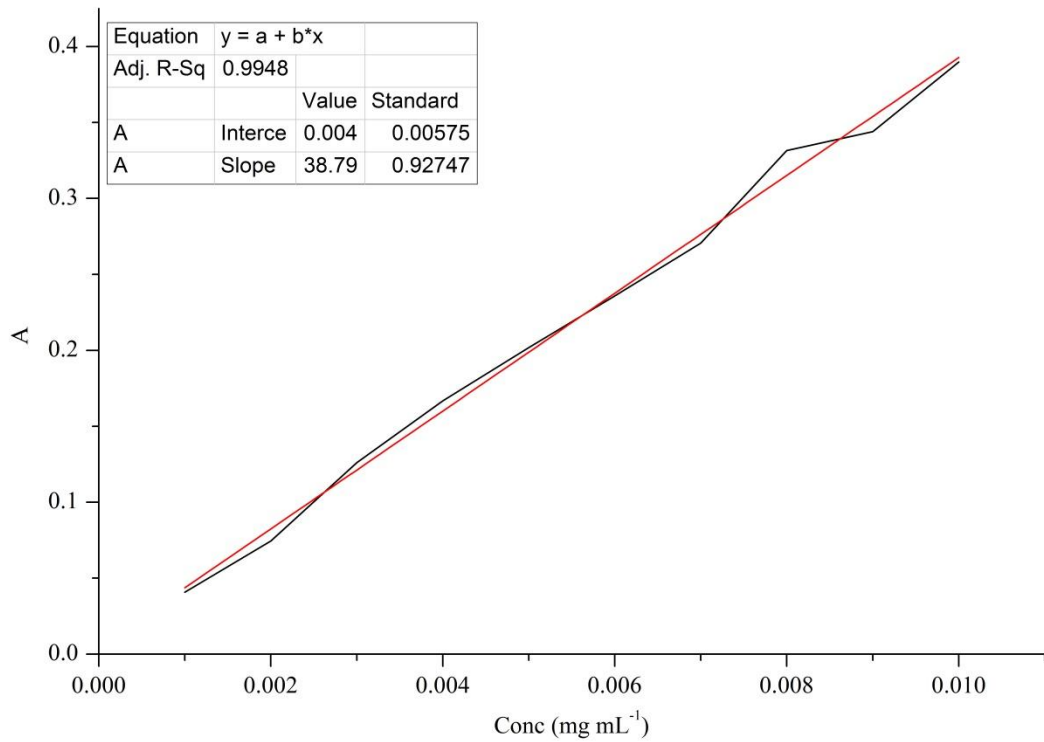
Figure 8: UV-Vis-NIR absorption of rGO in water.

Appendix C: Characterisation of Peptoids

1. Characterisation of (*N*lys*N*spe*N*spe)$_2$ (**14**)
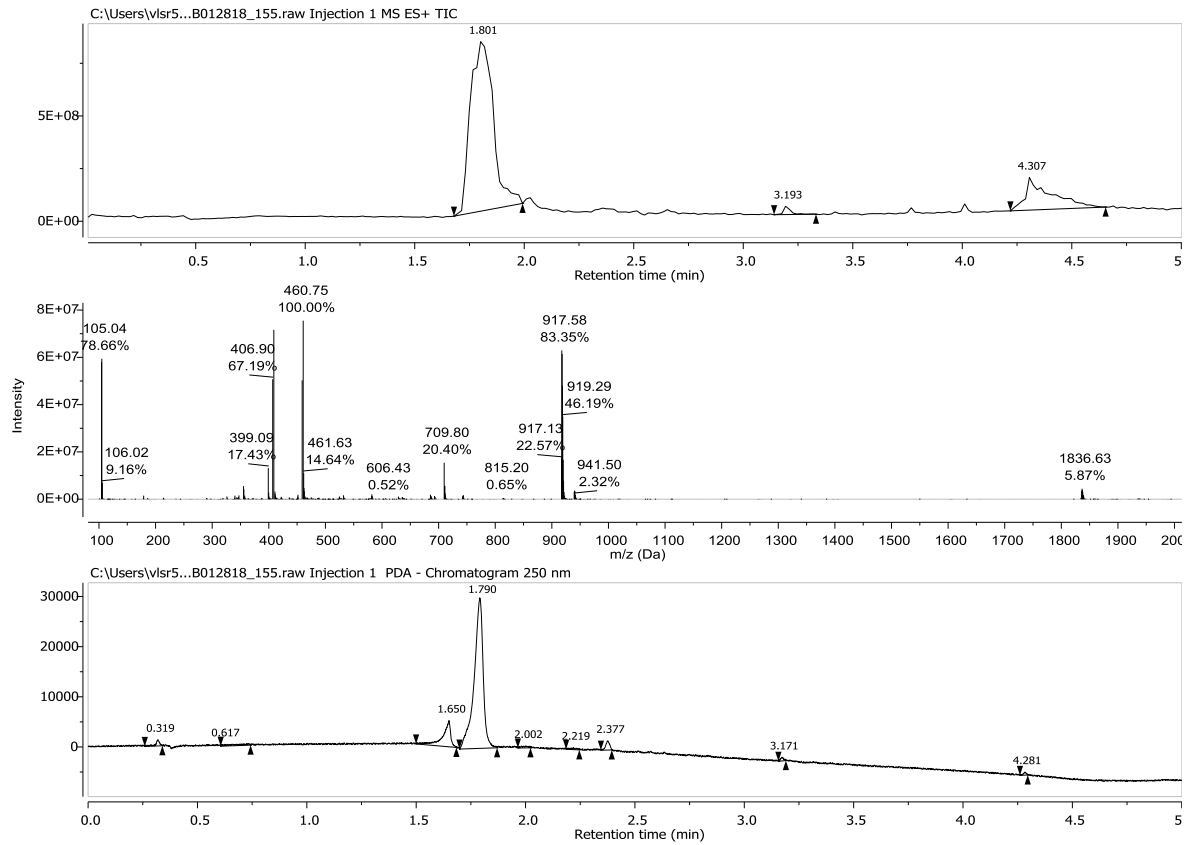
Figure 9: HR-LC MS of (*N*lys*N*spe*N*spe)$_2$ (**14**)

2. Characterisation of (*N*lys*N*spe*N*spe)$_3$ (**15**)

C:\Users\vlsr5...B024810_925.raw Injection 1 MS ES+ TIC
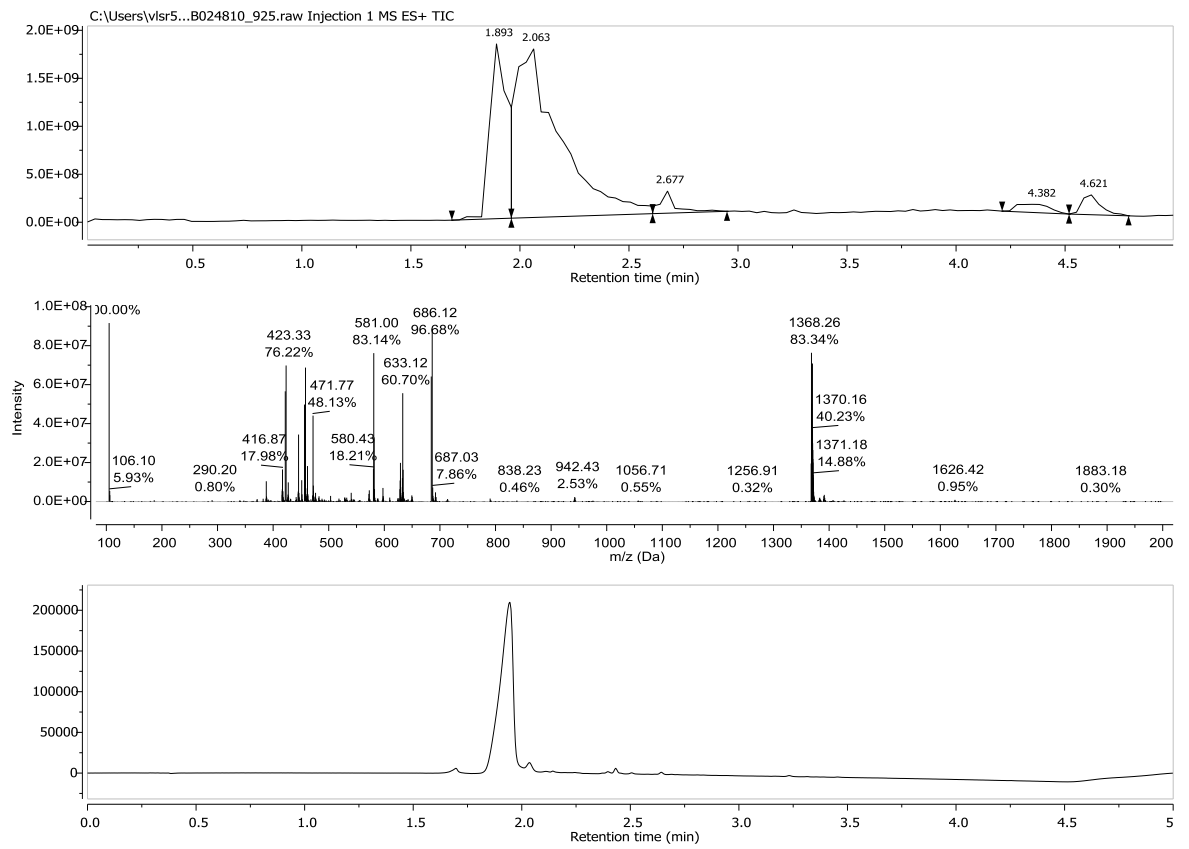
Figure 10: HR-LC MS of (*N*lys*N*spe*N*spe)$_3$ (**15**)

3. Characterisation of (*N*lys*N*spe*N*spe)$_4$ (**16**)
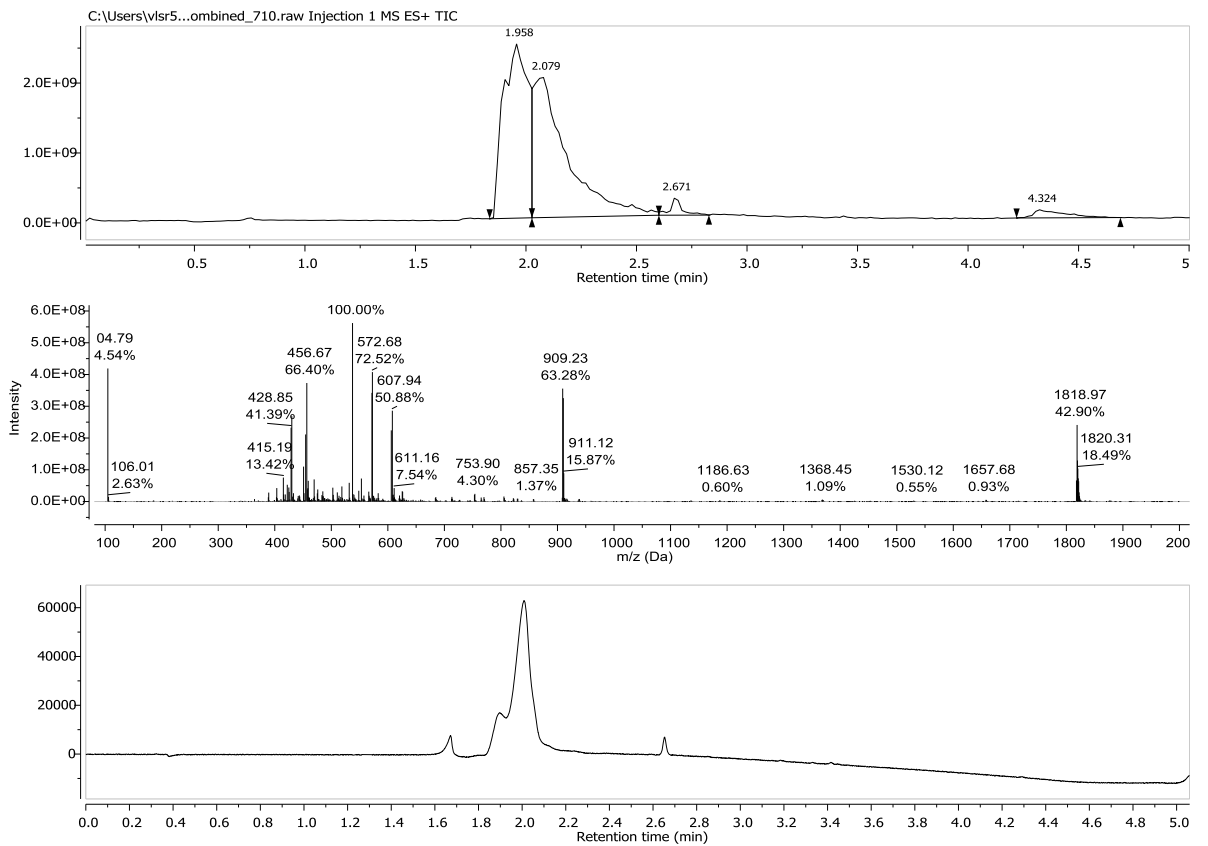
Figure 11: HR-LC MS of (*N*lys*N*spe*N*spe)$_4$ (**16**)

4. Characterisation of (*N*lys*N*spe*N*spe)$_6$ (**17**)
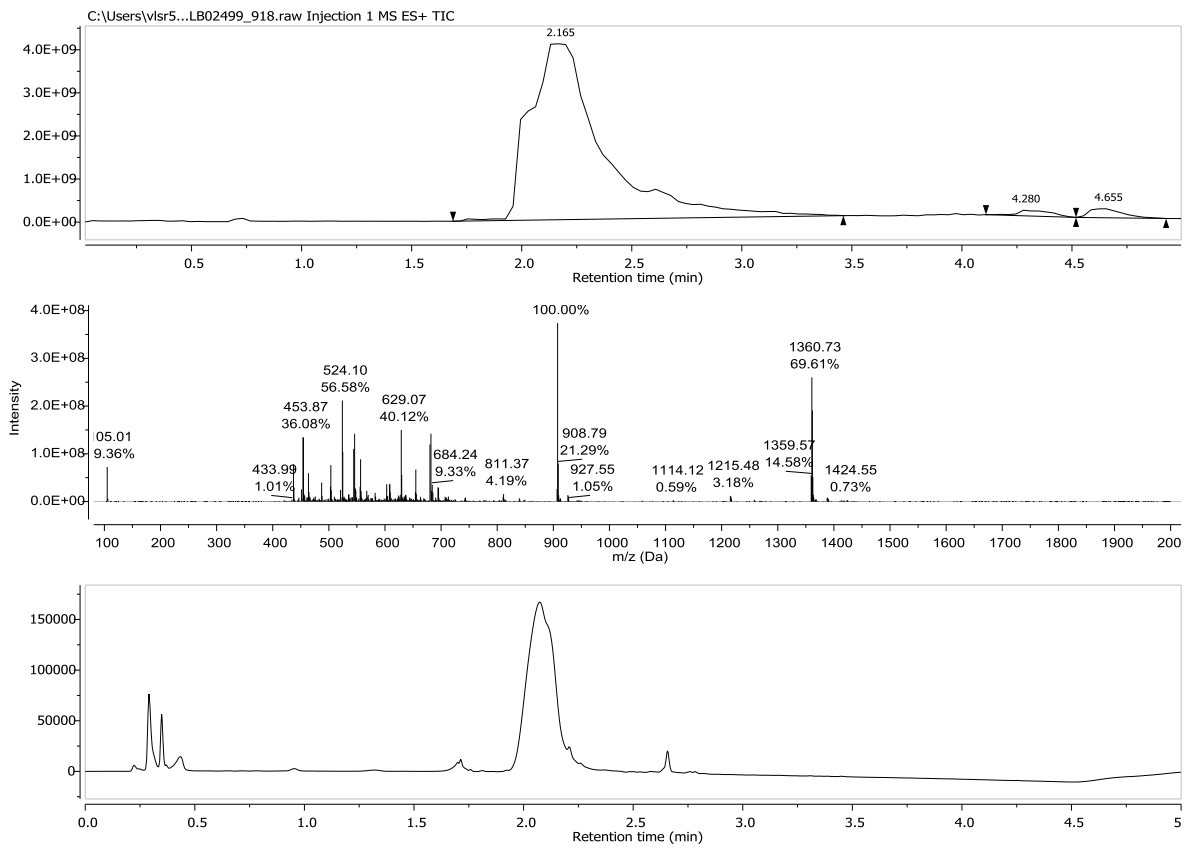
Figure 12: HR-LC MS of (*N*lys*N*spe*N*spe)$_6$ (**17**)

5.   Characterisation of Ac-*N*glu-*N*lys-*N*lys-Nlys-*N*phe (**18**)
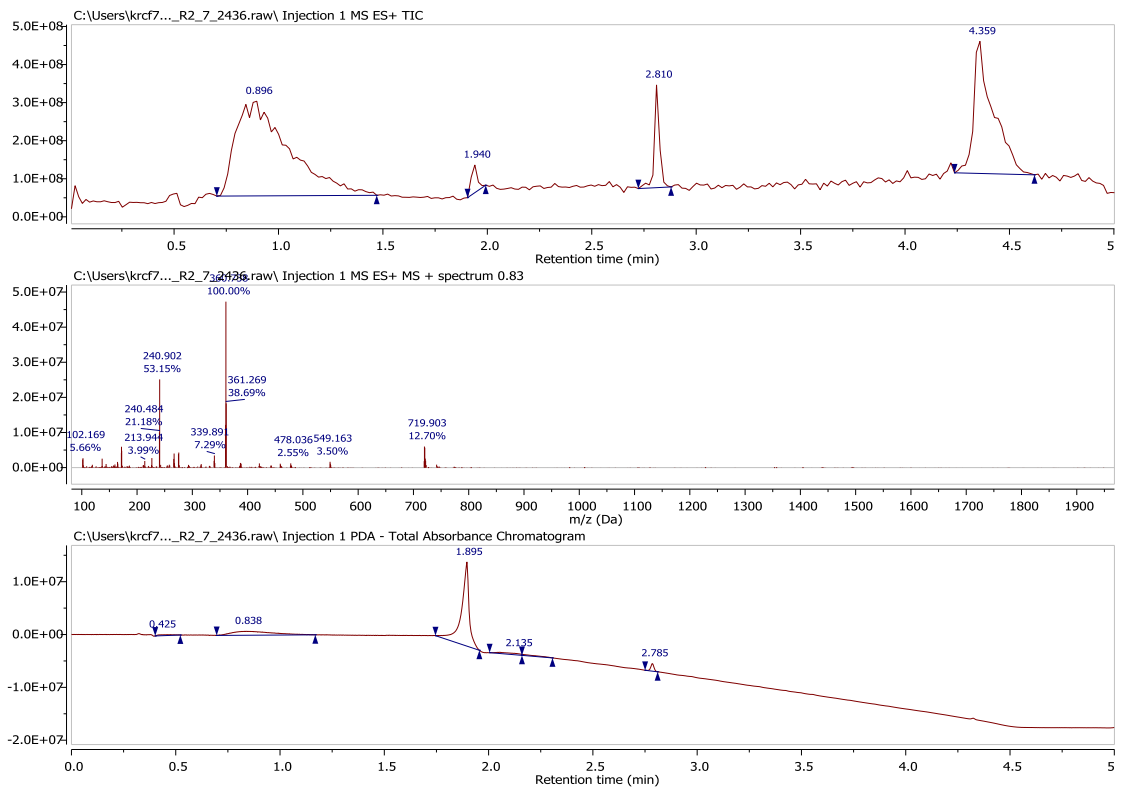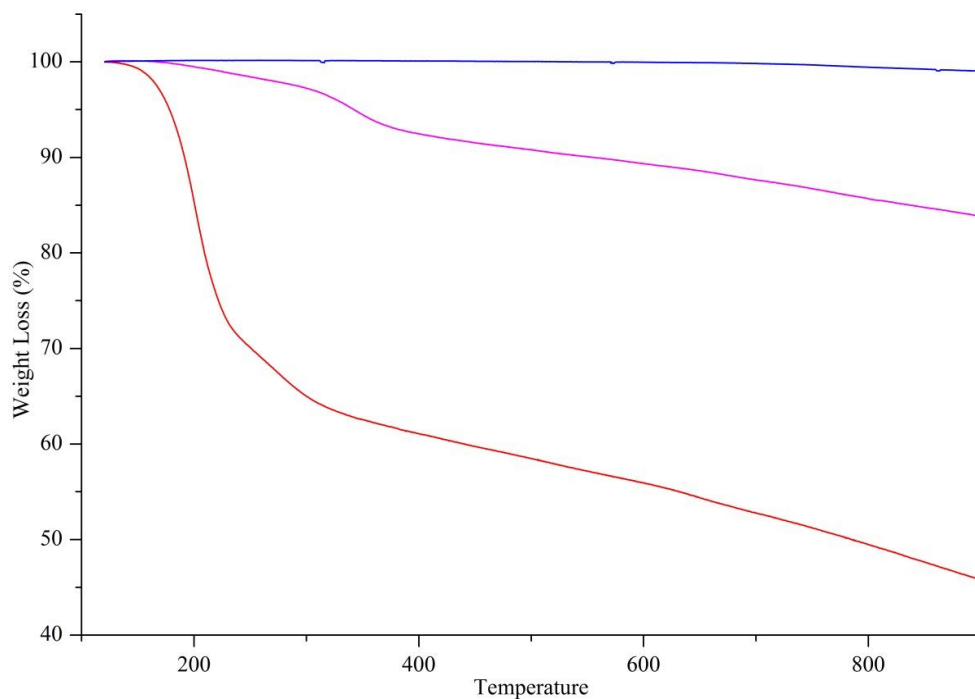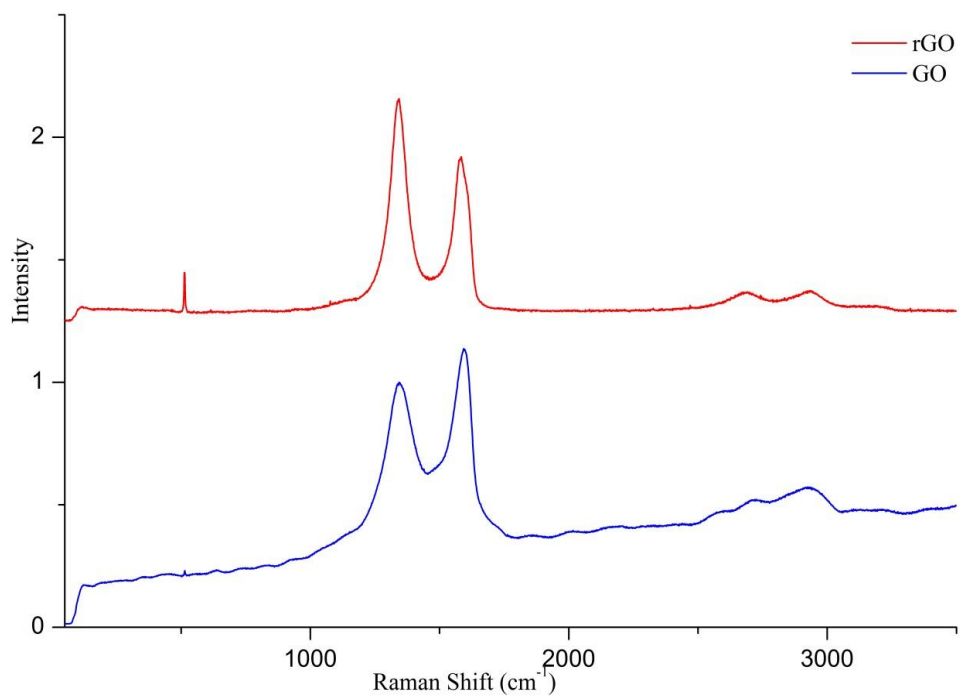

Figure 13: HR-LC MS of Ac-*N*glu-*N*lys-*N*lys-Nlys-*N*phe (**18**)

Appendix D: Characterisation of GO and rGO

Figure 14: TGA curves of graphite (**Blue line**), GO (**Red line**), and rGO (**Pink line**).

Figure 15: A representative Raman spectra (532 nm) of GO (**Blue line**), and rGO (**Red line**) normalised to G band.